2D and 3D quantitative TEM mapping of CoNi nanowires

Ingrid Marie Andersen

To cite this version:

Ingrid Marie Andersen. 2D and 3D quantitative TEM mapping of CoNi nanowires. Micro and nanotechnologies/Microelectronics. Université Paul Sabatier - Toulouse III, 2020. English. NNT : 2020TOU30205 . tel-03193994

HAL Id: tel-03193994
https://theses.hal.science/tel-03193994

Submitted on 9 Apr 2021

THÈSE

En vue de l'obtention du

DOCTORAT DE L'UNIVERSITÉ DE TOULOUSE

Délivré par l'Université Toulouse 3 - Paul Sabatier

Présentée et soutenue par

Ingrid Marie ANDERSEN

Le 26 octobre 2020

2D and 3D quantitative TEM mapping of CoNi nanowires

Ecole doctorale : **SDM - SCIENCES DE LA MATIERE - Toulouse**

Spécialité : **Nanophysique**

Unité de recherche :
CEMES - Centre d'Elaboration de Matériaux et d'Etudes Structurales

Thèse dirigée par
Etienne SNOECK et Christophe GATEL

Jury
Mme Martha McCARTNEY, Rapporteure
M. César MAGÉN, Rapporteur
Mme Agustina ASENJO BARAHONA, Examinatrice
M. Julian CARREY, Examinateur
M. Axel LUBK, Invité
M. Aurélien MASSEBOEUF, Invité
M. Thomas BLON, Invité
M. Etienne SNOECK, Directeur de thèse
M. Christophe GATEL, Co-directeur de thèse

THÈSE

En vue de l'obtention du

DOCTORAT DE L'UNIVERSITÉ DE TOULOUSE

Délivré par l'Université Toulouse 3 - Paul Sabatier

Présentée et soutenue par

Ingrid Marie ANDERSEN

Le 26 octobre 2020

Cartographies 2D et 3D de configurations magnétiques de nanofils de CoNi

Ecole doctorale : **SDM - SCIENCES DE LA MATIERE - Toulouse**

Spécialité : **Nanophysique**

Unité de recherche :
CEMES - Centre d'Elaboration de Matériaux et d'Etudes Structurales

Thèse dirigée par
Etienne SNOECK et Christophe GATEL

Jury
Mme Martha McCARTNEY, Rapporteure
M. César MAGÉN, Rapporteur
Mme Agustina ASENJO BARAHONA, Examinatrice
M. Julian CARREY, Examinateur
M. Axel LUBK, Invité
M. Aurélien MASSEBOEUF, Invité
M. Thomas BLON, Invité
M. Etienne SNOECK, Directeur de thèse
M. Christophe GATEL, Co-directeur de thèse

Acknowledgment

First of all, I would like to express my deepest appreciation to my defense jury committee. A special thanks to Martha McCartney and César Magén for accepting the role of referees and Julien Carrey for the role of the jury's president. To the rest of the jury and invited members, Agustina Asenjo, Aurélien Masseboeuf, Thomas Blon and Axel Lubk, thank you all for your good questions, animated discussions, and kind words. I am so grateful for all your feedback.

The work presented in this manuscript has been possible due to the effort and collaboration of several people. First and foremost, completing this work and my dissertation would not have been possible without the support and guidance of my dear supervisors, Christophe Gatel and Etienne Snoeck. Thank you for granting me this opportunity to do my thesis at the CEMES and allowing me to learn and use so many different techniques, and teaching me all you know about electron holography on magnetic samples. Thank you for your confidence and for giving me independence and flexibility to manage and perform my own experiments, and to try and fail, which has taught me so much. And, of course, thank you for your patience with me and all my "blah blah," and for your calming trust and encouragement when I would stress over deadlines or being nervous for presentations. It has been an honor, and I am forever grateful.

In addition, I want to express my immense gratitude to my out-of-lab collaborators that have joined me in completing the studies presented in this thesis. A most special thanks to Luis Alfredo Rodríguez (Universidad del Valle), Daniel Wolf, and Axel Lubk (IFW Dresden), I hope you know how special our collaborations have been to me and how much I have enjoyed working with you. I have learned so much from our hours at the microscope, our video conference meetings, as well as the visits and social outings before COVID-19. It has been a pleasure.

A big thanks to Agustina Asenjo, Manuel Vazquez, and Cristina Bran for inviting me to their lab at the ICMM in Madrid to learn about the synthesis of magnetic nanowires by electrodeposition. I am also grateful to Cristina Bran for providing me with the interesting nanowire sample that became the base of this work and doing her best to provide me with samples even when the situation made it difficult due to time constraints and even a lockdown.

I would also like to extend my deepest gratitude to Aurélien Masseboeuf, who has, since the start at CEMES, kept on including me in discussing different projects and been happy to teach me anything I asked. I have learned so much from you, both in terms of technical skills and the attitude of not giving up and keep trying different ideas.

I also had great pleasure of working with Olivier Fruchart, Michael Schöbitz, and Laura Alvaro Gomez at CEA Spintec. Thank you for giving me the opportunity to join in performing x-ray microscopy experiments at both PSI and SOLEIL and teaching me hands-on about time-resolved and *in situ* biasing experiments on nanowires. A special thanks to Michael Schöbitz for sharing your knowledge on *in situ* sample preparation and nanowire contacting by lithography and for teaching me that neat trick with the nitrile gloves.

Many thanks also to Javier Pablo Navarro, for your valuable advice in focused ion and electron beam deposition for sample contacting, and to César Magèn and José María de Teresa for receiving us in their lab at ICMA in Zaragoza.

I also want to give a big thanks to Michael Lehmann and Tore Niermann at TU Berlin for good conversations and for giving us access to do tomography experiments on their dedicated Titan microscope.

I could not have been successful without all the help and support from my in-lab colleagues. A big thanks to the I3EM group members, for your help, feedback, and discussion. A special thanks to Sophie for always volunteering as a test audience for my presentations, offering me life-saving chocolate, and with Florent, helped me work through challenges with the *in situ* setup at the I2TEM. Thank you, Mireille, for helping me with payment issues and booking (and sometimes re-booking) of my travels, always with a positive attitude and a friendly smile. A big thanks to Robin Cours and Raphaël Serra for showing me the ropes on the SEM/FIB and accepting my challenges in trying new approaches for preparing my samples. Thank you, Cécile Marcelot and Florent Houdellier, for your patience and enthusiasm in teaching me about TEM and for your trust, letting me spend long hours at the I2TEM. At least you have a nice little picture collection as a souvenir, Cécile, thank you for your contagious humor and our good conversations. Thanks also to Sebastien Joulie and Daniela Oliveros, for helping me perform my ASTAR experiments and data processing, and Maria Teresa Hungria for helping me with EELS measurements together with Cécile. Thanks to Abraao for always being happy and patient in helping me with any questions about lithography procedures in the cleanroom. And finally, a huge thanks to Lucas for joining and helping me in my *in situ* adventures. I might be biased (hoho), but I think we are a good team. I also gratefully acknowledge Christian at the electronics service and Dominique and Catherine at the sample preparation lab for always being helpful and lending me equipment again and again (and again).

In addition, I feel so grateful to have met so many genuinely kind people that have become my friends. A special thanks to Ségolène (or Mia?), Daniela, Camille, Silvia, Winnie, Soumaya for all the fun times and good conversations, both in and outside the lab, and for all the ones yet to come! Thank you Rémi for always reminding me of the worst-case scenarios, and more importantly, for being my high-society, cultural Opera-buddy. Also, a big thanks to Guillaume (best office roomie!), Romain, David Cameron, Melvyn, Rachma, Julian, Raj, Nicolas, and all my other fellow PhDs and Post-Docs for contributing to the supportive environment I experienced through my three years at CEMES.

Last but not least, I want to thank all my friends, my family, and my Boris for your endless love and support.

Abstract

Cylindrical magnetic nanowires (NWs) are currently subjects of high interest due to fast domain wall velocities and interaction with spin-waves, which are considered interesting qualities for developing future spintronic devices. This thesis aims to provide a wholesome quantitative and qualitative analysis of the local magnetic configuration in cylindrical Co-rich CoNi NWs with perpendicular magnetocrystalline anisotropy using state-of-the-art transmission electron microscopy (TEM) magnetic imaging techniques, mainly focused on two-dimensional (2D) and three-dimensional (3D) electron holography (EH). A correlative study between the NW's texture, modulation in composition, and magnetic configuration has been conducted. Further, the complex 3D nature of the domain and domain wall configurations have been analyzed using holographic vector field electron tomography (VFET) to retrieve all three components of the magnetic induction. Finally, I have successfully manipulated the magnetic configuration observed by Lorentz microscopy in Fresnel mode by the *in situ* injection of a current pulse.

A TEM study comparing the magnetic configuration to the local NW structure was performed on single NWs. The crystal phase analysis was done by precession electron diffraction assisted automated crystal orientation mapping in the TEM combined with compositional analysis by scanning-TEM (STEM) electron energy loss spectroscopy (EELS) for a detailed correlation with the sample's magnetic configuration. The results reveal a coexistence of *fcc* grains and *hcp* phase with its *c*-axis oriented close to perpendicular to the wire axis in the same NW, which is identified as the origin of drastic local changes in the magnetic configuration. Two main configurations are observed in the NW region: a chain of transversal vortex-like states and a longitudinal curling state. The chain or vortices are linked to the *hcp* grain with the

perpendicular magnetocrystalline anisotropy, as confirmed by micromagnetic simulations.

The 3D magnetic structure of the domains and domain walls observed in the *hcp* grain of the NWs has been studied for two different remnant states: after the application of a saturation field perpendicular (i) and parallel (ii) to the NW axis. The measurements were done using state-of-the-art holographic VFET to extract all three components of the magnetic induction in the sample, as well as a 3D reconstruction of the volume from the measured electric potentials, giving insight into the local morphology of the NW. The results show a stabilization of a vortex chain in the case of perpendicular saturation, but longitudinal curling states separated by transversal domain walls after applying a parallel external field.

Finally, preliminary Lorentz microscopy results are presented, documenting the manipulation of magnetic domain walls by the *in situ* injection of electrical pulses on a single cylindrical CoNi nanowire contacted by focused ion beam induced deposition. This is believed to be the forerunner for quantitative electrical measurements and *in situ* observations of domain wall dynamics using EH at the CEMES. A detailed protocol focusing on the crucial steps and challenges ahead for such a delicate experiment is presented, together with suggestions for future work to continue the developments.

Résumé

Les nanofils magnétiques constituent un domaine de recherche en plein essor. De section cylindrique, ils permettent la propagation des parois de domaines magnétiques à très grandes vitesses et des interactions fortes avec les ondes de spin, ce qui les rend particulièrement intéressants pour le développement de futurs composants de la spintronique. L'objectif de ce travail de thèse est de fournir une analyse quantitative et qualitative complète de la configuration magnétique locale dans des nanofils magnétiques cylindriques d'alliage CoNi à anisotropie magnétocristalline perpendiculaire en utilisant les techniques d'imagerie magnétique avancées de la microscopie électronique à transmission (MET), principalement axées sur l'holographie électronique (HE). Une étude corrélative entre les propriétés structurales, les variations locales de composition et les configurations magnétiques de ces nanofils a été réalisée. De plus, les configurations tridimensionnelles (3D) complexes des domaines et des parois magnétiques ont été analysées par tomographie holographique de champ vectoriel (THCV) afin d'obtenir les trois composantes de l'induction magnétique. Enfin, un protocole a été développé pour étudier in situ par microscopie de Lorentz la configuration magnétique de ces nanofils lors de l'injection d'impulsions de courant.

La première partie de ce travail est focalisée sur la corrélation des configurations magnétiques de nanofils individuels de CoNi avec les propriétés structurales et chimiques locales. L'orientation de la phase cristalline a été cartographiée en diffraction électronique par précession et combinée à des mesures de composition par spectroscopie de perte d'énergie des électrons. Les résultats révèlent une coexistence de grains de phase cfc et de phase hcp, cette dernière présente sa direction cristallographique c orientée presque perpendiculairement à l'axe du nanofil. Cette coexistence de phases cristallographiques est à l'origine de variations

localisées et abruptes de la configuration magnétique. Deux configurations principales ont été observées : une chaîne d'états transversaux par rapport à l'axe du nanofil, de type vortex, et un état longitudinal. Nous avons observés que les états transversaux sont liés à la phase hcp possédant une forte anisotropie magnétocristalline perpendiculaire, ce que confirment les simulations micromagnétiques.

Une autre partie de ce travail concerne l'étude de la structure magnétique 3D des domaines et des parois de domaines dans la phase hcp. Cette étude a été menée pour des états rémanents différents en fonction de l'application d'un champ de saturation perpendiculaire et parallèle à l'axe du nanofil. Les mesures ont été réalisées par la méthode THCV afin d'extraire les trois composantes de l'induction magnétique et reconstruire en 3D la configuration magnétique locale du nanofil. Les résultats montrent une stabilisation d'une chaîne de vortex dans le cas d'une saturation perpendiculaire, et des états d'enroulement longitudinaux séparés par des parois de domaine transversales après l'application d'un champ externe parallèle à l'axe du fils.

La dernière partie du manuscrit présente les résultats obtenus en microscopie de Lorentz in situ démontrant la possibilité de manipuler les parois des domaines magnétiques d'un nanofil de CoNi par injection d'impulsions électriques. Cette preuve de concept est considérée comme le précurseur des observations in situ de la dynamique des parois de domaines en EH. Un protocole précis, axé sur les étapes cruciales de préparation des échantillons et les développements à poursuivre pour réaliser ces expériences délicates, est détaillé.

Abbreviations

1D	one-dimensional
2D	two-dimensional
3D	three-dimensional
AAO	anodic aluminium oxide
AFM	antiferromagnetic
ASTAR	NanoMEGAS software for crystal orientation mapping
BFTEM	bright field transmission electron microscopy
CCD	charge coupled device
CCW	counterclockwise
C-FEG	cold field emission gun
CMOS	complimentary metal oxide semiconductor
CW	clockwise
DFTEM	dark field transmission electron microscopy
DP	diffraction pattern
DW	(magnetic) domain wall
EBL	electron beam lithography
ED	electron diffraction
EDX	energy dispersive x-ray spectroscopy
EELS	electron energy loss spectroscopy
EH	(off-axis) electron holography
fcc	face centered cubic (crystal structure)
FEBID	focused electron beam induced deposition
FFT	fast Fourier transform
FFT^{-1}	inverse fast Fourier transform
FIB	focused ion beam
FIBID	focused ion beam induced deposition
FM	ferromagnetic
FWHM	full width at half maximum

GIS	gas injection system
GMR	giant magnetoresistance
hcp	hexagonal close-packed (crystal structure)
HRTEM	high-resolution transmission electron microscopy
I2TEM	dedicated Hitachi HF3300-C *in situ* and interferometric TEM at CEMES
LBL	laser beam lithography
LLG	Landau-Lifshitz-Gilbert (equation)
LM	Lorentz microscopy
MCA	magnetocrystalline anisotropy
MFM	magnetic force microscopy
MIP	mean inner potential
MLLS	multiple linear least squares (spectral fitting)
MOKE	magneto-optical Kerr effect (microscopy)
MRAM	magnetic random access memory
MRI	magnetic resonance imaging
NW	nanowire
OL	objective lens
PED	precession electron diffraction
PEEM	photoemission electron microscopy
RKKY	Ruderman-Kittel-Kasuya-Yoshida (interaction)
SAED	selected area electron diffraction
SEM	scanning electron microscopy
S-FEG	Schottky field emission gun
STEM	scanning transmission electron microscopy
STXM	scanning transmission x-ray microscopy
TDW	transverse domain wall
TEM	transmission electron microscopy
TIE	transport of intensity equation
UV	ultraviolet (electromagnetic radiation)
VFET	vector field electron tomography
VLS	vapour-liquid-solid
XMCD	x-ray magnetic circular dichroism
XRD	x-ray diffraction

Contents

Chapter 1

Introduction and motivation

The history of magnetism takes us back to before 600 B.C. in ancient Greece where the first magnets, in the form of iron-oxide rocks (lodestones), were made close to a town in Asia Minor named "Magnesia ad Sipylum" and thus originating the words *magnetite* and *magnetism*.[1] Humans have taken advantage of magnetic phenomena to build tools since as early as the second century B.C., where the first documented version of the compass in old Chinese literature, the *south pointer*, has been dated back to. This first magnetic device consisted of a lodestone carved in the shape of a spoon to rest on its base and orient its handle with the earth's magnetic field.[2]

Today, magnets and magnetic devices have become a huge part of our daily life as crucial components in appliances ranging from credit cards or simple toys to more advanced household and tech devices. Important technologies in areas like transport, medicine, and communication have been developed based on the physics of magnets and electromagnetism. Some examples are high-speed maglev trains, Magnetic Resonance Imaging (MRI) machines, and hard disk drives.

As our understanding of magnetism and magnetic phenomena developed from being considered a sort of magic created by a lightning strike to the discoveries and founding of the field of electromagnetism in the 19th century (Ampère, Ørsted, Faraday and Maxwell), and the birth of quantum mechanics in the 20th century, we now understand more and more of the microscopic origin of magnetism and its possible applications. We now know that there are different types of magnetism: antiferromagnetism, ferrimagnetism, paramagnetism, and diamagnetism, other than ferromagnetism, which is the type of material first described as magnets in ancient texts and that can be magnetized into what is called a permanent magnet.[3]

When magnets are scaled down to the nano-regime, with dimensions comparable or smaller than some physical properties' characteristic length scales, new magnetic properties are observed.[4] One example of this is the super-paramagnetic state displayed by magnetic nanoparticles with their size reduced below the typical domain wall width.[5] Other examples are thin films with their magnetization oriented perpendicular to the sample plane in films with a strong uniaxial magnetocrystalline anisotropy and a transversal easy axis direction.[6]

For the past few decades, there has been an increased focus on researching new novel solid-state devices based on the physics of magnetism. Major advances include the discovery of the Giant Magnetoresistance (GMR) effect,[7,8] which was rewarded the Nobel Prize in Physics in 2007 due to its significant application in magnetic data storage. The knowledge that one can use electricity (charge) to manipulate magnetic spin through spin-charge interactions have led to the new field of applied magnetism called Spintronics,[9] where the goal is to make improved technological devices based on spin manipulation.[10,11] To achieve this and build the spintronic devices of the future, however, one needs to develop suitable nanostructures and materials, and increase our knowledge in their magnetic behavior.

1.1 Prospects for novel nanowire based devices

The electronics industry has long been reducing the size of devices in an exponentially decreasing manner, as famously pointed out by Dr. Gordon E. Moore,[12] in order to improve memory and processing time. However, we have reached a point where the development of semiconductor chips can no longer keep up with the so-called "Moore's law" due to a combination of lack of heat dissipation, due to closely packed structures on a chip, source-to-drain leakage due to a device size of close to the atom-scale, and high costs of research and development of new devices.[12,13] In order to continue the improvement of memory storage and processing power, spintronic devices are believed to be the building block for the technologies of the future.[10,11,14] Famous examples of such devices include the magnetic domain wall racetrack memory,[15] Magnetic Random Access Memory (MRAM) such as the spin-transfer torque MRAM,[16–18] or memory devices based on spin Hall/Rashba effect.[19,20]

The extraordinary recent developments in Nanoscience and technologies, combined with the improvements in nanofabrication techniques, make it possible to make smaller and more complex nanosystems.[21–25] Although many of the logic and memory options first suggested were based on thin films and nanostrips, *i.e.* well defined flat structures mainly produced by lithographic processes, cylindrical nanowires (NWs) have received much attention in the last years due to suppression of walker breakdown and prospects of magnetic domain wall (DW) velocities up to 1 km/s or large interaction with spin-waves.[26–29] If one can carefully design and understand the magnetic spin texture of nanowires, they could be building blocks for DW-based memory devices.

1.2 Progress in magnetic nanowire elaboration and measurement techniques

Magnetic nanowires can be elaborated by a variety of techniques, either by bottom-up approaches, like chemical vapor deposition,[30] molecular beam epitaxy,[31] focused electron beam induced deposition (FEBID),[32] or by top-down approaches, like UV-, electron- or ion-beam lithography (producing nanostrips).[33] Recent years have seen high popularity in template-assisted chemically synthesized nanowires, like electrodeposition. Advances in fabrication by such techniques enable the tuning of both size[34,35] and crystal structure,[36–38] as well as a vast mix of materials,[39–41] both in terms of creating new alloys and for growing heterostructured nanowires,[24,42,43] and make them relatively cheap to produce. One can even tune magnetocrystalline anisotropy (MCA) by engineering a monocrystalline *hcp* phase with a variable c-axis orientation relative to the wire axis.[44] This can result in an MCA challenging the normally dominant shape anisotropy in high ratio NWs and has been reported to be the origin of surprising magnetic configurations.[45,46]

Nanowires have often been approximated as one-dimensional systems in previous literature, arguably due to a tendency of a uniaxial magnetization along the wire axis due to the shape anisotropy. However, all three dimensions are needed to describe domain walls successfully,[47,48] and the complex domains that arise in cylindrical nanowires,[49] where especially three-dimensional states like vortices have been reported.[50,51] The understanding of the fine structures of domain walls in NWs is essential in order to achieve the necessary control for application in devices. However, the decrease in dimensions, together with the increased sophistication of nanosystems, put a huge demand on magnetic measurement techniques.[10] There are many different techniques to measure magnetic properties in materials. Some of them are based on averaged measurements, like vibrating sample magnetometer (VSM)[39,52] or nuclear magnetic resonance (NMR),[53] while others allow mapping of the magnetic properties of single nanostructures, like magnetic force microscopy (MFM),[33,54,55] x-ray based imaging techniques like x-ray magnetic circular dichroism (XMCD)[56] or scanning transmission x-ray microscopy (STXM),[57] or transmission electron microscopy (TEM) based magnetic imaging like Lorentz microscopy (LM)[22] and electron holography (EH).[58] To determine the local spin configurations of domain walls in nanostructures, high sensitivity and high spatial resolution magnetic mapping is required. Electron holography is one of the most powerful magnetic imaging techniques for studying local magnetic states with a high spatial resolution. Due to many great advances in TEM instrumentation, like the invention of aberration correction and the double biprism setup for EH, as well as the great increase in computational power the past decades,[10,59] EH can now enable the studying of the fine structure of domain walls with spatial resolution down to 5 Å. Still, like many other magnetic imaging techniques, EH can only offer a two-dimensional (2D) projection of the magnetic configuration. However, by combining EH with tomographic techniques, holographic vector field electron tomography (VFET) provides a reconstruction of all three components of the magnetic field in the sample with a spatial resolution below 10 nm.[60]

While it is crucial to understand the fine structure of magnetic domains and domain walls, the ultimate goal is for the structures to be used in devices, and for this, one needs to control the magnetic states through current injection. However, domain wall dynamics in cylindrical nanowires have almost only been studied theoretically by simulations,[61] and only a few experimental studies are starting to emerge for techniques like XMCD-PEEM (photoemission electron microscopy) and MFM.[62,63] While we have yet to see such an experiment performed in a TEM environment using magnetic imaging techniques, one can imagine that such an *in situ* method could uncover and enable the study of new magnetic phenomena.

1.3 Objectives and outline of the thesis

The aim of this thesis is to present a deep qualitative and quantitative analysis of local magnetic configurations in cylindrical Co-rich CoNi NWs with perpendicular magnetocrystalline anisotropy using state-of-the-art TEM magnetic imaging techniques, mainly focused on two-dimensional (2D) and three-dimensional (3D) EH. To ensure a wholesome understanding of the nanostructure and reveal the origin of the observed magnetic spin texture, the presented studies combine structural, spectroscopic, and magnetic mapping on single nanostructures to get correlative, quantitative results, revealing effects of local changes in crystal structure to the observed magnetic configurations. The remnant state has been studied after the application of an external magnetic saturation field with different orientations relative to the wire axis. The complex 3D nature of the magnetic spin texture has been uncovered using state-of-the-art holographic VFET and compared qualitatively and quantitatively to complimentary micromagnetic simulations.

Following the present introduction (*Chapter 1*), the rest of the thesis is organized into five chapters as follows:

Chapter 2, titled *Micromagnetism: an introduction*, gives an overview of the basic concepts in magnetism, covering the origin of magnetism on the atomic scale and the fundamentals of ferromagnetism. An introduction to the micromagnetic energies and the formation of magnetic domains and domain walls in ferromagnetic materials is presented, followed by a description of magnetic states in nanowires. Finally, a section covering micromagnetic simulations and its contribution to experimental magnetic measurements is presented.

In *Chapter 3*, titled "*Experimental Techniques*", the main methods used for fabrication and characterization of the magnetic nanostructures are described. A large part of Chapter 3 is dedicated to an introduction to transmission electron microscopy magnetic imaging, with a detailed explanation of electron holography and magnetic vector field electron tomography, the two main techniques used in the studies of the presented works in this thesis. An overview of the structural characterization and spectroscopy techniques used is then given before an explanation of the fundamentals of electrodeposition for the fabrication of magnetic nanowires.

Chapter 4, titled "*Effects of local structural changes on the magnetic configuration in CoNi nanowires*", presents quantitative studies of the complex magnetic configurations in $Co_{85}Ni_{15}$ cylindrical nanowires. The fine structural changes in magnetic states are studied by electron holography and correlated with structural and compositional measurements to reveal the origin of the observed exotic magnetic texture.

Chapter 5, titled "*Field tunable 3D magnetic states in CoNi nanowires*", explores the change in the magnetic remnant state of CoNi nanowire, with *hcp* phase and transversal oriented magnetocrystalline anisotropy, after the application of a saturation field (i) perpendicular and (ii) parallel to the wire axis. As a continuation of the research presented in Chapter 4, this study reveals all three components of the magnetic induction recorded using holographic vector field electron tomography and offers a deeper understanding and characterization of the magnetic domain walls in the 3D magnetic nanotextures.

Chapter 6, titled "*Preliminary in situ magnetic transport studies in the TEM,*" presents preliminary results from Fresnel imaging observations while respectively applying a magnetic field and injecting an electric current, in order to *in situ* study the stability, reproducibility, and manipulation of the magnetic configuration in a CoNi NW. The chapter also outlines a protocol for performing an *in situ* biasing experiment to study the magnetic domain wall motion in nanowires by electric pulse injection in the I2TEM. Extra focus is made on the challenges and conditions to successfully inject current in such NWs, and a call to action for future work is suggested, with the aim of achieving quantitative electric measurements combined with electron holography imaging of the domain wall structures.

Finally, *Chapter 7* gives a summary of this thesis and its main conclusions and offers an outline of future work that can be made as a continuation of the presented findings.

References

[1] E. D. T. de Lacheisserie et al. "Magnetism, from the dawn of civilization to today". In: *Magnetism*. Springer Science and Business Media, 2005. Chap. 1. ISBN: 0-387-22967-1.

[2] M. W. McElhinny. *The Earth's Magnetic Field: Its History, Origin, and Planetary Perspective*. Academic Press, 1984. ISBN: 0-12-491240-0.

[3] J. M. D. Coey. *Magnetism and Magnetic Materials*. Cambridge University Press, 2010. DOI: 10.1017/CBO9780511845000.

[4] C. L. Dennis et al. "The Defining Length Scales of Mesomagnetism: A Review". In: *Journal of Physics: Condensed Matter* **14** (2002), R1175–R1262. DOI: 10.1088/0953-8984/14/49/201.

[5] V. Skumryev et al. "Beating the Superparamagnetic Limit with Exchange Bias". In: *Nature* **423** (2003), pp. 850–853. DOI: 10.1038/nature01687.

[6] M. Hehn et al. "Nanoscale Magnetic Domain Structures in Epitaxial Cobalt Films". In: *Physical Review B* **54** (1996), pp. 3428–3433. DOI: 10.1103/PhysRevB.54.3428.

[7] M. N. Baibich et al. "Giant Magnetoresistance of (001)Fe/(001)Cr Magnetic Superlattices". In: *Physical Review Letters* **61** (1988), pp. 2472–2475. DOI: 10.1103/PhysRevLett.61.2472.

[8] G. Binasch et al. "Enhanced Magnetoresistance in Layered Magnetic Structures with Antiferromagnetic Interlayer Exchange". In: *Physical Review B* **39** (1989), pp. 4828–4830. DOI: 10.1103/PhysRevB.39.4828.

[9] S. Bhatti et al. "Spintronics Based Random Access Memory: A Review". In: *Materials Today* **20** (2017), pp. 530–548. DOI: 10.1016/j.mattod.2017.07.007.

[10] D. Sander et al. “The 2017 Magnetism Roadmap”. In: *Journal of Physics D: Applied Physics* **50** (2017), p. 363001. DOI: 10.1088/1361-6463/aa81a1.

[11] A. Hirohata et al. “Review on Spintronics: Principles and Device Applications”. In: *Journal of Magnetism and Magnetic Materials* **509** (2020), p. 166711. DOI: 10.1016/j.jmmm.2020.166711.

[12] G. E. Moore. “Cramming More Components Onto Integrated Circuits”. In: *Proceedings of the IEEE* **86** (1998), pp. 82–85. DOI: 10.1109/JPROC.1998.658762.

[13] M. M. Waldrop. “The Chips Are down for Moore’s Law”. In: *Nature News* **530** (2016), p. 144. DOI: 10.1038/530144a.

[14] S. A. Wolf et al. “Spintronics: A Spin-Based Electronics Vision for the Future”. In: *Science* **294** (2001), pp. 1488–1495. DOI: 10.1126/science.1065389.

[15] S. S. P. Parkin, M. Hayashi, and L. Thomas. “Magnetic Domain-Wall Racetrack Memory”. In: *Science* **320** (2008), pp. 190–194. DOI: 10.1126/science.1145799.

[16] A. D. Kent and D. C. Worledge. “A New Spin on Magnetic Memories”. In: *Nature Nanotechnology* **10** (2015), pp. 187–191. DOI: 10.1038/nnano.2015.24.

[17] S.-W. Chung et al. “4Gbit density STT-MRAM using perpendicular MTJ realized with compact cell structure”. In: *IEEE International Electron Devices Meeting* (2016), pp. 27.1.1–27.1.4. DOI: 10.1109/IEDM.2016.7838490.

[18] E. A. Montoya et al. “Immunity of Nanoscale Magnetic Tunnel Junctions with Perpendicular Magnetic Anisotropy to Ionizing Radiation”. In: *Scientific Reports* **10** (2020), p. 10220. DOI: 10.1038/s41598-020-67257-2.

[19] I. M. Miron et al. “Perpendicular Switching of a Single Ferromagnetic Layer Induced by In-Plane Current Injection”. In: *Nature* **476** (2011), pp. 189–193. DOI: 10.1038/nature10309.

[20] L. Liu et al. “Spin-Torque Switching with the Giant Spin Hall Effect of Tantalum”. In: *Science* **336** (2012), pp. 555–558. DOI: 10.1126/science.1218197.

[21] V. Gopal et al. “Rapid Prototyping of Site-Specific Nanocontacts by Electron and Ion Beam Assisted Direct-Write Nanolithography”. In: *Nano Letters* **4** (2004), pp. 2059–2063. DOI: 10.1021/nl0492133.

[22] L. A. Rodríguez et al. “Optimized Cobalt Nanowires for Domain Wall Manipulation Imaged by in Situ Lorentz Microscopy”. In: *Applied Physics Letters* **102** (2013), p. 022418. DOI: 10.1063/1.4776709.

[23] C. Phatak et al. “Visualization of the Magnetic Structure of Sculpted Three-Dimensional Cobalt Nanospirals”. In: *Nano Letters* **14** (2014), pp. 759–764. DOI: 10.1021/nl404071u.

[24] Y. P. Ivanov et al. “Modulated Magnetic Nanowires for Controlling Domain Wall Motion: Toward 3D Magnetic Memories”. In: *ACS Nano* **10** (2016), pp. 5326–5332. DOI: 10.1021/acsnano.6b01337.

[25] J. Pablo-Navarro et al. “Diameter Modulation of 3D Nanostructures in Focused Electron Beam Induced Deposition Using Local Electric Fields and Beam Defocus”. In: *Nanotechnology* **30** (2019), p. 505302. DOI: 10.1088/1361-6528/ab423c.

[26] M. Yan et al. “Beating the Walker Limit with Massless Domain Walls in Cylindrical Nanowires”. In: *Physical Review Letters* **104** (2010), p. 057201. DOI: 10.1103/PhysRevLett.104.057201.

[27] S. Da Col et al. “Observation of Bloch-Point Domain Walls in Cylindrical Magnetic Nanowires”. In: *Physical Review B* **89** (2014), p. 180405. DOI: 10.1103/PhysRevB.89.180405.

[28] S. Jamet et al. “Head-to-Head Domain Walls in One-Dimensional Nanostructures: An Extended Phase Diagram Ranging from Strips to Cylindrical Wires”. In: *Magnetic Nano- and Microwires*. Ed. by M. Vázquez. Woodhead Publishing, 2015. Chap. 25, pp. 783–811. DOI: 10.1016/B978-0-08-100164-6.00025-4.

[29] R. Hertel. “Ultrafast Domain Wall Dynamics in Magnetic Nanotubes and Nanowires”. In: *Journal of Physics: Condensed Matter* **28** (2016), p. 483002. DOI: 10.1088/0953-8984/28/48/483002.

[30] T. Kuykendall et al. “Metalorganic Chemical Vapor Deposition Route to GaN Nanowires with Triangular Cross Sections”. In: *Nano Letters* **3** (2003), pp. 1063–1066. DOI: 10.1021/nl034422t.

[31] D. Ren et al. “Single-Mode Near-Infrared Lasing in a GaAsSb-Based Nanowire Superlattice at Room Temperature”. In: *Nano Letters* **18** (2018), pp. 2304–2310. DOI: 10.1021/acs.nanolett.7b05015.

[32] J. Pablo-Navarro et al. “Tuning Shape, Composition and Magnetization of Three-Dimensional Cobalt Nanowires Grown by Focused Electron Beam Induced Deposition (FEBID)”. In: *Journal of Physics D: Applied Physics* **50** (2017), 18LT01. DOI: 10.1088/1361-6463/aa63b4.

[33] M. Jaafar et al. “Hysteresis Loops of Individual Co Nanostripes Measured by Magnetic Force Microscopy”. In: *Nanoscale Research Letters* **6** (2011), p. 407. DOI: 10.1186/1556-276X-6-407.

[34] C. Bran et al. “Spin Configuration of Cylindrical Bamboo-like Magnetic Nanowires”. In: *Journal of Materials Chemistry C* **4** (2016), pp. 978–984. DOI: 10.1039/C5TC04194E.

[35] J. Fernandez-Roldan et al. “Magnetization Pinning in Modulated Nanowires: From Topological Protection to the “Corkscrew” Mechanism”. In: *Nanoscale* **10** (2018), pp. 5923–5927. DOI: 10.1039/C8NR00024G.

[36] J. U. Cho et al. “Control of Magnetic Anisotropy of Co Nanowires”. In: *Journal of Magnetism and Magnetic Materials* **303** (2006), e281–e285. DOI: 10.1016/j.jmmm.2006.01.082.

[37] V. Vega et al. “Tuning the Magnetic Anisotropy of Co–Ni Nanowires: Comparison between Single Nanowires and Nanowire Arrays in Hard-Anodic Aluminum Oxide Membranes”. In: *Nanotechnology* **23** (2012), p. 465709. DOI: 10.1088/0957-4484/23/46/465709.

[38] Y. P. Ivanov et al. “Crystallographically Driven Magnetic Behaviour of Arrays of Monocrystalline Co Nanowires”. In: *Nanotechnology* **25** (2014), p. 475702. DOI: 10.1088/0957-4484/25/47/475702.

[39] E. M. Palmero et al. “Magnetic Behavior of NiCu Nanowire Arrays: Compositional, Geometry and Temperature Dependence”. In: *Journal of Applied Physics* **116** (2014), p. 033908. DOI: 10.1063/1.4890358.

[40] B. Rodríguez-González et al. “Structural and Magnetic Characterization of As-Prepared and Annealed FeCoCu Nanowire Arrays in Ordered Anodic Aluminum Oxide Templates”. In: *Journal of Applied Physics* **115** (2014), pp. 133904–133904. DOI: 10.1063/1.4870289.

[41] A. S. Samardak et al. “Variation of Magnetic Anisotropy and Temperature-Dependent FORC Probing of Compositionally Tuned Co-Ni Alloy Nanowires”. In: *Journal of Alloys and Compounds* **732** (2018), pp. 683–693. DOI: 10.1016/j.jallcom.2017.10.258.

[42] D. Reyes et al. “Magnetic Configurations in Co/Cu Multilayered Nanowires: Evidence of Structural and Magnetic Interplay”. In: *Nano Letters* **16** (2016), pp. 1230–1236. DOI: 10.1021/acs.nanolett.5b04553.

[43] E. Berganza Eguiarte et al. “Multisegmented Nanowires: A Step towards the Control of the Domain Wall Configuration”. In: *Scientific Reports* **7** (2017), p. 11576. DOI: 10.1038/s41598-017-11902-w.

[44] M. S. Arshad et al. “Effect of Magnetocrystalline Anisotropy on the Magnetic Properties of Electrodeposited Co–Pt Nanowires”. In: *Journal of Nanoparticle Research* **16** (2014), p. 2688. DOI: 10.1007/s11051-014-2688-4.

[45] K. Maaz et al. “Effect of Crystallographic Texture on Magnetic Characteristics of Cobalt Nanowires”. In: *Nanoscale Research Letters* **5** (2010), pp. 1111–1117. DOI: 10.1007/s11671-010-9610-5.

[46] M. S. Arshad et al. “The Role of the Crystal Orientation (c-Axis) on Switching Field Distribution and the Magnetic Domain Configuration in Electrodeposited Hcp Co–Pt Nanowires”. In: *Journal of Physics D: Applied Physics* **49** (2016), p. 185006. DOI: 10.1088/0022-3727/49/18/185006.

[47] J. M. Cowley. “Twenty Forms of Electron Holography”. In: *Ultramicroscopy* **41** (1992), pp. 335–348. DOI: 10.1016/0304-3991(92)90213-4.

[48] M. Staňo and O. Fruchart. “Magnetic nanowires and nanotubes”. In: *Handbook of magnetic materials*. Vol. 27. Elsevier, 2018. Chap. 3, pp. 155–267. ISBN: 9780444641618. DOI: 10.1016/bs.hmm.2018.08.002.

[49] R. Streubel et al. “Magnetism in Curved Geometries”. In: *Journal of Physics D: Applied Physics* **49** (2016), p. 363001. DOI: 10.1088/0022-3727/49/36/363001.

[50] Y. P. Ivanov et al. “Single Crystalline Cylindrical Nanowires – toward Dense 3D Arrays of Magnetic Vortices”. In: *Scientific Reports* **6** (2016), p. 23844. DOI: 10.1038/srep23844.

[51] C. Bran et al. “Direct Observation of Transverse and Vortex Metastable Magnetic Domains in Cylindrical Nanowires”. In: *Physical Review B* **96** (2017), p. 125415. DOI: 10.1103/PhysRevB.96.125415.

[52] Y. P. Ivanov et al. “Magnetic Structure of a Single-Crystal Hcp Electrodeposited Cobalt Nanowire”. In: *Europhysics Letters* **102** (2013), p. 17009. DOI: 10.1209/0295-5075/102/17009.

[53] V. Scarani, B. Doudin, and J.-P. Ansermet. “The Microstructure of Electrodeposited Cobalt-Based Nanowires and Its Effect on Their Magnetic and Transport Properties”. In: *Journal of Magnetism and Magnetic Materials* **205** (1999), pp. 241–248. DOI: 10.1016/S0304-8853(99)00513-2.

[54] T. Wang et al. “Magnetic Behavior in an Ordered Co Nanorod Array”. In: *Nanotechnology* **19** (2008), p. 455703. DOI: 10.1088/0957-4484/19/45/455703.

[55] E. Berganza et al. “Domain Wall Pinning in FeCoCu Bamboo-like Nanowires”. In: *Scientific Reports* **6** (2016), p. 29702. DOI: 10.1038/srep29702.

[56] S. Ruiz-Gómez et al. “Observation of a Topologically Protected State in a Magnetic Domain Wall Stabilized by a Ferromagnetic Chemical Barrier”. In: *Scientific Reports* **8** (2018), p. 16695. DOI: 10.1038/s41598-018-35039-6.

[57] M. Staňo et al. “Flux-Closure Domains in High Aspect Ratio Electroless-Deposited CoNiB Nanotubes”. In: *SciPost Physics* **5** (2018), p. 038. DOI: 10.21468/SciPostPhys.5.4.038.

[58] N. Biziere et al. “Imaging the Fine Structure of a Magnetic Domain Wall in a Ni Nanocylinder”. In: *Nano Letters* **13** (2013), pp. 2053–2057. DOI: 10.1021/nl400317j.

[59] A. Fernández-Pacheco et al. “Three-Dimensional Nanomagnetism”. In: *Nature Communications* **8** (2017), p. 15756. DOI: 10.1038/ncomms15756.

[60] D. Wolf et al. “Holographic Vector Field Electron Tomography of Three-Dimensional Nanomagnets”. In: *Communications Physics* **2** (2019), pp. 1–9. DOI: 10.1038/s42005-019-0187-8.

[61] H. Forster et al. “Domain Wall Motion in Nanowires Using Moving Grids”. In: *Journal of Applied Physics* **91** (2002), p. 6914. DOI: 10.1063/1.1452189.

[62] A. Wartelle et al. “Bloch-Point-Mediated Topological Transformations of Magnetic Domain Walls in Cylindrical Nanowires”. In: *Physical Review B* **99** (2019), p. 024433. DOI: 10.1103/PhysRevB.99.024433.

[63] M. Schöbitz et al. “Fast Domain Wall Motion Governed by Topology and Œrsted Fields in Cylindrical Magnetic Nanowires”. In: *Physical Review Letters* **123** (2019), p. 217201. DOI: 10.1103/PhysRevLett.123.217201.

Chapter 2

Micromagnetism: an introduction

2.1 Quantum origin of magnetism

2.1.1 Orbital and spin moments

Magnetism in materials derives from the magnetic moment of atoms, and more specifically, the angular momentum of their constitute electrons. There are two types of angular momenta of electrons: the orbital moment, **l**, which arises from the orbital motion of the electron around the atom nucleus, and the spin momentum, **s**, which is a quantum property intrinsic to the nature of electrons.

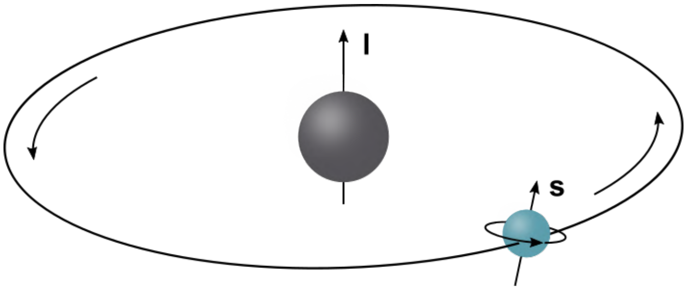

Figure 2.1: Schematics representing the two different angular momenta associated with an atomic electron: orbital angular momentum (**l**) and spin angular momentum (**s**)

2.1.2 Magnetic moment and spin-orbit coupling

For atoms composed of multiple electrons, the electrons' individual moments couple and give a total orbital angular momentum, $\mathbf{L}=\sum_i \mathbf{l}_i$, and a total spin angular moment, $\mathbf{S}=\sum_i \mathbf{s}_i$. From this, the electronic magnetic moment, μ, related to each total atomic angular momenta can be expressed as[1]

$$\mathbf{m}_L = -\mu_B \mathbf{L} \tag{2.1}$$

$$\mathbf{m}_S = -2\mu_B \mathbf{S} \tag{2.2}$$

where the Bohr magneton, $\mu_B = e\hbar/(2m) = 9.274 \cdot 10^{-24}$ J·T^{-1}, is a constant related to the electron charge e, the electron rest mass m, and the reduced Planck constant $\hbar$. An atom's total magnetic moment can therefore be expressed as[1]

$$\mathbf{m} = -\mu_B(\mathbf{L} + 2\mathbf{S}) \tag{2.3}$$

2.1.3 Pauli exclusion principle and Hund's rules

The Pauli exclusion principle states that two identical fermions (particles with half-integer spin, like electrons) cannot simultaneously occupy the same state within a quantum system.[2]

Hund's rules predict the ground state to determine the lowest energy state of an atom or an ion with multiple electrons.[2]From these rules it follows that the lowest energy state is reached by filling the electron shells with electrons of aligned spins and with one in each orbit. When all the states are occupied, electrons of opposite spin start to fill up the states, starting from the lowest energy state, until all states are filled with electron pairs of opposite spin. According to this, atoms with their electronic shells partly filled have a net spin magnetic moment with an amplitude greater than zero, while atoms with fully occupied shells have a net spin magnetic moment equal to zero. Thus, unpaired electrons in the atomic shells produce the magnetic response of the materials. This magnetic moment is given by[1]

$$\mathbf{m}_J = - g_J \mu_B \mathbf{J} \tag{2.4}$$

where $\mathbf{J}$ is the total electronic angular momentum of the unpaired electrons. g_J is the Landé g-factor given by[1]

$$g_J = 1 + \frac{J(J+1) + S(S+1) - L(L+1)}{2J(J+1)} \tag{2.5}$$

where L, S, and J are the different total quantum numbers.

2.1.4 Exchange interactions

From Equation 2.4 we see that both the orbital angular momentum and the spin angular moment contribute to the atomic magnetic moment, but the contribution due to spin is generally much larger. This is especially true for the ferromagnetic elements Fe, Co, and Ni, where the spin angular moment is about 10 times stronger than that of the orbital angular momentum.[1] In an assembly of atoms, like a crystal lattice, the atomic magnetic moments of neighboring atoms interact. This quantum phenomenon is called *exchange interaction*, and expresses the interaction energy of two unpaired electrons with spins $\mathbf{S}_i$ and $\mathbf{S}_j$ by[1–3]

$$\epsilon_{ex} = - 2J_{ij} \mathbf{S}_i \cdot \mathbf{S}_j \tag{2.6}$$

where J_{ij} is the exchange constant. For $J_{ij}>0$, a parallel alignment of the spins $\mathbf{S}_i$ and $\mathbf{S}_j$ will minimize the energy, while in the case of $J_{ij}<0$, an antiparallel alignment of the spins will result in the lowest energy. These two cases of exchange interactions give rise to two different types of magnetic order in the absence of an external magnetic field: $J_{ij}>0$, the parallel alignment of spins produces a long-range *ferromagnetic* (FM) order, while an antiparallel alignment of spins (when $J_{ij}<0$) results in an *antiferromagnetic* (AFM) order.

2.2 Fundamentals of ferromagnetism

Ferromagnetic materials are the ones most people refer to when they use the term "magnetic materials." They are materials with a strong magnetic behavior, like permanent magnets. From a macroscopic point of view, a ferromagnetic order on a microscopic scale induces a spontaneous magnetization when no magnetic field is applied. Here the *magnetization*, $\mathbf{M}$ is defined as the magnetic moment per volume unit at thermal equilibrium.[1,2] The existence of a net magnetization produces a magnetic induction field inside and around the material. By the mean-field approximation, one can assume that each magnetic atom experiences an effective magnetic induction field, $\mathbf{B}$ that is proportional to the total magnetization, $\mathbf{M}$ by[2]

$$\mathbf{B} = \lambda \mathbf{M} \tag{2.7}$$

where λ is the mean-field parameter that represents the strength of the interaction (Weiss constant). However, this induced magnetic exchange field is dependent on temperature, where the spin order gets destroyed at high temperatures. Above a critical temperature, the so-called *Curie temperature* (T_C), the spontaneous magnetization vanishes, and the magnetic moments are randomly oriented, producing a *paramagnetic* state and is then said to be *demagnetized*.[1] Ferromagnets can, thus, technically be considered as a subcategory of paramagnetic materials. The Curie temperature and spontaneous magnetization are two characteristic properties of ferromagnetic materials.

Another characteristic of ferromagnetic materials is that an external magnetic field has to be applied in order to preserve a long-range alignment of the spins on a macroscopic scale, despite the exchange interactions being strong enough to align the spins on a microscopic scale. The exchange interaction and thermal agitation do not contribute to the internal energy of the system alone on a micromagnetic scale: the energy contributions related to factors such as the crystal structure, the shape, external magnetic fields, stress, and magnetostriction also have to be taken into account.

2.3 Micromagnetic energies

As explained, in ferromagnetic materials, magnetic domains appear spontaneously. A magnetic domain is a region with a uniform magnetization.[4] The structure of a magnetic domain is determined by the different contributions to the system's total free energy in order to minimize it. To describe and explain a magnetic configuration, we must therefore have knowledge about these relevant contributing energies. We generally consider the system's free energy to be a sum of six contributions:[2,3]

$$\epsilon_{tot} = \epsilon_{ex} + \epsilon_a + \epsilon_d + \epsilon_Z + \epsilon_{stress} + \epsilon_{ms} \tag{2.8}$$

where ϵ_{ex}, ϵ_a and ϵ_d represent exchange energy, anisotropic energy and demagnetization energy respectively. These terms are all intrinsic properties of the ferromagnetic material and are always present in some way. ϵ_Z is the Zeeman energy, which describes the change in energy in the presence of an external magnetic field. The two last terms represent energies related to applied stress and magnetostriction and will be neglected further as their contributions usually are small, and they are not relevant for the systems studied in this thesis. The final stationary state of a magnetic system is the one which minimizes the total magnetic energy of the system, *i.e.*, the energy sum from Equation 2.8.

2.3.1 Exchange energy

As described in Section 2.1.4, exchange energy acts to either align or anti-align neighboring spins and is at the origin of spontaneous magnetization in ferromagnetic material. This important parameter can be interpreted for many magnetic materials by the Heisenberg model (simplified version in Section 2.1.4). For other materials, like insulators and metals, it can be necessary to use the superexchange model and the Ruderman-Kittel-Kasuya-Yoshida (RKKY) interaction, respectively, to describe indirect exchange interactions.[2]

Exchange stiffness, A, is a constant involved in the exchange energy, which describes the force acting to maintain the electron spin alignment. A can be expressed by its proportionality to the exchange constant, J, by[2]

$$A = JS^2\frac{Z_c}{a_0} \tag{2.9}$$

where S is the value for the individual spins, a_0 is the lattice parameter in a simple structure, and Z_c is the number of atoms in the unit cell. Ferromagnets with a Curie temperature well above room temperature generally have an A value of around $10\,\mathrm{pJ\,m^{-1}}$, where the value is A=$31\,\mathrm{pJ\,m^{-1}}$ for cobalt.[3]

2.3.2 Magnetocrystalline anisotropy

A material with magnetocrystalline anisotropy presents magnetic properties that depend on its crystal lattice structure and orientation. The related energy contribution reflects the interaction of the magnetization with the crystal lattice of the magnetic material and arises from each atomic moment being acted upon by a crystal field produced by the surrounding spins. Magnetocrystalline anisotropy is a manifestation of the local symmetry of the crystal lattice and is therefore intrinsic to the magnetic material.[1] Depending on the crystal structure, certain crystal axis directions, called *easy axis* directions, have a lower energy for aligning the magnetization with itself. Similarly, *hard axis* directions have a high energy cost and are thus less energetically favorable for the magnetization to align with these directions. Hard magnets present strong magnetocrystalline anisotropy, while it for soft magnetic materials is close to zero.[3]

In the case of a *uniaxial anisotropy*, the first term of the magnetocrystalline anisotropy energy is[3]

$$\epsilon_{a-\mathrm{uni}} = -\int K\sin^2(\theta)dV \tag{2.10}$$

where θ is the angle between the easy axis and the magnetization, and K is the anisotropy constant. This is the case for Co with a close-packed hexagonal crystal structure, where the easy axis is in [0001] direction.

For Ni, with a cubic crystal structure, the cube diagonals <111> are the easy directions, and so more than one magnetization direction is preferred by symmetry. In the cubic case the energy density is given by

$$\frac{\epsilon_{a-\mathrm{cub}}}{V} = K_0 + K_1(\alpha_1^2\alpha_2^2 + \alpha_2^2\alpha_3^2 + \alpha_1^2\alpha_3^2) \tag{2.11}$$

where K_0 and K_1 are anisotropy constants, V is the volume, and α_1, α_2 and α_3 are direction cosines, *i.e.*, the cosines of the angle between the magnetization and the crystal axis.

2.3.3 Demagnetizing energy

The *demagnetizing energy* ϵ_d, also called magnetostatic energy, is another anisotropic term related to the system's surfaces, and thus the shape of the considered material. The *demagnetization field* aims to minimize surface charges of the system and arises when the magnetization has a component normal to a surface, either internal or external to the material or when the magnetization is not uniform ($\nabla \cdot \mathbf{M}$ not equal to 0).[3] The corresponding magnetic energy in terms of the demagnetization field can be expressed by[3]

$$\epsilon_d = -\frac{1}{2}\int \mu_0 \mathbf{H}_d \cdot \mathbf{M} dV \tag{2.12}$$

where $\mathbf{H}_d$ is the demagnetization field, which depends on the magnetic configuration of the system, and consequently, on the shape of the magnetic material. For a specimen with magnetization oriented in one direction, "magnetic free poles" appear, producing a magnetic field with a direction opposite to the magnetization. The intensity of the demagnetization field, H_d is related to the magnetization magnitude, M by[3]

$$H_d = -NM, \tag{2.13}$$

where N is a *demagnetizing factor*, which depends on the shape of the specimen. For a sphere, N=1/3 in all directions, while for a long needle, N can be estimated to equal 0 for parallel magnetization and 1/2 for perpendicular magnetization direction with respect to the needle's elongation axis. Similarly, for a thin film (infinite plane) N=0 for magnetization parallel to the plane and N=1 for magnetization perpendicular to the thin film plane.[3]

2.3.4 Zeeman energy

The *Zeeman energy*, also called the external field energy, describes the energy contribution to a magnetic sample as a result of the magnetization **M** interacting with an external magnetic field **H**. It is expressed as[4]

$$\epsilon_Z = -\int \mathbf{M} \cdot \mathbf{H} dV \tag{2.14}$$

For a uniform external field, the Zeeman energy only depends on the average magnetization of the sample and not on the particular domain structure or system shape. This energy is minimal when **M** is parallel to the external field and maximized when **M** is aligned anti-parallel to **H**. If the external magnetic field is strong enough, the system will align the magnetic spins such that all the magnetic domains are magnetized parallel to the external field. In this condition, we say that the system is *saturated.*

2.4 Magnetic domains

A *magnetic domain* is a region in which the magnetization is uniform, *i.e.* pointing in the same direction. Magnetic domains generally form in the lowest energy-state in order for the system to minimize its total self-energy (Equation 2.8).[3] For instance, for a magnetic system in an equilibrium state free of external magnetic fields (ϵ_Z=0), with the temperature sufficiently low as to neglect any effects from thermal energy (*i.e.* $T \ll T_C$), a magnetization saturated along the easy magnetization direction would minimize the energies due to exchange ϵ_{ex} and magnetocrystalline anisotropy (ϵ_a). However, there will also be positive and negative "magnetic charges" generated at the surfaces of the system, producing a demagnetizing field. In order to decrease the demagnetization energy (ϵ_d), the local magnetization close to the charges tends to orient themselves parallel to the surface edge. On the other hand, this orienting of the magnetization disfavors the minimization of the energy terms ϵ_{ex} and ϵ_a. Consequently, the optimum solution for the system is to divide itself into smaller regions where the magnitude of the magnetization is the same at each point, but with different directions with respect to their neighboring regions or domains. From this example, we see that the competition of the different magnetic energy terms (Equation 2.8) leads to the formation of magnetic domains. The domains shapes and sizes are also dependent on the competition between these energy terms, which are defined by the magnetic parameters of the material: the exchange constant, A, the anisotropy constant K, the saturation magnetization M_s, as well as the shape of the magnetic system (with demagnetizing factor N), and the system's magnetic history.

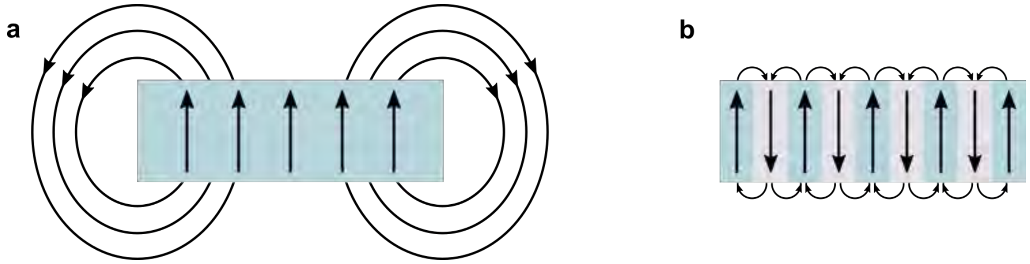

Figure 2.2: Formation of magnetic domains reduces the stray field: a) One domain with large magnetostatic energy b) Multiple magnetic domains formed with a reduced magnetostatic energy

2.4.1 Domain walls

The boundaries between magnetic domains are called *domain walls* (DW). These are non-uniform transitions regions where the magnetic moments realign over many atomic planes to transit continuously from one magnetic domain's magnetization direction to another.[2]

In general, two main types of domain walls are defined; Bloch and Néel types. To explain the difference between them, we will assume a system where there are two magnetic domains of opposite magnetization and a domain wall separating them, where the wall plane contains the anisotropy easy axis and is therefore parallel to the magnetization of the two domains, as illustrated in Figure 2.3.

In a Bloch wall, the magnetization transitions from one domain to the other by rotating parallel to the domain wall plane, as illustrated in Figure 2.3a. In this way, there will be no "magnetic charge" inside the wall as well as no magnetization perpendicular to the wall. As a consequence, the demagnetization field energy will remain zero over the domain wall.[4] This makes it the most common 180° DW.

For a Néel wall, the magnetization transitions by rotating transversely to the domain wall plane, as illustrated in Figure 2.3b. In our example, this would lead to magnetization oriented perpendicular to the wall, leading to an increase of the system's energy, and therefore be less favorable as a domain wall configuration in many cases. However, Néel walls do not produce any surface charges, and there is no stray field associated with this type of wall. For thin films where the thickness is thinner than the domain wall width, Néel walls have a lower magnetostatic energy than a Bloch wall since the demagnetization field becomes a large part of the total energy cost.[3]

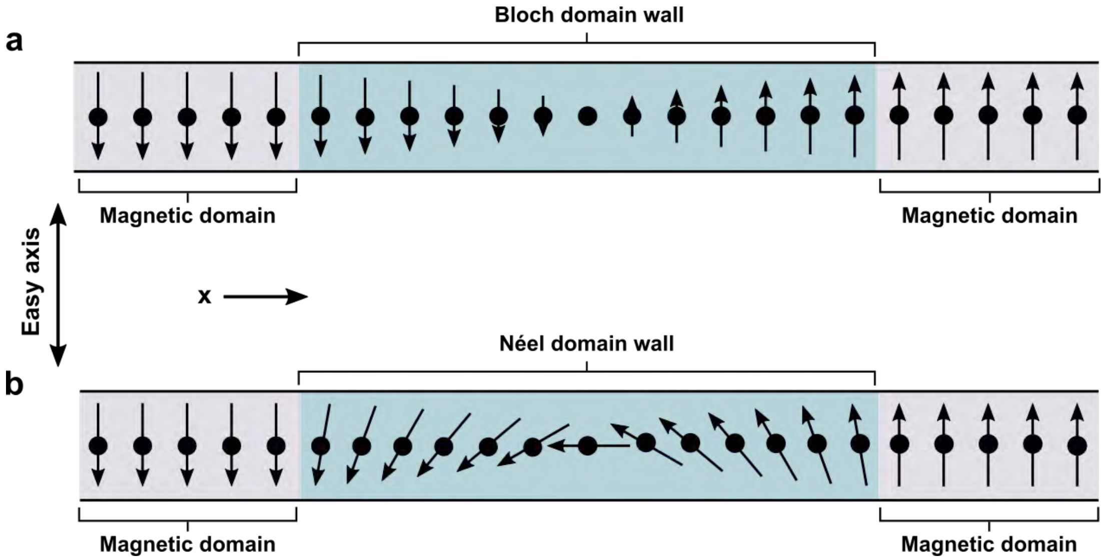

Figure 2.3: Schematic representation of the directional vectors of the magnetic moments in a a) Bloch domain wall with magnetic moments rotating out of plane and a b) Néel domain wall with magnetic moments rotating in-plane. Each case shows two magnetic domains (gray region) of opposite magnetization, separated by a domain wall (blue region).

As a domain wall is a continuous transition and not in one discontinuous jump between two domains, there can be no unique domain wall width definition. However, the most commonly used expression for the domain wall width of a 180° Bloch wall is[4]

$$W = \pi\sqrt{A/K} \tag{2.15}$$

where A is the exchange constant, and K is the anisotropy constant. These two parameters are therefore hugely important for the domain wall formation in a magnetic object. The magnetization in a system rotates under the influence of exchange and anisotropy, where the resulting domain wall positions and the domain orientation minimize the total magnetostatic energy of the system.[3]

2.5 States in magnetic nanowires

In cylindrical magnetic nanowires, the magnetic equilibrium state will be determined by the minimization of several energy terms (see Section 2.3); it depends on the material properties, the shape, and the interaction with other magnetic objects or external fields by dipolar coupling.

Nanowires are structures in which their cross-section diameter is of nanoscale size while their length can stretch over several microns. These nanostructures are generally considered as one-dimensional (1D) objects. Because of this generally high aspect ratio between the cross-section diameter and the length, magnetic nanowires possess a strong shape anisotropic energy while the demagnetizing factor becomes negligible. This shape anisotropy favors monodomain states where the magnetization is aligned parallel to the nanowire axis for a nanowire with a uniform magnetization without an external magnetic field.[5] This magnetic configuration generally appears in nanowires composed of soft magnetic materials.

However, the magnetic configuration becomes more complex when local contributions of magnetocrystalline anisotropy are added to the total energy term. If a nanowire is composed of a material with a significantly strong magnetocrystalline anisotropy, like is the case for *hcp* Co, its energy contribution can be strong enough to challenge that of the shape anisotropy.[6–8] Based on its orientation this can give rise to complex multi-domain configurations.

If the magnetocrystalline easy axis is also oriented so that a magnetization parallel to the nanowire axis is favored, then the case remains as for when the shape anisotropy is dominant and will likely result in a longitudinal monodomain state, like described for soft magnetic materials.[9]

On the other hand, if the magnetocrystalline easy axis points transversal to the nanowire axis, then the magnetization may also, in turn, be oriented transversal to the axis. In cylindrical nanowires, this has been found to form domains in which the magnetization rotates around the nanowire axis.[10–12]

2.6 Micromagnetic simulations

Being able to calculate domain wall structures is the most important contribution of micromagnetics to the analysis of domains.[4] Magnetic states in a ferromagnetic material can be simulated by the use of the Landau-Lifshitz-Gilbert (LLG)[4,13] equation, which defines the time evolution of the magnetization under a local effective magnetic field, $\mathbf{H}_{\mathit{eff}}$. The resulting magnetization motion is expressed as

$$\frac{d\mathbf{M}}{dt} = -\gamma\mathbf{M}\times\mathbf{H}_{\mathit{eff}} - \frac{\gamma\alpha}{M_s}\mathbf{M}\times(\mathbf{M}\times\mathbf{H}_{\mathit{eff}}), \tag{2.16}$$

where γ is the gyromagnetic ratio, and α is the damping parameter. The effective field can be expressed as

$$\mathbf{H}_{\mathit{eff}} = -\frac{1}{\mu_0}\frac{\partial E_{tot}}{\partial\mathbf{M}}, \tag{2.17}$$

where E_{tot} is the average energy density ($\epsilon_{tot}=\int E_{tot}dV$) and $\mathbf{M}$ is the magnetization. This effective field is then associated with the different micromagnetic energies that were discussed in Section 2.3. From the LLG (Equation 2.16) we see in the first term that $\mathbf{H}_{\mathit{eff}}$ exerts a torque on the magnetization vector, which induces a precession movement. The damping parameter in the second term, induces a temporal damping process allowing the magnetization to orient towards the effective field, until relaxing in a position aligned with $\mathbf{H}_{\mathit{eff}}$. However, the LLG equation is only valid assuming a continuous magnetization ($\mathbf{M}=\mathbf{M}(\mathbf{r})$) and a constant magnetization modulus that is equal to the saturation magnetization in every point ($|\mathbf{M}|=M_s$).

However, there are not many cases in which the LLG equation can be solved analytically. Numerical methods are, therefore, normally used. For this, there are plenty of different micromagnetic simulation packages available, like for example MuMax3,[14] GPMaget,[15] Nmag,[16] MicroMagnum,[17] and OOMMF,[18] which is the one used for the micromagnetic simulations in this work. For the numerical simulations, a representation of the magnetic system is made up of a mesh of *magnetic unit cells*, which in the case of OOMMF are in the shape of rectangular cubes. These unit cells should be smaller than the systems characteristic exchange length, $l_{ex}=\sqrt{2A/\mu_0 M_S^2}$, which normally has a value of 2-6 nm for most ferromagnetic materials.[3] The code then works to minimize the total energy of the simulated magnetic system. OOMMF takes the parameters of the systems exchange constant, the saturation magnetization, and the magnetocrystalline anisotropy as a vectorial value for the whole sample. One can also define an external magnetic field acting upon the sample. From a starting criterion, the simulation will run iteratively to minimize the energy until a given convergence criterion has been reached; this can be a certain number of iterations, a certain minimization of the spin torque, etc.

References

[1] C.-G. Stefanita. *Magnetism*. Springer, 2012. DOI: 10.1007/978-3-642-22977-0.

[2] C. Kittel. *Introduction to Solid State Physics*. 8th ed. Wiley, 2004. ISBN: 9780471415268.

[3] J. M. D. Coey. *Magnetism and Magnetic Materials*. Cambridge University Press, 2010. DOI: 10.1017/CBO9780511845000.

[4] A. Hubert and R. Schäfer. *Magnetic domains: The analysis of magnetic microstructures*. Springer, 1998. ISBN: 978-3-540-85054-0.

[5] M. Staňo and O. Fruchart. "Magnetic nanowires and nanotubes". In: *Handbook of magnetic materials*. Vol. 27. Elsevier, 2018. Chap. 3, pp. 155–267. ISBN: 9780444641618. DOI: 10.1016/bs.hmm.2018.08.002.

[6] R. Ferré et al. "Magnetization Processes in Nickel and Cobalt Electrodeposited Nanowires". In: *Physical Review B* **56** (1997), pp. 14066–14075. DOI: 10.1103/PhysRevB.56.14066.

[7] J. M. García et al. "Magnetic Behavior of an Array of Cobalt Nanowires". In: *Journal of Applied Physics* **85** (1999), pp. 5480–5482. DOI: 10.1063/1.369868.

[8] L. Vila et al. "Multiprobe magnetoresistance measurements on isolated magnetic nanowires". In: *Applied Physics Letters* 80 (2002), pp. 3805–3807. DOI: 10.1063/1.1478783.

[9] Y. Henry et al. "Magnetic Anisotropy and Domain Patterns in Electrodeposited Cobalt Nanowires". In: *The European Physical Journal B* **20** (2001), pp. 35–54. DOI: 10.1007/s100510170283.

[10] Y. P. Ivanov et al. "Magnetic Structure of a Single-Crystal Hcp Electrodeposited Cobalt Nanowire". In: *Europhysics Letters* **102** (2013), p. 17009. DOI: 10.1209/0295-5075/102/17009.

[11] C. Bran et al. “Direct Observation of Transverse and Vortex Metastable Magnetic Domains in Cylindrical Nanowires”. In: *Physical Review B* **96** (2017), p. 125415. DOI: 10.1103/PhysRevB.96.125415.

[12] S. Ruiz-Gómez et al. “Observation of a Topologically Protected State in a Magnetic Domain Wall Stabilized by a Ferromagnetic Chemical Barrier”. In: *Scientific Reports* **8** (2018), p. 16695. DOI: 10.1038/s41598-018-35039-6.

[13] L. Landau and E. Lifshits. “On the Theory of the Dispersion of Magnetic Permeability in Ferromagnetic Bodies”. In: *Physikalische zeitschrift der Sowjetunion* **8** (1935), pp. 153–169.

[14] A. Vansteenkiste et al. “The Design and Verification of MuMax3”. In: *AIP Advances* **4** (2014), p. 107133. DOI: 10.1063/1.4899186.

[15] L Lopez-Diaz et al. “Micromagnetic simulations using Graphics Processing Units”. In: *IOP Publishing* **45** (2012), p. 323001. DOI: 10.1088/0022-3727/45/32/323001.

[16] T. Fischbacher et al. “A Systematic Approach to Multiphysics Extensions of Finite-Element-Based Micromagnetic Simulations: Nmag”. In: *IEEE Transactions on Magnetics* **43** (2007), pp. 2896–2898. DOI: 10.1109/TMAG.2007.893843.

[17] C. Abert et al. “Magnum.Fe: A Micromagnetic Finite-Element Simulation Code Based on FEniCS”. In: *Journal of Magnetism and Magnetic Materials* **345** (2013), pp. 29–35. DOI: 10.1016/j.jmmm.2013.05.051.

[18] M. J. Donahue and D. G. Porter. *OOMMF User’s Guide*. Interagency Report. National Institute of Standards and Technology, 1999.

Chapter 3

Experimental techniques

3.1 Imaging magnetic domains

3.1.1 Introduction

The possibility to investigate the magnetic order in materials has, together with the improvement of computation time for micromagnetic simulations, significantly contributed to the understanding of magnetic phenomena that has led to the latest technological applications in the field of Nanomagnetism and Spintronics.[1]

There are many different magnetic mapping techniques, and some can even provide a direct observation of the magnetic configurations and the domain structures at a sub-micron scale. Some of the most used techniques are magneto-optical Kerr effect (MOKE) microscopy, magnetic force microscopy (MFM), x-ray magnetic circular dichroism (XMCD), scanning transmission x-ray microscopy (STXM), x-ray photoemission electron microscopy (PEEM), Lorentz microscopy (LM), and electron holography (EH), where the two latter techniques are TEM-based methods.

To quantitatively map the magnetic properties of nano-objects down to a nanometer scale, techniques capable of probing magnetic properties with a high spatial resolution and sensitivity are needed. Each of the magnetic imaging techniques has its advantages and limitations, and they offer a wide range of possibilities to study different magnetic phenomena in various experimental setups. A combination of techniques, together with the addition of micromagnetic simulations, is usually needed for a complete analysis of the magnetic domains and their configurations in a nanowire.

Different imaging techniques can be compared by certain criteria that determine their applications:[2]

The acquisition method: The image can be recorded using a parallel beam, where the signal in every point of the image is obtained simultaneously (*e.g.* XMCD-PEEM and LM), or the image can be acquired from a series of scans by a small probe across the sample, imaging region by region (*e.g.* MFM and STXM).

The physics behind the magnetic imaging: The signal of interest can be acquired through different interactions and will, therefore, help us obtain different information. Some techniques, like MFM, are sensitive to the stray field gradient. Other imaging techniques are sensitive to the direction of the magnetic polarization, as is the case for MOKE, XMCD, and STXM. The TEM based techniques are sensitive to the total magnetic flux density $\mathbf{B}$, which in the case of LM deflects the electrons by the Lorentz force, or for EH is observed as it couples to the electron phase as described by the Aharanov-Bohm equation.

The depth sensitivity: Some imaging techniques are only sensitive to the surface of the sample or a reduced depth, while others get signal from the whole sample volume. This is related to the type of probe-specimen interaction (as mentioned above) the technique is based on. Techniques that image the magnetic properties of the surface are MOKE, MFM, and XMCD, while techniques like LM, EH, and STXM record the signal from the whole volume of the sample.

The spatial resolution: On this point, EH can achieve the spatial resolution down to 1 nanometer. In comparison to the other techniques mentioned; MFM (25-50 nm), STXM (20-30 nm), XMCD-PEEM (25-40 nm), LM (10-100 nm) can all generally achieve a resolution of a couple of tens of nanometers, while MOKE generally has a lower spatial resolution of a few hundreds of nanometers limited by the wavelength of the probing light.

As already stated, the spatial resolution and the sensitivity of the signal are important criteria for the local study of magnetic properties. This is especially true for the study of domain wall structures. TEM-based techniques, and particularly EH, are well suited. EH provides quantitative information about the magnetic properties in the volume of the sample with a nanometer spatial resolution. External stimuli, like electrical bias or current, magnetic and electric fields, change in temperature, application of stress, or injection of light, can be applied *in situ*. One can also obtain a wide range of different information from the same specimen by using other TEM-based techniques like spectroscopy, electron diffraction, and high-resolution observations.

Because of all the advantages mentioned above, electron holography is the main magnetic imaging technique used in this work. This technique and its principles will be described in more detail in the following sections.

3.1.2 Image formation in TEM

A transmission electron microscope (TEM) offers high spatial resolution and can host a large variety of techniques, with a range covering diffraction, imaging, spectroscopy, and holography.[3] This makes it an attractive instrument for combining different characterization techniques to analyze nanostructures and their properties. The drawbacks of TEM are the need for electron transparent samples (ideally < 100 nm thick) and that the experiments are performed under a high vacuum in a limited space between the polar pieces of the objective lens. The sample preparation processes can therefore be complicated. Special training and knowledge of the TEM operation modes as well as the physical properties of electron-matter interactions are crucial to purposefully operate it and analyze the information gained from the measurements. However, as previously mentioned in this text, the rewards and possibilities of the TEM and its large variety of techniques are the main attractions.

In essence, the overall process of image formation in a TEM can be broken down into six steps:

1. The creation of the electron beam from a source and its acceleration.
2. The illumination of the sample by the electron beam.
3. The scattering of the electron beam from interaction with the specimen.
4. The formation of a diffraction pattern in the *back focal plane* of the objective lens.
5. The formation of an image of the specimen in the *image plane* of the objective lens.
6. The magnification and projection of the image (or diffraction pattern) on the detector plane.

In the first step, electrons are either generated by thermionic emission by heating the filament (tungsten or LaB_6) or by Cold Field Emission (C-FE) from a very small and sharp tungsten tip at room temperature. There is also a third source type, called Schottky Field Emission gun (S-FEG or just Schottky gun), where both electron extraction methods are combined. The C-FEG and Schottky gun create a highly coherent and bright electron beam, which is essential for techniques like EH, as compared to a thermionic gun, which provides a higher intensity beam but much less coherent.

After generation, the electron waves are accelerated to a value that is typically between 60 kV and 300 kV, after which it travels through the microscope's column of lenses, deflecting coils and stigmators, which shape the electron beam (probe size, convergence angle, electron dose) that is focused onto the sample. The electron wave then interacts with the sample through various physical processes. A diffraction pattern is then formed in the back focal plane of the objective lens, and an image of the sample is obtained in its image plane. The following lenses are used to magnify and project the image on the detector plane of the microscope. Figure 3.1 shows the schematics of this simplification of the beam path during image formation in a TEM.

As electrons interact strongly with both atom cores and the electron cloud as well as the surrounding electromagnetic fields, much of the information about the specimen properties

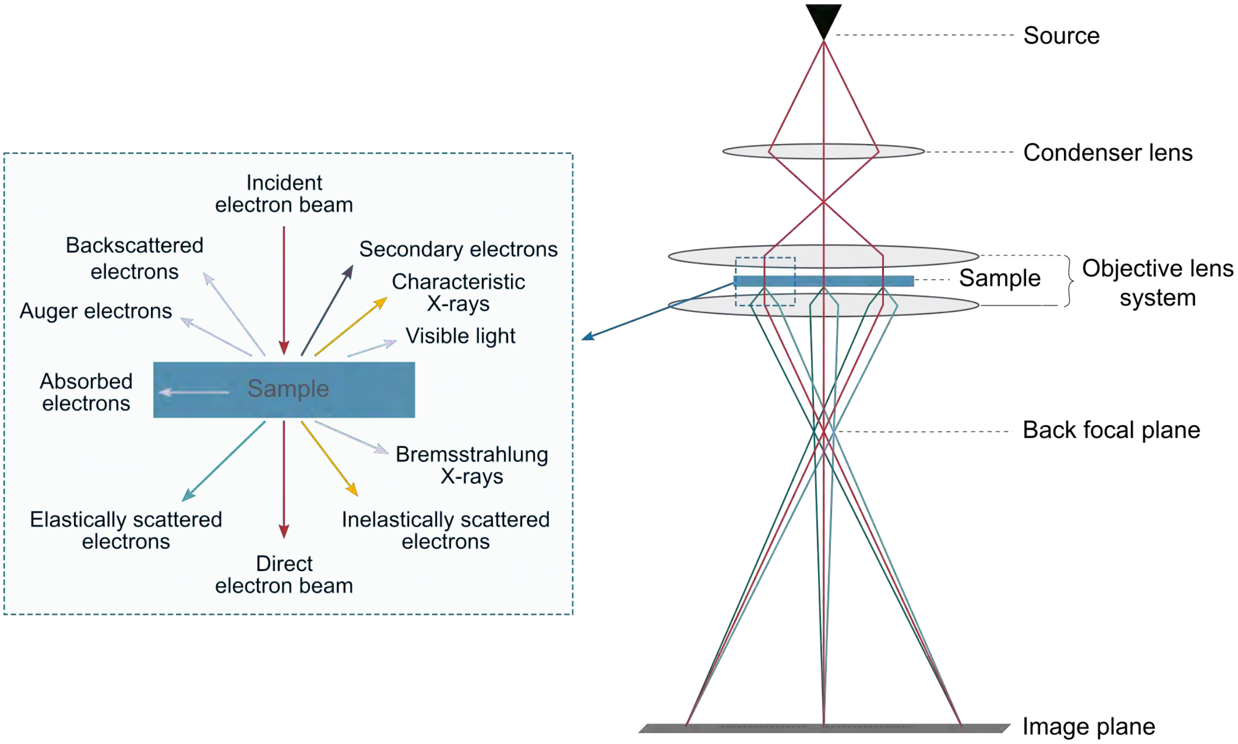

Figure 3.1: Schematics of the electron beam path in a TEM.

can be recovered (Figure 3.1). The different signals are detected through a large variety of sample characterization methods and make the TEM a key equipment for studies of materials at the nanoscale. For instance, during an inelastic scattering event, the electron loses a small amount of energy that is transferred to the sample, leading to the emission of various secondary signals (x-rays, visible light, secondary electrons, phonons, and plasmonic excitations) detected and analyzed by different techniques.[3] Examples of such techniques are x-ray energy-dispersive spectroscopy (XEDS), cathodoluminescence, and electron energy loss spectroscopy (EELS). The latter technique is described in more details in Section 3.5. In comparison, elastically scattered electrons do not lose any energy in the event. Elastic scattering in crystalline materials gives rise to Bragg diffraction. Bragg's law relates the periodicity and parameters of the crystal lattice with the incident and scattered angle of the electron wave. These elastically scattered electrons form the amplitude images of the specimen, electron diffraction patterns, and high-resolution images.

Mathematically, image formation in the TEM can be described by the use of the relativistic and time-dependent Schrödinger's equation, also known as the Dirac's-equation, to quantum mechanically explain the scattering of a high energy electron wave as it interacts with an object.[3] If we neglect the electron spin, we can express the electron function by

$$\frac{1}{2m_e}(\text{-}i\hbar\nabla + e\mathbf{A})^2\psi(x,y,z) = e[U^* + \gamma V]\psi(x,y,z) \tag{3.1}$$

where A is the magnetic potential and V the electric potential, e is the electron charge, m_e is the electron rest-mass, $\hbar$ the reduced Planck constant, and γ the relativistic Lorentz factor (γ=1+eU/m_ec^2). U^* is the relativistic corrected accelerating potential given by U^*=(U/2)(1+γ), where U is the non-relativistic accelerating potential. The solution of this equation gives the transmitted electron wave function, called the *object electron wave*. From a *weak phase object approximation*, *i.e.* considering the electrons to only be elastically scattered by the object with a slight change of their phase, neglecting any absorption effects of the electron wave by the object, the Dirac equation solved in the direct space $\mathbf{r}$=(x,y,z) for the object wave is expressed as[3]

$$\psi_{obj}(\mathbf{r}) = A(\mathbf{r})e^{i\phi(\mathbf{r})} \tag{3.2}$$

where $A(\mathbf{r})$ is the amplitude of the object wave and $\phi(\mathbf{r})$ is the induced phase shift of the electron wave after interacting with the sample object. The electron wave will then continue down the column's lens system and form a diffraction pattern in the objective lens' back focal plane and an image in the image plane. According to diffraction theory, electrons scattered by the same crystal lattice planes converge in a common point in the back focal plane, creating a patterned representation of the specimen in the reciprocal space, also known as a *diffraction pattern*. Diffractions patterns can be expressed mathematically by the Fourier transform ($\mathscr{F}$) of the object wave[3]

$$\Psi_{obj}(\mathbf{k}) = \mathscr{F}[\psi_{obj}(\mathbf{r})] \tag{3.3}$$

where $\mathbf{k}$ is the reciprocal vector. The Fourier transform $\Psi_{obj}(\mathbf{k})$ is defined as:

$$\Psi_{obj}(\mathbf{k}) = \int \psi_{obj}(\mathbf{r}) e^{2\pi i \mathbf{k}\cdot\mathbf{r}} d\mathbf{r}. \tag{3.4}$$

During the image formation process in a TEM, the object electron wave will be modified by various aberrations of the objective lens, such as defocus, astigmatism, and spherical aberrations. These effects can be accounted for in the mathematical expression multiplying the diffracted object wave function in reciprocal space by a *transfer function*, $T(\mathbf{k})$:

$$\Psi_{diff}(\mathbf{k}) = \Psi_{obj}(\mathbf{k}) T(\mathbf{k}) \tag{3.5}$$

The transfer function is generally expressed as

$$T(\mathbf{k}) = B(\mathbf{k}) e^{i\chi(\mathbf{k})} e^{-ig(\mathbf{k})}, \tag{3.6}$$

where $B(\mathbf{k})$ is a pre-exponential function associated with the use of a cut-off aperture and magnification effects, $g(\mathbf{k})$ is a damping function accounting for instabilities in the microscope due to factors like lens current, acceleration voltage, etc., and electron probe incoherence. $\chi(\mathbf{k})$ is the *phase contrast function*, containing the phase shifts induced by the lens aberrations. If we neglect the high order aberration factors, the phase contract function can be expressed by

$$\chi(\mathbf{k}) = \frac{2\pi}{\lambda}[\frac{C_S}{4}\lambda^4 k^4 + \frac{\Delta z}{2}\lambda^2 k^2 - \frac{C_A}{2}(k_y^2 - k_x^2)\lambda^2] \tag{3.7}$$

Here, C_S is the spherical aberration coefficient, C_A is the axial astigmatism coefficient, λ is the electron wavelength, and Δz is the defocus length.

An image of the object ($\Psi_{img}(\mathbf{r})$) is, finally, formed in the image plane of the objective lens. The image wave, expressed in real space, corresponds to an inverse Fourier transform of the diffraction wave:

$$\Psi_{img}(\mathbf{r}) = \mathscr{F}^{-1}[\Psi_{diff}(\mathbf{k})] = \mathscr{F}^{-1}[\Psi_{obj}(\mathbf{k})T(\mathbf{k})] \tag{3.8}$$

The electron wave will then continue to travel trough a series of intermediate and projector lenses which will transfer the image of the object to a conjugated plane where it will be detected by a fluorescent screen, a CCD camera or an other type of electron detector. In this detector plane, the object image will be recorded as an intensity map of the image wave $\Psi_{img}(\mathbf{r})$. The image intensity is expressed as the squared modulus of the image wave:

$$I(\mathbf{r}) = |\Psi_{img}(\mathbf{r})|^2 = \Psi_{img}(\mathbf{r}) \cdot (\Psi_{img}(\mathbf{r}))^* \tag{3.9}$$

For an ideal case, in a microscope without any optical defects, aberrations, aperture cut-off or incoherence ($T(\mathbf{k})$) and for a perfect focus (Δz=0), the intensity would be described by the squared modulus of the object electron wave amplitude:

$$I(\mathbf{r}) = |\Psi_{img}(\mathbf{r})|^2 = |A(\mathbf{r})|^2. \tag{3.10}$$

From this ideal case, only the amplitude of the object wave is recorded in the detected intensity image, while the information about the phase shift, $\phi(\mathbf{k})$, experienced by the electron wave interacting with the sample object is lost. Additionally, the amplitude is homogeneous in weak phase objects, hence resulting in an image without any contrast. As we will see in the following section, the ability to access the phase shift of the object electron wave is crucial for being able to study magnetic materials by TEM methods.

3.1.3 Magnetic imaging in a TEM

The phase of an electron wave is modified when it interacts with an object and any electromagnetic field in or surrounding it.

The phase shift at the origin is zero by convention. When interacting with an electromagnetic potential, the phase term of the electron wave is modified due to the Aharanov-Bohm effect as expressed by[4,5]

$$\phi(x,y) = \frac{\pi\gamma}{\lambda U^*}\int V(\mathbf{r})dz \text{ - } \frac{e}{\hbar}\int A_z(\mathbf{r})dz, \tag{3.11}$$

where $\lambda = \hbar/(2em_eU^*)^{1/2}$ being the relativistic electron wavelength, and A_z the component of the magnetic vector potential ($\mathbf{A}$) along the electron beam direction. One can further express Equation 3.11 as:[6]

$$\phi(x,y) = C_E\int V(\mathbf{r})dz \text{ - } \frac{e}{\hbar}\iint B_\perp(\mathbf{r})dxdz, \tag{3.12}$$

where V corresponds to the mean inner potential and $B_\perp$ is the component of the magnetic induction perpendicular to z, which is the direction of the incident electron beam. $C_E = \pi\gamma/\lambda U^*$ is a constant dependent on the accelerating voltage of the TEM ($6.52\cdot10^6$ V^{-1} m^{-1} for an acceleration voltage of 300 kV).

The Aharanov-Bohm equation (Equation 3.11 and Equation 3.12) indicates that when electrons propagate through a specimen, the resulting phase shift carries information about the magnetic vector potential (magnetic induction) as well as information about the electrostatic potential. The latter contribution arises from the sample's mean inner potential related to its composition and the density of excess electric charges, if present in the sample. Accessing electron beam phase shift makes it possible to quantitatively map the electric and the magnetic properties in the sample and the stray fields outside of it.

One important note is that only the in-plane components of the magnetic induction (*i.e.* components perpendicular to the beam direction) contribute to the phase shift. In other words, the magnetic component parallel to the electron beam cannot be detected by these two TEM techniques. Another point is that the detected phase shift corresponds to a projection and an integration of the potentials along the electron beam path. Consequently, a constant sample thickness or at least a sample with known shape and dimensions is often required to enable a good interpretation of the acquired data.

A common strategy to extracting information from the phase shift of the electron wave is

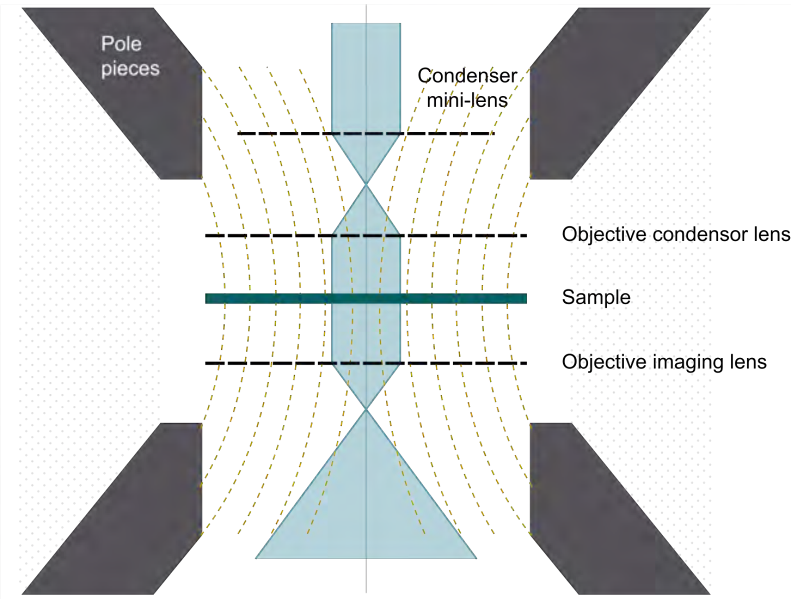

Figure 3.2: Schematic representation of the magnetic field (dashed yellow lines) inside a twin-type objective lens illustrated as a cross-section. Optical axis and electron wave path is illustrated in blue. Various lenses are marked by black stapled lines.

to tune the transfer function of the microscope in order to modulate the electron wave and obtain a series of images whose intensity is related to the phase shift. This strategy is used in high-resolution TEM (HRTEM) to resolve atomic columns, and it is known as *phase-contrast imaging*. In advanced TEM with a C_s-aberration corrector, the transfer function can be modulated through the phase-contrast function by a slight variation of the focal distance Δz.

3.1.4 The objective lens

The objective lens (OL) is the main and the strongest of the lenses in a TEM.[3] It is responsible for forming the first highly magnified image of our sample object and determines, therefore, the quality and spatial resolution of the final image. As for all the other TEM lenses, the OL is an electromagnetic lens that focuses the beam by creating a strong and concentrated axial magnetic field. The lens structure itself is composed of a copper coil winded inside a cylindrical yoke made out of a soft magnetic material, called the *pole piece*. The magnetic field is produced when a current is injected through the copper coils, and the strength of this field can be adjusted by changing the current, which in turn modifies the focal plane positions of the electromagnetic lens.

There are different types of objective lenses, but the most flexible types are the ones where the upper and lower pole pieces are separated.[3] In Figure 3.2, such a twin-type OL with a split pole piece is illustrated. In this optical system, the specimen is placed in the center of the gap between the pole pieces, immersing the sample in a very uniform and intense magnetic field. The fact that the configuration is a split pole piece, together with a small condenser lens placed in the upper part of the OL, gives the flexibility to change between different modes, from broad illumination in conventional TEM mode to a highly convergent beam for use in STEM.

The magnetic field inside the gap between the pole pieces, where the object sits, can be measured experimentally using a special holder equipped with a dedicated Hall probe fitted in the object position of a sample holder. Such a measurement has been conducted on the Hitachi HF3300-C *Interferometry In-Situ* TEM (I2TEM) microscope used in this work. The results measure a magnetic field of 1.87 T for the highest objective lens current value (18 A). The OL in the I2TEM can therefore produce a magnetic field that is strong enough to saturate most ferromagnetic materials, aligning the magnetization parallel to the optical axis (perpendicular to the image plane). Not only does this mean that the OL's magnetic field can alter the magnetic state of the sample, but it also minimizes the magnetic contrast due to the fact that TEM magnetic imaging is only sensitive to the magnetic induction components perpendicular to the electron path (*i.e.* in the image plane). This is why classical TEM conditions are not suitable to study magnetic configurations.

To perform magnetic imaging at the remnant state, the OL lens has to be turned off. Consequently, the remaining optical system has to be readjusted to compensate for the loss of the most important lens in the column. In dedicated TEMs for magnetic imaging, a special lens called the *Lorentz lens*, located just below the OL is used instead of the OL to magnify and form the image of the object. The Lorentz lens is much weaker than the OL and consequently with less focusing power. This small magnetic field, together with the remnant field of the OL polar pieces, leads to a residual magnetic field of less than 1 mT at the sample location. This small field can eventually be compensated for by the mini-condenser lens. Another solution is to use an additional object stage, named the *Lorentz stage*, located above the conventional stage. The Lorentz stage allows the OL to be used, but at a weaker current, *i.e.*, a longer focal length. The Hitachi I2TEM, designed in collaboration between CEMES-CNRS and Hitachi High Technology, is equipped with such a stage and provides a completely field-free condition (measured to 70 μT) in the sample object position.

The corresponding magnetic imaging modes are called *Lorentz modes* and are used for EH imaging as well as for LM. Unfortunately, the large spherical aberration, due to the long focal length (a few tens of millimeters), degrades the spatial resolution to a few nanometers and limits the total magnetic magnification. Fortunately, recent developments in aberration correction make it possible to correct this and thus improve the spatial resolution. In the I2TEM, a spatial resolution of 0.5 nm has been measured in Lorentz mode (*i.e.* the upper stage).

Once such a field-free environment is provided for the sample, information about the magnetic properties of the studied specimen is recovered by detecting the phase shift of the transmitted electron wave using a Lorenz mode imaging technique. We can then use either of the two previously discussed magnetic imaging techniques in a TEM, namely Lorentz microscopy and electron holography.

3.2 Lorentz microscopy

From a classical point of view, *Lorentz microscopy* is based on the Lorentz force. The Lorentz force ($\mathbf{F}_L$) is experienced by propagating electrons in a magnetic field $\mathbf{B}$, and is expressed by the following equation:

$$\mathbf{F}_L = \text{-}e\mathbf{v}\times\mathbf{B}, \tag{3.13}$$

where $\mathbf{v}$ is the electron velocity. For electrons traveling along the optical axis of a TEM (z-axis), the vector product $\mathbf{v}\times\mathbf{B}$ in Equation 3.13 implies an induced deflection of the electron trajectory, which only depends on the magnetic induction components perpendicular to the optical axis, *i.e*, B_x and B_y, as illustrated in Figure 3.3a. If the electrons pass through a

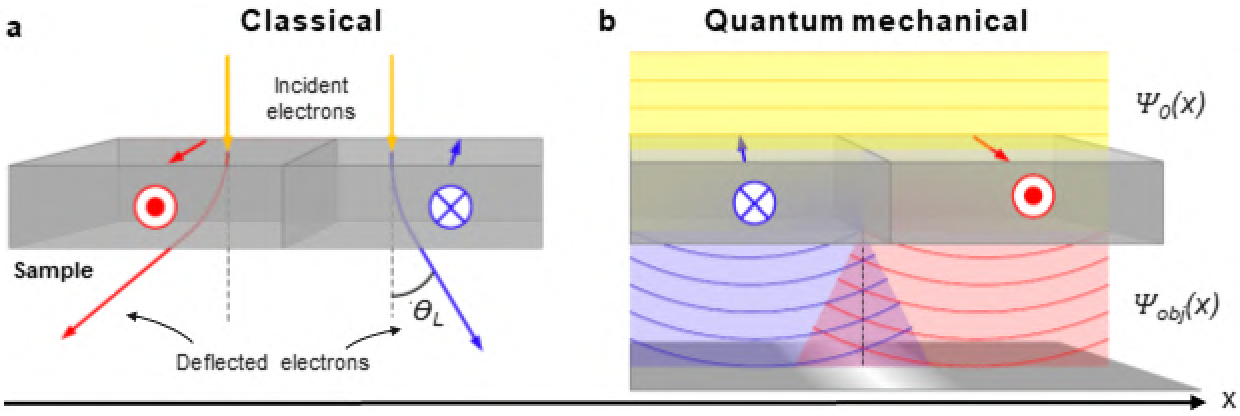

Figure 3.3: Illustration of the electron beam deflection (**a**) due to the Lorentz force and (**b**) from a quantum mechanical description, leading to an overlap of the two beams coming from different domains leading to interference fringes. The red and blue arrows in the sample represent the magnetization direction.[8]

thin sample, the magnetic induction of the sample will deflect the electron trajectory with an angle expressed by:[7]

$$\theta_L = \frac{e\lambda}{h} B_\perp t = C B_\perp t, \tag{3.14}$$

where $B_\perp$ is the magnitude of $\mathbf{B}_\perp$, t is the sample thickness, and h is the Planck constant. C is a pre-factor that depends on the acceleration voltage of the TEM, with an approximate value of $5 \cdot 10^{-7}$ rad nm^{-1} T^{-1} for 300 kV. However, the deflection angle due to the Lorentz is about one or two orders of magnitude lower than the typical Bragg diffraction angles produced by low-index atom planes.

The process can also be described from a quantum mechanical point of view by considering the electron beam as a wave. In this approach, the Lorentz force can be described as a phase shift of the electron wave. This is illustrated in Figure 3.3b. The magnetic induction is then represented by the magnetic vector potential inside the sample, $\mathbf{A}$, which induces a phase shift on the scattered electrons, expressed as:[9]

$$\phi_M(x,y) = -\frac{\pi\gamma}{\lambda U^*} \frac{e}{\hbar} \int A_z(\mathbf{r}) dz. \tag{3.15}$$

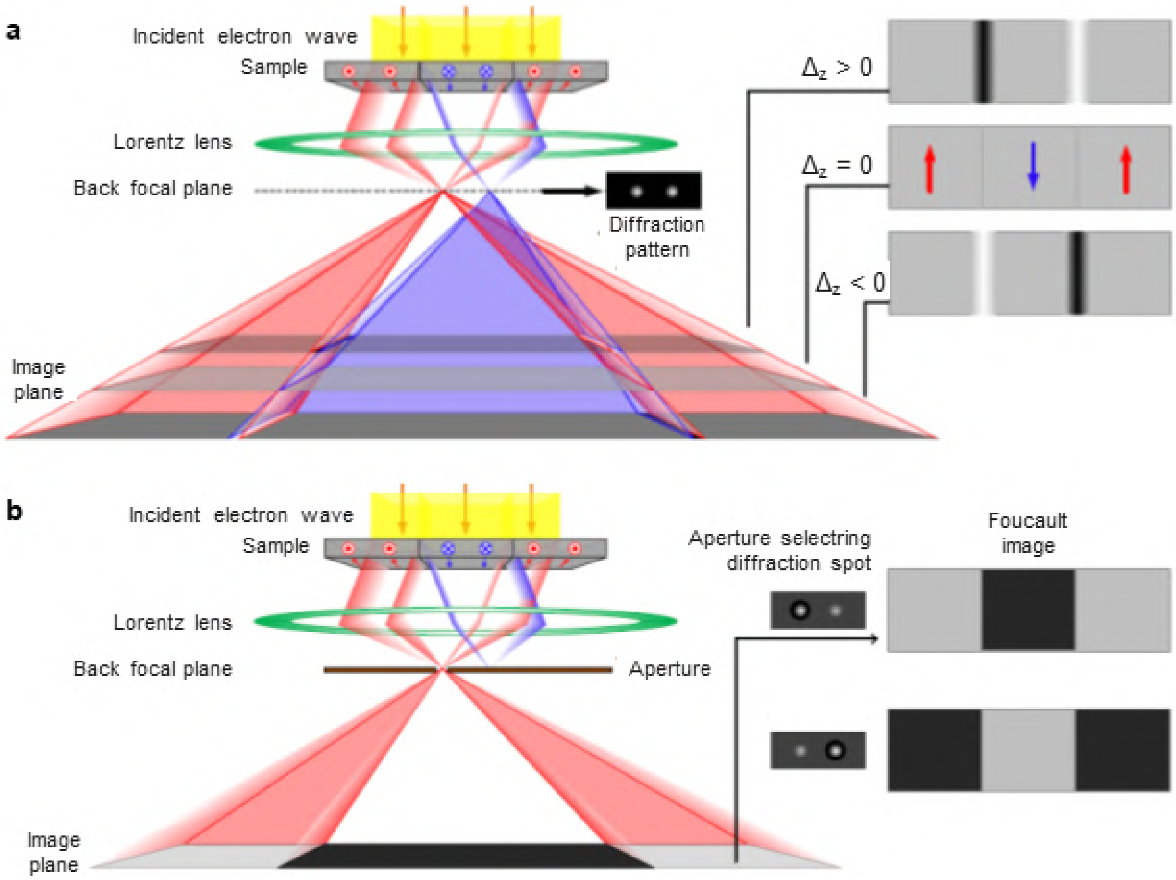

Figure 3.4: Illustration of the two Lorentz microscopy imaging modes: (**a**) Fresnel mode and (**b**) Foucault mode. The red and blue arrows in the sample represent the magnetization direction.[8]

In focus, the image formation process in LM is similar to that of conventional TEM. However, just as for the electron scattering process due to Bragg diffractions on the crystal lattice, the scattering due to different beam deflections induced by the magnetic nature of the sample will create a diffraction pattern in the back focal plane of the Lorentz lens. Apart from aberrations, mainly spherical aberrations, of the Lorentz lens, the image intensity in the image plane will only carry information about the amplitude and not any change due to phase shifts. The magnetic information of the sample can, thus, only be obtained through LM by altering the transfer function of the microscope. There are two main ways to do this: by defocusing the image (*Fresnel mode*), or by the use of an aperture to select one of the deflected beams in the back focal plane of the Lorentz lens (*Foucault mode*).[9,10] Figure 3.4 shows schematics illustrating the two Lorentz imaging modes.

Fresnel mode (defocus mode) is the most used one and is also the technique used in this work.

This mode offers a direct observation of the magnetic contrast due to magnetic domain walls (DW) in the sample, just by either under-focusing the Lorentz lens to image a plane above the sample plane or by over-focusing, to image a plane below the sample plane (Figure 3.4a). Using the classical description, the electron beam is deflected in opposite directions due to the Lorentz force acting on the electrons when transmitting the sample on each side of a magnetic DW. This results in either a convergence or divergence of the electrons, depending on the relative magnetization orientations in the two domains, resulting in bright or dark contrast lines, respectively, in the image plane. From a quantum mechanical point of view, the wave behavior of the electron beam leads to the appearance of interference fringes parallel to the DW due to an overlap of the two deflected beams in either domain, as illustrated in the over- and under-focused image planes in Figure 3.4a. Hence, Fresnel contrast only appears in defocused images.

While LM Fresnel mode offers the possibility of getting a fast and direct visualization of DWs, only qualitative information about the magnetic configuration in the sample is provided. However, this can be accounted for by the use of the so-called Transport of Intensity Equation (TIE) through a non-interferometric approach to the phase retrieval problem, developed by Dr. van Dyck. By using the TIE method, through the processing of a focal series of Lorentz images in Fresnel mode, one can retrieve quantitative information of the magnetic configuration in the sample.

3.3 Electron holography

As previously detailed in Section 3.1.2, when an electron wave interacts with a material, its amplitude and phase change. In conventional TEM, the phase information is lost, and only the spatial distribution of the intensity (the square of the amplitude) of the electron wave is recorded. As a consequence, the information about the electron beam phase shift from the electromagnetic fields due to the Aharonov-Bohm effect is lost. *Electron holography* (EH) is a powerful imaging technique that allows for accessing the phase shift of the electron wave resulting from interaction with a sample.[11,12] We can, thus, retrieve information about local variations in the magnetic induction and electrostatic potential within and surrounding the sample.

The concept of electron holography was first proposed by Denis Gabor in 1948 as a way to improve the limitations of electron microscopy caused by aberrations in the electromagnetic lenses.[13–15] This initial type of holography is called in-line holography. Nowadays, there are several types of electron holography with different microscopy setups that have been realized, and even more, are theoretically possible.[11,16,17] However, one setup, called *off-axis electron holography*, has more or less superseded the in-line setup, as it does not suffer from a so-called "conjugate twin image" that can cause disturbances in the reconstructed image when using in-line holography.[18] It is this type of holography that has been used in this work, and it will therefore be detailed in the following sections.

3.3.1 Off-axis electron holography

Off-axis electron holography is an interferometric imaging technique where one part of a highly coherent electron wave, called the “object wave,” passes through the sample object, interacting with the electromagnetic fields of the sample and its surroundings. The second part of the electron wave, called the *reference wave*, goes through a uniform area of the sample, ideally vacuum or an ultrathin, uniform carbon film, and will, therefore, not interact with any electromagnetic field from the sample. These two waves are then deflected by a Möllenstedt biprism, causing the two waves to interfere.[19] An illustration of the off-axis electron holography setup is shown in Figure 3.5. The resulting interference pattern, called the *hologram*, consists of both an intensity image, which mostly depends on the amplitude of the object wave (like in bright-field TEM)[12] and

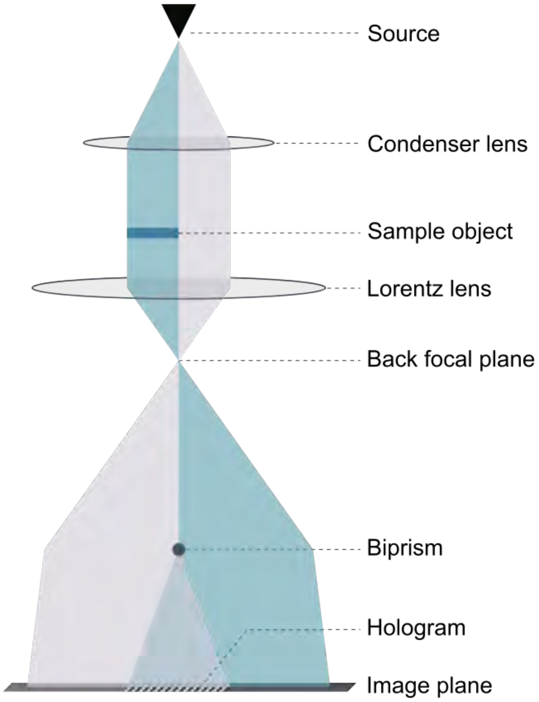

Figure 3.5: Principal TEM setup for off-axis electron holograph

interference fringes, with local periodicity variations and shifts due to the relative difference in phase of the object wave and the reference wave induced by the electrostatic and magnetic local fields of the sample. By analyzing these local fringe variations, one can extract the phase shifts and, thus, map the local electric and magnetic fields, as discussed in Section 3.1.3.

As explained in Section 3.1.2, only the amplitude A of the object wave is recorded in conventional TEM imaging, while all information about the phase shift, carried by $\phi(\mathbf{r})$, is lost. However, the hologram interference fringes resulting from the superposition of the object wave and the reference wave, keeps this phase shift information. If we consider two such coherent waves propagating along z direction, the reference wave expressed by $\psi_{ref}(\mathbf{r})=A_0(\mathbf{r})e^{i2\pi\mathbf{k}\cdot\mathbf{r}}$ and the object wave by $\psi_{obj}(\mathbf{r})=A(\mathbf{r})e^{i(2\pi\mathbf{k}\cdot\mathbf{r}+\phi(\mathbf{r}))}$, where $\mathbf{r}$ is the position vector and $\mathbf{k}$ is the wave vector. The intensity of the wave function at z=0 resulting from interference along the x-axis corresponds to:

$$I_{hol}(x,y) = |A_0(x,y)|^2 + |A(x,y)|^2 + 2A_0(x,y)\cdot A(x,y)\cdot\cos[2\pi\frac{\alpha_h}{\lambda}x + \phi(x,y)] \qquad (3.16)$$

where $A_0(x,y)$ is the amplitude of the uniform reference wave and $A(x,y)$ the amplitude of the object wave. Both the amplitude terms, which form a conventional bright-field image, and a sinusodial term, related to the phase shift information, are contained in the intensity of the hologram image. The sinusoidal term in Equation 3.16 expresses the interference fringe pattern of the hologram, where the period of the fringes (λ/α_h) depends on the two beams' deflection angle induced by the biprism, which is given by α_h and -α_h for the reference and the object wave respectively.

In Fourier space, a conventional bright-field image would be transformed in a central spot, called the direct beam or the *central band*. Comparatively, the Fourier transform of a hologram image contains a central band, and two additional collinear spots called *side bands*, which are equally displaced with respect to the center band (Figure 3.6(**b**)). It is in these sidebands where the information about the phase of the transmitted wave is stored, together with information about the image amplitude. From this, one can access the information about the amplitude as well as the phase shift of the object electron wave by choosing one of the sidebands and perform an inverse Fourier transform.

3.3.2 Phase reconstruction

The phase shift $\phi(x,y)$ and amplitude information is extracted by the Fourier analysis of the hologram. This process is shown in Figure 3.6. Firstly, a hologram is recorded using a digital camera with a CCD or a CMOS detector, like the one depicted in Figure 3.6(**a**). After this, a fast Fourier transform (FFT) of the hologram is calculated (Figure 3.6**b**), upon which a defined numerical mask (square, cosine, Butterworth or Gaussian, etc.) is applied to one of the sidebands, for which the inverse Fourier transform (FFT^{-1}) is calculated. From this we can calculate two images: the amplitude image and the phase image, as seen in Figure 3.6(**c-d**). The phase image represents the displacement or the variation in periodicity of the interference fringes compared to a reference area selected by the user (seen in the dotted square of Figure 3.6(**d**). The width of the fringes, often expressed by the *fringe spacing* (the inter-fringe distance), is the first important factor that defines the spatial resolution of the reconstructed images, as this decides the sensitivity of the detected phase shift.[20]

During the data processing, one also has to take into account the effect of the mask used when taking the FFT^{-1} of the sideband in reciprocal space. The size (radius) of the mask will partly define the spatial resolution of the resulting phase and amplitude images, in addition to determining the final signal-to-noise ratio of the images. The larger the mask radius in Fourier space, the higher the spatial resolution, but the smaller the signal-to-noise ratio. Consequently, it is important to find a good balance between low noise level, leading to a high phase sensitivity, and a high spatial resolution.

Another point to consider during this processing is the additional phase distortions due to the microscope itself and to the detection system, most prominently arising from Fresnel fringes from the biprism and distortions due to projector lenses and the optical fibers of the camera. Taking this into account, the intensity of the resulting hologram can be expressed as

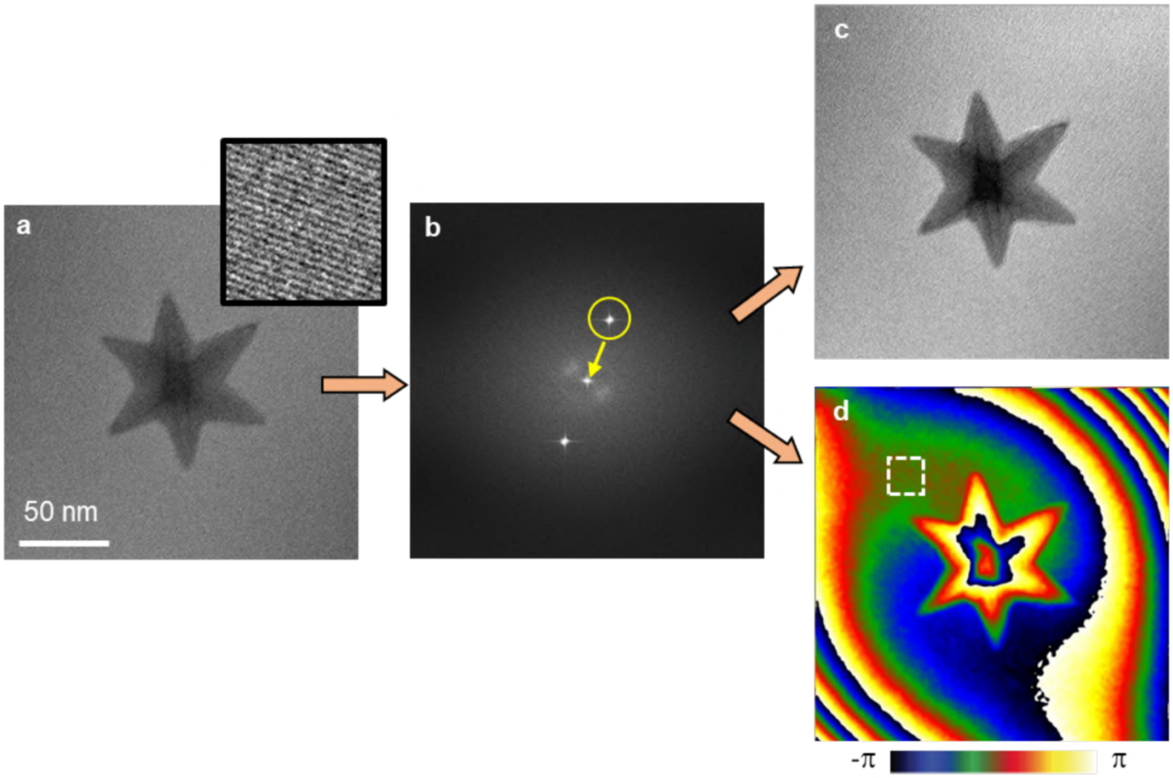

Figure 3.6: Extraction of amplitude and phase image from a hologram. (**a**) Hologram of a FeCo nanostar with an inset showing a magnification of the fringes. (**b**) Fast Fourier Transform (FFT) of image (**a**) showing a numerical mask applied on one side band marked by yellow circle. (**c**) amplitude image and (**d**) phase image calculated from the inverse FFT of the masked area in (**b**).

$$I_{hol}(x,y) = |A_0(x,y)|^2 + |A(x,y)|^2 + 2A_0(x,y) \cdot A(x,y) \cdot \cos[2\pi \frac{\alpha_h}{\lambda} x + \phi(x,y) + \phi_\mu(x,y)] \tag{3.17}$$

where $\phi_\mu(x,y)$ represents the sum of all phase shifts due to distortions from the microscope and the setup. This additional phase shift term due to artifacts ($\phi_\mu(x,y)$) often has a much higher value than the one presented by the electron-object interaction ($\phi(x,y)$) alone, which would compromise the whole analysis of the recovered date if left alone. It is therefore essential to remove this phase contribution from the data in order to get a representative analysis of the sample. This is achieved by calculating a reference phase image obtained from a *reference hologram*, which is recorded in an area without any object and field (ideally

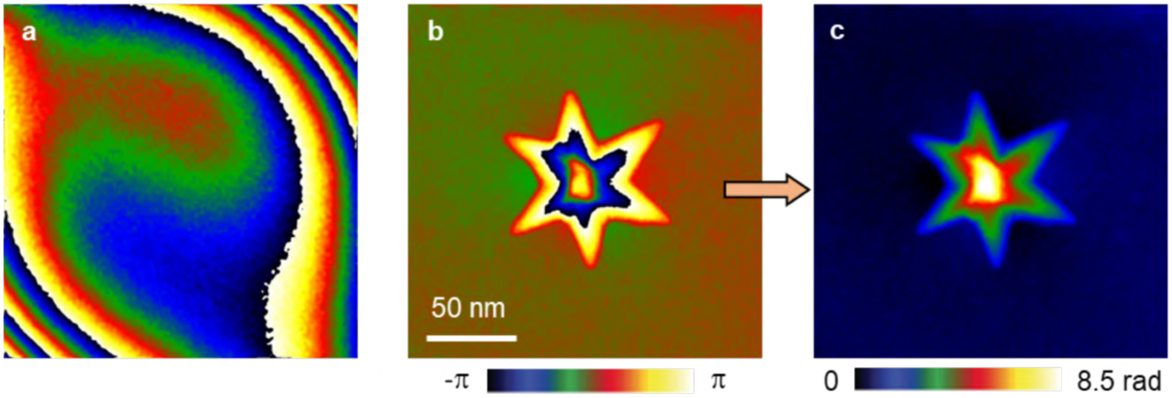

Figure 3.7: (**a**) Reconstructed phase image from reference area (vacuum). (**b**) Reconstructed phase image from object (image in Figure 3.6(**d**)) after subtracting reference phase image (**a**). (**c**) Unwrapped phase image of (**b**).

vacuum), and therefore only containing phase shift arising from artifacts of the TEM column itself: $\phi_\mu(x,y)$. The resulting reconstructed reference phase image is then subtracted from the reconstructed phase image of the object, removing the phase distortions due to the microscope setup.[21] This process is depicted in Figure 3.7

The resulting phase image displays phase shift values between -π and π creating discontinuities or jumps in phase. From this *wrapped image*, phase jumps can be removed by using an algorithm to make an *unwrapped* phase image with continuous variation of the phase shift, as seen in Figure 3.7(**c**).

There are many ways to perform the reconstruction process for electron holography images, with commercial scripts available for Gatan© Digital Micrograph, as well as many EH users choosing to develop their own computational routines. In this work, I used homemade scripts developed on Gatan© Digital Micrograph by Dr. Christophe Gatel and Dr. Martin Hÿtch.[22]

3.3.3 Magnetic phase shift contribution

As elaborated in Section 3.1.2, the electron wave gets a phase shift ($\phi(x,y)$) as a result of interacting with the electromagnetic potential of the sample object, with contributions from the electrostatic potential ($\phi_E(x,y)$) and the in-plane components of the magnetic field of the sample ($\phi_M(x,y)$), where the total phase shift may be expressed as:

$$\phi(x,y) = \phi_E(x,y) + \phi_M(x,y) \tag{3.18}$$

Using the Aharanov-Bohm equation (Equation 3.12), the in-plane components integrated along the electron beam direction (z-direction) can be calculated by the derivative function of the respective phase shifts. The in-plane components of the magnetic induction are expressed by:

$$\frac{\delta\phi_M(x,y)}{\delta x} = \frac{e}{\hbar}\int B_y(x,y,z)dz, \ \frac{\delta\phi_M(x,y)}{\delta y} = -\frac{e}{\hbar}\int B_x(x,y,z)dz \tag{3.19}$$

Quantitative information about the magnetic properties of the sample can, thus, be retrieved by separating the electrostatic and magnetic contributions to the phase shift. Experimentally, there are several ways of doing this; some are more suitable than others depending on the magnetic behavior of the sample and their implementation. The most commonly used technique is to record two hologram images, where one of them is taken after flipping the sample upside-down. This method was first proposed by Tonomura et al. considering the "time-reversal operation of the electron beam".[23] By flipping the sample (flipped 180°), the electrostatic contribution remains constant, but the magnetic contribution changes in sign. The magnetic contribution can thus be obtained by evaluating the difference of the phase images from the two holograms divided by two. The electrostatic contribution can, in turn, be calculated from the sum of both phase images divided by two. An example using this phase separation method is shown in Figure 3.8, where the phase image from the first acquisition is called *up* and the one recorded after the flip is called *down.* The main advantage of this method is that it can be applied in all cases, as the magnetic state of the sample is not altered, and this is why it is the phase separation procedure most commonly used and why it is the technique used in this work. The drawback of this method is, first of all, the extra time in manually flipping the sample and readjusting the experimental setup for finding and capturing the same object in a flipped configuration. More importantly, a numerical realignment of the up and down phase images has to be performed with additional scripts to correct for their relative shift and rotation before computing the half sum and the half difference.

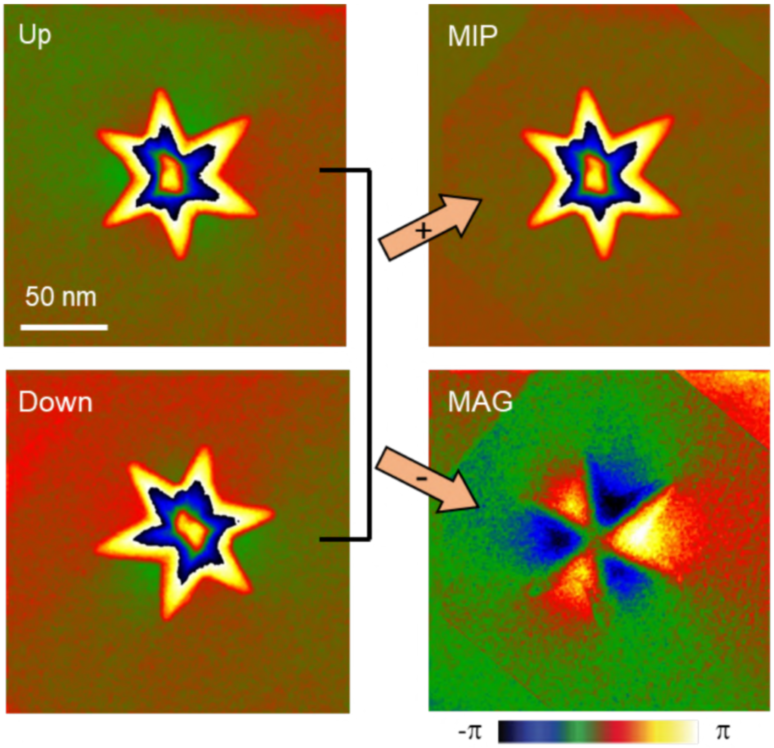

Figure 3.8: Separation of electrostatic (MIP) and magnetic (MAG) contributions to the phase shift.

Other procedures for separating the contributions to the phase shifts exist and all of them involve recording two holograms at different conditions. One can magnetically saturate the sample in two opposite directions, or one may record the two holograms at different temperatures (one above and one below T_C),[24,25] or change the acceleration voltage of the microscope between the two holograms. The former two are more commonly used than the latter. However, they both involve altering the magnetic state of the sample and can therefore not be used for all types of materials and magnetic configurations: for the saturation technique, non-saturated magnetic states cannot be studied (including domain walls), and the method using a change in temperature is difficult to perform for materials with a high T_C (like Co with T_C=1388 K),[26] as a dedicated temperature regulating sample holder is needed, and can also be problematic due to sample drift from heating. The third option, of changing the acceleration voltage, does not alter the magnetic state of the sample, as the magnetic state does not depend on the acceleration voltage (Equation 3.12), but it does affect the optical alignment of the microscope drastically, and thus compromises the stability of the microscope which makes the reconstruction process more difficult and therefore rarely practiced.

3.3.4 A dedicated microscope

The EH experiments in this work were carried out on the dedicated HF3300-C TEM of Hitachi High Technology (HHT) for which was specially developed in collaboration with the CEMES laboratory for *In-situ* and Interferometric TEM experiments, and therefore named the *I2TEM*. This electron microscope has an acceleration voltage of up to 300 kV.

It is fitted with a cold field emission gun to achieve a highly coherent beam, leading to a high sensitivity to the phase shift and an extra dedicated Lorentz stage located above the objective lens to provide a field-free position for the sample. It is also possible to use the normal sample stage for magnetic imaging by switching off the objective lens (as discussed in Section 3.1.4) and using the corrector TL11 lens as Lorentz lens to form the image. The microscope also has a spherical aberration corrector (CEOS B-COR Aplantor), which enables a resolution down to 0.5 nm in holography mode for both stages.

There are in addition three rotatable electrostatic biprisms installed in the I2TEM; one is placed below the gun, in the condenser system, to allow splitting of the electron beam for off-axis electron holography to increase the distance between the object and the reference wave at the object plane,[27] or tilting of the reference wave (for dark-field EH).[28] The two other biprisms (called BP1 and BP2), are placed in the imaging system. In this work, the two last biprisms have been used simultaneously in a so-called *double-biprism* setup to avoid Fresnel fringes and to have the possibility to adjust the interference area size and the fringe spacing independently.[29]

Automated drift-correcting software

A home-made software for instability compensation has been developed and installed on the I2TEM by Dr. C. Gatel. This software is used to compensate hologram fringes and sample drift in real-time by adjusting the beam tilt and stage, respectively. The two methods for correcting the specimen and fringe drift are controlled separately and can thus be used when appropriate. An example showing the difference between holograms taken with and without the control software is shown in Figure 3.9.

In principle, the real-time feedback control of the TEM is based on the analysis of the live-view image acquired by the camera by speed-optimized algorithms which continuously communicates information to the relevant parts of the microscope to adjust their parameters for correcting and/or compensating for instabilities. A prerequisite for this method is, thus, having a camera with a sufficiently fast acquisition time. Our system works with a high-speed 4k digital camera (OveView, Gatan Inc.) is operated at a full-frame rate of 25 images per second, which corresponds to a frame acquisition time of 40 ms. In holography mode, a temporal integration window of about 250 ms is usually set for a better visualization of the holographic fringes.

The specimen control process compensates for detected sample drift by mechanically moving the stage. This is favorable to do using the image shift as the sample can be moved independently of the interferometric fringes.[30] In order to detect and analyze the sample drift, a diagnostics tool for the specimen control, based on cross-correlation between a target and the current image region, is used after applying a low-loss filter to remove the hologram fringes and another dedicated filter for edge detection. For this, the user has to select a region of the hologram image with prominent features that are more easily detected by the software, like for example, amorphous materials or a sample edge, as shown by the blue squared region displayed in Figure 3.9a.

Lateral drift and fluctuations of the interference fringes in hologram images are often due to mechanical instabilities of the biprisms. In order to correct for this type of movement, the control software sends information to the microscope tilt coils, causing a controlled beam tilt that in turn results in a relative shift in the interference fringes.[32] Not only does this allow for longer acquisition times, giving a better fringe contrast, that can be crucial for resolving small fringe spacings (for higher spatial resolution), but it also enables advanced phase reconstruction methods, such as the π-shift (also called fringe-shift) method, to be used. This technique consists of recording two hologram images where their fringes are phase-shifted by exactly π radians,[33] which can drastically improve the fringe contrast, like shown in the example presented in Figure 3.9.

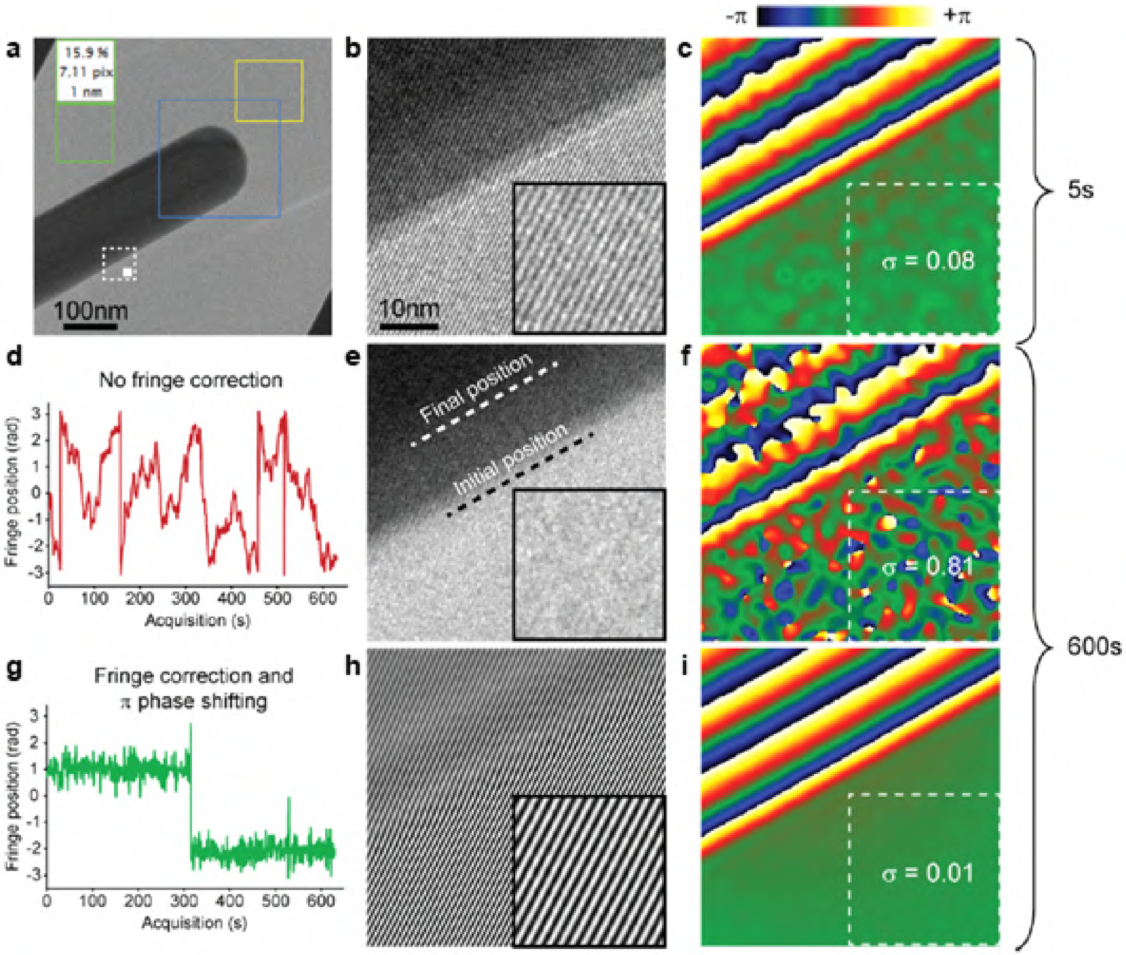

Figure 3.9: Compensation of drift of hologram fringes and specimen: (**a**) Hologram in camera-view with colored squares marking calibration tools for live analysis, where yellow is for fringe position, blue is for specimen position, and green for fringe spacing and contrast. (**b**) zoom-in of hologram fringes in dotted square marked in **a** after 5 s of exposure time, with (**c**) corresponding phase image showing local standard deviation σ. (**d**) Graph of fringe position for 600 s of exposure time without feedback control, with (**e**) and (**f**) displaying corresponding hologram and phase image, respectively. (**g**) Graph of fringe position for 600 s of exposure time with feedback control of both fringes and specimen position, with (**h**) and (**i**) displaying corresponding hologram and phase image, respectively.[31]

The holograms acquired in this work were gathered by the use of fringe drift compensation developed by Dr. Christophe Gatel et al.[31] with an exposure time of 160 seconds per hologram, including the π-shift method, and with an inter-fringe distance of 1.5 nm. The phase images with 3 nm of spatial resolution have been extracted from the holograms and treated using homemade software and the Fourier analysis described above.

3.3.5 Holographic vector field electron tomography

As discussed, one limitation of EH is that we only record the projection of the in-plane components of the magnetic induction. When imaging a NW, we thus, get a 2D projection of an object with a 3D distribution of the internal and external magnetic induction. *Holographic vector field electron tomography* (VFET) combines the technique of off-axis electron holography with electron tomography to provide a 3D reconstruction of electrostatic and magnetic potentials in all three Cartesian directions[17] with a spatial resolution down to a few nanometers.[34] One of the advantages of being able to reconstruct a 3D map of the electrostatic potential of the sample is that it gives an insight into the real 3D morphology of the imaged region through the iso-surface rendering of the 3D potential.[35] This can greatly improve any micromagnetic simulations performed to complement the experimental study as this will tighten the gap between the experimentally analyzed and simulated objects.[36]

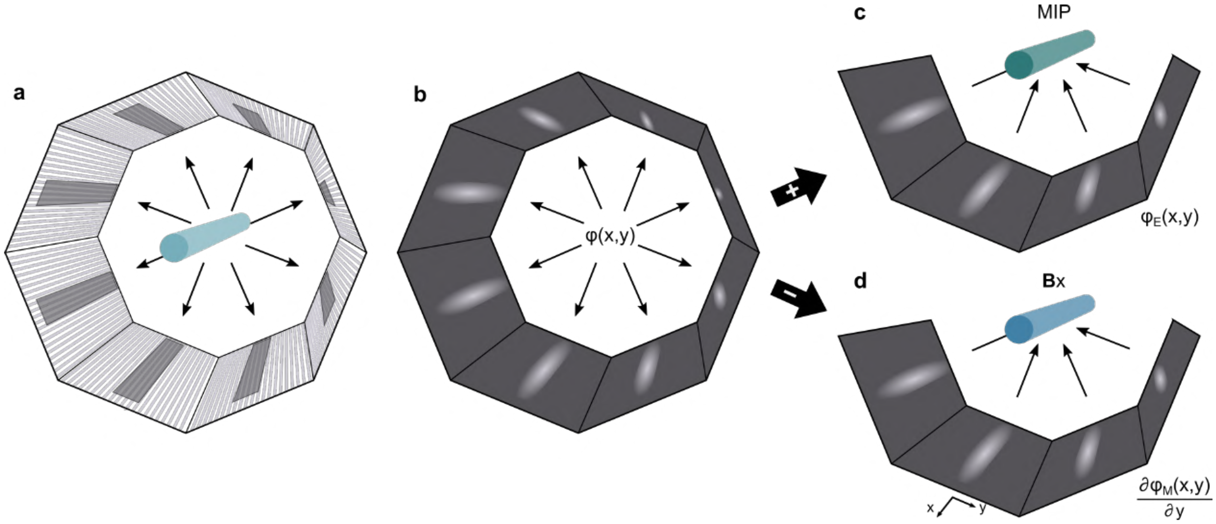

Figure 3.10: Principle of vector field electron holography and the tomography process. (**a**) Hologram tilt series recorded of the nanostructure, ideally covering a tilt range of 360°. (**b**) Holographic reconstruction to retrieve the phase image from each of the holographic projections from (**a**). The electrostatic and magnetic contribution to the phase shift is then separated from calculating half of the sum or difference (respectively) between the phase images from opposite projections. (**c**) The electric phase images can then be back-projected to obtain a 3D tomographic reconstruction of the electric potential. (**d**) The magnetic field components (B_x and B_y) are retrieved separately from differentiation in the in-plane direction perpendicular to the tilt axis before the tomographic reconstruction. The tilt series is thus repeated for two tilt axis, ideally with a 90° rotation relative to each other, in order to recover both **B**-field components.

Holographic VFET has been developed by Dr. D. Wolf and Dr. A. Lubk from Leibniz Institute in Dresden. The principle of holographic VFET, sometimes called electron holographic tomography,[35,37] is roughly illustrated in Figure 3.10. It starts with the acquisition of holograms, one with the object, and one reference hologram, at each tilt step. Ideally, the sample would be tilted ±90° with increments of around ±1°, to record projections from 180°. This is repeated after flipping the sample to record holograms from the same but opposite projections (like up and down configuration in Section 3.3.3). Ideally, this results in a full 360° tilt series of holograms around the tilt axis, as illustrated in Figure 3.10a, where the black arrows represent the projection directions. After this, the phase images are reconstructed for each of the electron holograms in the tilt-series, like in the process for conventional EH (Section 3.3.2), as is shown in Figure 3.10b. The phase images are then separated into their electrostatic and magnetic contributions to the phase shift by respectively calculating half of the sum or the difference between the two phase images of the same but opposite projections. This results in 180° tilt series for each of the electrostatic and the magnetic contributions. By performing tomographic reconstruction, one can then retrieve the 3D distribution of the electric potential (Figure 3.10c) as well as the B_x and B_y components of the magnetic **B**-field (Figure 3.10d). To reconstruct each of the two magnetic induction components in 3D, tilt series are performed around two different tilt axis orthogonally to each other, as illustrated in 3.11. From each tilt axis, the 3D axial magnetic field component is obtained by differentiating the magnetic phase image by its perpendicular direction before the tomographic reconstruction process, as noted in Figure 3.10d. For a more detailed explanation of the reconstruction and processing of the data, see the Communications Physics publication from 2019 by Dr. D. Wolf et al.[36] and the belonging supplementary information.

After this, the missing component of the magnetic induction, B_z, can be calculated by assuming $\nabla\cdot\,\mathbf{B} = 0$ and computing the projected components perpendicular to the tilt axis in one series (axis I), and use it to substitute into the reconstruction of the other tilt series (axis II).[38] The resulting 3D vector representations are called *tomograms*.

As mentioned, each tilt sub-series (up and down configuration) is ideally performed with a 180° range, resulting in a full 360° tilt series. However, even when using dedicated tomogra-

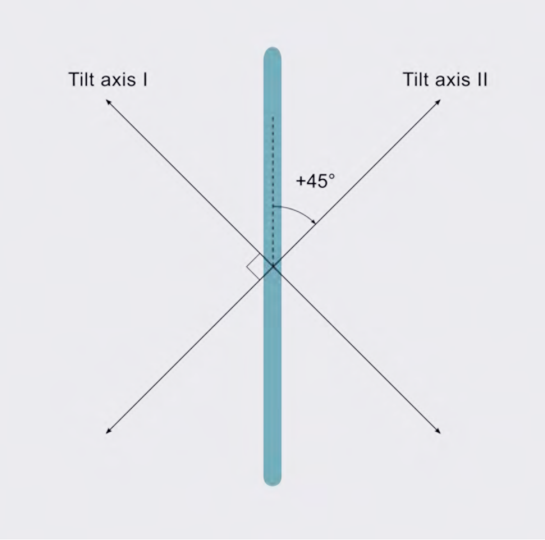

Figure 3.11: Illustration of a NW (green) lying on a carbon film of a TEM grid (gray). Two tilt axis with a 90° degree rotation with respect to each other, and with ±45° relative to the NW axis are indicated by black double-arrowed lines.

phy sample holders, there is usually a tilt limitation due to the holder geometry, if not the sample itself. In practice, experiments are performed using the highest possible tilt angles allowed by the sample and holder geometry, which is usually a sample tilt range of ±60° to ±70°[36] with increments of ±1 to ±3°.[34] Because of this, the reconstructed tomograms get an unavoidable direction-dependent reduction in the resolution called the *missing wedge artifact.*

Holographic VFET is an advanced and powerful technique, but also a challenging one. Apart from the requirements on the specimen posed by the TEM environment, the specimen to be inspected also has to be visible in every projection at tilt angles above 60° without being shadowed by other parts of the sample, the sample grid, or the sample holder itself. This calls for extra care being taken when preparing and choosing the object of interest regarding its position on the TEM grid in addition to having enough "free" space around it in all directions for recording a good reference image. Just like in EH, the sample should not have a too strong diffraction contrast in most zone axis. While in EH one only has to consider one projection, meaning that an eventual strong diffraction contrast can be avoided by a slight tilt off the zone-axis, holographic VFET records multiple projections and therefore also multiple grain orientations, and cannot as easily be avoided. In addition, the holographic VFET measurements require a highly stable environment, as the tilt series with image acquisitions often last several hours.

3.4 ASTAR: Structural characterization

Diffraction patterns (DPs) are characteristic maps of the electron wave angular distribution after a scattering event and are formed in the back focal plane of the beam trajectory. The angular distribution of the diffraction patterns is related to the structural properties of the specimen and can be used as a characterization method to determine the texture, structure, and orientation of the crystal grains of the sample.[3]

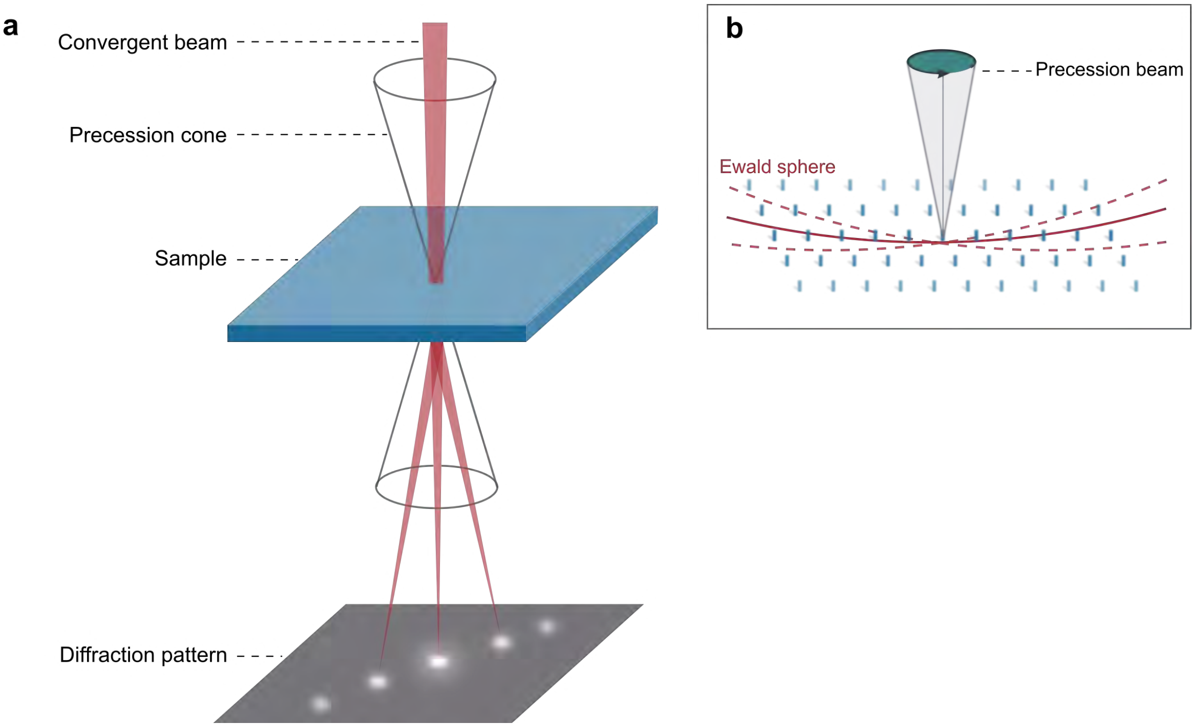

Figure 3.12: (**a**) Schematics of precession electron diffraction in a TEM. (**b**) Cone formed by pivoting the electron beam, resulting in a rocking of the Ewald sphere. The red line illustrates the Ewald sphere, and the stippled red lined show the sphere position as a result of pivoting the beam. The reciprocal lattice is represented by blue elongated spots (relrods).

In *precession electron diffraction* (PED), the illuminating lenses are set to form a small and parallel electron beam, which produces a spot diffraction pattern, as illustrated in Figure 3.12(**a**). By precessing the electron beam, a cone with a pivot point situated on the sample is formed. In reciprocal space, this causes a rocking of the Ewald sphere,[39] as illustrated in Figure 3.12(**b**). This results in a higher number of reflections and of higher-order Laue zones, which can reveal crystallographic symmetries that cannot always be detected by a single DP alone, as well as avoid the so-called 180 ambiguity problem that is connected to some zone axis.[40] Another advantage of PED is that the diffraction condition changes from dynamical (in regular ED) to quasi-kinematic due to an integration of the diffraction spots intensity.[39] This reduces background intensities as well as forbidden reflections that may arise in diffraction patterns due to dynamical scattering.

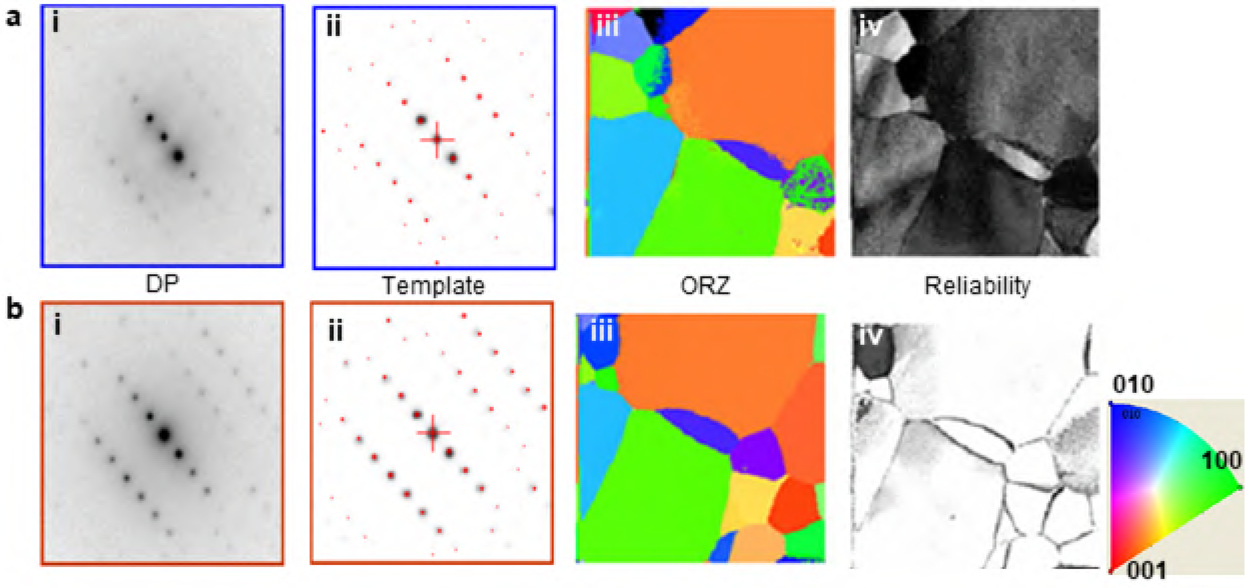

Figure 3.13: ASTAR DP analysis (**a**) showing standard electron diffraction results, and (**b**) with precession. (**i**) and (**ii**) show the acquired DP and the matched simulated DP from the database, respectively.[40] (**iii**) and (**iv**) show the crystal orientation map and the match reliability with respect to the fit with the simulated DP, respectively.[41]

ASTAR is a crystal orientation mapping TEM technique that uses PED to recognize and characterize crystal grains in a sample with a spatial resolution down to 2 nm.[41,42] The technique maps the sample area by scanning a precessing nanoprobe and recording PEDs from each point in the map defined by a given step size.[40,43] Each PED is then automatically matched to a crystal orientation from a database of generated theoretical diffraction patterns by the NanoMEGAS© ASTAR software, as shown in Figure 3.13. The software gives the highest fit for crystal structure and direction for each scanned region in the mapped area. The database of diffraction pattern template is generated from information about the space groups and lattice parameters of the crystal structure of the sample material. The acquired diffraction patterns are then compared with the pre-calculated templates by cross-correlation (Figure 3.13ii). The match with the highest correlation index value between the experimental PED and the DP from the template determines the phase and crystal orientation of the scan. This results in a pixel map with detailed information about the texture (crystallographic orientation and shape of the grains) of the scanned sample (Figure 3.13iii).

3.5 EELS: Compositional characterization

Electron energy-loss spectroscopy (EELS) is a quantitative chemical characterization technique based in a TEM. Contrary to spectroscopy techniques like energy dispersive x-ray spectrometry (EDX), EELS can detect and quantify the lighter elements of the periodic table, as well as provides a better spatial resolution and analytical sensitivity.[3,44,45]

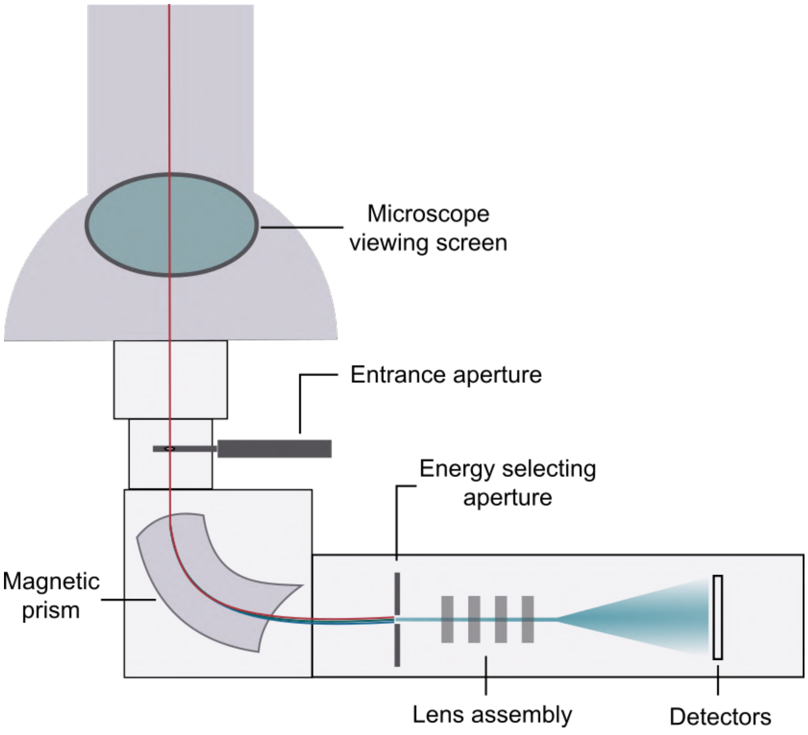

Figure 3.14: Electron energy loss spectroscopy instrumentation in a post-column setup on a TEM, with a typical 90° deflect angle magnetic prism.

In its simplest form, an electron spectrometer is mounted onto the TEM below the viewing chamber. By raising the fluorescent viewing screen of the TEM, the transmitted electrons enter into the spectrometer where they are differentiated according to their kinetic energy by passing through a magnetic spectrometer, where the magnetic field bends the incident beams around a circular trajectory whose bend radius depends on the electron speed (and, thus, energy). Figure 3.14 shows the basic schematics of energy loss detection instrumentation in a post-column setup. Since the initial electron energy, E_0, corresponding to the high voltage value of the microscope, is well defined, the difference in detected kinetic energy can be linked to the electrons' energy loss due to interaction with the specimen. The EEL spectrum can therefore offer information on identifying and also quantifying the composition of elements down to an atomic scale.[46] The resulting energy loss spectrum is normally represented as a direct plot of the electron intensity versus the energy loss.

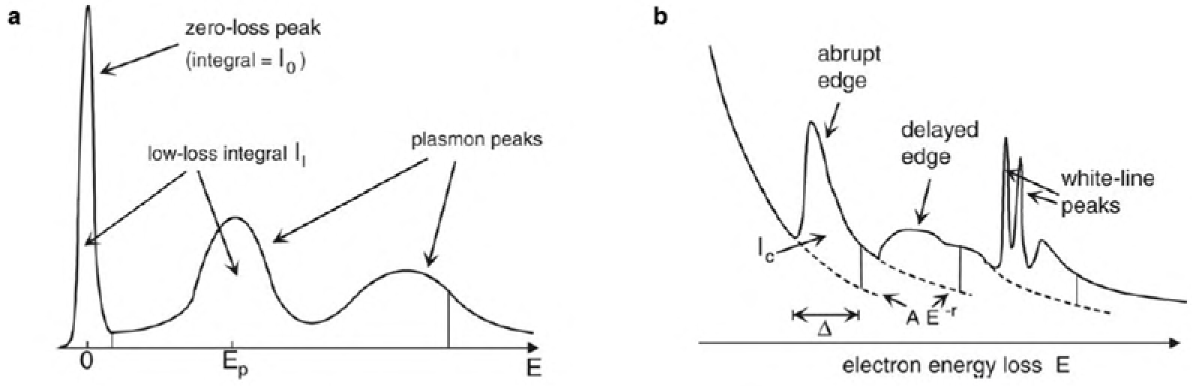

Figure 3.15: Figure showing typical EELS spectra: (**a**) show low-loss region and (**b**) show the core-loss region where the ionization edges are indicated together with their background, which is marked by the dashed line.[46]

The EEL spectrum is generally divided into two parts; the *low-loss* and *high-loss* spectra. The low-loss spectrum (generally < 50 eV)[47] contains a large peak at 0 eV caused by the directly transmitted and the elastically scattered electrons, called the *zero-loss* peak. A scheme of a typical low-loss spectrum is represented in Figure 3.15a. The low-loss region contains information about the band structure and the dielectric properties of a material, containing a prominent peak from plasma resonance of the valence atoms of the sample centered around 24 eV. In the region above 50 eV, the EELS measurements have a much lower signal intensity compared to the low-loss spectra. The high-loss spectrum consists of characteristic *ionisation edges* shaped like a quick rise in intensity followed by a gradual fall, as illustrated in Figure 3.15b. These edges arise from a beam electron exciting an inner shell electron to a state above the Fermi level. The ionization edges are particularly useful to analyze the lighter elements of the periodic table, giving the ionization energy and quantitative analysis of the composed elements.

In Scanning (S)TEM-EELS, the spectrum images are formed by scanning the sample pixel by pixel using a nanometer-sized convergent electron probe in STEM mode. To optimize the spatial resolution and detection limit of the technique, the electron probe should be as small in size as possible, with a high brightness, and ideally also with low noise, high stability, and a high maximal current.[48] The spatial resolution of STEM-EELS is determined by the probe size, which is limited by the spherical aberration of the lens. By the use of a corrector system in the TEM, a resolution down to 1 Å[48] can be achieved one can focus a beam with a larger convergent angle.

3.6 Nanowire growth: Electrodeposition

Nowadays, there are many different techniques that can be used to fabricate nanowires, such as the vapour-liquid-solid (VLS) technique,[49,50] electron or focused ion beam deposition,[51,52] and template-based synthesis.[53,54] There are also top-down nanofabrication techniques like electron beam, x-ray, and focused ion beam lithography,[55] that start from a bulk sample or thin film and are used in combination with lift-off processes to form nanostructures.

One of the most used template-based nanowire synthesis techniques is the *electrodeposition* technique. In this technique, nanowires of single metals or alloys are grown into membranes (polymers or alumina) with highly ordered pores of a defined diameter (Figure 3.16a). A large number of nanowires can, thus, be produced at a low cost and with the possibility to easily tune the composition and size.[56–59] This is the technique that was used to grow the magnetic nanowires studied in this work.

For the electrodeposition of pure metals and alloys, one uses the principle of reducing the cations of dissolved metal in the electrolyte by the gain of electrons from a *working electrode*, which forms a metal layer on the electrode. The shape of the metal formed by electrodeposition is controlled by making a template on the electrolyte surface.

A basic electrodeposition system, a three-electrodes cell, consists of three electrodes: an

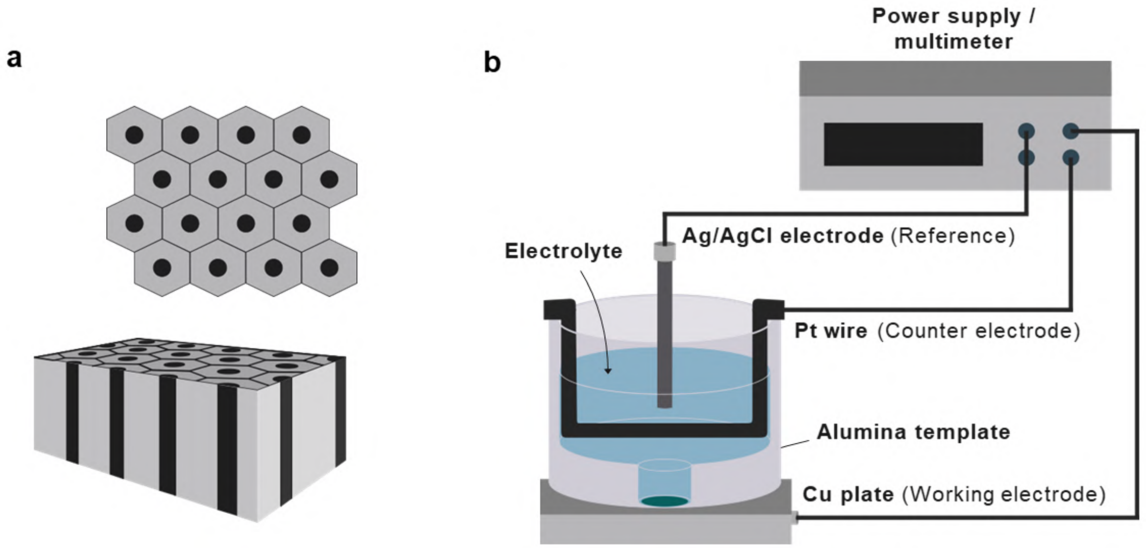

Figure 3.16: Figure showing (**a**) the ordered pores in an anodic aluminium oxide (AAO) template. (**b**) Schematics of electrodeposition setup, with three-electrodes cell and connected power supply.

anode (working electrode), a cathode and a reference. The three electrodes are immersed into the electrolyte solution, as illustrated in Figure 3.16b. The reference electrode is used to measure the characteristic response of the electric signal from the cathode. The electrodes are then controlled by an external circuit, and the electrodeposition can be performed in different ways:[60]

- A potentiostatic mode,[61] where the current is regulated to keep a certain voltage between the electrodes constant.
- A galvanostatic mode, where the current is held constant.
- An alternating mode where alternating voltage or current is applied.

Electrodeposition thus allows for the synthesis of nanowires with a variety of chemical compositions, crystal structures, and geometries by varying the parameters for the electrodeposition. For example, the composition can be varied using different electrolyte bath compositions as well as varying the applied voltage to deposit different materials from the solution.[62] Electrodeposited NWs with various crystallographic structures have been linked to changes in pH value of the electrolyte,[63] and the nanowire aspect ratio and geometry is dependent on both the template geometry.[64,65]

In this work, the nanowires were grown by electrodeposition into hexagonally oriented anodic aluminum oxide (AAO) templates in a three-electrode cell using a Watts-type bath as the electrolyte. An illustration of the electrodeposition setup and the three-electrodes cell can be seen in Figure 3.16b. For this setup, a thin layer of gold is sputtered onto the bottom of the alumina pores prior to the electrodeposition of the metallic nanowires. To secure a good contact with the pores, an additional small layer of Au is electrodeposited into the template pores with an Orosene© electrolyte. After the growth, the alumina template is dissolved in an aqueous solution of chromic oxide and phosphoric acid, in order to release the metallic NWs. After the deposition onto a carbon foil, the NWs can be studied individually in a TEM.

3.7 Dual Beam system

A *Dual Beam* is a system that combines Scanning Electron Microscopy (SEM) and Focused Ion Beam (FIB) in the same equipment.[66] Such a system allows for performing ion etching or deposition while keeping track of the process using the electron probe, without destroying the sample. This is a great advantage for fields like nanolithography and nanofabrication, TEM sample preparation, and a range of other applications (spectroscopy techniques, 3D characterization, etc.).

A standard Dual Beam setup consists of a vertical SEM column with a FIB column relatively tilted at 52°, as illustrated in Figure 3.17a. The sample is located on a rotatable podium at the point of coincidence of the ion and the electron beam. As the FIB column is tilted, the sample also has to be tilted 52° for ion milling or deposition normal to the surface. In our case, the FEI Helios Nanolab™ 600i, used in this thesis work, offers tilt angles ranging from -10° to 60° allowing to orient the sample for each of the columns, depending on the intended processes.

In this work, we have contacted some NWs using *Focused Ion Beam Induced Deposition* (FIBID) as a direct and local lithography process. There are many other available techniques based on the focused ion/electron beam capability in the Dual Beam environment, like the Focused Electron Beam Induced Deposition (FEBID - the electron counterpart of FIBID).

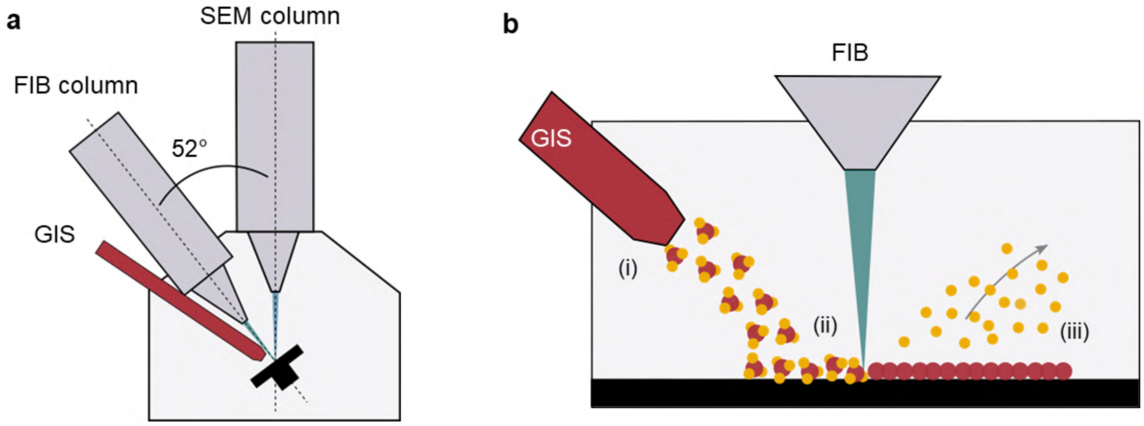

Figure 3.17: (**a**) Illustration showing the two-beam configuration in a Dual Beam instrument. (**b**) Basic schematic representation of the FIBID process: (i) injection of precursor molecules by the GIS, (ii) the ion beam scans over the substrate and cracks precursor molecules leading to a (iii) deposition of the intended (nonvolatile) material, while the volatile is evacuated through the normal vacuum system of the setup.[67]

However, I will next focus on describing the technique which has been used in this thesis, namely FIBID using a Ga+ source.

3.7.1 Focused ion beam induced deposition

FIBID is a direct-writing (mask-free) nanolithography technique used to create two- and three-dimensional material structures with nanometer resolution (down to ∼30 nm for lateral and on the order of 10 nm in thickness).[68,69] A simple illustration of the FIBID operation is shown in Figure 3.17b. The deposition process starts with the injection of the desired precursor gas through a needle-shaped Gas Injection System (GIS), which is placed some hundreds of micrometer above the sample surface. The precursor gas flows onto the sample surface, where it is absorbed by the substrate molecules.[70] Then, when the ion beam impinges the sample surface, the absorbed precursor gas is decomposed into volatile and nonvolatile products. The metallic component is, thus, deposited on the substrate as a thin film in the position where the beam was focused while the volatile material is evacuated through the vacuum system.

Through a controlled scanning of the FIB, one can use FIBID to create various, and even complex, patterns and structures. One application for this is to use FIBID to create electrical contacts, often by the use of Pt or W precursors, which can produce an electrode resistivity down to 100 $\mu\Omega\cdot$cm without post-treatment processes (like annealing).[69] This technique has its main advantage over laser and electron beam lithography (LBL and EBL) from being a single-step process, as well as a direct-writing technique, meaning that it resembles a pencil writing on paper, as opposed to LBL and EBL where several processes and masks are needed. However, one challenge with the FIBID technique is the competition between the deposition and the milling effect of the Ga-ions on the substrate. The milling is caused by the accelerated ions hitting the sample surface with a high momentum, causing surface-atom bond breaking. In other words, if there is not a sufficient amount of precursor molecule flux to the beam focus area, then the result will be milling of the sample instead of deposition. In order to avoid milling of the sample, one has to pay attention to the scanning rate, dwell time, and current of the ion beam to make sure that a sufficient amount of precursors replenishes before each scan.

When using FIBID, the *halo effect* also has to be taken into account. This side effect is especially important to consider when contacting a sample (in our case, a nanowire). A "halo" will occur around the main (intended) deposits due to a combination of two reasons:

- Some ions are scattered inside the already deposited structure and may cause dissociation of precursor molecules up to a few microns away from the ion beam position
- The secondary electrons generated from the substrate by the FIB are scattered away from the main deposition area and then decompose the precursor gas outside of the scanned area.

This indirect deposition outside the intended area is increased with the ion beam current, and the thickness naturally increases when several depositions are grown on the same area. In order to minimize the halo effect, both in thickness and in outstretch, we need to use low beam currents (less than the nA range) and try to reduce the dimensions of the intended deposits whenever possible. While the resistivity of this halo region is higher than the main deposits, we cannot neglect its effect as it could produce possible short circuits in the system, as well as unnecessary contamination of the contacted sample. This, together with difficulty in providing contacts with low enough resistivity for reliable electrical measurements due to

Ga-incorporation, provides the largest drawbacks with using FIBID for electric contacting of nanostructures, as compared with LBL or EBL.

References

[1] D. Sander et al. “The 2017 Magnetism Roadmap”. In: *Journal of Physics D: Applied Physics* **50** (2017), p. 363001. DOI: 10.1088/1361-6463/aa81a1.

[2] M. Staňo and O. Fruchart. “Magnetic nanowires and nanotubes”. In: *Handbook of magnetic materials*. Vol. 27. Elsevier, 2018. Chap. 3, pp. 155–267. ISBN: 9780444641618. DOI: 10.1016/bs.hmm.2018.08.002.

[3] D. B. Williams and C. B. Carter. *Transmission Electron Microscopy*. Springer, 2007. ISBN: 978-0-387-76501-3.

[4] Y. Aharonov and D. Bohm. “Significance of Electromagnetic Potentials in the Quantum Theory”. In: *Physical Review* **115** (1959), pp. 485–491. DOI: 10.1103/PhysRev.115.485.

[5] Y. Aharonov and D. Bohm. “Further Considerations on Electromagnetic Potentials in the Quantum Theory”. In: *Physical Review* **123** (1961), pp. 1511–1524. DOI: 10.1103/PhysRev.123.1511.

[6] H. Lichte and M. Lehmann. “Electron Holography—Basics and Applications”. In: *Reports on Progress in Physics* **71** (2008), p. 016102. DOI: 10.1088/0034-4885/71/1/016102.

[7] L. Reimer. “Particle Optics of Electrons”. In: *Transmission Electron Microscopy: Physics of Image Formation and Microanalysis*. Ed. by H. K. V. Lotsch et al. 2nd ed. Springer, 1997. Chap. 2, pp. 19–49. ISBN: 0-387-50499-0.

[8] L. A. Rodríguez. “In Situ Lorentz Microscopy and Electron Holography in Magnetic Nanostructures”. PhD thesis. Université Toulouse III Paul Sabatier, 2014.

[9] Y. Zhu, ed. *Modern Techniques for Characterizing Magnetic Materials*. Springer, 2005. DOI: 10.1007/b101202.

[10] M. de Graef and Y. Zhu. *Magnetic Imaging and Its Applications to Materials*. Academic Press, 2000. ISBN: 9780080531373.

[11] A. Tonomura. “Applications of Electron Holography”. In: *Reviews of Modern Physics* **59** (1987), pp. 639–669. DOI: 10.1103/RevModPhys.59.639.

[12] A Tonomura. *Electron Holography*. 2nd ed. Springer, 1999. ISBN: 978-3-642-08421-8.

[13] D. Gabor. “A New Microscopic Principle”. In: *Nature* **161** (1948), pp. 777–778. DOI: 10.1038/161777a0.

[14] D. Gabor. “Microscopy by Reconstructed Wave-Fronts”. In: *Proceedings of the Royal Society of London* **197** (1949), pp. 454–487.

[15] D. Gabor. “Microscopy by Reconstructed Wave Fronts: II”. In: *Proceedings of the Physical Society* **64** (1951), pp. 449–469. DOI: 10.1088/0370-1301/64/6/301.

[16] J. M. Cowley. “Twenty Forms of Electron Holography”. In: *Ultramicroscopy* **41** (1992), pp. 335–348. DOI: 10.1016/0304-3991(92)90213-4.

[17] P. A. Midgley and R. E. Dunin-Borkowski. “Electron Tomography and Holography in Materials Science”. In: *Nature Materials* **8** (2009), pp. 271–280. DOI: 10.1038/nmat2406.

[18] P. A. Midgley. “An Introduction to Off-Axis Electron Holography”. In: *Micron* **32** (2001), pp. 167–184. DOI: 10.1016/S0968-4328(99)00105-5.

[19] H. Lichte. “Gottfried Möllenstedt and His Electron Biprism: Four Decades of Challenging and Exciting Electron Physics”. In: *Journal of Electron Microscopy* **47** (1998), pp. 387–394. DOI: 10.1093/oxfordjournals.jmicro.a023609.

[20] H. Lichte. “Electron Holography: Optimum Position of the Biprism in the Electron Microscope”. In: *Ultramicroscopy* **64** (1996), pp. 79–86. DOI: 10.1016/0304-3991(96)00017-4.

[21] W. J. de Ruijter and J. K. Weiss. “Detection Limits in Quantitative Off-Axis Electron Holography”. In: *Ultramicroscopy* **50** (1993), pp. 269–283. DOI: 10.1016/0304-3991(93)90196-5.

[22] M. J. Hÿtch, E. Snoeck, and R. Kilaas. “Quantitative Measurement of Displacement and Strain Fields from HREM Micrographs”. In: *Ultramicroscopy* **74** (1998), pp. 131–146. DOI: 10.1016/S0304-3991(98)00035-7.

[23] A. Tonomura et al. “Holographic Interference Electron Microscopy for Determining Specimen Magnetic Structure and Thickness Distribution”. In: *Physical Review B* **34** (1986), pp. 3397–3402. DOI: 10.1103/PhysRevB.34.3397.

[24] J. C. Loudon, N. D. Mathur, and P. A. Midgley. “Charge-Ordered Ferromagnetic Phase in La 0.5 Ca 0.5 MnO 3”. In: *Nature* **420** (2002), pp. 797–800. DOI: 10.1038/nature01299.

[25] J. H. Yoo et al. “Behavior of Magnetic Domains in $La_{0.46}Sr_{0.54}MnO_3$ during the Ferromagnetic Phase Transformation Studied by Electron Holography”. In: *Physical Review B* **66** (2002), p. 212406. DOI: 10.1103/PhysRevB.66.212406.

[26] C. Kittel. *Introduction to Solid State Physics*. 8th ed. Wiley, 2004. ISBN: 9780471415268.

[27] T. Tanigaki et al. “Advanced Split-Illumination Electron Holography without Fresnel Fringes”. In: *Ultramicroscopy* **137** (2014), pp. 7–11. DOI: 10.1016/j.ultramic.2013.11.002.

[28] F. Röder et al. “Realization of a Tilted Reference Wave for Electron Holography by Means of a Condenser Biprism”. In: *Ultramicroscopy* **161** (2016), pp. 23–40. DOI: 10.1016/j.ultramic.2015.11.004.

[29] K. Harada et al. “Optical System for Double-Biprism Electron Holography”. In: *Journal of Electron Microscopy* **54** (2005), pp. 19–27. DOI: 10.1093/jmicro/dfh098.

[30] J. Liu et al. “Fully Mechanically Controlled Automated Electron Microscopic Tomography”. In: *Scientific Reports* **6** (2016), p. 29231. DOI: 10.1038/srep29231.

[31] C. Gatel et al. “Unlimited Acquisition Time in Electron Holography by Automated Feedback Control of Transmission Electron Microscope”. In: *Applied Physics Letters* **113** (2018), p. 133102. DOI: 10.1063/1.5050906.

[32] V. Boureau et al. “Off-Axis Electron Holography Combining Summation of Hologram Series with Double-Exposure Phase-Shifting: Theory and Application”. In: *Ultramicroscopy* **193** (2018), pp. 52–63. DOI: 10.1016/j.ultramic.2018.06.004.

[33] V. V. Volkov, M. G. Han, and Y. Zhu. “Double-Resolution Electron Holography with Simple Fourier Transform of Fringe-Shifted Holograms”. In: *Ultramicroscopy* **134** (2013), pp. 175–184. DOI: 10.1016/j.ultramic.2013.06.018.

[34] D. Wolf et al. “Electron Holographic Tomography”. In: *Current Opinion in Solid State and Materials Science* **17** (2013), pp. 126–134. DOI: 10.1016/j.cossms.2013.05.002.

[35] P. Simon et al. “Synthesis and Three-Dimensional Magnetic Field Mapping of Co2FeGa Heusler Nanowires at 5 Nm Resolution”. In: *Nano Letters* **16** (2016), pp. 114–120. DOI: 10.1021/acs.nanolett.5b03102.

[36] D. Wolf et al. “Holographic Vector Field Electron Tomography of Three-Dimensional Nanomagnets”. In: *Communications Physics* **2** (2019), pp. 1–9. DOI: 10.1038/s42005-019-0187-8.

[37] D. Wolf et al. “3D Magnetic Induction Maps of Nanoscale Materials Revealed by Electron Holographic Tomography”. In: *Chemistry of Materials* **27** (2015), pp. 6771–6778. DOI: 10.1021/acs.chemmater.5b02723.

[38] C. Phatak, M. Beleggia, and M. De Graef. “Vector Field Electron Tomography of Magnetic Materials: Theoretical Development”. In: *Ultramicroscopy* **108** (2008), pp. 503–513. DOI: 10.1016/j.ultramic.2007.08.002.

[39] R. Vincent and P. A. Midgley. “Double Conical Beam-Rocking System for Measurement of Integrated Electron Diffraction Intensities”. In: *Ultramicroscopy* **53** (1994), pp. 271–282. DOI: 10.1016/0304-3991(94)90039-6.

[40] E. F. Rauch et al. “Automated Nanocrystal Orientation and Phase Mapping in the Transmission Electron Microscope on the Basis of Precession Electron Diffraction”. In: *Zeitschrift für Kristallographie* **225** (2010), pp. 103–109. DOI: 10.1524/zkri.2010.1205.

[41] D. Viladot et al. “Orientation and Phase Mapping in the Transmission Electron Microscope Using Precession-Assisted Diffraction Spot Recognition: State-of-the-Art Results: REVIEW OF PACOM (ASTAR) APPLICATION”. In: *Journal of Microscopy* **252** (2013), pp. 23–34. DOI: 10.1111/jmi.12065.

[42] I. Ghamarian et al. “Development and Application of a Novel Precession Electron Diffraction Technique to Quantify and Map Deformation Structures in Highly Deformed Materials—as Applied to Ultrafine-Grained Titanium”. In: *Acta Materialia* **79** (2014), pp. 203–215. DOI: 10.1016/j.actamat.2014.06.063.

[43] J. Wang et al. “Effect of MgO Underlayer Misorientation on the Texture and Magnetic Property of FePt–C Granular Film”. In: *Acta Materialia* **91** (2015), pp. 41–49. DOI: 10.1016/j.actamat.2015.03.007.

[44] F. Hofer and P. Warbichler. “Application of EELS to the Microanalysis of Materials”. In: *Mikrochimica Acta* **91** (1987), pp. 125–134. DOI: 10.1007/BF01199484.

[45] F. Hofer and G. Kothleitner. “Quantitative Microanalysis Using Electron Energy-Loss Spectrometry: II. Compounds with Heavier Elements”. In: *Microscopy Microanalysis Microstructures* **7** (1996), pp. 265–277. DOI: 10.1051/mmm:1996121.

[46] R. F. Egerton and M. Malac. “EELS in the TEM”. In: *Journal of Electron Spectroscopy and Related Phenomena* **143** (2005), pp. 43–50. DOI: 10.1016/j.elspec.2003.12.009.

[47] F. Hofer et al. “Fundamentals of Electron Energy-Loss Spectroscopy”. In: *IOP Conference Series: Materials Science and Engineering* **109** (2016), p. 012007. DOI: 10.1088/1757-899X/109/1/012007.

[48] R. Pantel and G. Servanton. “Dopant Distribution Quantitative Analysis Using STEM-EELS/EDX Spectroscopy Techniques”. In: *Transmission Electron Microscopy in Micro-Nanoelectronics*. Wiley, 2013. Chap. 2, pp. 37–64. ISBN: 9781118579022. DOI: 10.1002/9781118579022.ch2.

[49] R. S. Wagner and W. C. Ellis. “Vapor-liquid-solid Mechanism of Single Crystal Growth”. In: *Applied Physics Letters* **4** (1964), pp. 89–90. DOI: 10.1063/1.1753975.

[50] D. Ren et al. “New Insights into the Origins of Sb-Induced Effects on Self-Catalyzed GaAsSb Nanowire Arrays”. In: *Nano Letters* **16** (2016), pp. 1201–1209. DOI: 10.1021/acs.nanolett.5b04503.

[51] J. Pablo-Navarro et al. “Tuning Shape, Composition and Magnetization of Three-Dimensional Cobalt Nanowires Grown by Focused Electron Beam Induced Deposition (FEBID)”. In: *Journal of Physics D: Applied Physics* **50** (2017), 18LT01. DOI: 10.1088/1361-6463/aa63b4.

[52] J. Pablo-Navarro et al. “Diameter Modulation of 3D Nanostructures in Focused Electron Beam Induced Deposition Using Local Electric Fields and Beam Defocus”. In: *Nanotechnology* **30** (2019), p. 505302. DOI: 10.1088/1361-6528/ab423c.

[53] Y. Henry et al. "Magnetic Anisotropy and Domain Patterns in Electrodeposited Cobalt Nanowires". In: *The European Physical Journal B* **20** (2001), pp. 35–54. DOI: 10.1007/s100510170283.

[54] E. D. Barriga-Castro et al. "Pseudo-Monocrystalline Properties of Cylindrical Nanowires Confinedly Grown by Electrodeposition in Nanoporous Alumina Templates". In: *RSC Advances* **7** (2017), pp. 13817–13826. DOI: 10.1039/C7RA00691H.

[55] D. McGrouther and J. N Chapman. "Nanopatterning of a Thin Ferromagnetic CoFe Film by Focused-Ion-Beam Irradiation". In: *Applied Physics Letters* **87** (2005), p. 022507. DOI: 10.1063/1.1992661.

[56] E. M. Palmero et al. "Magnetic Behavior of NiCu Nanowire Arrays: Compositional, Geometry and Temperature Dependence". In: *Journal of Applied Physics* **116** (2014), p. 033908. DOI: 10.1063/1.4890358.

[57] J. García et al. "Template-Assisted Co–Ni Alloys and Multisegmented Nanowires with Tuned Magnetic Anisotropy". In: *Physica Status Solidi (a)* **211** (2014), pp. 1041–1047. DOI: 10.1002/pssa.201300731.

[58] C. Bran et al. "Spin Configuration of Cylindrical Bamboo-like Magnetic Nanowires". In: *Journal of Materials Chemistry C* **4** (2016), pp. 978–984. DOI: 10.1039/C5TC04194E.

[59] E. Berganza Eguiarte et al. "Multisegmented Nanowires: A Step towards the Control of the Domain Wall Configuration". In: *Scientific Reports* **7** (2017), p. 11576. DOI: 10.1038/s41598-017-11902-w.

[60] G. Kartopu and O. Yalçın. "Fabrication and Applications of Metal Nanowire Arrays Electrodeposited in Ordered Porous Templates". In: *Electrodeposited Nanowires and their Applications*. Ed. by Nicoleta Lupu. Rijeka: IntechOpen, 2010. Chap. 5. DOI: 10.5772/39481. URL: https://doi.org/10.5772/39481.

[61] E. Matei et al. "Magnetic Configurations of Ni–Cu Alloy Nanowires Obtained by the Template Method". In: *Journal of Nanoparticle Research* **15** (2013), p. 1863. DOI: 10.1007/s11051-013-1863-3.

[62] V. M. Prida et al. "Electroplating and Magnetostructural Characterization of Multisegmented Co54Ni46/Co85Ni15 Nanowires from Single Electrochemical Bath in Anodic

Alumina Templates”. In: *Nanoscale Research Letters* **8** (2013), p. 263. DOI: 10.1186/1556-276X-8-263.

[63] Y. P. Ivanov et al. “Crystallographically Driven Magnetic Behaviour of Arrays of Monocrystalline Co Nanowires”. In: *Nanotechnology* **25** (2014), p. 475702. DOI: 10.1088/0957-4484/25/47/475702.

[64] H. Schlörb et al. “Magnetic Nanowires by Electrodeposition within Templates”. In: *Physica Status Solidi (b)* **247** (2010), pp. 2364–2379. DOI: 10.1002/pssb.201046189.

[65] L. A. Rodríguez et al. “Quantitative Nanoscale Magnetic Study of Isolated Diameter-Modulated FeCoCu Nanowires.” In: *ACS Nano* **10** (2016), pp. 9669–9678. DOI: 10.1021/acsnano.6b05496.

[66] R. J. Young and M. V. Moore. “Dual-Beam (FIB-SEM) Systems”. In: *Introduction to Focused Ion Beams: Instrumentation, Theory, Techniques and Practice*. Ed. by L. A. Giannuzzi and F. A. Stevie. Springer, 2005. Chap. 12, pp. 247–268. DOI: 10.1007/0-387-23313-X_12.

[67] G. Rius, X. Borrisé, and N. Mestres. “Metal-Induced Crystallization of Focused Ion Beam-Induced Deposition for Functional Patterned Ultrathin Nanocarbon”. In: *FIB Nanostructures*. Ed. by Z.M. Wang. Springer, 2013. Chap. 6, pp. 123–159. DOI: 10.1007/978-3-319-02874-3_6.

[68] R. Reyntjens S.; Puers. “A Review of Focused Ion Beam Applications in Microsystem Technology”. In: *Journal of Micromechanics and Microengineering* **11** (2001), pp. 287–300. DOI: 10.1088/0960-1317/11/4/301.

[69] J. M. D. Teresa et al. “Nanoscale Electrical Contacts Grown by Focused Ion Beam (FIB)-Induced Deposition”. In: *FIB Nanostructures*. Ed. by Z.M. Wang. Springer, 2013. Chap. 5, pp. 95–122. DOI: 10.1007/978-3-319-02874-3_5.

[70] K. Kant and D. Losic. “Focused Ion Beam (FIB) Technology for Micro- and Nanoscale Fabrications”. In: *FIB Nanostructures*. Ed. by Z.M. Wang. Springer, 2013. Chap. 1, pp. 1–22. DOI: 10.1007/978-3-319-02874-3_1.

Chapter 4

Effects of local structural changes on the magnetic configuration in CoNi nanowires

4.1 Motivation

The prospect of creating improved spintronic devices that are based on the manipulation and propagation of magnetic domain walls in nanostructures has motivated countless studies the past two decades,[1–5] and has been spurred on by the concept of magnetic domain wall racetrack memory that was presented by Stuart Parkin and his colleagues in the late 2000s.[6] Ferromagnetic cylindrical nanowires are receiving much interest as potential building blocks for such new technological devices. This interest is particularly sparked by the nature of their domain wall propagation, which is predicted to surpass the speed, which is usually limited by the Walked breakdown in structures like flat nanostrips and thin films.[7–9] Cylindrical magnetic NWs have therefore been much studied the past years to uncover and better understand their magnetic properties,[10,11] their domain wall configurations[12–14] and the effects of applied fields.[15]

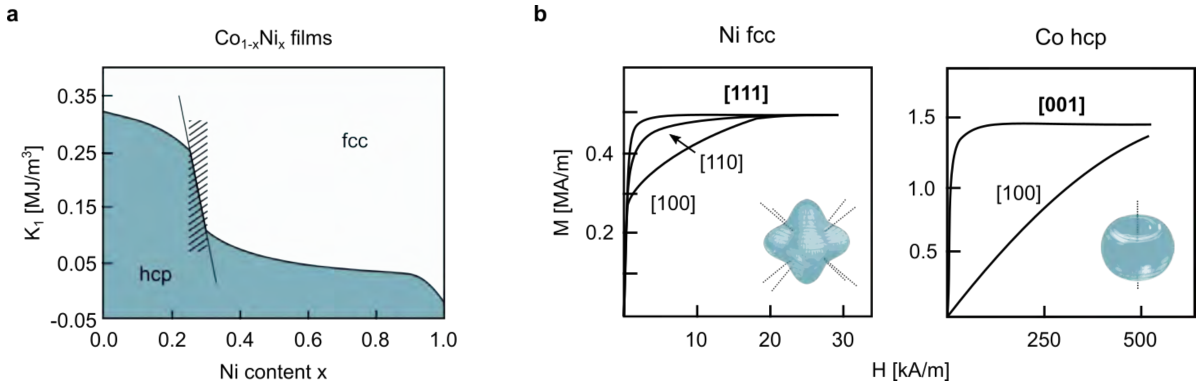

Figure 4.1: (**a**) The anisotropy constant K_1 as a function of the Ni content in CoNi films, showing the phase transition of *hcp* and *fcc* crystal structure, adapted from [16]. (**b**) Magnetization of single crystal Ni *fcc* and Co *hcp* as a function of field, H, with respective magnetocrystalline easy axis energy surfaces, adapted from [17]

In order to take advantage of the NWs potential for the development of new information storage and sensor devices, we need a detailed understanding of the magnetic configurations, and in particular, of the fine structures of their domain walls. A magnetic configuration is determined by the minimization of the magnetic energy of its system, as described in Section 2.3, where object shape, the intrinsic properties of the material, and its crystal structure are contributing factors.[11,13,18,19] The magnetic configurations of electrodeposited NWs can be tuned by adjusting their fabrication process to control their composition and crystal structure.[18,20,21]

The crystal structure of CoNi-alloy NWs can be modified by its Ni-content, as pure Co favors an *hcp* phase, while pure Ni forms *fcc* phase.[16] The *hcp* phase displays a strong uniaxial magnetocrystalline anisotropy with a magnitude great enough to challenge the shape anisotropy of a NW, while the *fcc* crystal structure has four magnetocrystalline axes and a lower magnetocrystalline effect of the system (Figure 4.1). Therefore, CoNi NWs with a high Ni content generally exhibit an *fcc* crystal structure[16,22] and a magnetic induction parallel to the NW axis. Contrary to this, by engineering a monocrystalline *hcp* phase with the *c*-axis (*hcp* magnetocrystalline easy axis) oriented close to perpendicular to the NW axis, the uniaxial magnetocrystalline anisotropy will challenge the large NW shape anisotropy.[10,18,23–26] This can result in complex and surprising magnetic configurations in cylindrical nanowires.[27–29] Tuning of the Co_xNi_{1-x} content, therefore, allows adjusting the magnetic easy axis orientation from parallel (with cubic anisotropy) to perpendicular (with uniaxial anisotropy) relative to the nanowire axis, making CoNi-alloy NWs interesting as potential building blocks for future devices.

To gain control over the magnetization states and reversal mechanisms, a precise analysis of the local structure and the magnetic configuration of a single nanowire is required. Although there have been many studies on the effects of crystal structure on the magnetic configurations in Co-based NWs,[11,15,27,30] as well as works addressing the possibility of *hcp* and *fcc* phase coexisting in the same NW,[22,25,26] there has been little report on how these phases can be mixed in a single NW and how this affects the magnetic configuration. A part of the reason might be that structural and chemical information about the sample often is determined by techniques like x-ray diffraction (XRD) and energy-dispersive x-ray spectroscopy (EDX) on assemblies or arrays of NWs,[18,20] that only provides a statistical average analysis of the samples. The effects of local variations in either magnetic, structural and chemical properties of a sample and how variations in one affect the two others, thus, have to be investigated with a high spatial resolution to be observed.

Such an in-depth study of the correlation between different sample properties demands versatile and advanced techniques with sufficient spatial resolution and sensitivity, which is unique to the TEM environment. In the study presented in this chapter, we exploit this versatility by performing local and quantitative TEM measurements of both the magnetic, structural, and compositional features of the same cylindrical CoNi NWs at the nanometer scale. The NWs studied here have an average diameter of 70 nm and nominal composition of $Co_{85}Ni_{15}$, *i.e.*, a low Ni content.

4.2 Experimental details

4.2.1 Nanowire fabrication

$Co_{85}Ni_{15}$ cylindrical nanowires were fabricated by electrodeposition (Section 3.6) into self-assembled pores of anodic aluminum oxide templates by Dr. Cristina Bran at the Instituto de Ciencia de Materiales de Madrid (ICMM) in Spain.

The alumina templates were made by a two-step anodization process on 99.999% Al substrates. The Al substrate was first cleaned by sonication in acetone and ethanol before subsequently being electropolished in a mixture of $HClO_4$ and ethanol (25:75) at 5°C for 300 seconds with an applied voltage of 20 V, prior to the anodization process. The Al substrates were then cleaned in distilled water (18.2 MΩ/cm) before starting. Both anodizations were carried out using oxalic acid electrolyte at $2-4$°C under 40 V constant voltage, with the first anodization lasting for 24 hours, and the second for 20 hours, resulting in hexagonal self-assembly of cylindrical pores with 40 nm in diameter and a 105 nm interpore distance.[31,32] The Al substrate was then chemically removed by a solution of $CuCl_2 \cdot 1H_2O$ and HCl. The remaining alumina barrier was then cleaned from the pore openings by immersion into a H_3PO_4 solution at 31°C for 90 minutes. This last step also enlarged the pore diameter to 70 nm.

The CoNi magnetic nanowires were then grown by electrodeposition in a three-electrode cell using a Watts-type bath as electrolyte, as described in Section 3.6. An electrolyte composition of 0.124 M $CoSO_4 \cdot 7H_2O$ + 0.085 M $CoCl_2 \cdot 6H_2O$ + 0.064 M $NiSO_4 \cdot 6H_2O$ + 0.064 M $NiCl_2 \cdot 6H_2O$ + 0.32 M H_3BO_3 was used for the fabrication of $Co_{85}Ni_{15}$ nanowires, with an applied electroplating voltage of -1.2 V versus the Ag/AgCl reference electrode. The pH value was kept at a constant value of around 3.0 pH.[14]

The electrodeposited NWs were then released from the template by dissolving the alumina, as explained in Section 3.6, to accommodate for TEM observations of single NWs. The dissolved NWs were then drop-casted onto a TEM carbon grid for the EH, STEM-EELS, and ASTAR measurements.

4.2.2 Magnetic imaging

The imaging of the remnant state magnetic configuration in single NWs was carried out by electron holography using a Hitachi HF-3300C (I2TEM) TEM operated at 300 kV following the procedure described in Section 3.3. The experiments were carried out in the normal stage of the I2TEM, with the objective lens switched off (TL11 mode). A magnetic field of 1.8 T was applied perpendicular to the sample plane (*i.e.* perpendicular to the wire axis) prior to the experiment by switching the objective lens on and off again. To improve the fringe contrast for EH, which can easily be compromised by instabilities of the setup and/or diffraction contrast in crystalline samples, corrective software was used when recording the holograms to minimize the fringe drift and increase the exposure time for maximizing both spatial resolution and the signal-to-noise ratio. This software and correction technique is described in more details in Section 3.3.4. The holograms were acquired with an inter-fringe distance of 1.5 nm for 160 seconds per hologram. Following the data treatment of the holograms, as described in Section 3.3.2 and 3.3.3, the final spatial resolution of the treated magnetic phase images is less than 3 nm.

4.2.3 Structural and chemical analysis

The crystal structure configuration of single nanowires was analyzed using the NanoMEGAS© ASTAR DigiSTAR system, as it provides a crystal orientation map of a large (µm scale) part of the sample. The technique is further described in Section 3.4. The measurements were performed on a Philips CM20-FEG TEM operated at 200 kV. The data was acquired using precession electron diffraction with spot size ∼1 nm, camera length 235 mm, mapped with a step size of 4 nm. The experiments and data treatment was performed in collaboration with Dr. Sébastien Joulié, who performed the measurements and provided the template database of diffraction patterns using the diffraction pattern generator (DiffGen) from the ASTAR software pack, calculated from Co and Ni values found on Crystallography Open Database,[33–37] an open-source web server of crystal structure atomic coordinates, and calculated for Co85Ni15 using Vegard's law. I performed the orientation identification processing of the collected diffraction patterns using the Diffraction Pattern Matching (INDEX) program from the ASTAR software pack and the analysis of the resulting orientation maps using ASTAR's Map Viewer in combination with the Oxford Instruments HKL Channel 5 Tango and Mambo software.

Both energy-dispersive x-ray spectroscopy (EDX) and scanning transmission electron microscopy - electron energy loss spectroscopy (STEM-EELS) were performed to study the compositional distribution of the NWs. The former was done on a Philips CM20-FEG TEM operated at 200 kV, while the STEM-EELS was performed on a probe-corrected JEOL ARM200F TEM operated at 200kV. Both measurements were performed in collaboration with Dr. Cécile Marcelot, who also performed the data treatment of the collected spectra. To recover both the high-loss and the low-loss EELS spectra, the measurements were performed in dual EELS mode using a GIF Quantum ER imaging filter and an energy resolution of 0.33 eV (measured at the FWHM of the zero-loss peak). The data were then analyzed using the MLLS (multiple linear least squares) fitting algorithm in Gatan© Microscopy Suite's Element Quantification tool in order to analyze the signal from the overlapping Co and Ni edges.

4.2.4 Micromagnetic simulations

To support the experimental results, micromagnetic simulations were performed using OOMMF[38] code. The simulations were performed in collaboration with Dr. Luis Alfredo Rodríguez at the Department of Physics at Universidad del Valle in Cali, Colombia. For the simulations, a representative 3D shape of the NW, with a diameter of 70 nm, was built by stacking magnetic unit cells of 5 x 5 x 5 nm^3, constructing regions defines as monocrystalline *fcc* or *hcp*, as defined by the magnetic parameters. The static micromagnetic simulations were performed starting from a state with randomly oriented magnetization for each magnetic cell. The simulation is then run until the total system energy is minimized. As no external field is applied, the resulting magnetic configuration represents a remnant state.

Unless mentioned otherwise, the simulations were performed using the following *base parameters* for *hcp* and *fcc* crystal phase:

Hcp **crystal phase base parameters**

- Saturation magnetization: $M_{s-hcp} = 1273\ \mathrm{kAm}^{-1}$.[14]
- Exchange constant: $A_{hcp} = 26 \times 10^{-12}\ \mathrm{Jm}^{-1}$.[26]
- Magnetocrystalline anisotropy: $K_{1-hcp} = 350\ \mathrm{kJm}^{-3}$ (uniaxial anisotropy, easy axis oriented 78° relative to NW axis as measured in the ASTAR experiment (see Section 4.4)).[16]

Fcc **crystal phase base parameters**

- Saturation magnetization: $M_{s-fcc} = 1273$ kAm^{-1}.[14]
- Exchange constant: $A_{fcc} = 26 \times 10^{-12}$ Jm^{-1}.[26]
- Magnetocrystalline anisotropy: $K_{1-fcc} = 100$ kJm^{-3} (cubic anisotropy, easy axis oriented 81° relative to NW axis).[16]

One or more of these parameters are varied in some of the presented simulations, with the purpose of simulating the effects these changes have on the remnant magnetic configuration. The changes in parameters are then specifically mentioned for these cases.

4.3 Imaging an inhomogeneous magnetic configuration

To get a general overview of the magnetic configurations of the single $Co_{85}Ni_{15}$ NWs, I first studied the sample in Lorentz microscopy (LM) Fresnel mode, as this magnetic imaging technique offers a large field of view, compared to EH, and thus provides a quick qualitative overview of the magnetic configuration of several NWs. As described previously, a magnetic field of 1.8 T was applied perpendicular to the image plane prior to the experiment. The purpose of this inspection of several NWs in Fresnel mode is to evidence possible deviations from such a continuous configuration that could indicate a domain wall, a vortex configuration, or a transversal domain, that will be studied in more details by EH in a second experiment. For instance, in different NWs, the Fresnel images have revealed black/white contrast lines running parallel to the wire, which correspond to a longitudinal magnetic configuration in the direction of the axis.

Figure 4.2 displays some examples of Fresnel images of NWs, where we can see that longitudinal contrast lines are dominating a large portion of the NWs, like for the NW depicted in Figure 4.2c. In addition, a peculiar patterned contrast shows up in some NWs, as indicated by the arrows in Figure 4.2a, b and d. Fresnel mode observations showed contrasts almost like a string of "bubbles," with alternating dark and light contrast in their core aligned parallel to the NW axis. While this type of pattern was not found in all NWs, it was observed

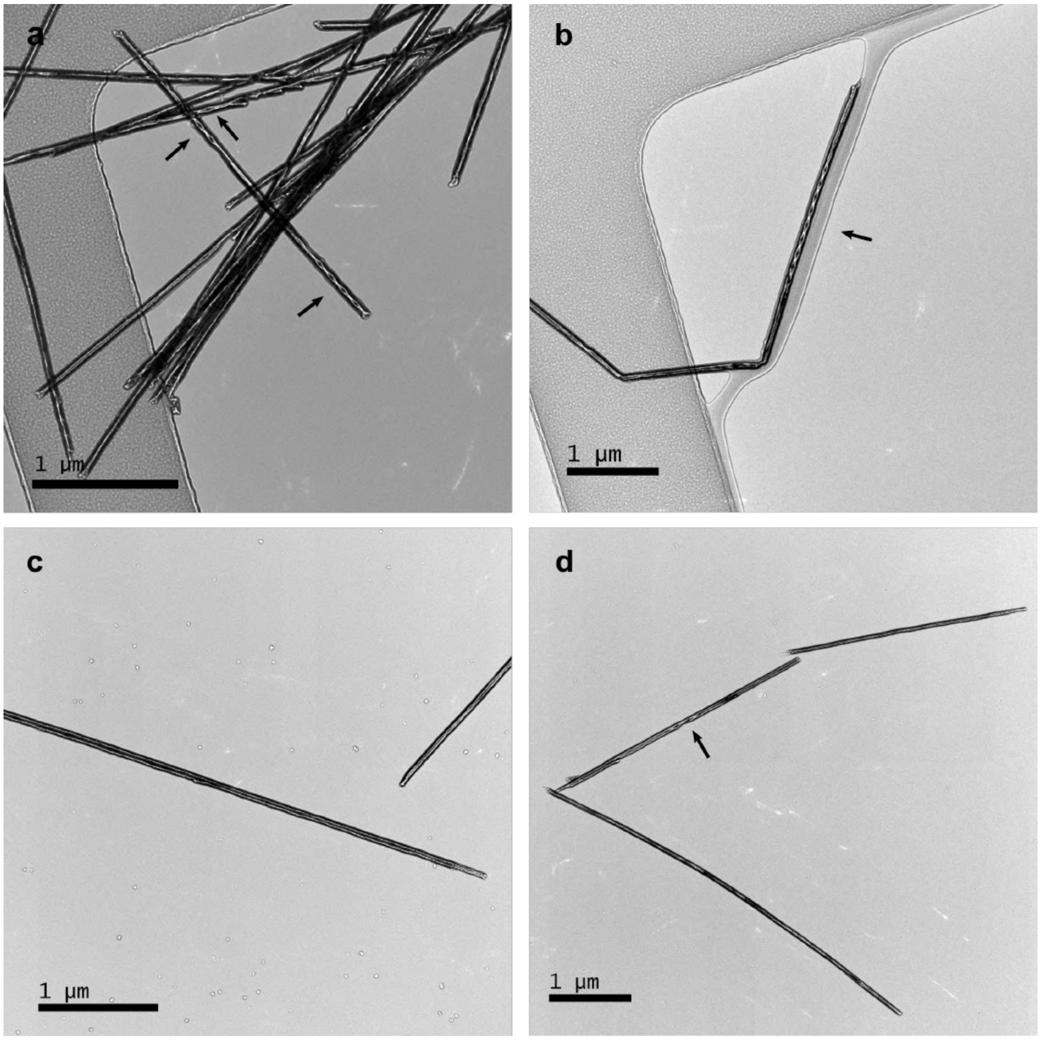

Figure 4.2: (**a**) Low-magnification bright field TEM (BFTEM) image of a representative NW (**b**) Zoom-in BFTEM of the squared region in (**a**). (**c**) Over-focused Fresnel image of the NW in (**a**). Zoom-in Fresnel image of the interesting region marked in (**c**), corresponding to the region in (**b**).

in about 10 to 20% of the inspected NWs. From this, I initiated a deeper study of this exotic configuration to reveal its origin, nature, and why it is not observed in all NWs in the sample.

The low-magnification bright-field TEM (BFTEM) image in Figure 4.3a shows the size and morphology of a representative CoNi NW displaying the unexpected characteristics mentioned above. The NW is lying on a carbon film, and the two circles with a lighter contrast, seen in the image, are vacuum areas due to holes in the carbon film. A Fresnel image of the corresponding NW at remnant state, reported in Figure 4.3c, displays the magnetic configuration of the region magnified in the zoomed image in Figure 4.3d. Figure 4.3d indicates that the contrast lines are qualitatively aligned with the NW axis in each extremity of the

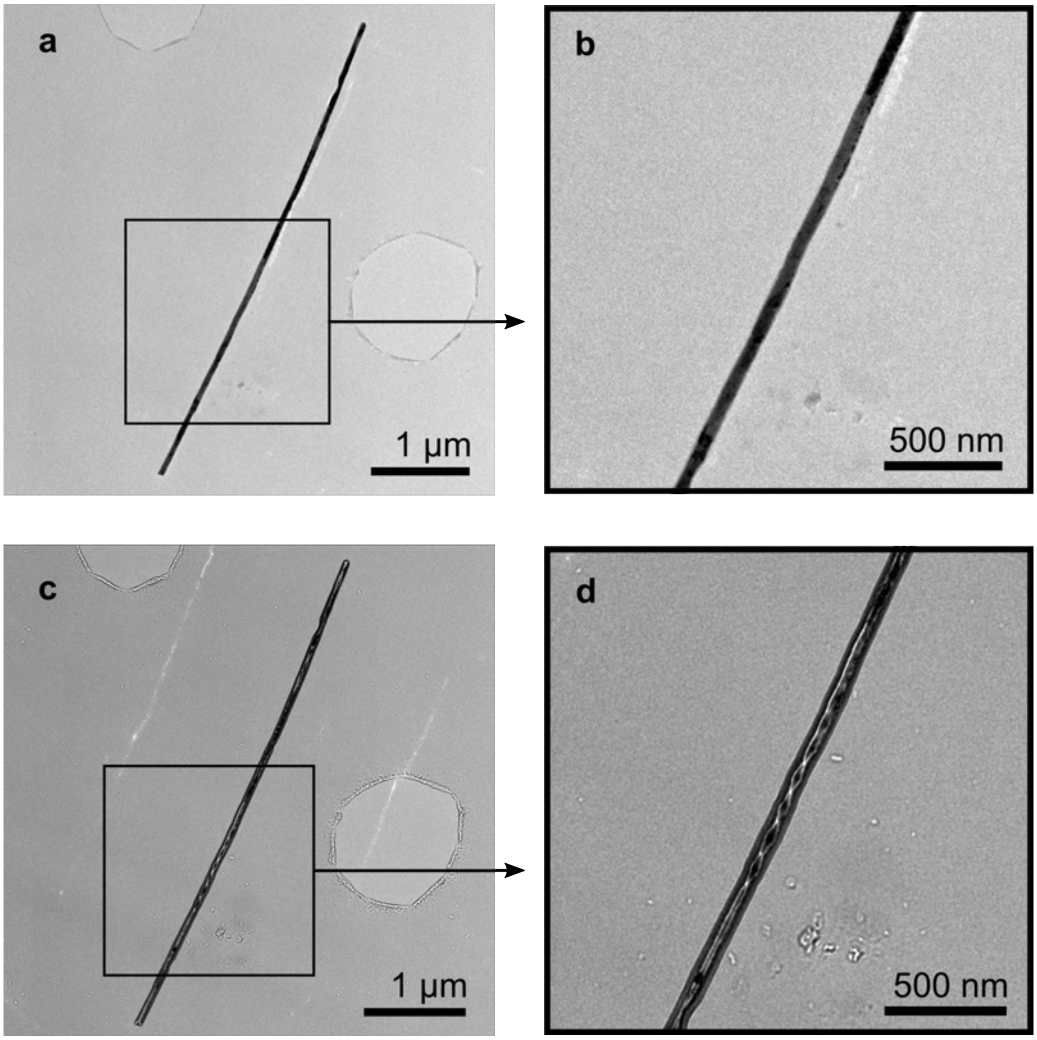

Figure 4.3: (**a**) Low-magnification bright field TEM (BFTEM) image of a representative NW (**b**) Zoom-in BFTEM of the squared region in (**a**). (**c**) Over-focused Fresnel image of the NW in (**a**). Zoom-in Fresnel image of the interesting region marked in (**c**), corresponding to the region in (**b**).

depicted NW segment, while the middle section presents the exotic contrast pattern discussed earlier. The BFTEM image of the corresponding region, seen in Figure 4.3b, shows that the NW does not have any large defects or changes in diameter in the region where the change in contrast appears in the Fresnel image. The contrast variations are therefore believed to come from a change in the magnetic configuration of the NW.

EH was, therefore, performed on the NW region with the inhomogeneous Lorentz contrast to get quantitative information about the in-plane components of the magnetic induction of the NW segment in this region. Figure 4.4b shows the magnetic phase image obtained of the boxed region in Figure 4.4a while Figure 4.4c displays the in-plane magnetic flux of this region by applying a cosine function on an amplified magnetic phase image. This was done to several NWs, and all of them show the same correspondence between the configurations imaged in Fresnel mode and by EH. We then focus our analysis on the presented NW, as it is representative for such specific magnetic configuration in these CoNi NWs.

The EH phase images evidence a complex magnetic configuration with four different regions, indicated as R1-R4 (R for "region") in Figure 4.4b. For simplicity, we define a coordinate system where the x-axis is along the wire axis, y-direction is oriented perpendicular to the NW axis, and the z-axis is along the electron beam path (*i.e.* perpendicular to the image plane). By following the isophase color contours in Figure 4.4b and the in-plane magnetic flux lines in Figure 4.4c, we observe that R1 and R4 show a net magnetic flux along the nanowire axis (indicated x-direction). A fully longitudinal magnetization can be expected in NWs where the magnetocrystalline anisotropy is either weak compared to the NW shape anisotropy or aligns with the NW axis. Contrary to this, R2 contains a chain of circular patterns aligned periodically in the middle of the nanowire. These circular formations are separated by a series of regions with the magnetic flux-lines oriented along the y-direction. This magnetic pattern corresponds to a chain of antiparallel domain-like regions whose magnetization is oriented perpendicular to the nanowire axis with alternating opposite direction, as marked by the white arrows in Figure 4.4c. In the case of a strong uniaxial magnetocrystalline anisotropy with the easy axis oriented perpendicular to the NW axis, its energy can be strong enough to counteract the NW shape anisotropy and thus align the magnetization away from the NW axis. The antiparallel coupling between adjacent domains allows for minimizing the dipole energy. This drastic change in magnetic configuration appears in a relatively small transition region ($<$ 100 nm) from R1 to R2 configurations. Contrary to this, a transition region seems to exist in R3, as it resembles R2, but with the isophase lines slightly oriented towards the nanowire axis. R3, therefore, looks like an intermediate state between that of R1/R4 and R2 regions. The EH analysis thus reveals three distinctly different magnetic configurations appearing within a limited section of the NW.

Going further in the analysis, I take advantage of the ability to get quantitative information about the in-plane magnetic flux of the sample from the EH data. By measuring the phase

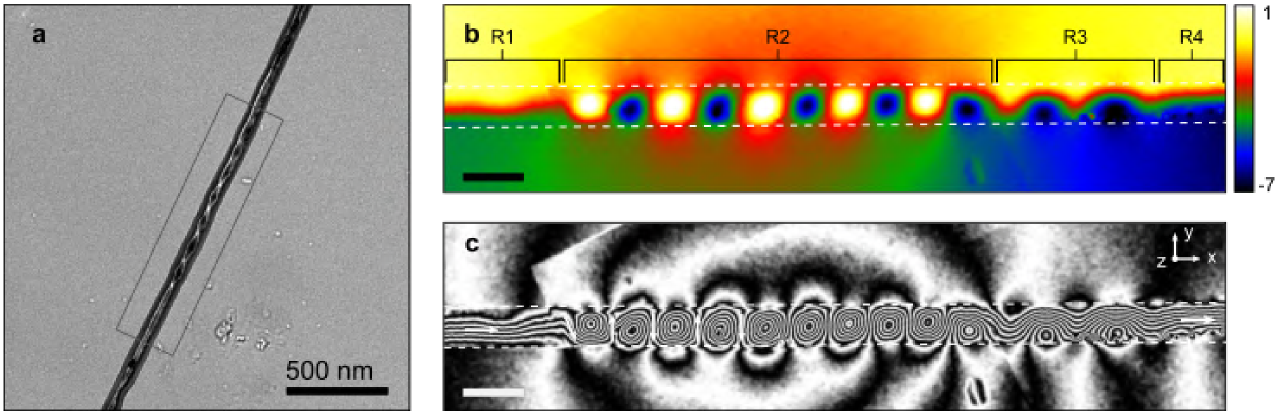

Figure 4.4: (**a**) Fresnel image showing NW region with local changes in magnetic configuration. (**b**) Reconstructed magnetic phase image from EH, with (**c**) showing corresponding magnetic flux image, both of NW region in boxed area from (**a**). Scale bars in (**b**) and (**c**) indicating 100 nm, and the region between the white stippled lines mark the NW position.

shift of the magnetic phase image across the NW axis (Figure 4.4b), the value of the in-plane magnetic induction in the x-direction of the sample can be extracted. Figure 4.5 shows the plotted phase shift measurements across the segments of R1 and R4 marked by gray arrows in the Figure 4.5 inset image. By assuming a circular cross-section with a uniform parallel magnetization along the NW axis, and using the equation for the ϕ_M term (Equation 3.18), I measured an x-component of the magnetic induction of 0.7 T in R1 and 1.0 T in R4. For a uniform magnetic configuration saturated along the NW axis, we would expect a magnetic induction of 1.6 T, based on the saturation magnetization of a $Co_{85}Ni_{15}$-alloy.[14] The measured magnetic inductions in both the R1 and R4 regions are thus much lower than the expected value for a fully parallel magnetization along the x-direction. We, thus, reconsider the assumptions on which the calculations were made to understand how the system deviates from it. While keeping the assumption of a cylindrical cross-section, as observed through the BFTEM images, this discrepancy could either (1) be due to a large deviation in the actual composition of the NW compared with the estimated one, or (2) due to the fact that the magnetization is not perfectly aligned parallel to the NW axis.

1. Considering a magnetization perfectly aligned along the NW axis, the measured value for the magnetic induction would correspond to the magnetization of a Ni_xCo_{1-x} alloy with a Ni content of more than 70%. This seems unlikely considering that previous spectroscopic studies performed on similar NWs elaborated by the same procedure

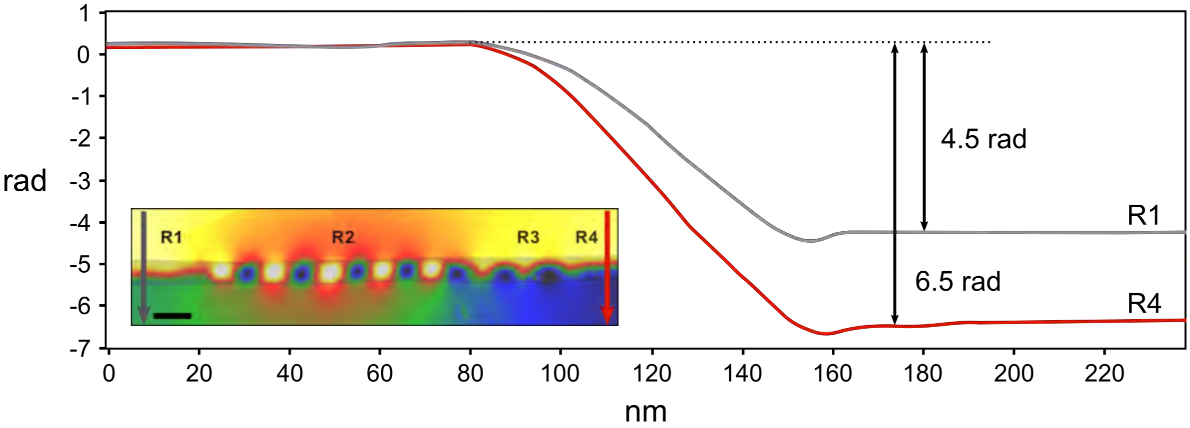

Figure 4.5: Plotted magnetic phase shift in radians per nm from the cross-sections indicated by arrows in inset image. Inset show magnetic phase shift image from Figure 4.4b with labeled magnetic regions R1-R4 and scale-bar indicating 100 nm.

found Co rich NWs with a mean content value of 15% Ni.[14]

2. The fact that the iso-phase lines in both region R1 and R4 in Figure 4.4b are parallel to the wire axis evidence that at least a partial magnetic component must be oriented along this direction. As the induction measured by EH is an integration along the TEM beam trajectory (z-direction) and a two-dimensional (2D) projection of the x- and y-components of the magnetic induction, a perfect rotation of the magnetization around the NW axis would result in zero net measured phase shift, as each y-component of the magnetic induction would have an equal but opposite counterpart (illustrated by red arrows in Figure 4.6), and the technique is inherently blind to the z-components (illustrated by yellow arrows in Figure 4.6). Only components along the NW axis would therefore be detected in such a rotation/curling configuration. We therefore assume that this reduced measured axial magnetic induction comes from a rotational component of the magnetization around the NW axis, and hence, that it is not oriented parallel to the wire axis, but curling around it.

Further, we see from Figure 4.5 that even though the two regions look similar in preliminary investigations, the phase shifts across R1 and R4 are different. The measured magnetic induction in the x-direction is actually 30% smaller for R1 than in R4. This is qualitatively illustrated by the difference in density of flux lines in the two regions in Figure 4.4c. Two possible magnetic configurations that can give rise to such characteristics are: a longitudinal

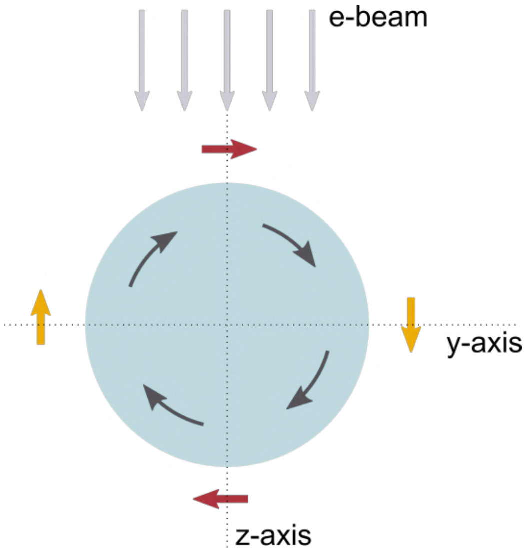

Figure 4.6: Illustration of rotational magnetization in a nanowire, showing the cross section (yz-plane) of the cylindrical NW in blue. Gray arrows show magnetic spins forming a perfect vortex (no x-component) around the NW's core. Yellow and red arrows represent magnetic contributions along z-axis and y-axis, respectively, for the right/top and left/bottom half of NW as separated by the z-axis/y-axis, resulting in opposite but equal yellow/red vectors. As the e-beam is not sensitive to the components along the z-axis (its own incident axis), the magnetic components represented in yellow will not be seen. The hologram is formed by an integration along the beam trajectory ($z$direction), resulting in zero detected phase shift, due to equal but opposite y-component at any beam path along the z-direction.

magnetic vortex state or a curling state around the NW axis. Both of these magnetic configurations present a combination of rotation and parallel components relative to the NW axis. Assuming that R1 and R4 consist of the same type of magnetic configuration, in the case of a vortex state, one could explain the difference in the measured magnetic induction of the two regions from a size difference of the vortex core, as discussed by Bran et al.[39] and Ivanov et al.[40] However, we could expect a vortex state to display an inhomogeneity in the measured induction across the NW due to the core, while we see continuous slopes of measured phase shift in Figure 4.5, demonstrating a more uniform magnetic induction component along the NW cross-section. From this, I conclude that R1 and R4 have a curling magnetic configuration, where the variations in measured axial induction arise from a change in rotation angle of the curling with respect to the nanowire axis. The high value of the measured phase shift in R4 relative to that of R1 comes from a smaller curling angle, *i.e.* a more elongated rotation along the NW axis, leading to a stronger measured magnetic induction in the x-direction. Similarly, the curling in R1 has a large rotation angle relative to the NW axis and a more compressed rotation giving a weaker x-component of the induction as compared to R4. These deductions, based on the quantitative analysis of the magnetization x-components, will be confirmed and detailed by holographic vector field electron tomography (VFET) experiments presented in 5.5.

Moving on to the R2 magnetic configuration, Figure 4.4b and 4.4c imply a series of antiparallel magnetic domain-like regions oriented perpendicular to the nanowire axis along the y-direction, as indicated by the white arrows in Figure 4.4c. These transversal domain-like states are separated by regions with circular isophase lines, which are a type of vortex state where the core is oriented perpendicular to the NW axis along the z-direction. The circular isophase lines come from the in-plane magnetic induction vectors rotating around this transversal vortex core, where the neighboring vortices have either opposite chirality or polarity, such that the rotation in the x-y-plane alternates between clockwise and counter-clockwise direction, while the core is oriented in either positive or negative z-direction with no trending pattern. One surprising feature of this region is that, according to the EH results in Figure 4.4b and 4.4c, the vortex-like states are larger in size than the transversal domain-like regions.

Finally, the magnetic region in the R3 segment appears to be a transitional configuration between the two above-mentioned types, *i.e.* a chain of transversal magnetic vortices (R2) and a curling magnetic state (R1 and R4). From the R2 configuration, the vortex states disappear and the magnetic flux parallel to the NW axis increases as we move towards the R4 domain and into a curling state.

4.4 Structural and chemical analysis: a correlative study

To further investigate the large changes of the magnetic configurations within a NW segment of less than a few microns length, we performed local structural and chemical analysis of this segment. The structural analysis was performed by local electron diffraction experiments using the ASTAR NanoMEGAS© system and software to perform a scan of the NW region.[41,42] For each pixel of the mapped area, with a step size of 4 nm, a precession electron diffraction

(PED) patterns were obtained. The recorded PED patterns were then automatically compared to a template database of calculated patterns for different crystalline directions based on the *fcc* and *hcp* crystal structure, as described in more details in Section 3.4. For this work, the calculated diffraction patterns were generated for a $Co_{85}Ni_{15}$-alloy *hcp* phase lattice parameters $a = b = 2.5$ Å, $c = 4.065$ Å, and space group $P6_3$/mmc, and for an *fcc* phase with $a = b = c = 3.54$ Å, and Fm3m space group. The values were calculated using Vegard's law from crystallographic parameters of Co and Ni found on Crystallography Open Database, and compared to known values of similar CoNi alloys to ensure a good estimated value. The results are shown in Figure 4.7, where Figure 4.7a presents a virtual bright field image of the scanned NW region. Images Figure 4.7b-d display the crystal orientations of the close-packed directions relative to the x-, y-, and z-directions, respectively. From these images, we see that there are three main crystal grain directions, most prominently recognizable in Figure 4.7b. This becomes more evident in Figure 4.7e, which displays a map of the regions with the highest match for *hcp* crystal phase (red) versus *fcc* phase (blue). Here we see that both *fcc* and *hcp* crystal phase are present in the NW segment, and that these three main crystal grains are made up of two *fcc* grains separated by an elongated *hcp* grain. A coexistence of *hcp* and *fcc* phase has already been reported for electrodeposited CoNi NWs.[22,26] However, surprisingly, we did evidence a crystal grain boundary running almost parallel to the NW axis, as seen in Figure 4.7e. Considering the *fcc* phase being oriented with their (111) planes on average oriented at 81° from the NW axis, the *hcp* can be considered as a sequence of (111) stacking faults of the *fcc* phase, the $(0001)_{hcp}$ and $(111)_{fcc}$ planes being parallel. This implies that the [0001] direction of the *hcp* phase is also oriented at this orientation from the NW axis, as measured to be an average value of 78°. I then assume that the change in crystal phase has been caused by (111) stacking faults of the *fcc* phase transitioning from *fcc* to *hcp*, the *hcp* magnetocrystalline anisotropy easy axis oriented in correspondence, in agreement with the measurements.

As the EH and the ASTAR measurements were conducted on the same NW segment, it allows for a direct comparison of the complimentary results, taking advantage of the flexibility of working in a TEM environment. Figure 4.7f shows the magnetic phase image from Figure 4.4b superimposed with Figure 4.7e to only display the region with *hcp* phase. This

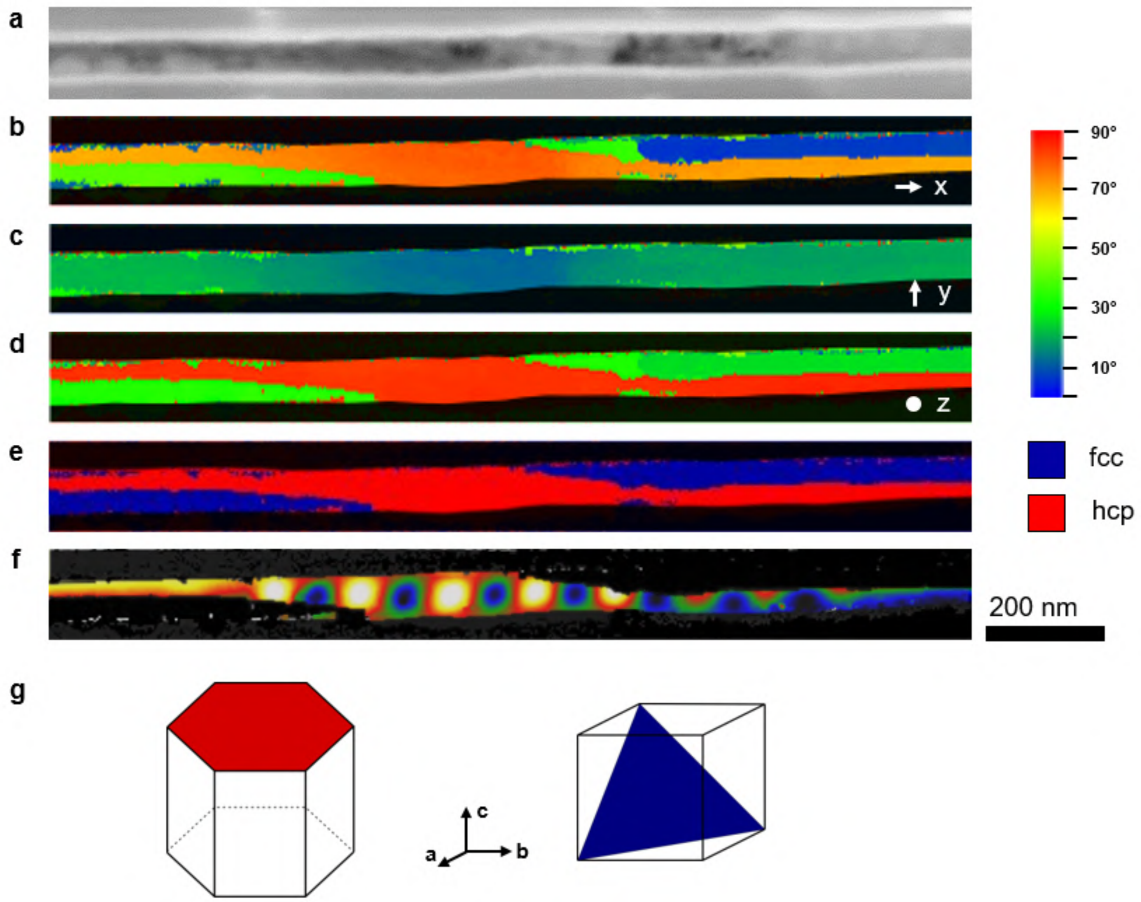

Figure 4.7: Results from ASTAR structural measurements of the NW region. (**a**) Virtual bright field image of mapped NW region. (**b-d** Crystal orientation maps of NW region in (**a**) showing [111]*fcc* and [0001]*hcp* direction color coded by angular deviation with respect to (**b**) x-, (**c**) y- and (**z**) directions. (**e**) Crystal phase map of NW region in (**a**), where blue color marks *fcc* phase and red *hcp* phase. (**f**) magnetic phase image only showing the *hcp* region from (**e**). (**g**) *hcp* and *fcc* close packed planes.

overlapping clearly indicates that the chain of transverse domain-like regions is mainly located in the *hcp* grain. This is in good correspondence as we know that the *fcc* and *hcp* phase have very different values of the anisotropy constant, with respectively a weak cubic, and a strong uniaxial magnetocrystalline anisotropy.[16,43] The *hcp* grain, therefore, has a strong enough magnetocrystalline anisotropy that can challenge the shape anisotropy of the NW and aligning the magnetization towards its *c*-axis instead of along the wire axis (as for *fcc* phase), giving a transverse magnetic component.[44]

In the search for a complete picture of the origin of this local structural change, I decided to perform a chemical analysis by EDX and STEM-EELS in collaboration with Dr. C.

Marcelot (engineer at the CEMES laboratory). We first conducted EDX measurements on several NWs, to detect any change in composition along the NW. The results of one of these measurements are displayed in Figure 4.8. They have been obtained on a different NW from the one previously discussed, but still from the same batch and deposited on the carbon grid. I then performed complimentary EH observations on the same NW (a combination of 11 holograms to study the whole area). Figure 4.8b shows the wrapped magnetic phase image, revealing two regions with a vortex chain configuration, as indicated by the arrows. The EDX mapping data are qualitatively displayed in Figure 4.8c-e, showing nickel in green (c), cobalt in red (d), and oxygen in blue (e). The results indicate an inhomogeneity in composition along the NW axis, which is most prominently seen in the variation in green-contrast in Figure 4.8c, reflecting a fluctuation in Ni content of between 6 at.% (atomic percentage) and 18 at.%. By directly comparing the EDX results with those from EH, a correlation is evidenced between the vortex chains and a lower Ni content, as indicated by the yellow arrows. However, it is worth noting that, while both chains seem to be connected with a region with a lower Ni content, there are other regions with a low Ni content that do not display any vortex chain (white arrows).

EDX measurements can provide a quick qualitative overview of the general sample content across the whole NW. However, as the mean diameter of the sample NWs is 70 nm, and the chemical grain boundary runs parallel to the NW axis, EDX measurements cannot provide a sufficient spatial resolution to study the region of the crystal grain interfaces. STEM-EELS experiments were then performed to go deeper into the local variations of chemical properties. Both line spectra and spectral maps were acquired, mapping the region of a grain boundary to shed light on the origin of the *hcp*/*fcc* phase change.

Figure 4.9 presents STEM-EELS results obtained of the same NW as studied in Section 4.3. Figure 4.9a shows the BFTEM image of the studied NW, where the boxed region is the scanned area. The compositional results are displayed in Figure 4.9c-d, showing the Co and Ni content maps, respectively, in atomic percentages extracted from the recorded spectra using MLLS fitting.[45] A point to note is that these values neglect oxygen content, caused by possible oxidation of the sample. This is part of the reason why the pixels near the NW

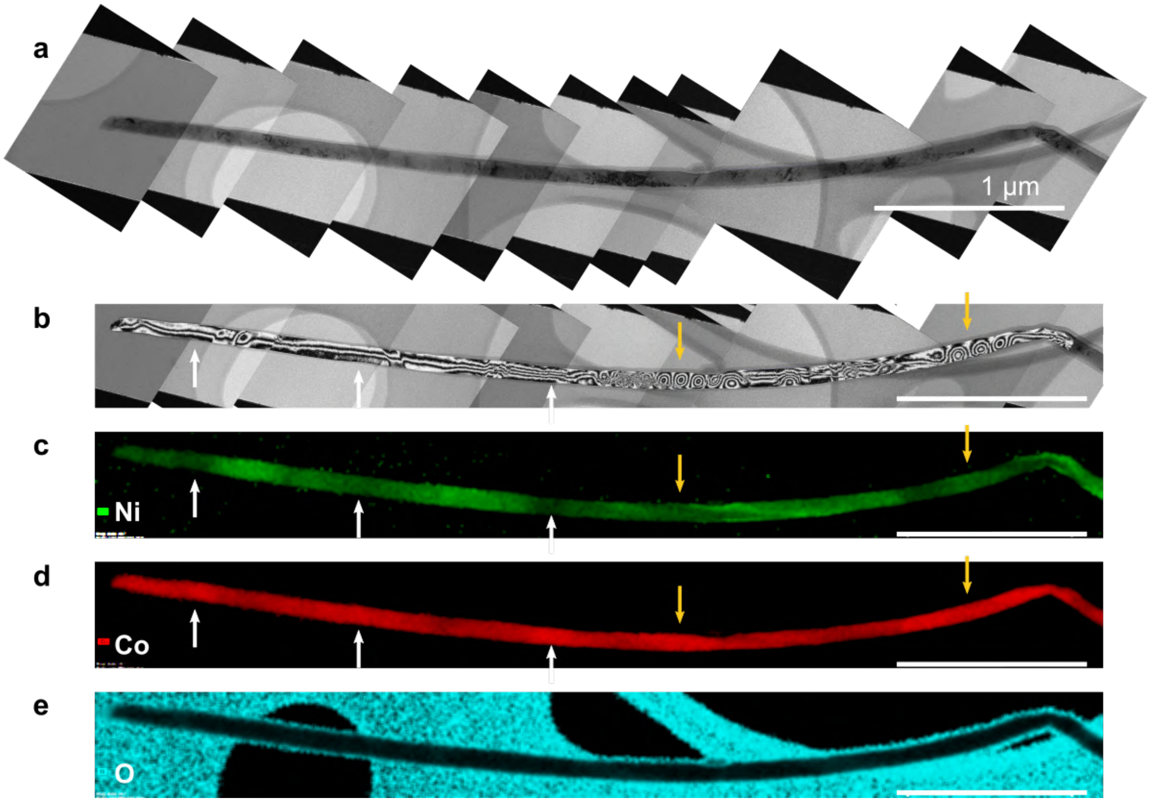

Figure 4.8: Qualitative results from EDX of CoNi NW. (**a**) Stitched BFTEM images resulting from EH experiment of analyzed region. (**b** Magnetic flux image of analyzed NW region, placed on BF image background to reduce the visual disturbance from the holey carbon film. (**c**) - (**e**) show respectively compositional maps of Ni, Co and O content in at.% from the same NW region as in (**a**) and (**b**). The color contrast qualitatively represents a relative change in content.

edges are strongly deriving in value. The stippled line in the composition maps represents the position of the grain boundary directly visible in Figure 4.9a. The maps reveal a difference in composition between the two grains: the Co content is higher in the *hcp* structure (average of 89% Co and 11% Ni in square I in Figure 4.9c) than in the *fcc* structure (average of 80% Co and 20% Ni in square II in Figure 4.9d), which then contains less Co, in agreement with established knowledge about Co-Ni phase diagrams.[16] However, the lowest Co content measured in square I (Figure 4.9c) is 85.5%, while the highest Co content in square II (Figure 4.9d) is 82%, which gives a compositional threshold around 80-85% of Co to stabilize *hcp* phase. This is higher than previously reported levels, which are found to be around 70-75% Co[16,46] films or in bulk CoNi alloys at room temperature. A more systematic and extensive study is needed to clearly conclude an accurate threshold, keeping in mind that it also partly depends on the elaboration process.

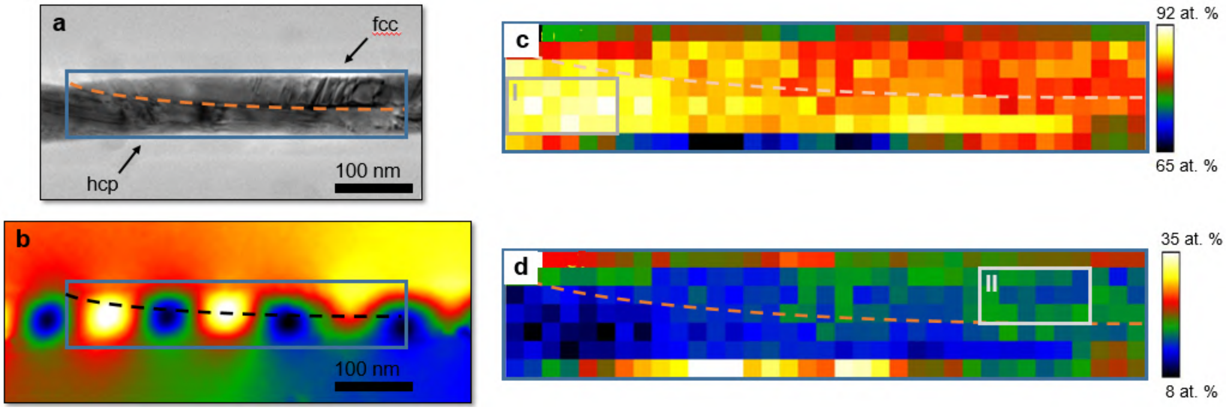

Figure 4.9: Results from spectroscopic measurements of the NW region. (**a**) BFTEM image of analyzed region. (**b** Magnetic phase image of analyzed region. (**c**) and (**d**) show respectively compositional maps of Co and Ni content from boxed region in (**a**).

The chemical and structural analysis of the NW region shows that the chain of vortex states is located in the large grain of mainly *hcp* phase (R2), and the curling state is located in regions seemingly with a coexistence of *fcc* and *hcp* phase grain (R1 and R4). The measurements further indicate that the magnetic transition region R3 is located roughly along the *hcp*/*fcc* grain boundary, where both the structure and the composition is likely to change. It comes out of our complimentary TEM experiments that the drastic variation of the magnetic configuration in such CoNi NWs arises from the change in crystal phase induced by an inhomogeneous composition distribution.

4.5 Micromagnetic simulations

In order to better understand the complex magnetic configuration presented in Figure 4.10, static micromagnetic simulations of the remnant state using OOMMF code[38] have been performed. The first results of these simulations are reported in Figure 4.10 where we build a 2.5 μm long cylindrical shaped nanowire segment with a diameter of 70 nm, consisting of a 2 μm long *hcp* phase and a 0.5 μm long *fcc* segment, as depicted in Figure 4.10a. The crystal grains are assumed monocrystalline and, for a simplified starting point, the grain boundary is set perpendicular to the NW axis. For the *hcp* phase segment, we used the base magnetic parameters started in Section 4.2.4 and a uniaxial magnetocrystalline anisotropy. We did not take into account any deformation in the NW, nor any oxidation layer, and the roughness is

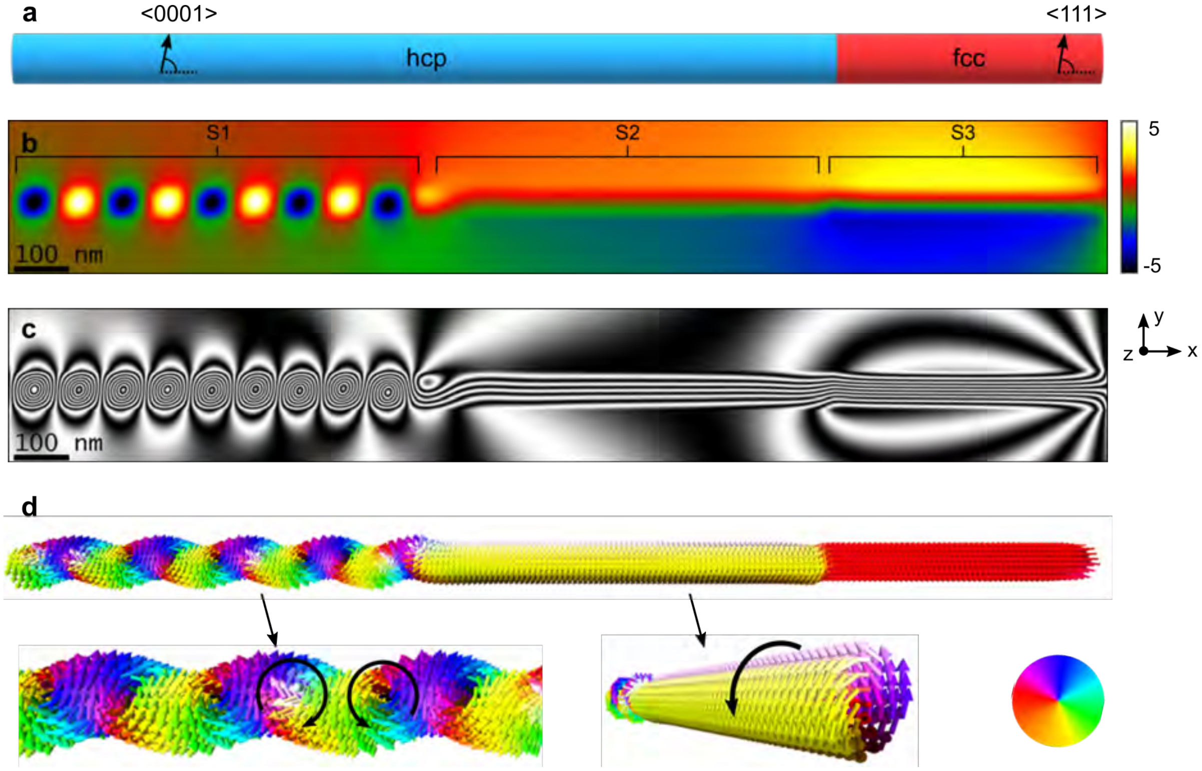

Figure 4.10: Results from micromagnetic simulation. (**a**) NW representation for the simulation, with a 2 μm long *hcp* region with magnetocrystalline easy axis 78° relative wire axis, and a 500 nm long *fcc* region with a magnetocrystalline easy axis at 81° (**b**) Generated magnetic phase image and (**c**) corresponding flux image from the resulting simulation based on the structure in (**a**). Inset in (**b**) show experimental phase image from Figure 4.4. (**d**) 3D representation of the simulation results showing the magnetic vectors with directions indicated by the color wheel. Zoomed-in in images cut-outs of the vortex chain and curling state displayed below in (**d**).

null. The *fcc* phase was simulated using a cubic magnetocrystalline and the base parameters listed in Section 4.2.4, with the exception of the saturation magnetization that was set to $M_{s-fcc} = 989$ kAm^{-1}.

Figure 4.10b-d shows the main results of the OOMMF simulations, where Figure 4.10d offers a 3D representation, for a better visualization of the simulated magnetic states. The overall magnetic phase image generated from the simulations and its corresponding flux lines image (Figure 4.10b-c) is globally in agreement with the experimental one: although the simulated magnetic phase shift image and its corresponding magnetic flux lines image are not exactly the same as the experimental one, we still recognize similar characteristics of the magnetic regions in the two cases. The simulation gives a chain of vortex-looking domains in the region marked as S1 (S for "*simulated*") in Figure 4.10b, which is very similar to the experimental results corresponding to R2 in Figure 4.4b. This region is followed by a curling state, marked S2, that stretches from the end of S1 to the grain interface of the *hcp* and *fcc* region. We point out that the curling state in this simulation appears in the *hcp* grain, and not in the *fcc* grain. Finally, the *fcc* segment contains a magnetic configuration parallel to the NW axis, as is expected due to the weak cubic magnetocrystalline anisotropy, *i.e.*, no rotative component.

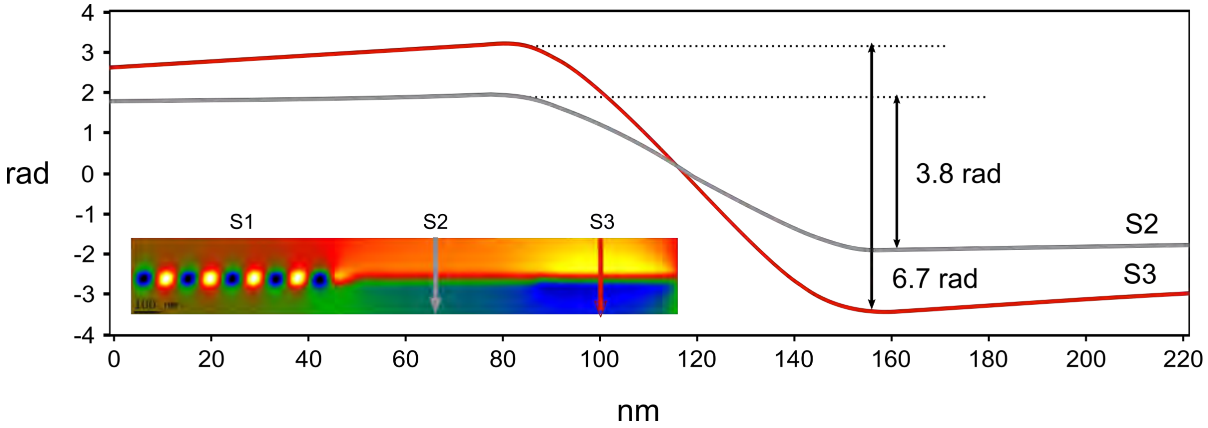

Figure 4.11: Plotted magnetic phase shift from simulation results in radians per nm from the cross-sections indicated by gray arrows in inset image. Inset show magnetic phase shift image from Figure 4.10b with labeled magnetic regions S1-S3 and scale-bar indicating 100 nm.

From a quick and qualitative comparison of the experimental and simulated results, the magnetic regions S1, S2, and S3 seem to correspond respectively to the magnetic regions R2, R1, and R4, of the experimental magnetic phase image. From this, one might be tempted to believe that the S2 region fits well with the R1 region, and the same for regions S3 and R4. However, while the vortex chain (S1) does indeed have a good correspondence with the experimental results (R2), the simulated magnetic configurations S2 (*hcp*) and S3 (*fcc*) must be further investigated. Figure 4.11 shows the plotted phase shift quantitative measurements of the simulated phase image across the S2 and S3, marked by a gray and red arrow in the inset (similarly to Figure 4.5 for the experimental results). The simulations indicate a phase shift of 3.8 radians (0.65 T) for S2, and 6.7 radians (1.15 T) for S3. While these values are comparable in magnitude to the experimental ones (0.7 T for R1 and 1.0 T for R4), we must consider the parameters we used for the OOMMF calculations and the fact that the simulated NW is very simplified in comparison to the real CoNi NW deeply analyzed in Section 4.4 by spectral and structural measurements. The simulated environment is noise-free, consisting of perfect and uniform geometries and monocrystalline crystal segments, *i.e.*, does not take into account any roughness or modulations in diameter, composition, or texture.

To understand the magnetic configuration more in-depth, we conducted a series of simulations for each crystal phase. I will now present these results and explain the parameters used in the two phases.

4.5.1 The *hcp* segment

First, we wanted to study the effects on the resulting remnant configuration of M_s variations (and thus the NW composition) and of the orientation of the magnetocrystalline easy axis for an *hcp* segment (S1 and S2). A summary of the results is presented in Figure 4.12. As for the *fcc* phase simulations, no vacuum space around the NWs was considered to optimize the simulation time. The simulated magnetic phase images in Figure 4.12a, therefore, reflect the magnetic flux only inside the nanowire and do not show any stray fields.

The simulations of S1 show chains of vortices formed in the *hcp* grain in the simulations for all the considered M_s values. However, a slight tilt in the isophase lines between the vortices is evidenced in Figure 4.12a. It is believed to come from the non-perpendicular component of the *c*-axis, causing the magnetization of the perpendicular domains to stabilize around the axis of the magnetocrystalline anisotropy, as earlier discussed. Accordingly, the isophase lines between the vortices in Figure 4.12b are perpendicularly oriented. Another pattern we see from the simulation results in Figure 4.12a and b is plotted in Figure 4.12c, namely a reduction in the core-to-core distance of the vortices in a chain as M_s increases. The origin of this is still unclear, but it is a curious piece of information that could help estimate or confirm the M_s value from experiments.

It comes out of the simulations that while lower M_s values result in a continuous vortex chain at remanence, small "deformations" in the vortex chains occur after a certain threshold, marked by gray arrows in Figure 4.12a and b. These characteristics resemble that of region R3 in the experimental EH phase image presented in Figure 4.4. By comparing the simulation series performed using a *c*-axis orientation angle of 77° and 90° respectively (Figure 4.12a and b) we see that the threshold for such a chain "deformation" to appear when $\mathrm{M}_s \geq 1.3$ T for

c-axis of 77°, and $M_s \geq 1.4$ T for 90°. In addition, we see that a curling state can be formed between vortex chains for higher M_s values. An example of this is highlighted in the boxed region of Figure 4.12a, and detailed in the 3D representation of the magnetization vectors in Figure 4.12c. According to the simulations, the curling states can appear for $J_s \geq 1.4$ T for c-axis of 77°, and $J_s \geq 1.6$ T for 90°, but appear more often, and are longer in length for the former case. Some marked curling state cases in Figure 4.12b (90°) are very short (200 nm) and are difficult to differentiate between curling state or a so-called "deformation," like the example marked by the red arrow in Figure 4.12b. These simulations indicate that both vortex chain and curling state are stabilized in *hcp* phase with a magnetocrystalline easy axis close to perpendicular to the NW axis, due to the transversal component of the anisotropy.

The simulation of the *hcp* S2 segment indicates a curling configuration that is argued to be the case for the experimental results R1 and R4. An important point is that this curling state only appears in the OOMMF simulation of the *hcp* grain, and we did not manage to simulate it in the *fcc* grain; whatever the magnetic parameters we used, the remnant magnetic configuration always stabilized with the magnetization perfectly parallel to the NW axis (see above). It then comes out from our simulations that the curling state observed experimentally in the CoNi NW is induced by the *hcp* phase portion of the segment in regions R1 and R4 in Figure 4.4b. It is, thus, also likely that R1 and R4 do have a curling configuration. We assume a possible interaction between the *fcc* and the *hcp* grains of these regions leads to an oscillation in the longitudinal component of the magnetic state, likely due to the interplay between the anisotropies. Such complicated interaction between *fcc* and *hcp* grains is however difficult to simulate.

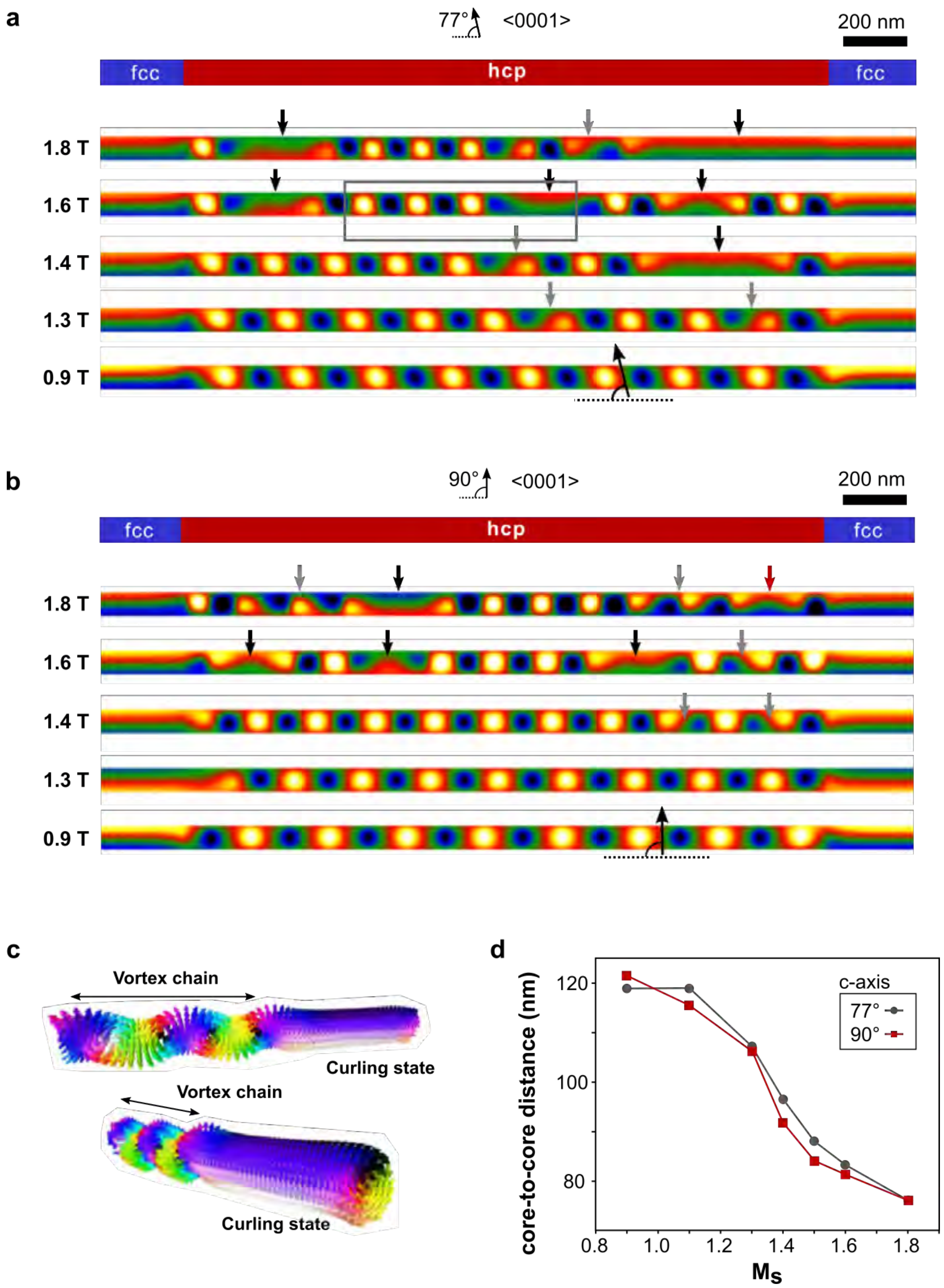

Figure 4.12: Results from OOMMF simulations of monocrystalline *hcp* and *fcc* NW. (**a**) and (**b**) Top: simulated cylindrical container representing the NW, with monocrystalline *hcp* grain in red, surrounded by two *fcc* regions. Below: simulated magnetic phase image with variation of saturation magnetization, shown for *hcp* magnetocrystalline easy axis orientation of 77° and 90° relative to the NW axis, in (**a**) and (**b**), respectively. The black and gray arrows mark different magnetic configurations. (**c**) 3D magnetic vector representation of the boxed magnetic region in (**a**). (**d**) Plot of core-to-core distance of the vortices for each simulation. Red and gray plot represent 77° and 90° *c*-axis orientation respectively.

4.5.2 The *fcc* segment

A similar micromagnetic study was performed for *fcc* phase. Let us consider the simulated magnetic configuration in S3 (*fcc*), which is a magnetic domain uniformly magnetized along the NW axis. As mentioned, we see from Figure 4.5 that the phase shift measured across this region is comparable to the R4 region of the experimental EH results. In order to simulate an *fcc* grain displaying a similar phase image, and measured phase shift along the cross-section, as was found in the experimental results, the M_{s-fcc} had to be set to 989 $\mathrm{kAm^{-1}}$. However, while the M_s value used for the simulated *fcc* does achieve a good experimental/simulated agreement, it is too weak considering the composition of the nanowire we measured. If we consider a Co composition at the lower level of what was found from our spectroscopic study (Section 4.4), which was 75% Co and 25% Ni, the appropriate $M_{s(\mathrm{Co75Ni25})}$ value would be 1202 $\mathrm{kAm^{-1}}$, which corresponds to about 1.5 T. With this in mind, a saturation magnetization $M_{s-fcc} = 989$ $\mathrm{kAm^{-1}}$ (*fcc*), corresponding to 1.24 T, is too low. Figure 4.13 displays some of the results from a simulation study on a monocrystalline *fcc* phase NW segment with diameter of 75 nm and length of 3.5 μm. The simulations were performed using the *fcc* grain base parameters stated in Section 4.2.4. We then performed three series of simulations varying the magnetic parameters. Figure 4.13a shows the resulting simulated magnetic phase image of the remnant state of the NW for a series of simulations where the anisotropy value $\mathrm{K_1}$ is varied. Notice how the constructed simulation container only includes the NW and no surrounded vacuum that would show the resulting stray fields but would have increased the processing time. The plot in Figure 4.13b displays the measured phase shift across the NWs for each of the simulations. The inset image, which is a zoom-in of the simulation plots, witnesses a very small effect of the changes in $\mathrm{K_1}$ to the remnant magnetization orientation of the NW. A 3D reconstruction of the remnant state in the middle region of the NW, displayed at the bottom of Figure 4.13a, shows that the magnetization is completely parallel to the NW axis. It, thus, indicates that the anisotropy value K_1 changes (within the used range) do not result in a curling state. Similar simulation series were performed by varying the exchange constant, A, between 26×10^{-12} $\mathrm{Jm^{-1}}$ and 0.05×10^{-12} $\mathrm{Jm^{-1}}$. This series was simulated twice; once using the base M_s value of 1273 $\mathrm{kAm^{-1}}$ (J_s = 1.6 T), and one using $M_s = 1035$ $\mathrm{kAm^{-1}}$ ($J_s = 1.3$ T). Figure 4.13b shows that, similar

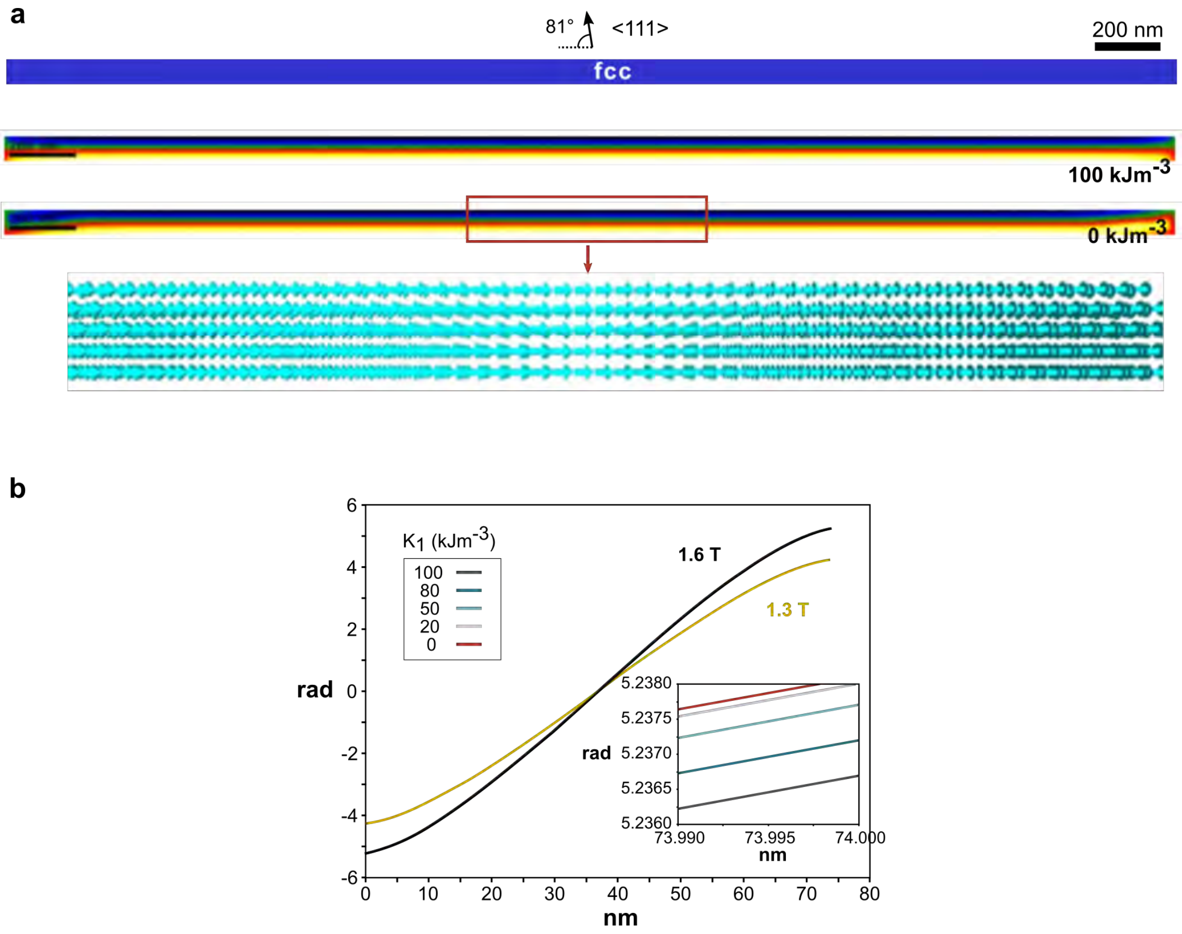

Figure 4.13: Results from OOMMF simulations of monocrystalline *fcc* NW. (**a**) Tom: blue cylindrical container represents the simulated NW. Below: simulated magnetic phase images where the magnetocrystalline anisotropy value K_1 is varied. Bottom: 3D magnetic vectors of the boxed region. (**b**) Plotted magnetic phase shift in radians per nm from cross-sectional measurements from simulation series where exchange constant, A, varied. The series was simulated for two different Ms values: $M_s = 1273$ kAm^{-1} ($J_s = 1.6$ T) and $M_s = 1035$ kAm^{-1} ($J_s = 1.3$ T), gray and red plot, respectively. Inset show zoom-in of the 1.6 T plot, identifying the minuscule change in curves.

to the previous set of simulations, the phase shift profiles do not present a clear variation for different values of A. However, the total phase shift variation is reduced when M_s is decreased.

From the analysis of the change in phase found experimentally, we believe that there is a rotative part of the magnetization in the magnetic domains imaged in R1 and R4 (Figure 4.4b). However, we did not manage to simulate such a curling state in a monocrystalline *fcc* phase segment. If there is no rotative part, then the M_s has to be reduced to fit the experimental results ($M_{s-fcc} = 989$ kAm^{-1}), but this does not correlate with the NW composition measured by EELS. From this, we conclude that we can only simulate a curling state in the *hcp* phase, and it might perhaps also be necessary to take aspects like roughness into the calculation.

4.6 Conclusion

This study has exploited the huge flexibility of complementary imaging and spectroscopic TEM techniques to study a single specimen. I have carried out a thorough quantitative local study, analyzing the magnetic remnant state and correlating it with the chemical and structural information from single cylindrical textured $Co_{85}Ni_{15}$ nanowires, with a diameter of 70 nm. Chemical analyses by EDX and STEM-EELS have confirmed the general composition of the NW, and evidenced local variations, which have been linked to changes in crystal structure thanks to local ASTAR precession diffraction experiments. The structural analyses uncover a coexistence of both *fcc* and *hcp* crystal phases in the same NW. The studied NW segment was found to have three main crystal grains, made up of two *fcc* grains separated by a long *hcp* grain, with a crystal grain boundary running almost parallel to the NW axis.

Magnetic imaging by Fresnel and EH has revealed a complex and inhomogeneous magnetic configuration, consisting of periodical antiparallel transverse domain-like regions separated by transverse-vortex states of alternating chirality and/or polarity. This chain of vortices is found to appear in *hcp* regions of the NW exhibiting a c-axis oriented at 78° relative to the NW axis. This close-to-perpendicular orientation of the easy axis is believed to counterbalance the shape anisotropy, resulting in magnetic domains with transversal components. An axial curling magnetic state was evidenced in the part of the NW where *fcc* phase and *hcp* phase coexist within the same NW cross-section. Two curling domains were studied in-depth, and a quantitative difference in the longitudinal magnetic induction was measured between them. This difference is believed to originate from a variation in curling angle relative to the NW axis, where a smaller curling angle leads to a stronger measured x-component of the magnetic induction. A transition state between the chain of vortices and the curling state has also been analyzed. Although this state is not yet fully understood, it has experimentally been linked with a local change in composition and crystal phase, and similar-looking transitions have also been found between vortex chains and curling states in micromagnetic simulations.

The experimental results have been compared to micromagnetic simulations performed using OOMMF code. The latter revealed that both the vortex chain and curling state is formed within the *hcp* phase of the Co-rich CoNi NW. This leads us to assume that the experimentally observed curling state is induced by the *hcp* phase of the segment where *fcc* and *hcp* coexist with a grain boundary parallel to the NW axis. The simulations also show that only a parallel magnetic domain can be formed in pure *fcc* grains. The micromagnetic simulations have revealed the effect of a change in composition on the magnetic configuration in *hcp* phase with perpendicular *c*-axis, where a lower M_s stabilizes a longer vortex chain with a larger distance between vortex cores, while a higher M_s shortens the inter-core distance of the vortices in a chain, as well as produces curling states.

This experimental study combined with micromagnetic simulations demonstrates the strong correlations between crystal structure and composition, and the consequence for the magnetic configurations in CoNi NWs. The effects of local crystalline changes due to a small variation in composition are found to affect the magnetic configuration in the NW drastically, and can, therefore, not be neglected in order to understand complex magnetic structures like the one studied here. Hence, the use of a correlative microscopy investigation has been a great advantage in this work, where magnetic, structural, and spectroscopic analysis were performed on the exact same area.

Although much of these configurations have been revealed and confirmed, there are still questions and aspects of this system that are not fully understood. One drawback with EH is that it only allows for recovering a 2D projection of the in-plane magnetic induction, and for a system exhibiting a complex 3D magnetic configuration, this can, in the worst case, pose some misconceptions when analyzing the data. While we have confirmed the existence of the vortex chain by OOMMF simulations, the performed simulations were very much a simplified system compared to the real experimentally studied complex structure with interacting imperfect crystalline grains. Further work will be conducted to simulate a more true-to-life version of the experimental system.

References

[1] H. Forster et al. “Domain Wall Motion in Nanowires Using Moving Grids”. In: *Journal of Applied Physics* **91** (2002), p. 6914. DOI: 10.1063/1.1452189.

[2] C. Burrowes et al. “Non-Adiabatic Spin-Torques in Narrow Magnetic Domain Walls”. In: *Nature Physics* **6** (2010), pp. 17–21. DOI: 10.1038/nphys1436.

[3] T. Koyama et al. “Observation of the Intrinsic Pinning of a Magnetic Domain Wall in a Ferromagnetic Nanowire”. In: *Nature Materials* **10** (2011), pp. 194–197. DOI: 10.1038/nmat2961.

[4] E. M. Palmero et al. “Vortex Domain Wall Propagation in Periodically Modulated Diameter FeCoCu Nanowire as Determined by the Magneto-Optical Kerr Effect”. In: *Nanotechnology* **26** (2015), p. 461001. DOI: 10.1088/0957-4484/26/46/461001.

[5] D. Sander et al. “The 2017 Magnetism Roadmap”. In: *Journal of Physics D: Applied Physics* **50** (2017), p. 363001. DOI: 10.1088/1361-6463/aa81a1.

[6] S. S. P. Parkin, M. Hayashi, and L. Thomas. “Magnetic Domain-Wall Racetrack Memory”. In: *Science* **320** (2008), pp. 190–194. DOI: 10.1126/science.1145799.

[7] L. Berger. “Emission of Spin Waves by a Magnetic Multilayer Traversed by a Current”. In: *Physical Review B* **54** (1996), pp. 9353–9358. DOI: 10.1103/PhysRevB.54.9353.

[8] M. Yan et al. “Beating the Walker Limit with Massless Domain Walls in Cylindrical Nanowires”. In: *Physical Review Letters* **104** (2010), p. 057201. DOI: 10.1103/PhysRevLett.104.057201.

[9] R. Hertel. “Ultrafast Domain Wall Dynamics in Magnetic Nanotubes and Nanowires”. In: *Journal of Physics: Condensed Matter* **28** (2016), p. 483002. DOI: 10.1088/0953-8984/28/48/483002.

[10] J. M. García et al. "Magnetic Behavior of an Array of Cobalt Nanowires". In: *Journal of Applied Physics* **85** (1999), pp. 5480–5482. DOI: 10.1063/1.369868.

[11] Y. P. Ivanov et al. "Magnetic Structure of a Single-Crystal Hcp Electrodeposited Cobalt Nanowire". In: *Europhysics Letters* **102** (2013), p. 17009. DOI: 10.1209/0295-5075/102/17009.

[12] S. Da Col et al. "Observation of Bloch-Point Domain Walls in Cylindrical Magnetic Nanowires". In: *Physical Review B* **89** (2014), p. 180405. DOI: 10.1103/PhysRevB.89.180405.

[13] N. Biziere et al. "Imaging the Fine Structure of a Magnetic Domain Wall in a Ni Nanocylinder". In: *Nano Letters* **13** (2013), pp. 2053–2057. DOI: 10.1021/nl400317j.

[14] C. Bran et al. "Direct Observation of Transverse and Vortex Metastable Magnetic Domains in Cylindrical Nanowires". In: *Physical Review B* **96** (2017), p. 125415. DOI: 10.1103/PhysRevB.96.125415.

[15] H.-G. Piao et al. "Intrinsic Pinning Behavior and Propagation Onset of Three-Dimensional Bloch-Point Domain Wall in a Cylindrical Ferromagnetic Nanowire". In: *Applied Physics Letters* **102** (2013), p. 112405. DOI: 10.1063/1.4794823.

[16] A. Carl et al. "HCP-FCC Phase Transition in Co-Ni Alloys Studied With Magneto-Optical Kerr Spectroscopy". In: *MRS Online Proceedings Library Archive* **343** (1994), pp. 351–356. DOI: 10.1557/PROC-343-351.

[17] J. M. D. Coey. *Magnetism and Magnetic Materials*. Cambridge University Press, 2010. DOI: 10.1017/CBO9780511845000.

[18] Y. P. Ivanov et al. "Crystallographically Driven Magnetic Behaviour of Arrays of Monocrystalline Co Nanowires". In: *Nanotechnology* **25** (2014), p. 475702. DOI: 10.1088/0957-4484/25/47/475702.

[19] C. Gatel et al. "Size-Specific Spin Configurations in Single Iron Nanomagnet: From Flower to Exotic Vortices". In: *Nano Letters* **15** (2015), pp. 6952–6957. DOI: 10.1021/acs.nanolett.5b02892.

[20] V. Vega et al. "Tuning the Magnetic Anisotropy of Co–Ni Nanowires: Comparison between Single Nanowires and Nanowire Arrays in Hard-Anodic Aluminum Oxide Mem-

branes”. In: *Nanotechnology* **23** (2012), p. 465709. DOI: 10.1088/0957-4484/23/46/465709.

[21] J. U. Cho et al. “Control of Magnetic Anisotropy of Co Nanowires”. In: *Journal of Magnetism and Magnetic Materials* **303** (2006), e281–e285. DOI: 10.1016/j.jmmm.2006.01.082.

[22] E. D. Barriga-Castro et al. “Pseudo-Monocrystalline Properties of Cylindrical Nanowires Confinedly Grown by Electrodeposition in Nanoporous Alumina Templates”. In: *RSC Advances* **7** (2017), pp. 13817–13826. DOI: 10.1039/C7RA00691H.

[23] R. Ferré et al. “Magnetization Processes in Nickel and Cobalt Electrodeposited Nanowires”. In: *Physical Review B* **56** (1997), pp. 14066–14075. DOI: 10.1103/PhysRevB.56.14066.

[24] Z. Liu et al. “Shape Anisotropy and Magnetization Modulation in Hexagonal Cobalt Nanowires”. In: *Advanced Functional Materials* **18** (2008), pp. 1573–1578. DOI: 10.1002/adfm.200701010.

[25] M. S. Arshad et al. “Effect of Magnetocrystalline Anisotropy on the Magnetic Properties of Electrodeposited Co–Pt Nanowires”. In: *Journal of Nanoparticle Research* **16** (2014), p. 2688. DOI: 10.1007/s11051-014-2688-4.

[26] A. S. Samardak et al. “Variation of Magnetic Anisotropy and Temperature-Dependent FORC Probing of Compositionally Tuned Co-Ni Alloy Nanowires”. In: *Journal of Alloys and Compounds* **732** (2018), pp. 683–693. DOI: 10.1016/j.jallcom.2017.10.258.

[27] K. Maaz et al. “Effect of Crystallographic Texture on Magnetic Characteristics of Cobalt Nanowires”. In: *Nanoscale Research Letters* **5** (2010), pp. 1111–1117. DOI: 10.1007/s11671-010-9610-5.

[28] M. S. Arshad et al. “The Role of the Crystal Orientation (c-Axis) on Switching Field Distribution and the Magnetic Domain Configuration in Electrodeposited Hcp Co–Pt Nanowires”. In: *Journal of Physics D: Applied Physics* **49** (2016), p. 185006. DOI: 10.1088/0022-3727/49/18/185006.

[29] D. Reyes et al. “Magnetic Configurations in Co/Cu Multilayered Nanowires: Evidence of Structural and Magnetic Interplay”. In: *Nano Letters* **16** (2016), pp. 1230–1236. DOI: 10.1021/acs.nanolett.5b04553.

[30] E. Berganza Eguiarte et al. “Multisegmented Nanowires: A Step towards the Control of the Domain Wall Configuration”. In: *Scientific Reports* **7** (2017), p. 11576. DOI: 10.1038/s41598-017-11902-w.

[31] E. M. Palmero et al. “Magnetic Behavior of NiCu Nanowire Arrays: Compositional, Geometry and Temperature Dependence”. In: *Journal of Applied Physics* **116** (2014), p. 033908. DOI: 10.1063/1.4890358.

[32] B. Rodríguez-González et al. “Structural and Magnetic Characterization of As-Prepared and Annealed FeCoCu Nanowire Arrays in Ordered Anodic Aluminum Oxide Templates”. In: *Journal of Applied Physics* **115** (2014), pp. 133904–133904. DOI: 10.1063/1.4870289.

[33] R. T. Downs and M. Hall-Wallace. “The American Mineralogist Crystal Structure Database”. In: *American Mineralogist* **38** (2005), pp. 389–395.

[34] S. Gražulis et al. “Crystallography Open Database - an Open-Access Collection of Crystal Structures”. In: *Journal of Applied Crystallography* **42** (2009), pp. 726–729. DOI: 10.1107/S0021889809016690.

[35] S. Gražulis et al. “Crystallography Open Database (COD): An Open-Access Collection of Crystal Structures and Platform for World-Wide Collaboration”. In: *Nucleic Acids Research* **40** (2012), pp. D420–D427. DOI: 10.1093/nar/gkr900.

[36] S. Gražulis et al. “Computing Stoichiometric Molecular Composition from Crystal Structures”. In: *Journal of Applied Crystallography* **48** (2015), pp. 85–91. DOI: 10.1107/S1600576714025904.

[37] A. Merkys et al. “COD::CIF::Parser: An Error-Correcting CIF Parser for the Perl Language”. In: *Journal of Applied Crystallography* **49** (2016), pp. 292–301. DOI: 10.1107/S1600576715022396.

[38] M. J. Donahue and D. G. Porter. *OOMMF User’s Guide*. Interagency Report. National Institute of Standards and Technology, 1999.

[39] C. Bran et al. “Spin Configuration of Cylindrical Bamboo-like Magnetic Nanowires”. In: *Journal of Materials Chemistry C* **4** (2016), pp. 978–984. DOI: 10.1039/C5TC04194E.

[40] Y. P. Ivanov et al. “Single Crystalline Cylindrical Nanowires – toward Dense 3D Arrays of Magnetic Vortices”. In: *Scientific Reports* **6** (2016), p. 23844. DOI: 10.1038/srep23844.

[41] D. Viladot et al. “Orientation and Phase Mapping in the Transmission Electron Microscope Using Precession-Assisted Diffraction Spot Recognition: State-of-the-Art Results: REVIEW OF PACOM (ASTAR) APPLICATION”. In: *Journal of Microscopy* **252** (2013), pp. 23–34. DOI: 10.1111/jmi.12065.

[42] E. F. Rauch et al. “Automated Nanocrystal Orientation and Phase Mapping in the Transmission Electron Microscope on the Basis of Precession Electron Diffraction”. In: *Zeitschrift für Kristallographie* **225** (2010), pp. 103–109. DOI: 10.1524/zkri.2010.1205.

[43] V. Scarani, B. Doudin, and J.-P. Ansermet. “The Microstructure of Electrodeposited Cobalt-Based Nanowires and Its Effect on Their Magnetic and Transport Properties”. In: *Journal of Magnetism and Magnetic Materials* **205** (1999), pp. 241–248. DOI: 10.1016/S0304-8853(99)00513-2.

[44] Y. Henry et al. “Magnetic Anisotropy and Domain Patterns in Electrodeposited Cobalt Nanowires”. In: *The European Physical Journal B* **20** (2001), pp. 35–54. DOI: 10.1007/s100510170283.

[45] P. Longo et al. “Atomic Elemental and Chemical Analysis of SrTiO3/LaMnO3 Multilayers Using Fast Simultaneous EELS and EDS Analysis in DigitalMicrograph”. In: *Microscopy Today* **23** (2015), pp. 44–53. DOI: 10.1017/S1551929515000589.

[46] T. Nishizawa and K. Ishida. “The Co-Ni (Cobalt-Nickel) System”. In: *Bulletin of Alloy Phase Diagrams* **4** (1983), pp. 390–395. DOI: 10.1007/BF02868090.

Chapter 5

Field tunable 3D magnetic states in CoNi nanowires

5.1 Introduction

The following study is a continuation of the research presented in Chapter 4.

Although NWs often have been approximated as 1D nanostructures, as soft magnetic NWs tend to display domains with their magnetization aligned along the wire axis due to a strong shape anisotropy,[1] their DW spin textures must still be described with two or three directional components.[2,3] This means that we need to consider the three-dimensionality of the spin texture of NWs. This is especially important for NWs with a strong magnetocrystalline anisotropy oriented perpendicular to the NW axis, which can lead to domains with transversal magnetization components and complex spin configurations as shape anisotropy is no longer dominating.[4] This was concluded in Chapter 4 where electron holography, with its high resolution and sensitivity, has to be supplemented with micromagnetic simulations to get a view of the 3D magnetic structure.

In order to gain an in-depth understanding of magnetic phenomena in nanostructures, we need to consider all three dimensions. This places difficult criteria and challenges on magnetic characterization techniques, as it calls for an imaging technique with nanometer spatial resolution, as well as a three-dimensional representation of magnetic domains and domain walls. Fortunately, due to the recent developments in instrumentation and increase in computer power,[1,5] there are already a small number of techniques that are advancing to fit this need by combining magnetic imaging using electrons,[6,7] and soft[8] or hard[9,10] x-rays with tomographic reconstruction methods.

The last few years, there have been great advances in 3D vector field magnetic imaging. For hard x-ray imaging, the development of a dual-axis approach has enabled the reconstruction of the three directional vectors[11] and the recent study combining x-ray tomography for flat samples and pump-probe experimental setup to get time-resolved 3D information of magnetization dynamics in a magnetic microdisc.[12] While the resolutions in these studies are estimated to 33 nm and 50 nm, respectively, it has been predicted that the spatial resolution for such x-ray techniques has the potential to improve to be of the order of 20 nm thanks to advances in x-ray optics.[11]

Further progress has also been made on the side of electron holographic tomography, where a recent study managed to reconstruct all three Cartesian components of the magnetic induction, named holographic vector field electron tomography (VFET), with a spatial resolution of less than 10 nm.[13] Although the TEM environment imposes a strong criterion to the sample size, it can offer a high spatial resolution and sensitivity that allows for imaging the fine magnetic structure of small nanostructures[14] like nanoparticles[15] or nanowires with a diameter of a few nanometers.[16] Holographic VFET combines EH with tomographic reconstruction techniques to record the in-plane magnetic induction from different projections around two perpendicular tilt axes.[17] The full tilt series from each of the tilt axis allows the 3D reconstruction of one of the three magnetic **B**-field components, *e.g.* B_x and B_y. The third component, B_z, can then be computed by solving the Maxwell equation $\nabla \cdot \mathbf{B} = 0$. A more detailed explanation of holographic VFET can be found in Section 3.3.5, where a rough illustration of the principle and workflow of the technique is presented in Figure 3.10.

The aim of this study is to analyze the 3D magnetic configurations and domain wall structures of cylindrical CoNi nanowires which display a *hcp* crystal structure with the *c*-axis oriented perpendicular to the nanowire axis, by the combined use of EH and holographic

VFET. The nanowires have been observed and selected prior to the holographic VFET experiment, using BFTEM and defocused Lorentz imaging on the I2TEM microscope to make sure that the NWs are correctly oriented on the carbon foil for the large tilting angles without being overshadowed by the grid or neighboring specimen, and to ensure the existence of a vortex chain. In order to study the effects of the magnetic history on the magnetic remnant state, the holographic VFET measurements were performed for two cases: after the application of an external saturation field (i) perpendicular and (ii) parallel to the nanowire axis. ASTAR measurements were carried out after the VFET experiments as the sample tends to get highly affected by carbon-based contamination from the ASTAR observations. Micromagnetic simulations have been carried out to complement the experimental results and to give further information about the magnetic characteristics of the sample nanowire.

5.2 Experimental details

5.2.1 Nanowire fabrication

The $Co_{85}Ni_{15}$ cylindrical nanowires were made by electrodeposition (Section 3.6) into self-assembled pores of anodic aluminium oxide templates. The NWs were fabricated by Dr. Cristina Bran at the Instituto de Ciencia de Materiales de Madrid (ICMM) in Spain, and are from the same sample batch as the ones studied in Chapter 4 (see Section 4.2.1 for more details on the synthesis of the NWs).

5.2.2 Quantitative 3D magnetic imaging

In order to get a 3D reconstruction of the magnetic induction, we performed holographic vector-field electron tomography on the NW sample. The holographic tilt series were performed on the *FEI Titan 80-300 Holography Special Berlin* TEM instrument at the Technical University of Berlin in Germany, equipped with a 2k slow-scan CCD camera (Gatan Ultrascan 1000 P). The experiments were performed by Dr. Daniel Wolf from Institute for Solid State Research (IFW) in Dresden and myself. The holograms were acquired at 300 kV in image-corrected Lorentz-Mode (conventional objective lens turned off and the first transfer lens of the C_s corrector used as a pseudo Lorentz lens) using a double biprism setup.[18] A tomography sample holder (Model 2040 from Fischione Instruments, Inc.) was used to achieve the high tilt angles and manual in-plane rotation necessary to rotate the sample in between two tilt series and reconstruct both the B_y and B_x components. The third magnetic $\mathbf{B}$-field component, B_z, is later calculated from $\nabla \cdot \mathbf{B} = 0$. Further details about holographic VFET; its acquisition process, the holographic reconstruction steps, and data processing are presented in Section 3.3.5.

The hologram tilt series was recorded at a magnification of SA 155 kx. The interference fringes were formed using a double biprism setup with an upper biprism voltage of 26 V and a lower biprism voltage of 120 V, producing an inter-fringe spacing of 4.95 pixels (∼3 nm) per fringe. The tilting process was performed using a home-made semi-automatic software package ("THOMAS")[19] for efficient acquisition of an object and a reference hologram at each projection.

For the first tilt series, the NW was rotated in-plane to an angle of -44.0° between the wire axis and the tilt axis. The second tilt series was recorded after an in-plane rotation of 89.8° relative to the first position (ideally 90°), resulting in an angle of 45.8° between NW axis and the tilt axis. Two additional tilt series were recorded after flipping the sample and recording the corresponding, but flipped, versions of the two previous series. For each tilt series, a tilt range from -66° to +66° was used, with a step size of 3°.

An external magnetic field was applied before each experiment using the microscope objective lens at 87.6% stimulation, which corresponds to a generated magnetic field of 2 T in the beam direction (orthogonal to image plane). To achieve a perpendicular saturation magnetization of the NW, the 2 T field was applied at 0° tilt in the up-configuration, while a quasi-parallel saturation was done by tilting the sample 71° before applying the field.

Prior to the holographic VFET experiment, the sample was checked in the I2TEM (Hitachi HF-3300C) operated at 300 kV using Fresnel imaging. The observations were carried out in the normal stage of the I2TEM, with the objective lens switched off (TL11 mode). A magnetic field of 1.8 T was applied perpendicular to the sample plane (*i.e.* perpendicular to the wire axis) prior to the experiment by switching the objective lens on and off again.

5.2.3 Structural analysis

Crystal grain and orientation maps of the studied nanowires were obtained by precession electron diffraction (PED) on a Phillips CM20-FEG TEM using the ASTAR NanoMEGAS© DigiSTAR system, in the same fashion as described for the experiments and data processing in Chapter 4. This technique is also described in more details in Section 3.4. The observations and orientation identification processing of the PEDs was done in collaboration with colleague and Ph.D. student Daniela Oliveros who performed the ASTAR measurements.

5.2.4 Micromagnetic simulations

Comparative micromagnetic simulations were performed by Dr. L. A. Rodríguez at the Department of Physics at Universidad del Valle in Cali, using OOMMF[20] code and the same micromagnetic base parameters as presented in Chapter 4. A cylindrical 3D shape with a 70 nm diameter consisting of a 1200 nm long *hcp* segment with a 200 nm *fcc* phase segment on either side was used to simulate the CoNi NW studied in this chapter. The *hcp* phase region is representing the region with a large *hcp* grain that has been found experimentally (Figure 5.3b). The simulations were run to relax the magnetic states after two different initial conditions: with all the magnetic spins oriented along the NW (i) z-axis and (ii) x-axis, simulating the saturation field directions of the experimental measurements.

5.3 Textured cylindrical CoNi nanowire

Figure 5.1 shows information about the morphology and structure of a cylindrical CoNi nanowire using a combination of TEM-based techniques. The 3D volume rendering depicted in Figure 5.1a is reconstructed from the electrostatic potential using holographic VFET and reveals a slight deformation of the intended cylindrical geometry of the NW. However, although the NW does not have a perfectly circular cross-section, it appears to be fairly straight and uniform in thickness, with the exception of a split in the NW tip. The BFTEM image in Figure 5.1b reveals a mean NW diameter of 75 nm (±4 nm) in the imaged region and the existence of different crystallographic grain orientations, which are visible due to change in diffraction contrast.

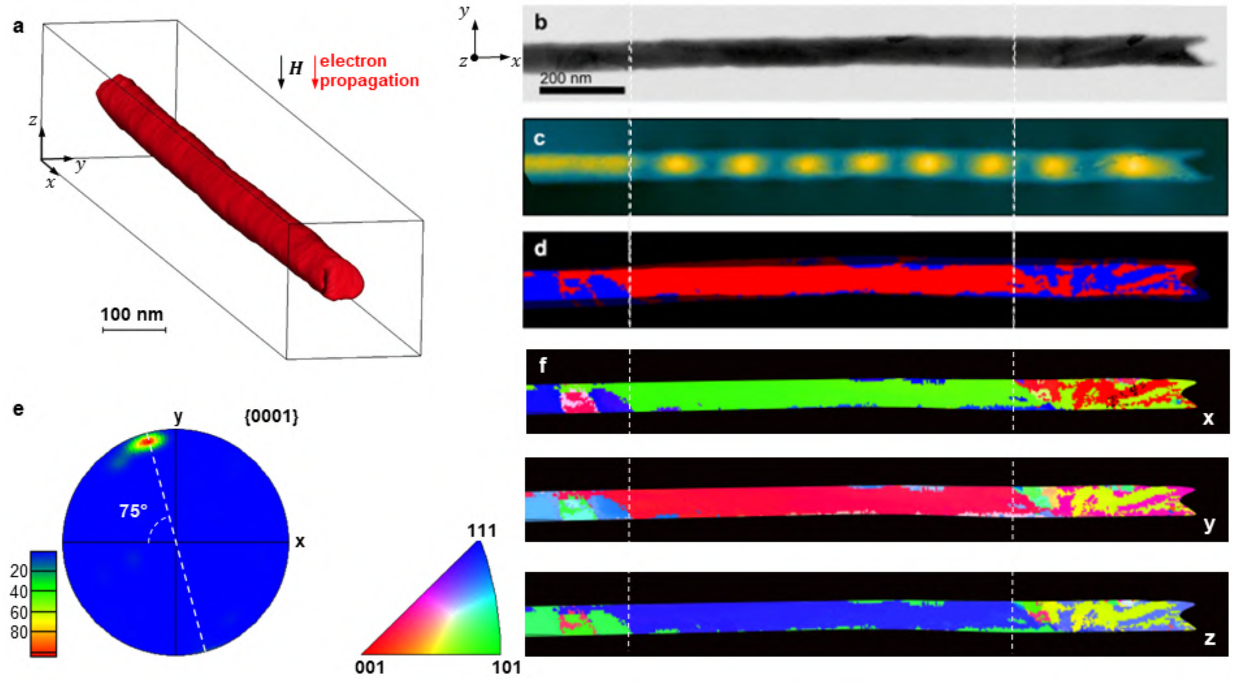

Figure 5.1: Morphology, crystallographic structure of studied CoNi NW sample after applying an external magnetic field perpendicular to NW axis and the *hcp* *c*-axis. (**a**) Iso-surface rendering of NW extracted from the 3D electrostatic potential reconstructed by holographic VFET. (**b**) BFTEM image of region of interest. (**c**) EH reconstructed phase image containing both electrostatic and magnetic contribution to the phase shift. Electron beam direction indicated in (a). (**d**) Structural map from ASTAR measurements. Highest match for *fcc* and *hcp* crystal phase indicated by blue and red regions, respectively. (**e**) Pole figure of the equal area projection of the upper hemisphere showing *hcp* 0001 oriented 75° relative NW axis. (**f**) Crystal grain orientation map relative x-, y-, and z- direction represented by color legend.

A deeper structural analysis performed by ASTAR measurements (Figure 5.1d), shows the coexistence of *hcp* (red) and *fcc* (blue) crystal phase within the studied NW segment. An *hcp* grain stretching ∼1 µm along the NW axis, is oriented with its *c*-axis almost perpendicular (75°) to the NW axis.

5.4 Perpendicular saturation: Chain of vortex configurations

Figure 5.2 presents the main results of holographic VFET performed at remnant state after applying a magnetic saturation field perpendicular to the NW axis, along the *z*-axis. The resulting magnetic configuration is a chain of transverse-vortex states (Figure 5.2a) stretching across the region of the *hcp* grain and almost until the tip of the NW. This confirms the findings from the study in Chapter 4 where we determined this magnetic structure, and we linked its existence to *hcp* grain with perpendicular anisotropy after applying a saturation field with an orientation similar to this VFET experiment. By excluding the last two vortices before the tip (furthest to the right), the vortices have an average core-to-core distance of 77 nm (±7 nm). Following the enumeration in Figure 5.3, the second to last (number 14) and last (number 15) inter-core distance are respectively 17% and 36% longer than the average value of the rest of the core-to-core segments. This is believed to be linked to the polycrystalline nature of the NW segment close to the tip, as revealed by the structural map in Figure 5.3b. From a previously performed micromagnetic study (see Section 4.5.1), we know that the inter-core distance of the vortex chain depends on the saturation magnetization M_s of the NW. The vortex core periodicity in the micromagnetic simulations performed with an M_s value of 1 273 kA·m^{-1}, is 74.4 nm. This is only 4% smaller than the average inter-core distance found experimentally and smaller than the uncertainty based on the resolution of the reconstructed VFET results. As the simulated periodicity corresponds well with the experimental one, we can assume that the M$_s$ value used in this simulation is a good estimation for the saturation magnetization of the $\mathrm{Co_{85}Ni_{15}}$ NW.

The vortices are separated by regions with magnetization pointing in alternately positive and negative *y*-axis. While they can be seen in Figure 5.2as small segments between vortices, they are more clearly seen in Figure 5.2b, where the positive and negative B_y components are represented by blue and yellow color contrast, respectively. Figure 5.2b shows that the *y*-component remains of a constant sign, positive or negative, that only switches by the vortex cores. The system can thus also be viewed as a series of transversal domains alternating between positive and negative *y*-direction (Figure 5.2e), creating vortices at the domain walls separating them. From this, we can also view the system as a kind of double Halbach array, as illustrated looking at the magnetic vectors in Figure 5.2d, meaning that the vortices are contributing to reducing the stray field outside of the NW that would otherwise be stronger in the case of a sequence of antiparallel transverse domains.

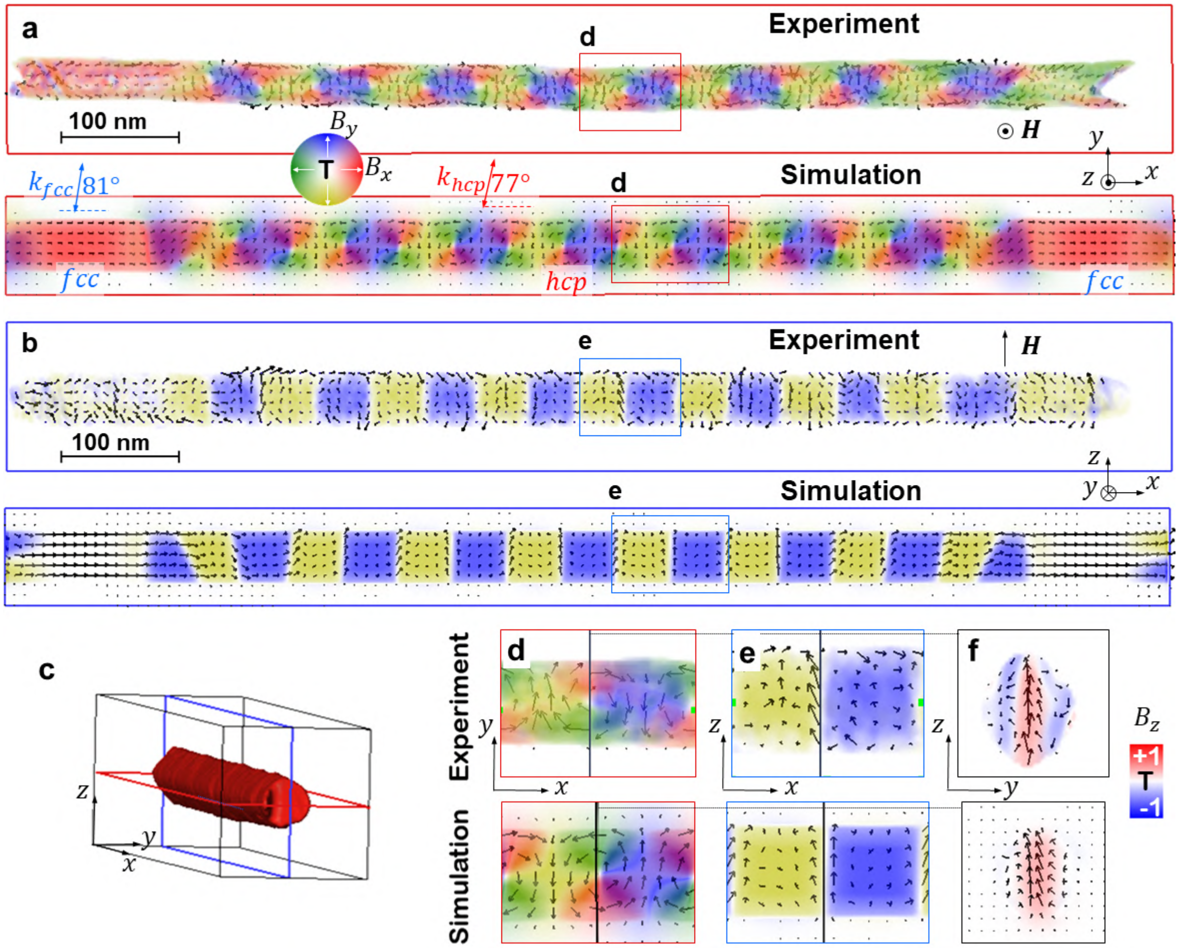

Figure 5.2: 3D reconstruction of the magnetic B-field inside CoNi NW by holographic VFET and comparison with micromagnetic simulation after magnetizing the NW in z-direction. (**a**) Central axial (xy)-slice through the 3D B-field inside the NW shown by arrow-plot and color-coded volume rendering of B_x and B_y according to the color-wheel revealing a vortex chain in the *hcp* region. (**b**) Central axial (xz)-slice through the 3D B-field inside the NW visualized by arrow-plot and color-coded volume rendering of B_y. (**c**) Iso-surface rendering of the electrostatic potential, obtained by holographic VFET, shows the NW morphology. The position of the axial slices (a) and (b) is shown as red and blue rectangles. (**d**,**e**) Zoom-in of the regions indicated in (a) and (b). (**f**) Cross sectional slice (yz) through the vortex-core marked as black vertical line in (d,e) superimposed by the color-coded B_z component.

The 3D magnetic configuration of the vortices' core is a particularly interesting point that we wanted to investigate. One such vortex core is shown in Figure 5.2f, where the experimental holographic VFET results show a configuration with the magnetic vectors pointing in the positive z-direction. By comparison, this is also the case for every single vortex core in the simulated vortex chain. Unfortunately, we did not manage to resolve every single vortex core due to a lack of resolution when smoothing the data during the reconstruction process

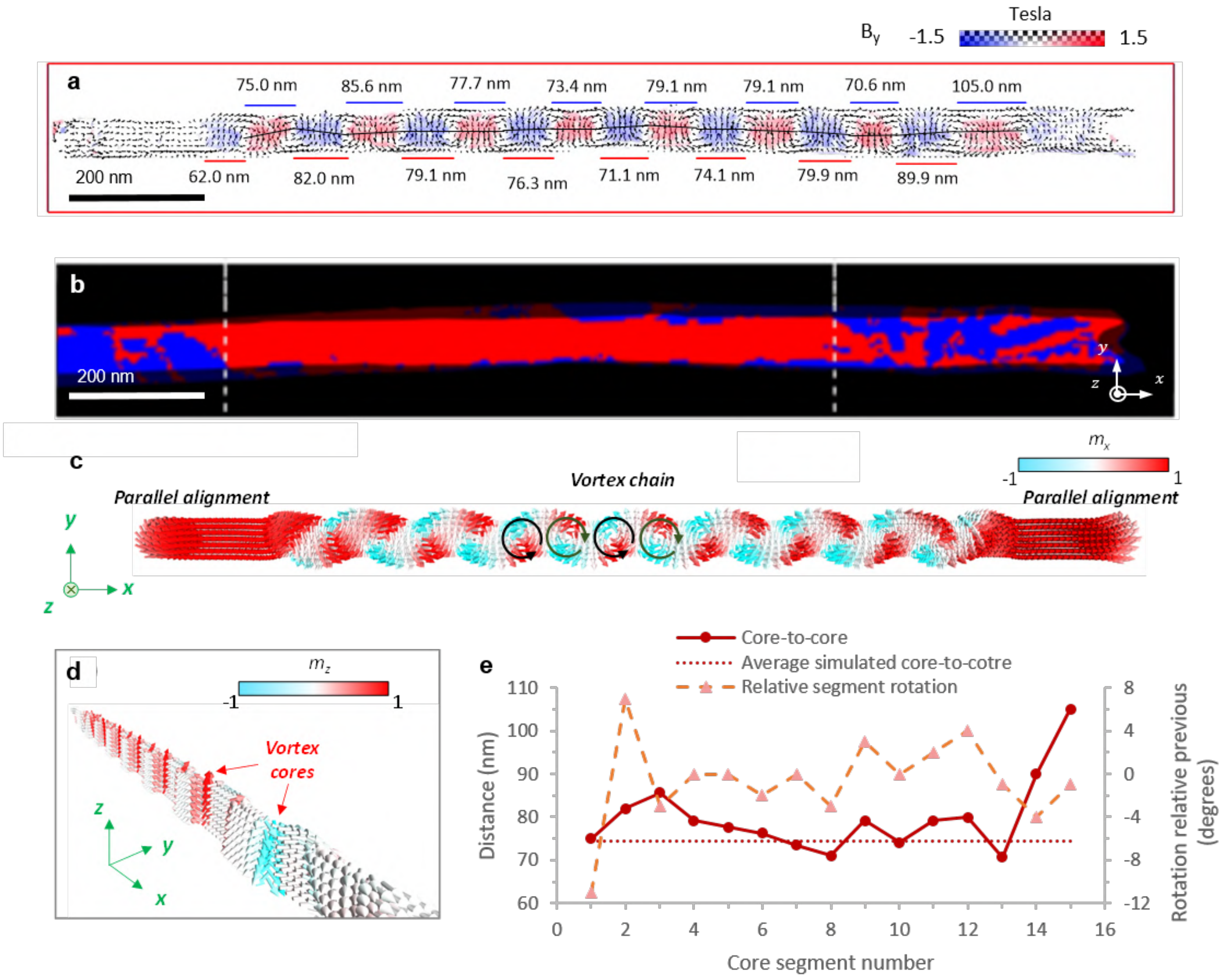

Figure 5.3: Direct comparison of magnetic configuration after perpendicular saturation and structural data. (**a**) Central axial (xy)-slice through the 3D B-field inside the NW visualized by arrow-plot and color-coded volume rendering of B_y. (**b**) Structural map from ASTAR measurements. Highest match for *fcc* and *hcp* crystal phase indicated by blue and red regions, respectively (from Figure 5.1). (**c**) 3D vector map of the remnant state after the application of a perpendicular H_{sat}. Colors represent the x-component of the reduced magnetization $m_x = M_x/M_S$. (**d**) A longitudinal-section view allows observing the vortex cores. (**e**) Plot showing vortex displacements in the chain relative its right-hand neighbor. Dark line shows the inter-core distance in nanometers for experimental results, and dark dotted line shows average inter-core distance from micromagnetic simulations, and the light stippled line shows angle of a line segment passing through the vortex core and its neighbor relative to the x-axis.

and because of some unresolved spatial frequencies due to the missing wedge problem (see Section 3.3.5). We can, therefore, only speculate that the analyzed core is representative of the behavior of all of them, as suggested by the simulation (Figure 5.3d). The fact that all the vortex cores, with the exception of one canted core at the end of the chain, display a positive z-direction flux is most likely due to the perpendicular saturation field that was applied prior to this experiment. The full nature of the vortex core is complex, but we can generally conclude that they mostly have a rotation in the xy-plane of the magnetic vectors around the core, which is oriented along the z-axis (out of plane), and therefore perpendicular to both the NW axis and the magnetization of the domains seen with alternately a strong positive or negative B_y component. However, while we evidence a magnetic flux in negative z-direction towards either side of the core in the experimental results, the simulation only shows a decay of its amplitude. Considering the entire magnetic configuration of the vortex chain, we see that most of the magnetic modulation is in the xy-plane, with a relatively weak B_z component at the vortex core of around 0.5 T. There are regions with stronger B_z components at the outer layer of the NW, but these are believed to come from a mix of artifacts and perhaps due to the small oxidation layer at the NW surface.

From this, we can conclude that for a $Co_{85}Ni_{15}$ NW region of *hcp* phase with c-axis oriented close to perpendicular to the NW axis, the remnant magnetic configuration after applying a magnetic saturation field oriented perpendicular to both the wire axis (x-axis) and the magnetocrystalline anisotropy easy axis ($\sim y$-axis) stabilizes into a chain of transverse-vortices, confirming previous research on these NWs[4] carried out by 2D electron holography (Chapter 4). These vortices can be considered as the domain walls separating anti-parallel transverse domains oriented along the y-axis.

5.5 Parallel saturation: Longitudinal curling domains

Figure 5.4 presents the main results of holographic VFET at remnant state performed on the same area as the previous observations, but after applying a magnetic saturation field along the NW axis, in positive the x-direction. The resulting magnetic configuration, depicted in Figure 5.4a, shows a very different magnetic configuration compared to the previous: instead of a chain of transverse-vortex states separating antiparallel domain-like regions oriented along the y-axis, a more longitudinal magnetic configuration is evidenced.

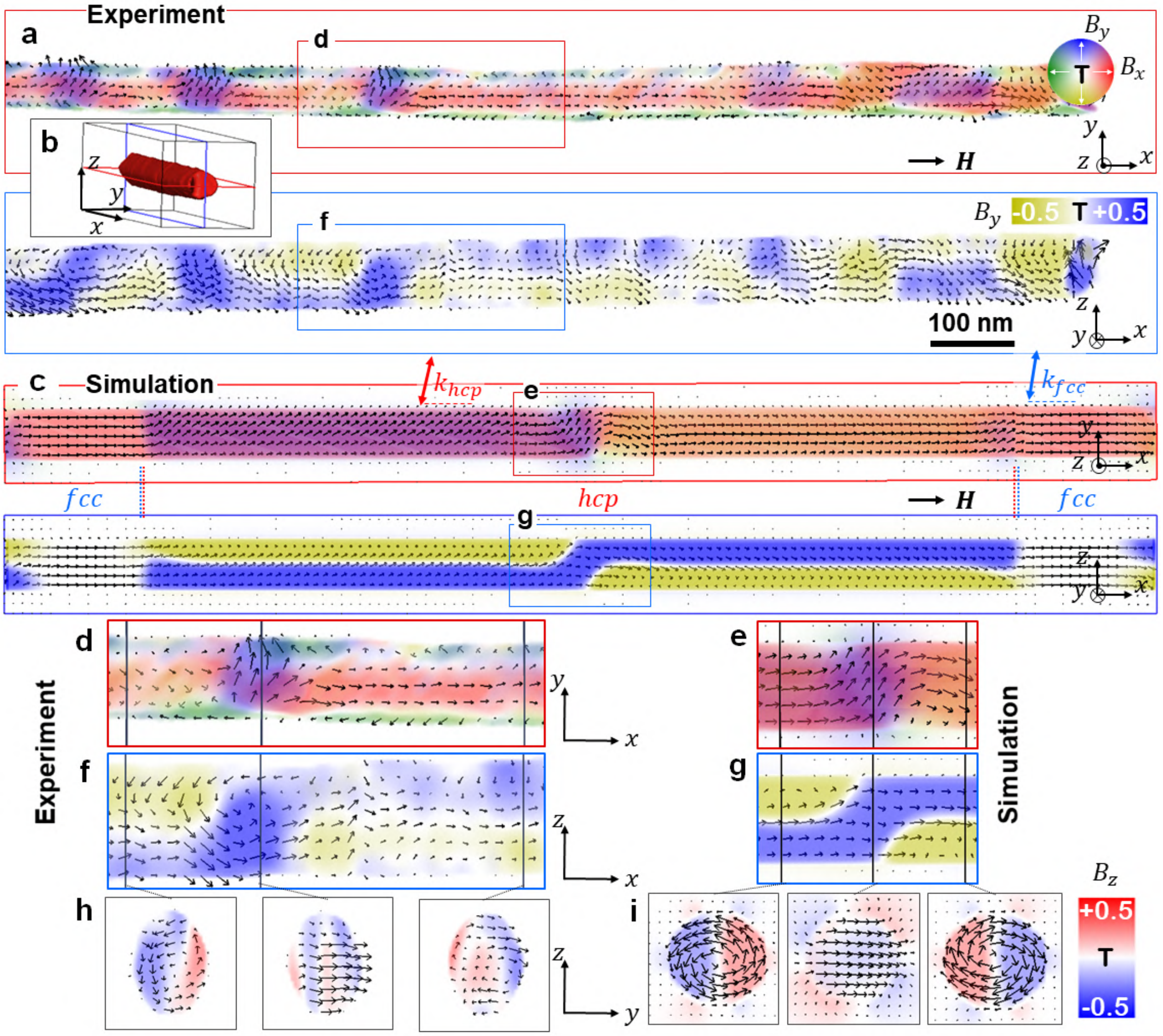

Figure 5.4: 3D reconstruction of the magnetic B-field inside CoNi NW by holographic VFET and comparison with micromagnetic simulation after magnetizing the NW in axial x-direction. (**a**) Central slices in axial (xy) and (xz) direction through the 3D B-field inside the NW visualized by arrow-plots and color-coded volume rendering of B_x and B_y reveal a complex picture in the *hcp* region. (**b**) Iso-surface rendering of the electrostatic potential obtained by holographic VFET shows the NW morphology. The positions of the axial slices **a** are depicted as red and blue rectangles. (**c**) Micromagnetic model of the NW by assuming an *hcp* region in between a *fcc* region with corresponding crystalline anisotropy axes k_{hcp} and k_{fcc}. (**d-g**) Zoom-in of the regions indicated in **a** and **c**. (**h**,**i**) Cross sectional slices (yz) at positions marked as black vertical lines in **d-g** superimposed by the color-coded B_z component show the transition between two vortex states with opposite chirality separated by a transversal domain wall.

Looking at the results in Figure 5.4a, we see that the magnetic flux generally runs in the positive B_x throughout the entire NW segment, but that there are smaller regions with a stronger B_y component. Further, by looking at the xz-plane orientation in Figure 5.4a, we observed that the B_y components are reversing in sign through the cross-section in a single NW segment, while B_x remains constant. This indicated that the magnetization is rotating around the NW axis. In addition, we observe regions where the B_y components are reversing in sign from positive to negative (blue to yellow contrast in Figure 5.4a) through the NW cross-section, and others where the B_y components go from negative to positive. This indicates that in these two types of regions, the magnetization is rotating with opposite helicity. I call such regions, where the magnetization rotation has the same helicity, curling domains. Two curling domains with different helicity are separated by a domain wall that is studied in the following.

The zoomed-in regions displayed in Figure 5.4d and 5.4f allow us to study the region between two curling domains in more details. The domain walls between two curling domains display a stronger positive B_y component, as indicated by the vector field arrows in Figure 5.4d, and by blue color contrast in Figure 5.4f. Figure 5.4h displays cross-sectional slices of the locations marked by a black line in Figure 5.4d and 5.4f, showing the x-direction view from the first domain, the middle of the domain wall, and the second domain. From these, we can clearly see that, from this view, the magnetic configuration changes from a counterclockwise to a clockwise rotation, and that the wall separating them is a transverse domain wall (TDW). This corresponds with the micromagnetic simulations that also show the formation of two curling domains of opposite helicity separated by a TDW when relaxed after being magnetized along the NW axis.

Although there is a general correlation between the experimental and the simulated results, the two are not perfectly identical. First of all, the micromagnetic simulation shows the formation of two equal-sized curling domains of opposite helicity, while the experimental result evidences three curling domains of different length, and even if it qualitatively agrees with the simulation, the magnetic configuration in the region close to the NW end is difficult to precisely determine. In addition, the overall magnetic configuration is much more turbulent in the experimental case, as a contrast to the simulation results which display a homogeneous rotation within the whole lengths of the respective curling domains, and a distinct symmetry of the magnetic flux in the transition regions of the TDW. It is believed that most of the difference can be explained by the fact that the micromagnetic simulations are performed for a perfect system with a completely uniform and monocrystalline segment with no modulations in magnetization nor any deformations or changes in the diameter of the NW. Magnetic domains separated by a DW appear when it is energetically favorable for the whole system, essentially to reduce the magnetostatic energy. In the presented CoNi NW system, where neither head-to-head nor tail-to-tail domain configurations are observed, we speculate if the creation of two domains with opposite helicity separated by a TDW effectively reduces the stray field and thus lower the total energy of the system. The fact that the two curling domains obtained in the simulation have the same size indicated that the two clockwise (CW) and counterclockwise (CCW) helicities are degenerate in energy. This was not obvious as the simulations show that the curling states are slightly canted, due to the uniaxial anisotropy of the *hcp* phase, which is not oriented perfectly perpendicular to the NW axis, and produces a small amount of magnetic charges at the NW surface and stray fields outside the NW. The experimental results also support the hypothesis of helicity degeneracy as both CW and CCW curling domains are observed. However, as the NW is not a perfect and homogeneous system, pinning sites, like crystal grain boundaries, diameter modulations, *etc.*, can change the curling domain configuration into a more energetically favorable one. From the iso-surface rendering of the NW reconstructed from the electrostatic potential found by holographic VFET, displayed in Figure 5.1, we can see that the NW segment does not have a perfectly circular cross-section, even if there is not any abrupt or large local change in thickness. We also know from the structural mapping performed by ASTAR measurements that there are local variations in crystal orientation and even changes in crystal structure within these NWs. Figure 5.5 shows a direct comparison of the experimental magnetic configuration in the case of longitudinal saturation, and the structural map found by ASTAR for the same NW region. We can generally distinguish four different curling domains in the inspected NW segment, which are marked by the black arrows in Figure 5.5a. The first three domain walls (from the left) are TDW pointing in the positive y-direction, while the last one points in the negative y-direction. This is best seen for the curling domain looking at the blue and yellow color code of the B_y component on the xz-plane image in Figure 5.5a. The position of the last negative-y

TDW is located where the more polycrystalline region of the NW tip meets the larger *hcp* grain. This last curling domain also has an overall stronger B_x component compared to the other three curling domains, which is in accordance with the notion of the region not having the same uniaxial magnetocrystalline anisotropy as for the domains located in the region of the large *hcp* grain.

The existence of smaller crystal grains in the structure is also believed to be the origin of the more turbulent magnetic configuration in the experimental NW as compared to the

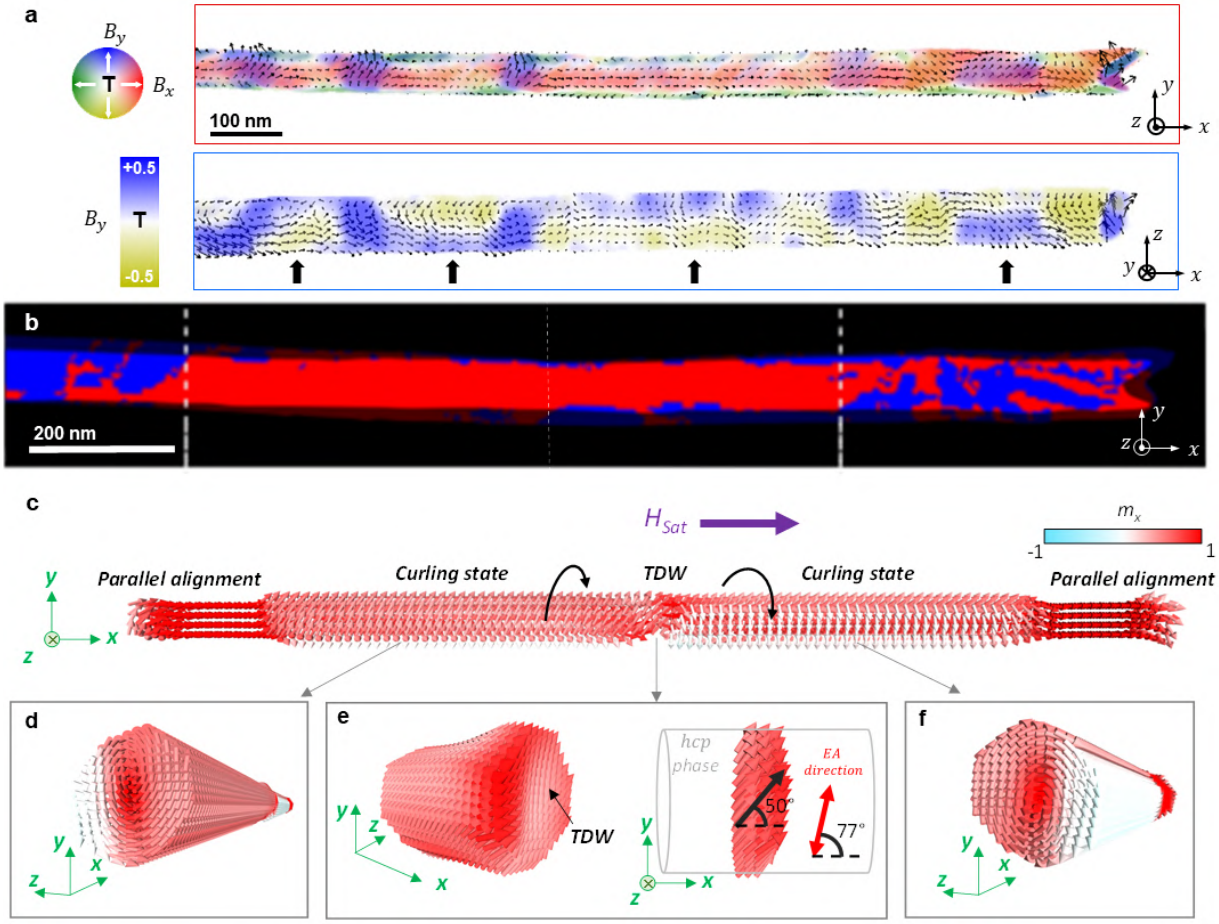

Figure 5.5: Direct comparison of magnetic configuration after parallel saturation and structural data. (**a**) Central slices in axial (xy) and (xz) direction through the 3D B-field inside the NW visualized by arrow-plots and color-coded volume rendering of B_x and B_y reveal a complex picture in the *hcp* region. The black arrows mark four curling domains. (**b**) Structural map from ASTAR measurements. Highest match for *fcc* and *hcp* crystal phase indicated by blue and red regions, respectively (from Figure 5.1). (**c**) Simulated 3D vector map of the remnant state after the application of a parallel saturation field. Cross section view of a curling state with a (**d**) negative and (**f**) positive chirality, and (**e**) the transversal domain wall.

simulations. We observe a clear correlation between the magnetic configuration close to the NW tip, where there is a different looking curling domain compared to the rest of the wire segment, and the polycrystalline structure found in the same segment. The fact that crystal structure can largely influence the magnetic spin-texture of a sample has been documented by previous studies[21,22] and is in correspondence with our previous study presented in Chapter 4 and published in ACS Nano.[4]

These experimental studies combined with the micromagnetic simulations, allow us to conclude that after applying a magnetic field oriented parallel to the wire axis in a $Co_{85}Ni_{15}$ NW region of *hcp* phase with *c*-axis oriented close to perpendicular to the NW axis, the resulting remnant magnetic configuration consists of curling domains oriented in the same direction as the applied magnetic field. Neighboring domains display a total magnetic flux in the same direction, but their rotations have opposite helicity around the NW core. We also found that regions with a more *fcc*-rich or polycrystalline structure can also promote a curling configuration, but the B_x component was measured to be stronger, which is in agreement with the reduced impact of a transverse uniaxial magnetocrystalline anisotropy.

5.6 Conclusions

The work presented in this chapter has used the holographic VFET technique to reconstruct the 3D magnetic configuration of the remnant state in a $Co_{85}Ni_{15}$ NW with a diameter of 70 nm, mainly consisting of a large *hcp* phase segment with its magnetocrystalline easy axis oriented close to perpendicular (75°) to the NW axis. We have performed detailed quantitative and local studies on the NW segment for two different initial magnetic conditions by correlating the 3D magnetic imaging results with crystal phase mapping by ASTAR and micromagnetic OOMMF simulations to understand the origin of the observed remnant magnetic states with a different magnetic history. Holographic VFET measurements were performed after the application of a magnetic field strong enough to saturate the sample in two directions, (i) perpendicular to the wire axis and the *hcp* magnetocrystalline easy axis, and (ii) parallel to the wire axis. The 3D magnetic vector field results reveal a tunable magnetic configuration that varies with the applied field direction. For an H-field applied perpendicular to the wire axis, the magnetic configuration relaxes into a series of transverse and antiparallel domains separated by vortices with their core aligned along the applied magnetic field direction, while for a saturation parallel to the wire axis, the remnant configuration consists of longitudinal curling domains separated by transverse domain walls.

The 3D magnetic imaging has confirmed the hypothesis of the study presented previously in Chapter 4 performed on the same sample using electron holography, and offered additional details and understanding of the highly three-dimensional magnetic spin texture. In the case of the perpendicular saturation, the new results reveal that the vortex cores are pointing in the same z-direction, in the direction of the applied field, and thus that the neighboring vortices have opposite helicity. However, the B_z component in the vortex core is weaker than expected (around 0.5 T), meaning that the largest part of the magnetic vector field is oriented in the xy-plane (image plane), and the vortex cores are slightly canted. The whole system can be viewed as a double Halbach array where the vortices act to reduce the stray field spreading out of the NW. Holographic VFET reveals that the magnetic configuration in the remnant state obtained after parallel saturation, consists of curling domains oriented in the same x-direction, aligned with the applied field, but with opposite helicity. The domain walls separating these curling domains have been identified as transverse DWs. Such helicity reversal between domains and the DW has also been confirmed by micromagnetic simulation, leading to the understanding that the switch in helicity between two domains causes a reduction of the stray field, making this state more energetically favorable than one large curling domain.

Although we have obtained a very detailed understanding of these magnetic configurations, there are still some areas that remain unclear that would require even more studies. We did not manage to resolve the fine structure of all the vortex cores from the holographic VFET studies and the complexity of this imaging technique makes this difficult to improve. Another way of getting more information could be by performing simulations, taking into account more parameters than what we used for the micromagnetic simulations with the assumptions made to simplify the system. It could also be of great interest to perform tomographic ASTAR measurements for a 3D structural comparison of the 3D magnetic configuration.

However, we do believe that we have a good understanding of this system, and how its structural configuration and magnetic history enables us to vary between these two very different magnetic configurations. Our next step would be to study what happens when applying small fields or current pulses to study the effect.

References

[1] A. Fernández-Pacheco et al. “Three-Dimensional Nanomagnetism”. In: *Nature Communications* **8** (2017), p. 15756. DOI: 10.1038/ncomms15756.

[2] P. Fischer et al. “Launching a New Dimension with 3D Magnetic Nanostructures”. In: *APL Materials* **8** (2020), p. 010701. DOI: 10.1063/1.5134474.

[3] M. Staňo and O. Fruchart. “Magnetic nanowires and nanotubes”. In: *Handbook of magnetic materials*. Vol. 27. Elsevier, 2018. Chap. 3, pp. 155–267. ISBN: 9780444641618. DOI: 10.1016/bs.hmm.2018.08.002.

[4] I. M. Andersen et al. “Exotic Transverse-Vortex Magnetic Configurations in CoNi Nanowires”. In: *ACS Nano* **14** (2020), pp. 1399–1405. DOI: 10.1021/acsnano.9b07448.

[5] D. Sander et al. “The 2017 Magnetism Roadmap”. In: *Journal of Physics D: Applied Physics* **50** (2017), p. 363001. DOI: 10.1088/1361-6463/aa81a1.

[6] T. Tanigaki et al. “Advanced Split-Illumination Electron Holography without Fresnel Fringes”. In: *Ultramicroscopy* **137** (2014), pp. 7–11. DOI: 10.1016/j.ultramic.2013.11.002.

[7] P. Simon et al. “Synthesis and Three-Dimensional Magnetic Field Mapping of Co2FeGa Heusler Nanowires at 5 Nm Resolution”. In: *Nano Letters* **16** (2016), pp. 114–120. DOI: 10.1021/acs.nanolett.5b03102.

[8] R. Streubel et al. “Retrieving Spin Textures on Curved Magnetic Thin Films with Full-Field Soft X-Ray Microscopies”. In: *Nature Communications* **6** (2015), pp. 1–11. DOI: 10.1038/ncomms8612.

[9] C. Donnelly et al. “Three-Dimensional Magnetization Structures Revealed with X-Ray Vector Nanotomography”. In: *Nature* **547** (2017), pp. 328–331. DOI: 10.1038/nature23006.

[10] M. Suzuki et al. “Three-Dimensional Visualization of Magnetic Domain Structure with Strong Uniaxial Anisotropy via Scanning Hard X-Ray Microtomography”. In: *Applied Physics Express* **11** (2018), p. 036601. DOI: 10.7567/APEX.11.036601.

[11] C. Donnelly et al. “Tomographic Reconstruction of a Three-Dimensional Magnetization Vector Field”. In: *New Journal of Physics* 38 (2018), p. 083009. DOI: 10.1088/1367-2630/aad35a.

[12] C. Donnelly et al. “Time-Resolved Imaging of Three-Dimensional Nanoscale Magnetization Dynamics”. In: *Nature Nanotechnology* **15** (2020), pp. 356–360. DOI: 10.1038/s41565-020-0649-x.

[13] D. Wolf et al. “Holographic Vector Field Electron Tomography of Three-Dimensional Nanomagnets”. In: *Communications Physics* **2** (2019), pp. 1–9. DOI: 10.1038/s42005-019-0187-8.

[14] H. Lichte. “Electron Holography: Optimum Position of the Biprism in the Electron Microscope”. In: *Ultramicroscopy* **64** (1996), pp. 79–86. DOI: 10.1016/0304-3991(96)00017-4.

[15] C. Gatel et al. “Size-Specific Spin Configurations in Single Iron Nanomagnet: From Flower to Exotic Vortices”. In: *Nano Letters* **15** (2015), pp. 6952–6957. DOI: 10.1021/acs.nanolett.5b02892.

[16] E. Snoeck et al. “Quantitative Magnetization Measurements on Nanometer Ferromagnetic Cobalt Wires Using Electron Holography”. In: *Applied Physics Letters* **82** (2003), pp. 88–90. DOI: 10.1063/1.1532754.

[17] P. A. Midgley and R. E. Dunin-Borkowski. “Electron Tomography and Holography in Materials Science”. In: *Nature Materials* **8** (2009), pp. 271–280. DOI: 10.1038/nmat2406.

[18] K. Harada et al. “Optical System for Double-Biprism Electron Holography”. In: *Journal of Electron Microscopy* **54** (2005), pp. 19–27. DOI: 10.1093/jmicro/dfh098.

[19] D. Wolf et al. “Towards Automated Electron Holographic Tomography for 3D Mapping of Electrostatic Potentials”. In: *Ultramicroscopy* **110** (2010), pp. 390–399. DOI: 10.1016/j.ultramic.2009.12.015.

[20] M. J. Donahue and D. G. Porter. *OOMMF User’s Guide*. Interagency Report. National Institute of Standards and Technology, 1999.

[21] B. Rodríguez-González et al. “Structural and Magnetic Characterization of As-Prepared and Annealed FeCoCu Nanowire Arrays in Ordered Anodic Aluminum Oxide Templates”. In: *Journal of Applied Physics* **115** (2014), pp. 133904–133904. DOI: 10.1063/1.4870289.

[22] J. Cantu-Valle et al. “Mapping the Magnetic and Crystal Structure in Cobalt Nanowires”. In: *Journal of Applied Physics* **118** (2015), p. 024302. DOI: 10.1063/1.4923745.

Chapter 6

Preliminary *in situ* magnetic transport studies in the TEM

Ferromagnetic nanostructures are considered the building blocks for the development of future spintronic devices.[1] However, as dimensions are continuing to decrease, some believe the development is approaching a fundamental limit to how small functional spintronic devices can get.[2] This has sparked a hunt for solid-state based devices using magnetic domain wall propagation for information storage.[3,4] As a result, a lot of studies have been conducted to understand the magnetic switching and domain wall propagation in magnetic thin films and nanostructures under the stimuli of an electric current.[5–8] Recent developments and advances in nanofabrication techniques,[9–12] have enabled the creation of more sophisticated nanostructures, and novel magnetic materials with curved geometries have gained more attention due to chiral effects,[13,14] where cylindrical nanowires are interesting candidates as they have the potential of high DW motion from the absence of a Walker limit.[1,15] In addition, electrodeposition of arrays of cylindrical NWs into alumina templates now allows for mass-producing metallic NWs with the ability to tune their magnetic parameters through shape, composition, and crystal structure.[11,16–18]

Despite being considered interesting candidates for the development of new novel spintronic devices, and an increasing amount of experimental results studying the remnant magnetic states and domain walls in such NWs have emerged the past two decades,[19–24] the domain wall dynamics in cylindrical nanowires have almost exclusively been studied theoretically by simulations,[25–27] and only a few experimental studies have been reported.[28] A point that has been established is that domain walls in cylindrical nanowires and nanotubes have different dynamic properties from what has been observed in thin films and strips. Their cylindrical geometry gives rise to chiral symmetry breaking and the existence of DWs that can propagate without being limited by the Walker breakdown,[1,15] which is known to limit the DW velocity in thin films and nanostrips.[26] Such systems are predicted to reach a DW velocity close to 1 km/s,[29] and a propagation $>$ 600 m/s has already been observed experimentally (although this is believed to be lower than the actual velocity due to pinning).[28]

Domain walls can be nucleated in various ways in a magnetic nanowire: They might be nucleated in larger parts or in designed reservoir structures in some part of the structure, and then pinned in a part of the wire (for example, in a fabricated junction area)[30] to later be propagated by applying an external magnetic field or an electric current. Another way is to apply a magnetic field in the opposite direction of the NW magnetization, large enough to initiate a reversal process of the magnetization, forming a head-to-head domain wall.[25] The DW might propagate all the way to the other end of the nanowire, leaving the new magnetic state fully reversed,[31] or it might be pinned at an inhomogeneity somewhere in the NW. Such a pinning site can, for example, be a modulation in diameter,[32] composition, crystal structure, *etc.*

In this chapter, I will present preliminary studies of the magnetic DW dynamics in NWs by *in situ* TEM measurements. The studied NWs are from the same CoNi sample that has been thoroughly studied by electron holography, holographic VFET and characterized through spectroscopic and structural measurements in Chapters 4 and 5. After all, it is the final prospect of being able to develop solid-state devices that is the large-scale motivation of these studies. The chapter is split into two parts, one presenting the results of a study on the transverse vortex chain under the application of magnetic fields. The second part shows a preliminary study of transverse vortices and domain wall propagation in longitudinal curling magnetic configuration by the application of electric current pulses.

6.1 *In situ* Fresnel imaging applying an external magnetic field

In this first experiment, the objective was to test the stability and reproducibility of the transverse vortex chain that has been revealed and studied in *hcp* crystal grains with a close-to-perpendicular c-axis direction relative to the wire axis (Chapter 4 and Chapter 5). Figure 6.1 displays an overview of the studied $Co_{85}Ni_{15}$ NW. The NW segment depicted in the BFTEM image in Figure 6.1a has a length of 1.7 μm long and has a nominal diameter of 70 nm. During the elaboration process, the NWs were subject to undefined magnetic fields in random orientations relative to the NW axis. In order to have a controlled knowledge of the magnetic history of the NW, I applied a 1.8 T magnetic perpendicular to the wire axis by turning on the TEM objective lens (OL) at zero tilt. From the Fresnel image (Figure 6.1b and d) we see that the same area of the NW switches between two remnant magnetic configurations, an "as-was" state (Figure 6.1b) and after the application of the perpendicular magnetic field (Figure 6.1d). Looking at the reconstructed magnetic phase images of the two states (respectively Figures 6.1c and 6.1e), we observe that the "as-was" state is dominated by a longitudinal magnetic configuration (Figure 6.1c), with strong resemblance of the curling state discussed in Chapter 5, while the latter state displays a vortex chain (Figure 6.1e), such as the ones that have been studied in details in Chapter 4 and Chapter 5. Based on our previously presented studies, we can expect the vortex chain to be located in a region with an *hcp* crystal phase oriented such that its c-axis is perpendicular to the NW axis.

In order to test the stability and reproducibility of the vortex chain, I performed *in situ* overfocused Fresnel imaging in the I2TEM by conducting a series of tilt experiments and gradually applying a magnetic field to the vortex chain configuration with different orientations and strengths. The magnetic field was applied using the conventional objective lens, as previously explained, with an estimated field strength of 121 mT/A in the direction perpendicular to the image plane (negative z-direction) that can be tuned by the strength of the current injected into the lens. The selected NW is oriented 85° relative to the α-tilt axis in the image plane (Figure 6.2a). First, the NW was tilted 45° around the α-tilt axis, giving the NW axis a directional component in the beam direction (Figure 6.2b), *i.e.*, the external magnetic field

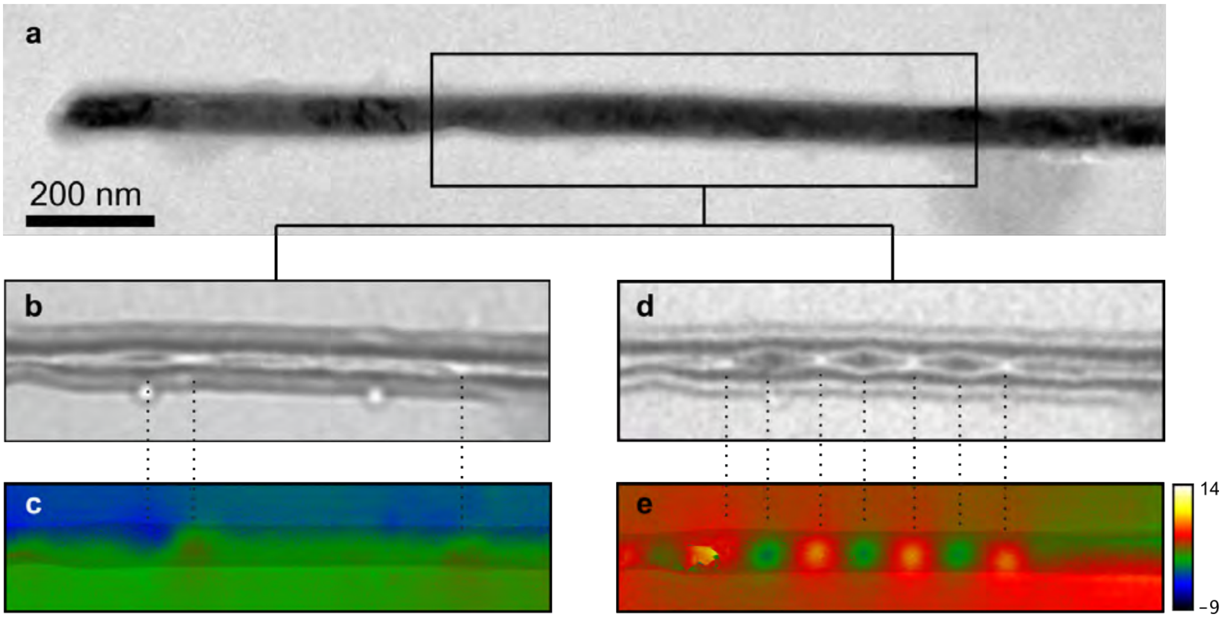

Figure 6.1: Magnetic imaging of NW at remnant before and after applied magnetic field (**a**) Bright-field TEM image of studied NW. (**b**) and (**d**) show Fresnel microscopy image, and (**c**) and (**e**) the reconstructed magnetic phase image of the boxed region in (**a**). (**b**)-(**c**) show the "as-was" magnetic state, and (**d**)-(**e**) the remnant state after applying 1.8 T (OL=18A) perpendicular to the image plane.

direction. In this way, a magnetic field could be applied with a component parallel to the NW axis. Starting from a vortex chain configuration induced by a perpendicular saturation field ($\alpha = 0$), the in-plane applied magnetic field is gradually increased by tilting the sample to $\alpha = \pm 45°$, until there is a change in the magnetic configuration, and eventually all the vortices were gone. A summary of these results is presented in Figure 6.3, where Figure 6.3b-d show the application at a negative tilt, and Figure 6.3e-g at a positive tilt. From Figure 6.1d-e, we can recognize the over-focused Fresnel image of a vortex chain by comparing it to the EH results, where the "holes" (dark) and "knots" (white) represent clockwise and counter-clockwise vortices. Using this information, we see that the initial state, for both positive and negative tilt, contains a vortex chain with four "holes" (clockwise vortices). From the results in Figure 6.3 we see that the chain is reduced by the visual loss of one "hole" at 34 mT effective field applied along the NW axis. After this, the configuration appears to be stable until the entire vortex chain disappears around 53 mT. A similar process is observed when the field is applied in the opposite direction along the NW axis (positive tilt), but here there are four visible "holes" up to an applied in-plane field of -53 mT, where one "hole" is deformed, followed by a loss of the entire vortex chain at -58 mT. Note that it is the "hole", or vortex, in the same relative position that first changes in both the positive and the negative tilt case. As the vortex states only can be nucleated in *hcp* crystal grains, the fact that we do not see a propagation of the vortices outside of the initial chain region might suggest that the chain covers the grain, and that the vortices are annihilated when reaching the end of the grain. Unfortunately, we do not know the direction of the curling domains on either side of the vortex chain. In order to highlight the vortex chain and clearly differentiate the location of the vortices, the Fresnel images were acquired with a lower defocus than what is necessary to see the magnetization direction of the curling domains in this system. We can therefore just speculate that the slight variation of the applied field necessary to manipulate the vortex chain is due to a change in the applied field directionality versus the direction of surrounding curling states. Testing this hypothesis could be an interesting experiment for future work on this system. However, we can conclude that we do manage to manipulate the vortex chain with the application of a longitudinal magnetic field component of magnitude around 55 mT in both positive and negative directions.

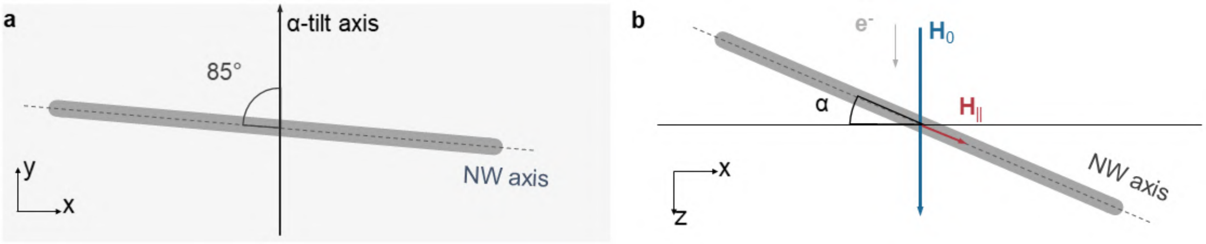

Figure 6.2: (**a**) Schematics showing the α-tilt axis relative to the NW axis in the xy-plane. (**b**) Illustration of the field component applied parallel to the NW axis ($\mathbf{H}_{||}$) relative to the α-tilt angle and the field applied by the objective lens ($\mathbf{H}_0$).

While both the vortex chain and the curling state have distinct transverse components, the latter also has a longitudinal nature. It, therefore, makes sense logically if there is a switching in the state from a transversal vortex chain to a curling state when a magnetic field of a certain amplitude is applied parallel to the NW axis. This is what we see; the entire vortex chain is switched around an effective magnetic field magnitude of 55 mT. Another observation made in this experiment is that the vortex chain was consistently reproduced in the same place by again applying a saturation field at zero-tilt, hence perpendicular to the NW axis.

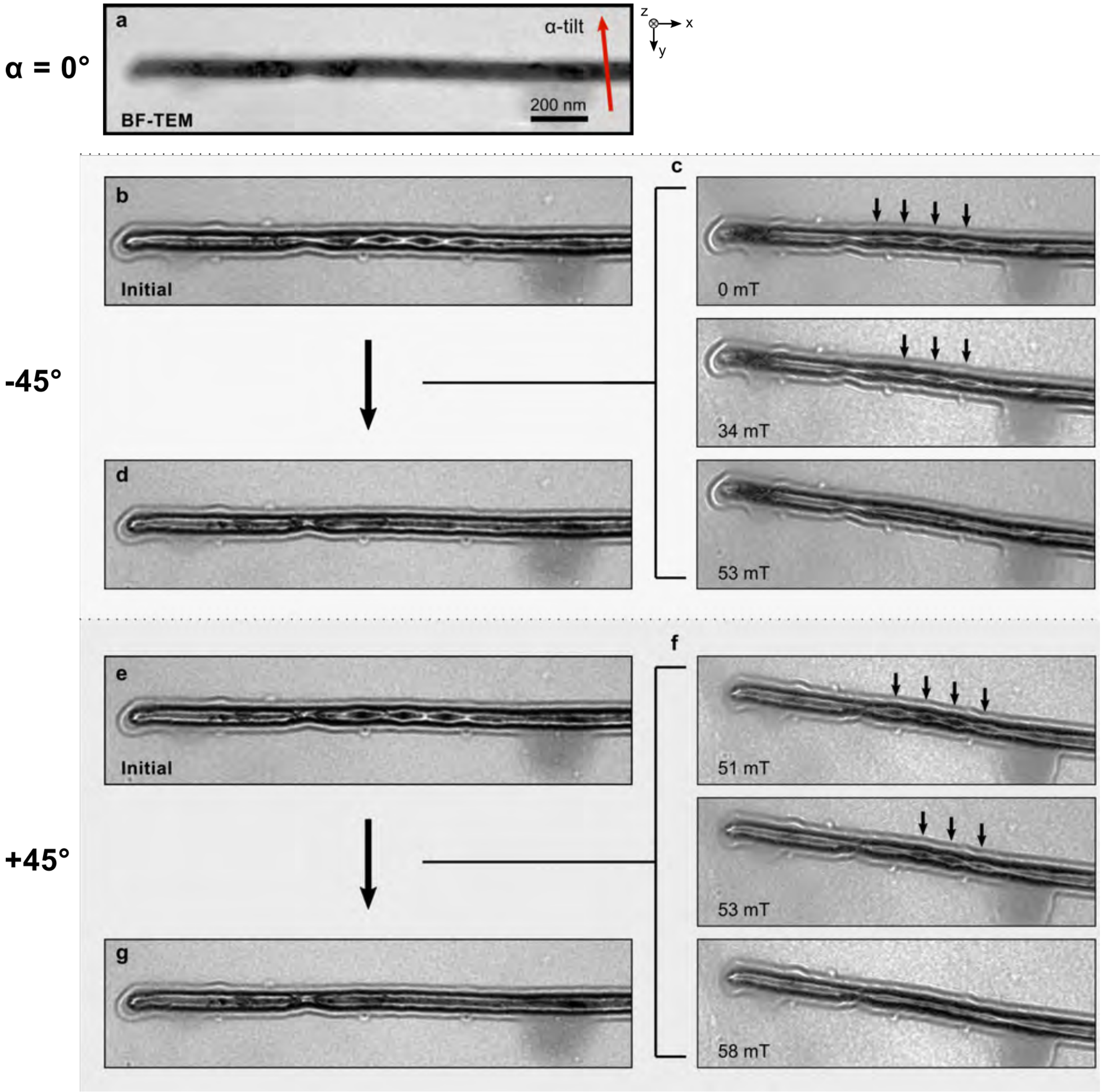

Figure 6.3: Results of *in situ* magnetic field application along the NW axis. (**a**) Bright-field TEM image of studied NW, where red arrow indicate the α-tilt axis. (**b**)-(**g**) Fresnel images showing change in magnetic configuration from applied field along NW axis in both positive and negative x-direction by repeating the measurement at -45° (**b**)-(**d**) and +45° (**e**)-(**g**) α-tilt.

As a second experiment, I wanted to further test the limits to the reproducibility of the vortex chain, or rather, if a perpendicular field at any direction would stabilize a vortex state at remnant state as long as the field is applied normal to the wire axis. For this, I used the same field strength (1.8 T) at different tilt angles, with the tilt axis (β-tilt) oriented parallel to the NW axis, causing the NW to rotate around its axis such that the projection of the NW

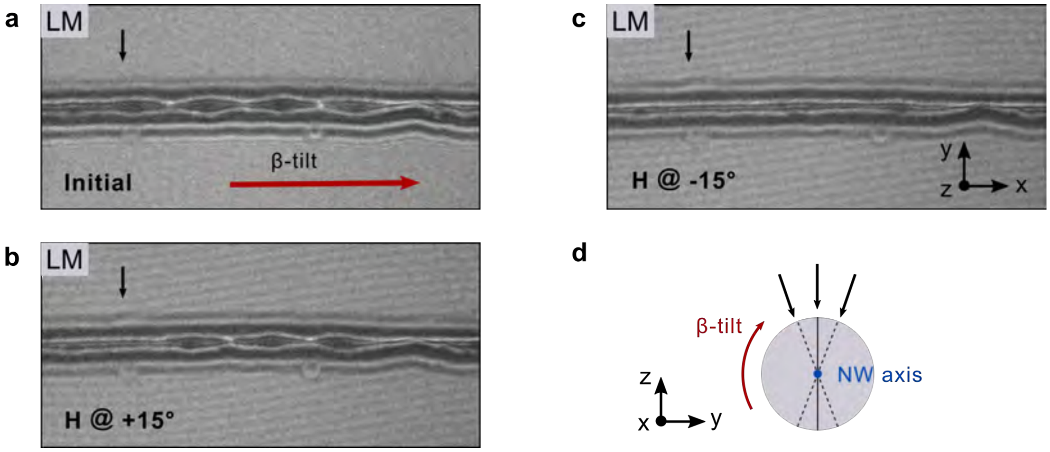

Figure 6.4: Results of *In Situ* magnetic field application at different projections perpendicular to the NW axis. (**a**) Over-focused Fresnel image of the initial magnetic state obtained after applying a -1.9 T field (out of the plane). The images were recorded at remnant state after applying a saturation field of +1.9 T (into the plane) at a β-tilt of, (**b**) +15° and (**c**) -15 °. The red arrow in (**a**) indicates the β-tilt axis. All displayed images recorded at 0° tilt. (**d**) Schematics of NW cross-section, where black arrows indicate magnetic field direction at different tilt angles.

changes (Figure 6.4d). In this way, the effective applied field, H, equals the field generated by the objective lens, H_0, but applied at different angles relative to the NW. This is illustrated in Figure 6.4d, where the black arrows indicate the direction of the effective magnetic field relative to the NW cross-section (the gray area) at different tilt angles. Figure 6.4 shows the over-focused Fresnel image of the remnant magnetic state after applying a 1.9 T field at a β-tilt of 0° (a), +15° (b), and $-15°$ (c). The initial state, shown in Figure 6.4, is a vortex chain with four clockwise vortices ("holes"). When applying the same field at an incident angle of 15° (Figure 6.4b) the chain is reduced to three "holes," while the entire vortex chain disappears when the field is applied at $-15°$ tilt (Figure 6.4c).

From what we previously knew about the vortex state, we assume that the region where this state is formed has a *hcp* crystal phase with an easy axis close to perpendicular relative to the NW axis, as the formation of such a transversal magnetic configuration is due to the strong magnetocrystalline anisotropy of such a crystallography.[33] Since the magnetic configuration is caused by a strong anisotropy, it is in good correspondence that we see this directional dependence of the saturation field to form the vortex chain. This also explains why the chain is only observed in around 10-20% of the studied NWs (see Chapter 4), as the NWs are drop cast, and therefore, deposited with random orientation relative to the beam axis. From this, we can conclude that the process is linked to the crystal grain orientation relative to the applied magnetic field in such a way that the c-axis has to simultaneously be oriented close to perpendicularly to both the NW axis (x-axis) and the applied magnetic field (z-axis). While a more thorough and systematic study is needed to quantify the range of deviance from the orthogonal axis where a transverse vortex chain may be nucleated, the presented results suggest the limit to be less than $\pm 15°$.

By performing *in situ* Fresnel microscopy experiments on a transverse vortex chain by applying an external magnetic field of different orientations and magnitude, we learn that the vortex chain is relatively stable towards longitudinally applied magnetic field up to around 30 mT, while the entire chain moves to the end of the *hcp* grain and is annihilated at an applied field of around 55 mT, and the magnetic configuration is replaced by a curling state. The vortex chain can be re-nucleated at the same place by applying a saturation field perpendicular to the NW axis and orthogonal to the c-axis. For a saturation field applied with a small degree ($< \pm 15°$) of variation from the direction orthogonal to the c-axis, a reduced vortex chain can be nucleated, while a too large of a variation leads to a curling configuration at remnant state.

6.2 Preliminary *in situ* Fresnel imaging injecting a current

In Section 6.1 we learned that the magnetic configuration could be manipulated through the application of a magnetic field. However, the development of systems or spintronic devices requires the manipulation of the magnetic spin-structure using electric current. The aim of this study is, therefore, to develop a method to perform *in situ* magnetic imaging in the TEM while injecting an electric current into the NW in order to directly observe its effect on the magnetic configuration of the NW. Such *in situ* biasing experiments demand special nanofabrication methods to isolate and contact single NWs with low resistivity contacts in order to be able to control, tune and characterize the current pulse sent through it.

6.2.1 Experimental methods and development

Several *in situ* magnetic manipulation and domain wall transport studies have been published on contacted nanostructures using magnetic imaging techniques like MFM,[5] Kerr microscopy,[34] synchrotron-based techniques like XMCD-PEEM,[28] and a few TEM based experiments using Fresnel imaging.[8] Even though biasing experiments in electron holography mode have been performed at CEMES,[35] there was no technique and protocol to contact and perform *in situ* TEM experiments on a nanowire. The pursuit for performing an *in situ* biasing experiment in the TEM to observe DW manipulation in a contacted NW, therefore, had to start with the establishment of an experimental setup and methodology.

In order to gain some hands-on experience and learn about the setup and criteria needed for such an *in situ* magnetic imaging, I had the opportunity to join Dr. Olivier Fruchart, Dr. Aurélien Masseboeuf (Spintec, Grenoble), and respectively Micheal Schöbitz (Pollux beamline at the Swiss Light Source facility at the Paul Scherrer Institut in Villigen, Switzerland), and Laura Álvaro Gómez (HERMES beamline at the SOLEIL facility in Saint-Aubin, France), to assist in performing *in situ* scanning transmission x-ray microscopy (STXM) imaging of contacted NWs. Most of the processes and setups for STXM experiments either directly used or adapted for a TEM based experiment.

To successfully perform such an experiment in a TEM environment, there are a number of points that need to be covered:

- A single isolated magnetic nanowire has to be placed or localized on a support.
- The support has to be equipped with electrodes, onto which the NW will be electrically contacted, by making nm to µm scale connections.
- The sample support has to be mounted on a dedicated biasing sample holder to be inserted into the TEM to allow for current injection through mm scale connections.
- A means to inject and measure electric currents is needed. The injection of current is provided by a current generator through macroscopic contacts connected to the sample holder.

- A video recording camera with a high frame count frequency is needed, as the studied phenomena are not static and are difficult to observe by normal image acquisition.

Compared to a synchrotron-based experiment, the TEM environment demands additional criteria regarding the sample preparation:

- First of all, the sample and the support have to be electron transparent, effectively meaning that the area of interest (sample plus support) cannot have a thickness of more than 100 nm for I2TEM studies performed at 300 kV.
- The sample support has to be designed to fit onto a dedicated sample holder, while at the same time not have an effective thickness larger than what is allowed by the gap between the objective lens pole pieces (∼1 cm), where the sample usually is placed. As a consequence, the volume available inside the TEM for the connected sample (chips, wires, *etc.*) is very limited. These are important aspects to remember when designing the sample support chip and electrode contacts. In addition, as a downside to the excellent spatial resolution of the TEM, the field of view is limited.
- Finally, the TEM is operated under a high vacuum, a requirement that can cause many problems. Complex biasing samples that have undergone several preparation steps may compromise the vacuum level by being less clean and containing highly outgassing materials such as silver paste. In addition, there is less dissipation of thermal energy, which may cause the sample to burn more easily unless measures are taken to either conduct the heat or to limit the current. These are important aspects to consider when designing and preparing a sample for TEM biasing experiments.

Nanowire dispersion and selection

The nanowires used in this study are the same type of $Co_{85}Ni_{15}$ as the ones presented in Chapter 4 and Chapter 5. These NWs have been synthesized by electrodeposition into pores of anodic aluminum oxide templates, performed by Dr. Cristina Bran at ICMM in Madrid. For more details of the fabrication process, see Section 4.2.1. The nanowires, dissolved in ethanol, were drop cast onto the electron-transparent membrane. In order to avoid breaking or damaging any NWs, the use of an ultrasonic bath to disperse the wires was reduced as much as possible in order to preserve the NWs since they were intended for being contacted. However, this aspect is more important to avoid for longer NWs, as they can more easily break.

Sample holder

A dedicated sample holder with biasing possibility is required for the current injection. At the start of this thesis work I used the only available biasing stage at the CEMES; the Gatan© HC3500 holder. This sample holder, displayed in Figure 6.5a-c, has the drawback of a sample mounting process consisting of gluing the sample in place with silver paste, followed by the use of a wedge bonder to make the connection between the sample holder and the electrodes on the sample support. This is a time consuming procedure, much due to the occasionally tedious process of wire bonding, which can take up a timespan of between 30 min to 4 hours, depending on factors like: the number of contacts needed, the time to find suitable parameters, and, seemingly, luck. In addition, the sample holder should be cleaned and kept under vacuum at least overnight leading up to the TEM experiment, in order to be able to reach the desired vacuum, much due to the use of silver paste. All of this makes it so that the sample should be prepared at least one day in advance of the experiment. A consequence of this is that only one sample can be prepared at a time, meaning that an unsuccessful attempt or a destroyed sample will compromise the experiment time slot, and a new couple of days will have to be set aside for a next attempt with a new sample, *etc.*

With the purpose of simplifying the sample mounting for *in situ* experiments, Dr. Christophe Gatel and Dr. Aurélien Masseboeuf have collaborated with Hummingbird Scientific© to acquire an *in situ* sample holder specifically designed for biasing experiments in the I2TEM. Figure 6.5d-f presents an overview of the sample holder, where the contacts between the sample and the holder are made by the same principle as a USB-stick. This principle makes it possible to switch between samples in minutes, enabling experiments of multiple specimen to be conducted in the same session. Another improvement that accompanies the Hummingbird sample holder is the possibility of having nine contacts, while the Gatan© holder only had four.

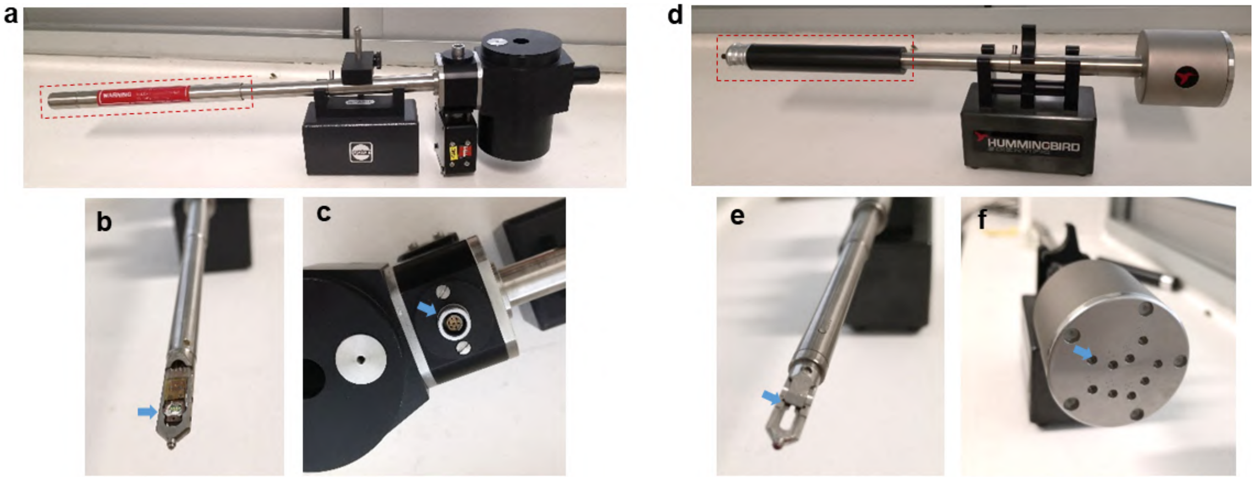

Figure 6.5: Overview of the two biasing sample holders (**a**) Gatan HC3500 with sample holder tip protection indicated in stippled square, with (**b**) showing the holder tip with sample position indicated by arrow, showing a sample glued on by silver paste and contacted to the holder by wedge bonding, and (**c**) biasing and heat control housing with connections indicated by arrow. (**d**) Hummingbird Heating + Biasing sample holder, respectively, with sample holder tip protection indicated in stippled square (**e**) showing the empty holder tip with sample position indicated by arrow, and (**f**) the biasing control housing with connections. Arrow indicates one of the nine contact points.

Nanowire contacting

I attempted several techniques to contact a single NW placed on a support that is electron transparent. The first attempts were done using the Gatan$^{\copyright}$ holder on home-made silicon chips with silicon electron transparent oxide membranes and gold electrodes for contacting (Figure 6.6a(i)), where I used focused ion beam induced deposition (FIBID) (3.7.1) of tungsten (W) and platinum (Pt). One example is displayed in Figure 6.6a(ii). At this point, the contacting was done to practice the technique and observe the contact quality, as I did not have any suitable NWs for magnetic observations.

As an alternative approach, I used commercial TEMwindows$^{\copyright}$ lift-out grids by SiMPore$^{\copyright}$ in which I cut a hole in the 400 nm thick Silicon Nitride film using FIB milling in order to create a vacuum region between two gold electrodes and place a single NW across it. For this, I used the micromanipulator in the Dual Beam setup to pick up a selected NW and place it over the trench. I then fastened each end of the NWs onto the gold electrodes located on either side of the hole (Figure 6.6b(i)). A micromanipulator is a mechanically movable tungsten probe used to pick up and transport "micro" objects and lamella for sample preparation by gluing the objects to the tungsten tip using FIBID or FEBID (focused electron beam induced deposition), and then releasing it from the tip by FIB milling. While this was possible for NWs with a diameter greater than 120 nm (Figure 6.6b(ii)), it was a tedious process with low reproducibility and proved to be practically impossible for thinner NWs, much due to the large size of the Omniprobe tip relative the NW and the limited resolution in performing the FEBID of Pt, which effectively caused the Pt deposition to glue the NW to the surface rather than to the Omniprobe. While this is an efficient method for other purposes, it was not suitable for contacting NWs with the appropriate thickness for TEM imaging. The ability to drop cast the NWs straight on to an electron transparent membrane, and then selecting a suitable NW out of the randomly placed ones, thus, seemed to be the better solution.

Contact electrodes: Laser and electron lithography are widely used to produce high-quality electric contacting of nanosystems. I had the opportunity to stay a week at the Spintec lab in Grenoble with Dr. Aurélien Masseboeuf, where I learned a procedure for contacting nanowires for *in situ* biasing experiments by laser lithography. Any lithographic process roughly consists of illuminating a desired pattern in a resist layer (usually spin-coated onto the substrate), where the illuminated area of the resist either hardens or becomes soluble, leaving a "positive" or a "negative" pattern in the resist layer (Figure 6.7).[36] The lithographically made pattern in the resist is further used as a mask for processes like etching or deposition of material followed by a lift-off process to achieve the desired construction. For the making of electric contacts on a nanowire, the desired material (usually gold) is sputtered onto the sample surface with the lithographically made resist pattern, followed by the removal of the remaining resist (lift-off), leaving the patterned gold that was deposited on the exposed substrate (Figure 6.7). Two major advantages of using this technique for contacting are that it creates high-quality contacts with low resistivity and without damaging or altering the sample (in our case, a NW) itself. There are a variety of lithographic techniques that can fit different needs, whether it is to create large structures (UV lithography with mask) or to make detailed and intricate patterns (electron beam lithography) required for high-resolution devices. In addition to the increased accuracy for the fabrication of small (nano)structures, an advantage of electron beam lithography is that it is a *direct write* technique using a scanning

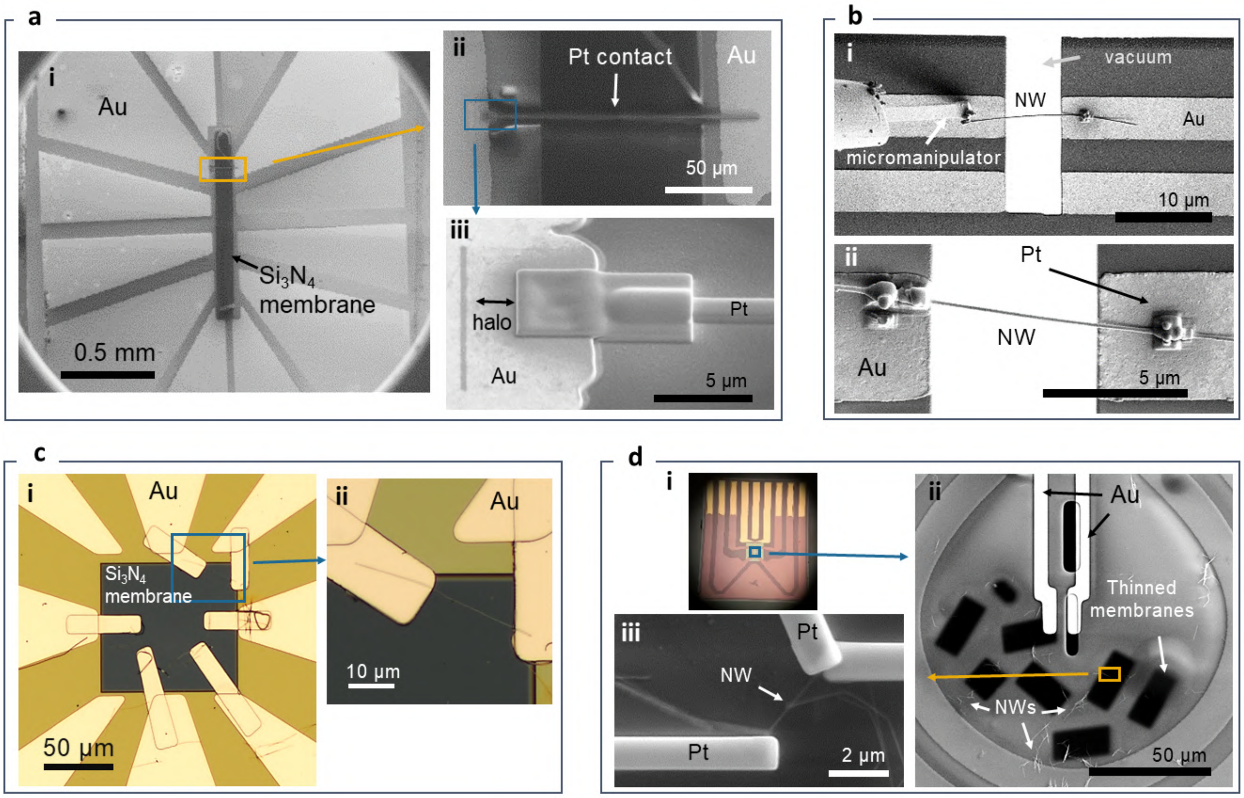

Figure 6.6: Overview of attempted NW contacting strategies. (**a**) FIBID contact from electrode to electrode, showing SEM images of Pt (i) chip overview, (ii) the Pt deposited contact, and (iii) zoom-in on junction at the right electrode, showing FIBID halo-effect. (**b**) Displacement of NW across vacuum gap, showing SEM image of (i) placement using a micromanipulator, and (ii) finished product with each NW end connected to Au electrodes by Pt deposition. (**c**) Laser lithography of gold contacts, showing (i) membrane and electrode overview, and (ii) zoom-in of contacted NW. (**d**) commercial Hummingbird chips, with (i) showing the entire chip, (ii) a SEM image of membrane area showing thinned membrane regions and drop cast NWs, and (iii) a SEM image of the contacted NW.

probe to illuminate the region of interest, where the "mask" is instead digital coordinates loaded onto the lithography machine, describing the pattern to be made.

The largest drawback is that it is a slow and expensive process and is thus best suited for small structures or prototyping rather than mass production.[37] As a less accurate, but considerably faster direct writing alternative, laser lithography uses a UV laser beam as the exposing radiation. While the latter two techniques are called "direct write," it is important to remember that this only refers to the lack of a physical mask needed for the exposure step to make the pattern in the resist layer. Contacting by lithographic processes still requires multiple steps like development, cleaning, sputtering/etching, and in some cases, lift-off processes to reach the finished product, which have to be delicately performed when dealing with a thin (< 50 nm) electron transparent membrane. This is the largest drawback of laser and electron lithography compared to FIBID/FEBID for electrically contacting NWs.

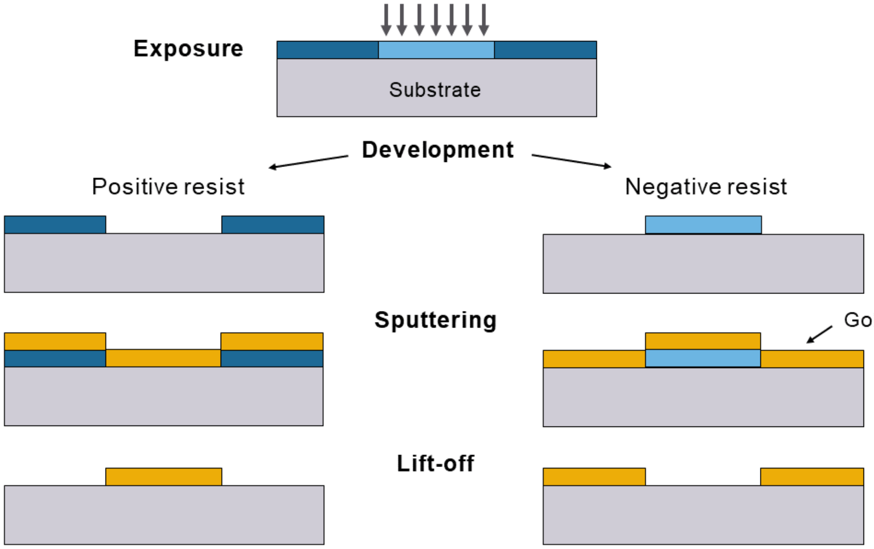

Figure 6.7: Schematics lithography process to pattern gold contacts on a sample substrate. The resist pattern acts as a mask to deposit the gold onto the substrate through sputtering and lift-off process.

Since gold contacts made by lithographic processes usually are of higher quality (lower resistivity) as compared to tungsten or platinum electrodes made by FIBID, I wanted to transfer the knowledge and procedures I had learned in Grenoble to CEMES and make the sample contacts by lithography. However, one important step for the contacting of NWs that I learned in Grenoble is to perform argon milling right before the gold sputtering inside the same chamber without breaking the vacuum. The purpose of this step is to clean the sample surface and remove the oxidation layer on the NW's surface, which is crucial in order to get a good electric contact for nanostructures materials that have a relatively fast oxidation rate compared to their size. At this time, we did not have the ability to perform this pre-procedure of argon milling before the gold sputtering deposition at CEMES. However, I still wanted to test it, as a successful contact would drastically improve the *in situ* experiment. In an attempt to reduce the sample oxidation as much as possible I used some newly made nickel NWs, that had been electrodeposited and sent to me by Dr. Cristina Bran just a couple of weeks before. As Co-Ni alloys oxidize faster with a higher Co content,[38] my hope was that by using a fairly "fresh" NW batch made out of nickel, instead of mainly cobalt ($Co_{85}Ni_{15}$), I could test the possibility of contacting without the argon milling step. The NW contacting was performed on homemade electrode membrane chips ($Si/SiO_2/Si_3N_4$) that I made in the CEMES clean-room using UV lithography (Figure 6.6c). Unfortunately, my attempt was unsuccessful as the contact was too poor due to the oxidation layer. However, the CEMES clean-room received a new sputtering machine in December 2019, which has the potential to perform in-chamber argon milling prior to gold sputtering. While a protocol for its usage is still under development, this missing step will enable electric contacting of nanostructures using the laser lithography facility at CEMES in the near future.

When the new Hummingbird sample holder arrived, I switched to using dedicated contacting chips for this holder, as the absence of wire bonding step, needed to mount and contact the sample chips to the Gatan holder (see above), saves hours of sample preparation and the risk of destroying the sample either mechanically or by unintentionally creating a discharge during the wedge bonding process that may destroy the sample. Since the attempts using displacement by a micromanipulator and contacting by lithography (without argon milling step) has been unsuccessful, I went back to using FIBID in the FEI Dual Beam setup (Section 3.7). Some commercially made Hummingbird chips were bought for biasing and heating experiments (Figure 6.6d(i)). However, the membrane was only provided with two small electron transparent windows, and the probability for a suitable, single NW to be deposited on one of them is very small. I, thus, attempted to create more thinned electron transparent membrane regions by FIB milling the chip from the backside of the membrane (Figure 6.6d(ii)). This was quite challenging as the chips are square in shape, and we only have a FIB sample stand for circular samples. I, therefore, had to get creative in the insertion of the sample, resulting in not being able to obtain a perfect 52-degree tilt angle (perpendicular to the ion beam) for the milling. As a consequence, the resulting membrane thickness did not turn out perfectly uniform. After repeating the steps of thinning the membrane and depositing NWs to look for suitable candidates, three times, I finally found a suitable NW, upon which I used FIBID to make Pt contacts and connect it to the gold electrodes (Figure 6.6d(iii)). However, when inserting it into the TEM, it quickly became clear that it was too thick and that the resulting thickness of the membrane was irregular. Perhaps it would have been more successful if I had a proper stand to perform the FIB milling more accurately, but I understood that a large ($>$ 50 μm), thin and uniform membrane is the better option for drop cast NWs.

In order to have a sample suited for the Hummingbird holder, equipped with a sufficiently large and thin membrane, custom made electric biasing chips were designed by Dr. Aurélien Masseboeuf and produced through lithographic processes at the LAAS-CNRS laboratory in Toulouse. Each chip consists of one 100 μm-by-100 μm large and 30 nm thick electron transparent Si_3N_4 membrane with nine 200 nm thick gold electrodes available for contacting single nanostructures (Figure 6.9a). This system has been used in the following study, presented in Section 6.2.2. The studied CoNi NW was contacted using FIBID with an ion beam energy of 8 kV and a current of 21 pA. The electrodes were formed by depositing Pt using a rectangle deposition mode and a bottom-to-top raster scanning pattern with a dwell time of 200 ns and an overlap of 50%. However, prior to the contacting of the NW, when inserting the empty chips into the Hummingbird sample holder to check for flat signals on all connections, some of the contacts had characteristics of a short circuit. While the presented chip was characterized before contacting, in order to avoid selecting compromised electrodes, it is not yet clear what caused this behavior. This uncertainty makes the measured characterization of the transmitted electric pulse unreliable and is believed to be the main reason why we cannot obtain quantitative information on the real current density sent in the NW. This issue will be discussed further in Section 6.2.2.

In situ **electric pulse injection**

The DW motion phenomena we want to study are in the range of several hundreds of meters per second,[29] hence, we have to send electric pulses of the same temporal range, *i.e.* nanoseconds. In addition, current-induced DW motion in ferromagnetic NWs and strips require a current density on the order between 10^{11} and 10^{13} $A{\cdot}m^{-2}$).[28,39] Due to the increase of the total impedance of the setup when using short nanosecond pulses, the transmitted signal can be reduced to about 20% of the original intensity.[40] In addition, the sample holder has to support high-frequency signals in order to inject nanosecond pulses into the sample. Generating a single, nanosecond long pulse of current, with a sufficiently high amplitude, into a NW contacted by lithographically made electrodes, required a specific and advanced power supply.

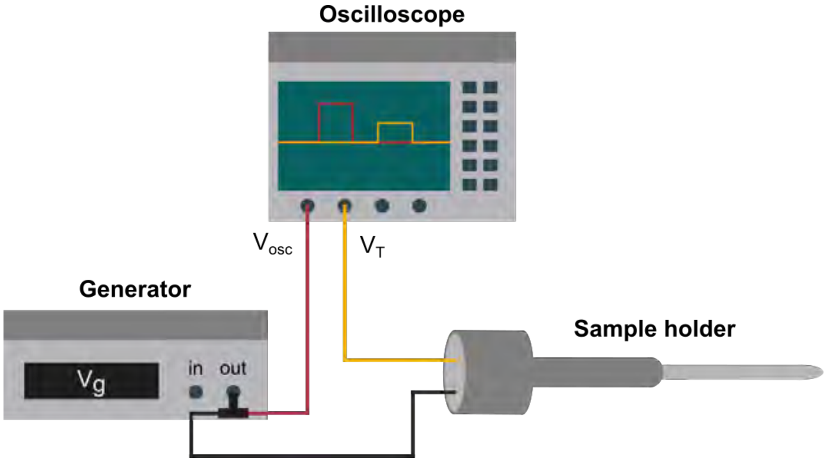

Figure 6.8: Schematics of the electronic setup used in the experiment.

In the presented results, the electric pulses were generated by a Keysight technologies 8110A single channel 150MHz pulse pattern generator. It has an output frequency of 1.0 Hz to 150 MHz and can generate pulses with an amplitude of up to 10.2 V when connected to a 50 Ω device. The generated pulses were monitored by an oscilloscope both at the pulse generator output and after the sample (the "transmitted" pulse) as illustrated in Figure 6.8. For this, a Teledyne LeCroy WaveJet 334A benchtop oscilloscope with a bandwidth of 350 MHz was used.

The following two settings are the parameters of the generated square wave pulses as programmed:

1. V_g = 10.2 V, W_g = 8 μs
2. V_g = 10.2 V, W_g = 10 μs

where V_g is the pulse amplitude and W_g its temporal width as defined by the generator. The resistance of the system was measured to be R = 172 Ω.

6.2.2 *In situ* Fresnel imaging injecting a current pulse

Figure 6.9 presents an overview of the contacted NW on the biasing chip, where Figure 6.9a shows a low-magnification BFTEM image of the Si_3N_4 membrane, and the squared region marks the region of the studied contacted NW displayed in Figure 6.9b. The contacted NW segment is 4.7 µm long, from electrode to electrode, as indicated by the black arrow in Figure 6.9b. The NW inset in Figure 6.9b shows a gradual increase of the NW diameter in the region close to the Pt contact. The Pt electrodes are deposited by FIBID with a Ga$^+$ beam. FIBID always creates a halo effect around the main deposited structure (Figure 6.6a(iii)), due to Ga-ions that disperse in the surface around the target area and create a small layer of deposition around the targeted area (see Section 3.7.1) as observed in the region around the patterned electrode.

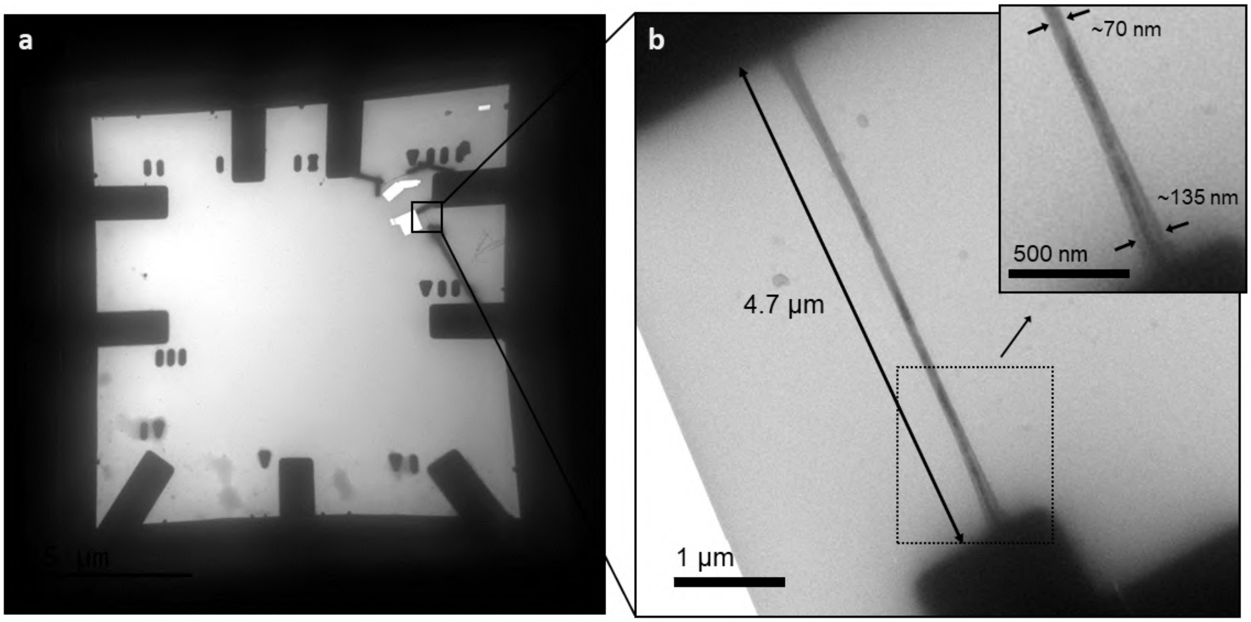

Figure 6.9: Overview of the *in situ* sample chip showing (**a**) the chip membrane with lithographically made gold contacts and (**b**) the NW contacted by FIBID-made Pt electrodes.

Figure 6.10 displays an overview of the middle region of the NW where the first current injection experiment was performed. The diffraction pattern and associated dark-field TEM (DFTEM) image shown in Figure 6.10a-b indicate that the bright areas in the DFTEM image are *hcp* grains. There are possibly other *hcp* phase regions with orientations such that the $01\bar{1}0$ reflection does not appear. However, the DFTEM image evidences a nanocrystalline structure, with at least three small-to-medium sized *hcp* crystal grains in this region, with length of $\sim$330 nm, $\sim$30 nm, and $\sim$220 nm measured along the wire axis, for respectively the top, middle and bottom grain (the bottom grain stretched further than image). In addition, Figure 6.10c reveals two prominent diameter modulations of the NW, as indicated by the black arrows. We know from previous studies that both crystal grains or grain boundaries, and local variation in shape can act as DW pinning sites.[11,32,41] A small chain of transverse vortex states, marked by the black arrows in Figure 6.10d(i), was stabilized in the location of the 200 nm long *hcp* grain after applying a 1.8 T field in the direction of the electron beam, *i.e.*, perpendicular to the wire axis. Since Fresnel image characteristics of a transverse vortex chain have been imaged and compared to EH results in previous chapters and subsections of this thesis, we are confident that it is this type of observed configuration, depicting the characteristic "holes" and "knots," as discussed in Section 6.1. The vortex chain seems to consist of two vortices (one "hole" and one "knot"), and possibly also a third tilted one, as it was described earlier to appear around crystal grain boundaries (Section 5.4).

Using the experimental setup explained in Section 6.2.1 and the pulse generator parameters # 1, a single square pulse was injected to the NW, giving a readout of $V_{osc} = 8.18$ V and $V_{oT} = 3.96$ V, for respectively the oscilloscope and transmitted signal (see Figure 6.8). Based on the measured transmitted signal and an estimated NW diameter of 70 nm, this corresponds to a current density $j = 6 \cdot 10^{12}$ A·m^{-2} ($\Delta j = 1 \cdot 10^{12}$ A·m^{-2} due to diameter variations). While this value indeed is in the expected range for DW propagation, due to some of the aforementioned issues with the experimental setup, we do not consider these measurements to be reliable as we are not sure of what exactly is being measured. A more rigorous setup will therefore be needed in order to characterize the transmitted electric pulse through the NW.

Figure 6.10d shows (i) the initial magnetic configuration and (ii) the final remnant state after the pulse. The results indicate that the electric pulse has caused a change in magnetic configuration from a transverse-vortex state (i) to a curling state (ii). Firstly, this proves that the generated pulse has had an effect on the NW, and secondly, that it is sufficient to move the transverse vortex and switch the state. Based on the previously presented micromagnetic simulation study of the *hcp* grain (Section 4.2.4) we know that the transverse vortex state can only be stabilized in an *hcp* grain with the *c*-axis close to perpendicular to the wire axis. It is, therefore, believed that the transverse vortex states propagate to the end of the *hcp* grain where they are annihilated. What remains is a curling domain (also called a longitudinal vortex domain). Note that the magnetic configuration in both (i) and (ii) contains a head-to-head or tail-to-tail longitudinal vortex domain configuration, as the curling domain above the vortex chain has a contrast going from dark (left side) to light (right side) inside the NW, while the wire region below the vortices reversely shows a light-to-dark contrast, indicating opposite directionality of the longitudinal magnetic components. In the first case (i), the vortex chain acts as an effective "domain wall," while the second case (ii), is believed to have a transverse DW in the same region. One question that arises is: why does not the domain wall continue to propagate in order to switch the entire NW? The BFTEM image of the NW (Figure 6.10b) shows that there are two locations with diameter variations on both sides of the vortex chain, as indicated by the black arrows in Figure 6.10c. These diameter modulations may act as pinning sites and, thus, prevent further switching of the magnetic configuration in this region.

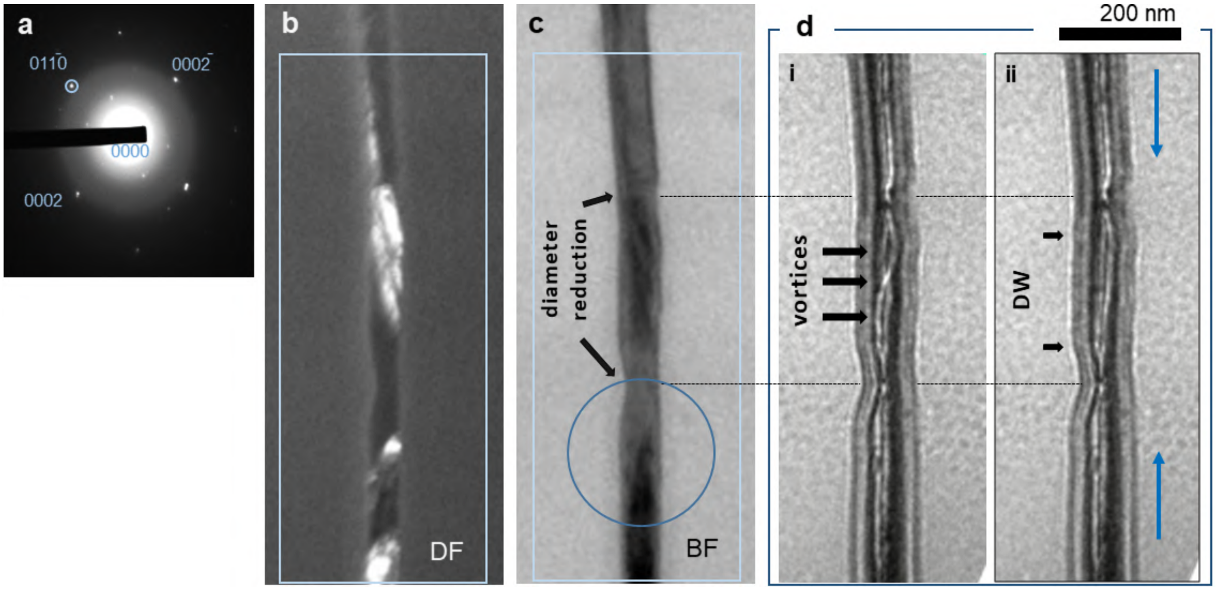

Figure 6.10: Overview of NW region for *in situ* electric pulse injection on a vortex state (**a**) DP of the selected area encircled in **c**. (**b**) dark-field image from the 01$\bar{1}$0 diffraction spot encircled in **a**. (**c**) BFTEM image of the region of interest. (**d**) Over-focused Fresnel images where i and ii show the switching process of the magnetic configuration from transverse vortex state (i) before pulse injection, to a curling state (ii) after pulse. The blue arrows in **d**(ii) indicate the curling domain directions, which are the same as in **d**(i).

I further wanted to study the nucleated DW presented above to see if it can be moved again by (re)injecting current and to check for possible DW pinning in the NW. This was done by sending pulses using the pulse generator settings # 2 and recording the change in the magnetic configuration by *in situ* over-focused Fresnel imaging. An overview of the results is presented in Figure 6.11. Each of the images displayed in Figure 6.11a were taken after successively injecting the same generated pulse (Setting # 2). In order to more easily see the DW while using a lower magnification (to get a larger field of view), the Fresnel images were acquired with a larger defocus than for the Fresnel images in Figure 6.10. One can, however, assume that it is the same type of DW, as the magnetization direction in the top domain versus the one in the lower domain remains the same, while the domain size changes, *i.e.* the domain walls move. The longitudinal vortex domain switching process is estimated to have a temporal length on the order of ns.[28] The images have been acquired using 10 frames per second recording, which is not fast enough to image any intermediate states, nor to estimate the speed of the domain wall motion. This is a limitation of the current experimental setup, meaning that increasing the acquisition frequency is a clear improvement point for further experiments.

Some qualitative observations can, however, be made from the gathered results: DW movements triggered by the pulse injection are evidenced, and it seems that the DWs are pinned in some specific positions. When marking the DW location in Figure 6.11a 1-8, it is clear that the DWs stop within the same region. The DFTEM image in Figure 6.11b shows these DW locations, marked by blue transparent circles, relative to the regions with $01\bar{1}0$ *hcp* diffraction contrast. There is a clear correspondence between the DW positions and the illuminated *hcp* grains, *i.e.*, we then assume the grain boundaries to act as pinning sites for the DW.

The DWs appear to be pinned within the same area of the NW, but almost alternately above/below the previous DW pinning. If one considers that the same DW is propagating in all the images, it would mean that the DW moves alternately in the positive and negative directions, although the same electron pulse polarity is injected. This is inconsistent from a magnetic point of view, as the DW movement is expected to be the result of spin-torque effect, or due to the generated Ørsted field. There will undoubtedly be some heating effects due to the considerable current density sent through the sample. We cannot disregard the possibility of the DW displacement being due to thermal effects, whose amplitude is unknown, combined with effects of the Ørsted field and spin-torque. However, the T_C of Ni is 628 K

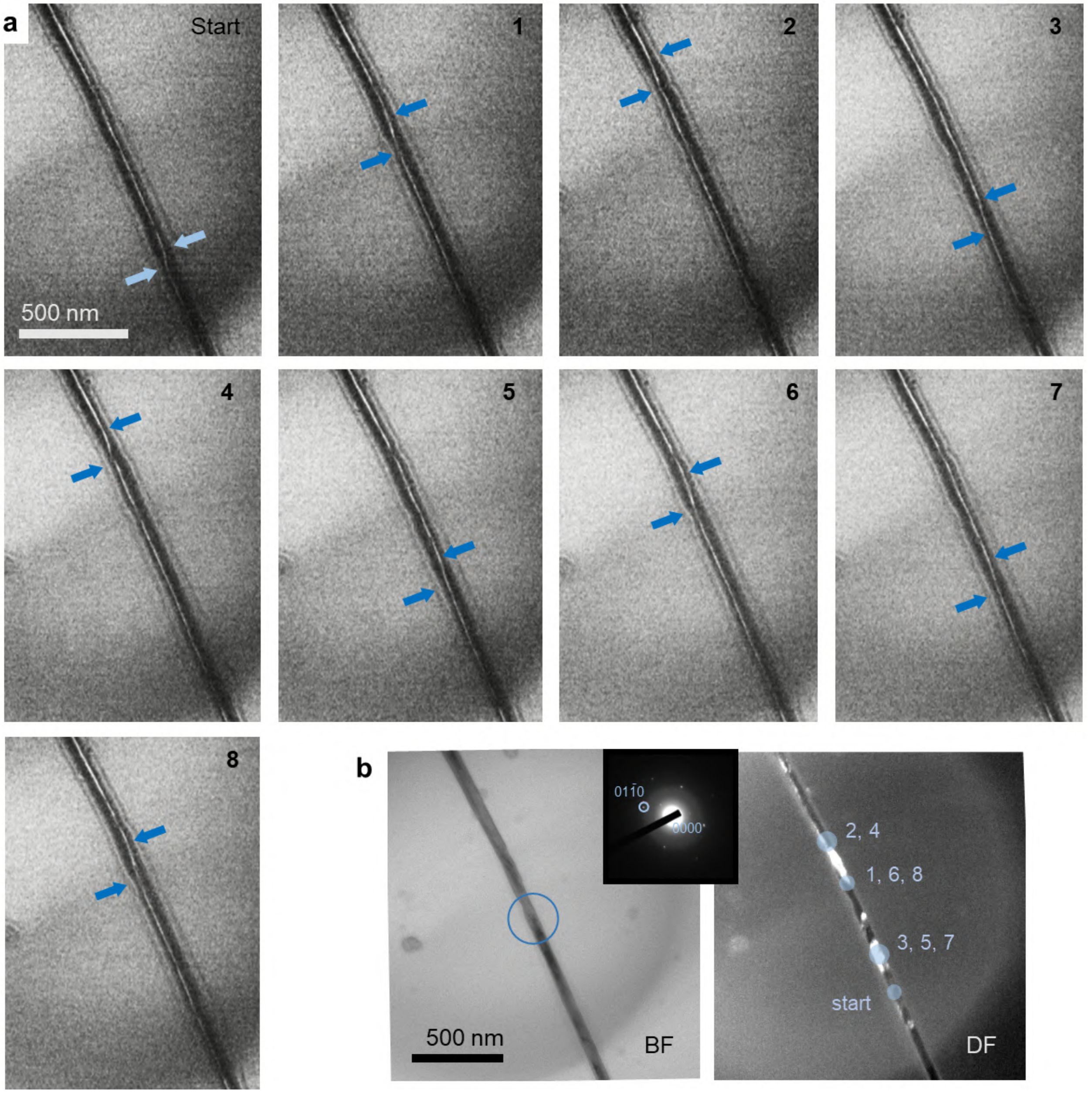

Figure 6.11: Overview of domain wall propagation through *in situ* electric pulse injection *in situ* sample(**a**) Over-focused Fresnel images showing the initial state and the relaxed states after eight consecutive pulse injections. The DW starts and end in each case is marked by blue arrows. (**b**) Shows the BFTEM and DFTEM image of the inspected NW region. The DFTEM image is formed using the diffraction spot marked in the DP (inset) made by SAED on the encircled region in the BFTEM image. The light-blue regions marked in the DFTEM image correspond to a DW position after the indicated pulses.

and Co has the highest Curie temperature of $T_{\text{C-Co}} = 1388$ K,[42] meaning that the T_C value for Co-rich CoNi is higher than the temperature that is likely to be reached due to the current pulse (without destroying the sample). It is also unlikely that the system would relax into the same "head-to-head" configuration, just with a displaced DW going alternately "up" or "down" in the NW, after cooling. We may also assume that the successive injection of the same pulse with the same shape and polarity induces the nucleation and displacement of a new DW outside of the field of view, which get pinned in at the same region after each pulse. However, the Fresnel images in Figure 6.11 show only a change in DW location, while the surrounding curling domain remains in a "head-to-head" configuration. The hypothesis of nucleation, propagation, and pinning of new DWs explanation would lead to an alternation between head-to-head and tail-to-tail DWs, which is not in line with our observations.

It is, therefore, impossible to make a conclusion based on the gathered data, as we are missing crucial physical parameters in order to understand what is going on. Hence, we need to improve and redo the experiment in order to get reliable quantitative information about the nature of the injected current. The electric chips and the electric contacts have to be improved and thoroughly characterized in order to determine the transmitted pulse reliably. Also, the current sample holder does not support ultra-high frequencies, which is a problem when we aim to inject pulses with nanosecond temporal length. Acquiring a suitable sample holder, as well as a generator powerful enough to create such short single pulses, while keeping an amplitude of at least 10 volts is therefore of high importance for the future development of this *in situ* biasing experiment. This preliminary study has, however, demonstrated that within the procedures I developed and the general setup, it is possible to contact a $\sim$7 μm long nanowire with 70 nm diameter for the purpose of performing *in situ* biasing experiments in the I2TEM.

6.3 Conclusion and outlook

This preliminary study has used *in situ* over-focused Fresnel imaging to study DW propagation in $Co_{85}Ni_{15}$ nanocrystalline NWs, either by the application of a magnetic field or an electric current pulse. By studying a transverse vortex chain under fields applied in various orientations and with different strengths, we have found that the transverse vortices can be moved by a 55 mT field applied parallel to the NW axis. Some transverse vortices could be propagated by the use of a weaker field (~ 35 mT), but the entire chain of vortices was found to propagate to the end of the *hcp* grain and get annihilated at ±55 mT. It is important to remember that the field was applied using the objective lens by tilting the sample to obtain a parallel component of the field, meaning that, simultaneously with the parallel magnetic field, the NW experiences a large perpendicular component of the field. It would therefore be interesting to perform an experiment with the field oriented perfectly parallel to the NW axis. Further, the chain was found to be reproducible when the application of a strong (saturation) magnetic field was oriented at the exact same orientation relative to both the NW axis and the *hcp* *c*-axis directions. The field should ideally be applied perfectly perpendicular to the NW axis and at the same time orthogonal to the *c*-axis for optimal chain nucleation, as a curling state will form instead of the chain if the field orientation deviates too much from this optimal direction.

Transverse vortex states were also moved by electric pulse injection. We have obtained some qualitative results showing changes in the magnetic configuration stimulated by the injection of single current pulses. However, several improvements to the experimental setup have to be made to get quantitative information on the DW displacement processes:

- First of all, the electric contacting chips have to be more reliable to ensure no short circuitry.
- Secondly, the electric contacting of the NW should be done using lithographic processes in order to get high-quality contacts with sufficiently low resistivity so that the measured response is characteristic of the NW and not due to the contacts themselves. Contacting by lithography also avoids sample contamination and incorporation of Ga when using FIBID. For the NWs studied in this work, we could have performed electron lithography. However, it would be an extremely time consuming process in order to shape the electrode size that this experiment demands. One way to reduce the time could be to combine electron and laser lithography. Another way is to increase the NW length (> 10 μm) to better suit the alignment accuracy and overall resolution of laser lithography.
- There is also a large potential for improvement of the image acquisition, both in terms of sensitivity and processing time. One can already improve the recorded frames per

second in the existing setup at the I2TEM by reducing the image resolution, achieving an acquisition time of down to a few milliseconds between frames. However, this is still not close enough to the ideal time scale of DW motion. CEMES is in the process of acquiring a new direct detection camera (DDE), which should be 10 times more sensitive and 10-100 times faster than the current camera (OneView) in the I2TEM. Such an improvement might not still be enough to catch DWs in motion, but it can perhaps detect some initial switching or relaxation processes.

- Another prospect for future experiments is to go from Fresnel imaging to electron holography, observing the DW dynamics.

While it might sound like many steps are left in order to gain quantitative information, these are all points that are feasible to overcome with some invested time (and money). In addition, I have obtained the first successfully contacted NW and moved a DW in two years while having started out with no experience or protocol. I, therefore, think that this will be a realistic goal in the near future.

References

[1] R. Hertel. “Ultrafast Domain Wall Dynamics in Magnetic Nanotubes and Nanowires”. In: *Journal of Physics: Condensed Matter* **28** (2016), p. 483002. DOI: 10.1088/0953-8984/28/48/483002.

[2] P. Fischer et al. “Launching a New Dimension with 3D Magnetic Nanostructures”. In: *APL Materials* **8** (2020), p. 010701. DOI: 10.1063/1.5134474.

[3] D. Sander et al. “The 2017 Magnetism Roadmap”. In: *Journal of Physics D: Applied Physics* **50** (2017), p. 363001. DOI: 10.1088/1361-6463/aa81a1.

[4] A. Hirohata et al. “Review on Spintronics: Principles and Device Applications”. In: *Journal of Magnetism and Magnetic Materials* **509** (2020), p. 166711. DOI: 10.1016/j.jmmm.2020.166711.

[5] A. Yamaguchi et al. “Real-Space Observation of Current-Driven Domain Wall Motion in Submicron Magnetic Wires”. In: *Physical Review Letters* **92** (2004), p. 077205. DOI: 10.1103/PhysRevLett.92.077205.

[6] L. Bocklage et al. “Dependence of Magnetic Domain-Wall Motion on a Fast Changing Current”. In: *Physical Review Letters* **103** (2009), p. 197204. DOI: 10.1103/PhysRevLett.103.197204.

[7] C. Burrowes et al. “Non-Adiabatic Spin-Torques in Narrow Magnetic Domain Walls”. In: *Nature Physics* **6** (2010), pp. 17–21. DOI: 10.1038/nphys1436.

[8] X. Z. Yu et al. “Skyrmion Flow near Room Temperature in an Ultralow Current Density”. In: *Nature Communications* **3** (2012), p. 988. DOI: 10.1038/ncomms1990.

[9] L. A. Rodríguez et al. "Optimized Cobalt Nanowires for Domain Wall Manipulation Imaged by in Situ Lorentz Microscopy". In: *Applied Physics Letters* **102** (2013), p. 022418. DOI: 10.1063/1.4776709.

[10] C. Phatak et al. "Visualization of the Magnetic Structure of Sculpted Three-Dimensional Cobalt Nanospirals". In: *Nano Letters* **14** (2014), pp. 759–764. DOI: 10.1021/nl404071u.

[11] Y. P. Ivanov et al. "Modulated Magnetic Nanowires for Controlling Domain Wall Motion: Toward 3D Magnetic Memories". In: *ACS Nano* **10** (2016), pp. 5326–5332. DOI: 10.1021/acsnano.6b01337.

[12] J. Pablo-Navarro et al. "Diameter Modulation of 3D Nanostructures in Focused Electron Beam Induced Deposition Using Local Electric Fields and Beam Defocus". In: *Nanotechnology* **30** (2019), p. 505302. DOI: 10.1088/1361-6528/ab423c.

[13] R. Hertel. "Curvature-Induced Magnetochirality". In: *SPIN* **3** (2013), p. 1340009. DOI: 10.1142/S2010324713400092.

[14] R. Streubel et al. "Magnetism in Curved Geometries". In: *Journal of Physics D: Applied Physics* **49** (2016), p. 363001. DOI: 10.1088/0022-3727/49/36/363001.

[15] M. Yan et al. "Beating the Walker Limit with Massless Domain Walls in Cylindrical Nanowires". In: *Physical Review Letters* **104** (2010), p. 057201. DOI: 10.1103/PhysRevLett.104.057201.

[16] J. U. Cho et al. "Control of Magnetic Anisotropy of Co Nanowires". In: *Journal of Magnetism and Magnetic Materials* **303** (2006), e281–e285. DOI: 10.1016/j.jmmm.2006.01.082.

[17] J. García et al. "Template-Assisted Co–Ni Alloys and Multisegmented Nanowires with Tuned Magnetic Anisotropy". In: *Physica Status Solidi (a)* **211** (2014), pp. 1041–1047. DOI: 10.1002/pssa.201300731.

[18] E. D. Barriga-Castro et al. "Pseudo-Monocrystalline Properties of Cylindrical Nanowires Confinedly Grown by Electrodeposition in Nanoporous Alumina Templates". In: *RSC Advances* **7** (2017), pp. 13817–13826. DOI: 10.1039/C7RA00691H.

[19] N. Biziere et al. "Imaging the Fine Structure of a Magnetic Domain Wall in a Ni Nanocylinder". In: *Nano Letters* **13** (2013), pp. 2053–2057. DOI: 10.1021/nl400317j.

[20] S. Da Col et al. "Observation of Bloch-Point Domain Walls in Cylindrical Magnetic Nanowires". In: *Physical Review B* **89** (2014), p. 180405. DOI: 10.1103/PhysRevB.89.180405.

[21] A. Fernández-Pacheco et al. "Three Dimensional Magnetic Nanowires Grown by Focused Electron-Beam Induced Deposition". In: *Scientific Reports* **3** (2013), p. 1492. DOI: 10.1038/srep01492.

[22] D. Reyes et al. "Magnetic Configurations in Co/Cu Multilayered Nanowires: Evidence of Structural and Magnetic Interplay". In: *Nano Letters* **16** (2016), pp. 1230–1236. DOI: 10.1021/acs.nanolett.5b04553.

[23] L. A. Rodríguez et al. "Quantitative Nanoscale Magnetic Study of Isolated Diameter-Modulated FeCoCu Nanowires." In: *ACS Nano* **10** (2016), pp. 9669–9678. DOI: 10.1021/acsnano.6b05496.

[24] C. Bran et al. "Direct Observation of Transverse and Vortex Metastable Magnetic Domains in Cylindrical Nanowires". In: *Physical Review B* **96** (2017), p. 125415. DOI: 10.1103/PhysRevB.96.125415.

[25] H. Forster et al. "Domain Wall Motion in Nanowires Using Moving Grids". In: *Journal of Applied Physics* **91** (2002), p. 6914. DOI: 10.1063/1.1452189.

[26] A. Thiaville et al. "Micromagnetic Understanding of Current-Driven Domain Wall Motion in Patterned Nanowires". In: *Europhysics Letters* **69** (2005), pp. 990–996. DOI: 10.1209/epl/i2004-10452-6.

[27] J. A. Fernandez-Roldan et al. "Electric Current and Field Control of Vortex Structures in Cylindrical Magnetic Nanowires". In: *Physical Review B* **102** (2020), p. 024421. DOI: 10.1103/PhysRevB.102.024421.

[28] M. Schöbitz et al. "Fast Domain Wall Motion Governed by Topology and Œrsted Fields in Cylindrical Magnetic Nanowires". In: *Physical Review Letters* **123** (2019), p. 217201. DOI: 10.1103/PhysRevLett.123.217201.

[29] M. Yan et al. "Fast Domain Wall Dynamics in Magnetic Nanotubes: Suppression of Walker Breakdown and Cherenkov-like Spin Wave Emission". In: *Applied Physics Letters* **99** (2011), p. 122505. DOI: 10.1063/1.3643037.

[30] W. Y. Lee et al. “Domain Nucleation Processes in Mesoscopic Ni80Fe20 Wire Junctions”. In: *Journal of Applied Physics* **87** (2000), pp. 3032–3036. DOI: 10.1063/1.372295.

[31] R. Hertel. “Computational Micromagnetism of Magnetization Processes in Nickel Nanowires”. In: *Journal of Magnetism and Magnetic Materials* **249** (2002), pp. 251–256. DOI: 10.1016/S0304-8853(02)00539-5.

[32] E. Berganza et al. “Domain Wall Pinning in FeCoCu Bamboo-like Nanowires”. In: *Scientific Reports* **6** (2016), p. 29702. DOI: 10.1038/srep29702.

[33] I. M. Andersen et al. “Exotic Transverse-Vortex Magnetic Configurations in CoNi Nanowires”. In: *ACS Nano* **14** (2020), pp. 1399–1405. DOI: 10.1021/acsnano.9b07448.

[34] I. M. Miron et al. “Fast Current-Induced Domain-Wall Motion Controlled by the Rashba Effect”. In: *Nature Materials* **10** (2011), pp. 419–423. DOI: 10.1038/nmat3020.

[35] J. F. Einsle et al. “In Situ Electron Holography of the Dynamic Magnetic Field Emanating from a Hard-Disk Drive Writer”. In: *Nano Research* **8** (2015), pp. 1241–1249. DOI: 10.1007/s12274-014-0610-0.

[36] L. F. Thompson. “An Introduction to Lithography”. In: *Introduction to Microlithography.* Ed. by L. F. Thompson, C. G. Willson, and M. J. Bowden. AMERICAN CHEMICAL SOCIETY, 1983. Chap. 1, pp. 1–13. DOI: 10.1021/bk-1983-0219.ch001.

[37] L. Lü, J. Y. H. Fuh, and Y. S. Wong. “Fundamentals of Laser-Lithography Processes”. In: *Laser-Induced Materials and Processes for Rapid Prototyping.* Ed. by L. Lü, J. Y. H. Fuh, and Y. S. Wong. Springer, 2001. Chap. 2, pp. 9–38. DOI: 10.1007/978-1-4615-1469-5_2.

[38] W. W. Smeltzer. “Oxidation of Nickel-Cobalt Alloys in the Range of Curie Temperatures”. In: *Acta Metallurgica* **7** (1959), pp. 191–198. DOI: 10.1016/0001-6160(59)90073-2.

[39] W. C. Uhlig et al. “Direct Imaging of Current-Driven Domain Walls in Ferromagnetic Nanostripes”. In: *Journal of Applied Physics* **105** (2009), p. 103902. DOI: 10.1063/1.3125526.

[40] R. Shimotsu, D. Wang, and T. Namihira. “Performance of a Low Impedance Nanosecond Pulse Generator”. In: *IEEE 21st International Conference on Pulsed Power (PPC)* (2017), pp. 1–4. DOI: 10.1109/PPC.2017.8291299.

[41] E. Berganza Eguiarte et al. “Multisegmented Nanowires: A Step towards the Control of the Domain Wall Configuration”. In: *Scientific Reports* **7** (2017), p. 11576. DOI: 10.1038/s41598-017-11902-w.

[42] J. M. D. Coey. *Magnetism and Magnetic Materials*. Cambridge University Press, 2010. DOI: 10.1017/CBO9780511845000.

Chapter 7

General conclusion and future prospects

This thesis aims to exploit the high spatial resolution and range of techniques possible in the TEM to perform a detailed local magnetic characterization of Co_{85}Ni15 NWs. Both 2D and 3D electron holographic techniques were employed to present a deep quantitative analysis of the magnetic configurations, combined with structural and spectroscopic techniques to draw a wholesome understanding of the sample. This chapter will present a conclusion of the thesis and offer an outlook on possible further research.

7.1 Relation between magnetic configuration, composition and crystal structure

The first study of the Co-rich CoNi NW sample was concerned with understanding the local magnetic configuration and its origin. The remnant states of the sample NWs were, therefore, studied by the use of EH, revealing a complex magnetic configuration with large local variations. Complimentary structural and spectroscopic mapping was performed on the same region as for the magnetic imaging, revealing a textured grain structure consisting of both *fcc* and *hcp* phases. By correlating the results from the different techniques, we found small modulations in the composition and that the changes in magnetic configurations were linked to local variations in the crystal structure. Three different magnetic configurations were identified in the sample: a chain of transverse vortex states, a curling state, and a transitional configuration between the two aforementioned states. The correlative study shows that the chain of transverse vortex states is located in a region with a *hcp* crystal phase with its magnetocrystalline easy axis (c-axis) oriented close to perpendicular with respect to the NW axis. In contrast, while the curling or transitional states were found in regions with *hcp* and *fcc* phases coexisting in the same cross-sectional region. Micromagnetic simulations confirmed the stabilization of the vortex chain, as well as a longitudinal vortex state in a perfect monocrystalline *hcp* phase NW segment, and that a pure *fcc* phase only results in a parallel orientation of the magnetic spins along the wire axis.

The transverse vortex chain had a good correspondence between the experimental results and simulations, enabling the quantification of the magnetic parameters of the NW. The inter-core distance of the vortices in the chain was found, by micromagnetic OOMMF simulations, to partially vary with the saturation magnetization, and thus acted as a good confirmation on its value. While the existence of a curling state in the NW was not completely understood from this study, the phase image and reduction in measured phase shift across the wire axis of the longitudinal vortex state found in parts of the *hcp* segment in the simulations resemble the characteristics of what we have called a curling state. This, therefore, strengthens our hypothesis, but further studies were needed to conclude.

While a lot was revealed about the magnetic configurations in the sample and how it was tied to inhomogeneities in the crystal structure, the study left us with some unanswered questions, especially regarding the existence and nature of the so-called curling domain. In many ways, the fact that the magnetic imaging only gave us one projection as well as an integration of the magnetic contribution along the beam direction seemed to be the most limiting factor for us to understand this system, as it had proven to be very three-dimensional in its spin texture. This was solved by conducting a follow-up study using holographic VFET for 3D reconstruction of the magnetic induction, as will be presented next. However, there is another aspect of this experiment that could also be improved, and that is the spectroscopic and structural mapping. Again, there is the aspect of only getting a 2D representation of a 3D structure. The use of a tomographic mapping technique combined with ASTAR and EELS or EDX could provide even further insight, as our results have suggested that several grains, even with different crystal structures (*fcc* and *hcp*) can coexist within the same cross-section of the NW.

7.2 Three-dimensional magnetic imaging and field-tunable states

As a continuation of the previous study, we wanted to perform 3D magnetic imaging on the CoNi NW system in order to characterize and understand the spin texture in all three dimensions. We also wanted to understand when the observed chain of transverse vortices occurs and test the effect of magnetic history by imaging the remnant state at the *hcp* grain after the application of two different saturation fields: (i) perpendicular and (ii) parallel to the wire axis. The magnetic imaging was done using holographic VFET, which enabled us to retrieve all three components of the magnetic induction in the NW sample, revealing completely different magnetic configurations for the two cases. In the case of a magnetic field applied perpendicular to the NW axis, we observed a transverse vortex chain, while the parallel saturation leads to a configuration consisting of longitudinal vortex domains separated by transverse domain walls. The latter is believed to be the type of magnetic configuration that is called curling domain in Chapter 4.

The results from the 3D holography experiments, correlated with micromagnetic simulations, confirm the conclusions of the previous study (Ch.4) as well as offer new insight and details about the magnetic spin configuration of each of the states. For the vortex chain, we learn that vortex cores are all pointing in the same positive z-direction that is pointed both perpendicular to the wire axis and orthogonal to the *hcp* c-axis, which is the same direction as the applied saturation field. However, the measured B_z component is relatively weak compared to the in-plane components (B_x and B_y). The transverse vortex chain can be viewed as a series of transverse domains with their magnetization alternately pointing in positive and negative y-direction, making the transverse vortex states the DWs. Accordingly, the system is like a double Halbach array, where the existence of the vortices acts to reduce the stray field outside of the NW. Regarding the longitudinal magnetic configuration, the curling domains (longitudinal vortices) all point in the same positive x-direction, *i.e.* the direction of the applied magnetic field. However, their magnetization rotates around the wire axis with opposite helicity. This behavior, and the existence of a transverse DW, has been confirmed by micromagnetic simulations.

Although this study was performed using state-of-the-art holographic VFET instrumentation, we did not manage to resolve all the vortex cores from the chain. However, we are currently at the limit of how much more we can get out of this technique due to its already complex setup, as well as aspects like the wedge loss effect, which is a common issue among tomographic techniques. One way of getting around this could be to perform detailed simulations of a transverse vortex and render simulated phase images from different projections and compare them to experimental magnetic phase images gathered by EH for the same orientations. While this method is less ideal than the thought of being able to perform tomographic holography of a single transverse vortex state, it would give the sufficient resolution needed to resolve a small vortex core. It could also be interesting to try combining the state-of-the-art technique of holographic VFET with the costume made interferometric microscope the I2TEM, and its newly added stabilization software (Section 3.3.4), which could potentially improve the final spatial resolution of the reconstructed tomograms. In terms of exploring the potential of these magnetic configurations for applications in future spintronic devices, a natural next step would be to perform experiments to characterize their stability and DW dynamics *in situ* under the application of external fields and electric currents. As presented in the following, some first attempts on such a study have been performed in this thesis work. However, there is much room for improvements and future studies that should be performed to build on this, as will be elaborated on in the following section.

7.3 Magnetic manipulation by external application of magnetic field and electric current

Finally, a preliminary study concerning the change of the characterized magnetic configurations in the CoNi NWs when subject to an externally applied magnetic field or an electric current has been presented. This work had a twofold purpose:

- From a physics point of view, the objective was to test the stability, reproducibility, and displacement of the observed DWs and magnetic configurations formed in the NWs.
- As a second goal, I wanted to develop an experimental method and protocol for performing *in situ* biasing experiments on contacted NWs in the I2TEM, as this was not yet established in our laboratory.

Although there are still many improvements to make on this last point, I have presented an experimental development that managed to inject a detectable change of the magnetic configuration in the contacted NW. I have, therefore, performed two types of *in situ* Fresnel imaging experiments in the I2TEM: by applying an external magnetic field and injecting an electric pulse.

For the magnetic field *in situ* experiments, I tested the stability and reproducibility of a vortex chain by orienting the field either along the NW axis or perpendicular to it with different angles. The vortex chain was annihilated when applying a parallel magnetic field component of around 55 mT. In addition, the vortex chain was consistently reproduced when a saturation field was applied perpendicular to the wire axis at zero tilt, while it for different projections (±15° tilt around the wire axis) only stabilized a reduced vortex chain, or no chain at all (curling domain). This evidences the existence of an ideal orientation of the magnetic field relative to the NW that is believed to be linked to the orientation of the *hcp* grain where the vortex chain forms, where the applied field should be perpendicular to the wire axis, as well as orthogonal to the magnetocrystalline easy axis (c-axis). Further, both a small vortex chain and a head-to-head domain wall between two curling states were manipulated by injecting an electric pulse using the presented *in situ* biasing experimental setup. The presence of DW pinning at crystal grain interfaces was also observed.

While only qualitative results came out from the observed changes in magnetic configuration triggered by the pulse injection, there are plenty of solutions presented to improve the sample and the experimental setup to work towards getting quantitative measurements to accompany the magnetic observations in future experiments. The electronic chips should be improved and fully characterized prior to experiments, as well as the NW contacting should be upgraded to low resistivity lithographically made gold contacts for reliable electronic measurements. The current system is also believed to be limited by the bandwidth of sample holder and slow data recording, making us unable to, respectively, send nanosecond pulses and image magnetic switching or relaxation processes before and after DW movement. These are all points that should be improved for conducting future experiments. While there are many improvements to be made in order to reach an ideal *in situ* setup for performing DW displacement measurements, there are concrete solutions to all of the existing problems, and so I am confident that we will reach the goal, given the required time and money to realize the needed upgrades, many of which are already in the process. Among the improvement steps that have already been initiated, there is the production of new reliable chips with electron transparent membranes, the installment of in-chamber argon milling step before gold sputtering for in-house lithography contacting, the process of ordering a direct detection camera which is more sensitive and faster than the existing one, and ongoing discussions of acquiring a high-frequency biasing sample holder.

The work presented in this thesis is an example of the flexibility and diversity of the TEM and how a variety of techniques can be used to get local and detailed information about the properties of a nanostructure and its magnetic configurations through correlated studies, both in 2D and 3D.

7.4 Prospects

The interesting, tuneable magnetic configurations found to stabilize in *hcp* phase regions are a motivation to develop perfectly monocrystalline *hcp* NWs with the *c*-axis perpendicular to the wire axis. Such a structure would enable long vortex chains to stretch across most of the wire and propagate without being annihilated due to change in the crystal phase.

The optimal NW would ideally have a uniform cylindrical cross-section and a wire length of at least 10 μm for easy contacting. To produce such ideal NWs, it would be necessary to conduct a study for optimizing the NW growth.

In addition, it would be interesting if the vortex chain length in such a uniform *hcp* NW can be varied and controlled using a local magnetic field with a defined area. Based on the knowledge that vortex states only stabilize when applying a magnetic field orthogonal to the NW axis and the *c*-axis, one could potentially use differently angled magnetic writing heads to either form vortices or annihilate them (form a curling state) depending on the field orientation. In addition, if one can find a way to controllably switch the vortex direction or rotation, perhaps by applying positive or negative fields, they could potentially be used as memory bits for solid-state devices, with three read/write states (up, down, curling). If one, also, can achieve a stable and controlled propagation of the states by current injection, this structure would be of great impact for new novel Spintronic devices based on the race track memory.[1] From a practical point of view, such a complex experiment would not only need reliable quantitative measurements, but also the integration of contacted electromagnetic writing heads. This would require additional sample preparation procedures of lithographic processes, and the knowledge to produce writing heads of small scale and high quality.[2]

Further, there is also the analogy of the vortex chain being viewed as a double Halbach array. From this, one can speculate if an electric current could induce an oscillation when passing through the vortex chain configuration, like for permanent magnet undulators.[3] This could potentially produce radiation with wavelength depending on the vortex chain periodicity,[4] like for free-electron lasers, which would be very interesting for application in communication devices. Such an experiment can be performed using radiation detection measurements on a contacted NW.

The proposed, highly advanced experiments would need the combined knowledge and expertise from several disciplinary fields within nanotechnology, including advanced micro- and nanofabrication (NW growth, electric contacting, making of magnetic writing heads), static and dynamic nanomagnetism, sensitive magnetic imaging, and measurement techniques, and technical knowledge about electromagnetic devices and reading heads. As few laboratories specialize in all of these fields, this project could be realized by close collaboration between different research facilities. These prospects show the remaining potential that this NW structure holds for exciting new research that could have a significant impact on the development of future solid-state devices.

References

[1] S. S. P. Parkin, M. Hayashi, and L. Thomas. “Magnetic Domain-Wall Racetrack Memory”. In: *Science* **320** (2008), pp. 190–194. DOI: 10.1126/science.1145799.

[2] J. F. Einsle et al. “In Situ Electron Holography of the Dynamic Magnetic Field Emanating from a Hard-Disk Drive Writer”. In: *Nano Research* **8** (2015), pp. 1241–1249. DOI: 10.1007/s12274-014-0610-0.

[3] J. B. Majernik N.; Rosenzweig. “Halbach Undulators Using Right Triangular Magnets”. In: *Physical Review Accelerators and Beams* **22** (2019), p. 092401. DOI: 10.1103/PhysRevAccelBeams.22.092401.

[4] J. Bahrdt. “Shaping Photon Beams with Undulators and Wigglers”. In: *Synchrotron Light Sources and Free-Electron Lasers: Accelerator Physics, Instrumentation and Science Applications.* Ed. by E. J. Jaeschke et al. 1st ed. Springer, 2020. Chap. 16, pp. 851–933. ISBN: 978-3-030-23201-6.

Résumé étendu de la Thése

Cartographies 2D et 3D de configurations magnétiques de nanofils de CoNi

Directeurs de thèse: Dr. Etienne Snoeck (CEMES - CNRS)
Dr. Christophe Gatel (CEMES - CNRS)

Objectifs et plan de la thèse

L'objectif de cette thèse est de présenter une analyse qualitative et quantitative approfondie des configurations magnétiques locales dans des CoNi nanofil cylindriques riches en CoNi avec une anisotropie magnétocristalline perpendiculaire en utilisant les techniques d'imagerie magnétique MET de pointe, principalement axées sur l'holographie électronique (HE) bidimensionnel (2D) et tridimensionnel (3D). Afin d'assurer une compréhension complète de la nanostructure et de révéler l'origine de la texture du spin magnétique observée, les études présentées combinent la cartographie structurale, spectroscopique et magnétique sur des nanostructures individuelles pour obtenir des résultats quantitatifs corrélatifs, révélant les effets des changements locaux de la structure cristalline sur les configurations magnétiques observées. L'état résiduel a été étudié après l'application d'un champ de saturation magnétique externe avec différentes orientations par rapport à l'axe du fil. La nature 3D complexe de la texture du spin magnétique a été découverte à l'aide d'un tomographie holographique de champ vectoriel (THCV) de pointe et comparée qualitativement et quantitativement à des simulations micromagnétiques complémentaires.

Après la introduction (**Chap. 1**) qui situe le contexte général et donne les objectifs du travail, un chapitre (**Chap. 2**) donne un aperçu des concepts de base du magnétisme, couvrant l'origine du magnétisme à l'échelle atomique et une introduction aux énergies micromagnétiques et à la formation des domaines magnétiques. Ensuite, un chapitre (**Chap. 3**) détaille les outils expérimentaux utilisés au cours de cette thèse. La suite du manuscrit est ensuite organisé en quatre chapitres comme suit :

Chap. 4 présente des études quantitatives des configurations magnétiques complexes dans les nanofils cylindriques de $Co_{85}Ni_{15}$. Les fines modifications structurelles des états magnétiques sont étudiées par holographie électronique et corrélées avec des mesures de structure et de composition pour révéler l'origine de la texture magnétique exotique observée.

Chap. 5 explore le changement de l'état magnétique résiduel des nanofils de CoNi, avec une anisotropie magnétocristalline orientée en phase *hcp* et transversale, après l'application d'un champ de saturation (i) perpendiculaire et (ii) parallèle à l'axe du fil. Dans le prolongement des recherches présentées dans Chap. 4, cette étude révèle les trois composantes de l'induction magnétique enregistrées par l'utilisation de la tomographie électronique à champ vectoriel holographique et permet de mieux comprendre et caractériser les parois des domaines magnétiques dans les nanotextures magnétiques 3D.

Chap. 6 présente les résultats préliminaires des observations d'imagerie de Fresnel en appliquant un champ magnétique et en injectant un courant électrique, respectivement, afin d'étudier *in situ* la stabilité, la reproductibilité et la manipulation de la configuration magnétique dans un CoNi nanofil. Le chapitre décrit également un protocole pour réaliser une expérience de polarisation *in situ* dans le but d'étudier le mouvement de la paroi du domaine magnétique dans les nanofils par injection d'impulsions électriques dans l'I2TEM. L'accent est mis sur les défis et les conditions nécessaires pour réussir à injecter du courant dans ces nanofils. De plus, de futurs travaux sont suggérés dans le but de réaliser des mesures électriques quantitatives combinées à l'imagerie holographique électronique des structures des parois des domaines.

Enfin, **Chap. 7** donne un résumé de cette thèse ainsi que ses principales conclusions, et offre un aperçu des travaux futurs qui peuvent être réalisés dans le prolongement des résultats présentés.

Chap. 3 : Techniques expérimentales

L'imagerie magnétique dans un MET

La possibilité d'étudier l'ordre magnétique dans les matériaux, ainsi que l'amélioration du temps de calcul pour les simulations micromagnétiques, ont contribué de manière significative à la compréhension des phénomènes magnétiques qui a conduit aux dernières applications technologiques dans le domaine du nanomagnétisme et de la spintronique. Pour cartographier quantitativement les propriétés magnétiques des nano-objets à l'échelle du nanomètre, il faut des techniques capables de sonder les propriétés magnétiques avec une résolution spatiale et une sensibilité élevées. Chacune des techniques d'imagerie magnétique a ses avantages et ses limites, et elles offrent un large éventail de possibilités pour étudier différents phénomènes magnétiques dans divers dispositifs expérimentaux. Une combinaison de techniques, associée à l'ajout de simulations micromagnétiques, est généralement nécessaire pour une analyse complète des domaines magnétiques et de leurs configurations dans un nanofil.

Un microscope électronique à transmission (MET) offre une haute résolution spatiale et peut accueillir une grande variété de techniques, avec une gamme couvrant la diffraction, l'imagerie, la spectroscopie et l'holographie.[1] Cela en fait un instrument intéressant pour combiner différentes techniques de caractérisation afin d'analyser les nanostructures et leurs propriétés. Les inconvénients du MET sont le besoin d'échantillons transparents aux électrons (idéalement d'une épaisseur < 100 nm) et le fait que les expériences sont réalisées sous vide

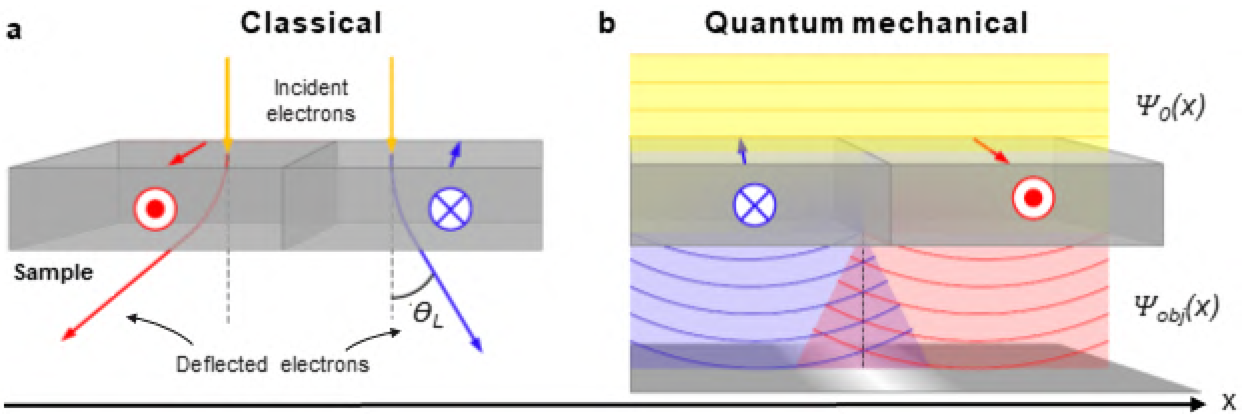

Figure 7.1: Illustration de la déviation du faisceau d'électrons (**a**) due à la force de Lorentz et (**b**) d'après une description de la mécanique quantique, entraînant un chevauchement des deux faisceaux provenant de domaines différents et donnant lieu à des franges d'interférence. Les flèches rouges et bleues de l'échantillon représentent la direction de l'aimantation.^{2}

poussé dans un espace limité entre les pièces polaires de la lentille de l'objectif. Les processus de préparation des échantillons peuvent donc être compliqués. Une formation spéciale et une connaissance des modes de fonctionnement du MET ainsi que des propriétés physiques des interactions électron-matière sont cruciales pour l'utiliser de manière ciblée et pour analyser les informations obtenues à partir des mesures. Cependant, les avantages et les possibilités du MET et sa grande variété de techniques sont les principaux attraits.

Microscopie de Lorentz D'un point de vue classique, *la Microscopie de Lorentz* (ML) est basé sur la force de Lorentz. La force de Lorentz ($\mathbf{F}_L$) est ressentie par la propagation des électrons dans un champ magnétique $\mathbf{B}$, et est exprimée par l'équation suivante :

$$\mathbf{F}_L = \text{-}e\mathbf{v} \times \mathbf{B}, \tag{7.1}$$

où $\mathbf{v}$ est la vitesse de l'électron. Pour les électrons se déplaçant le long de l'axe optique d'un MET (axe z), le produit vectoriel $\mathbf{v} \times \mathbf{B}$ en Equation 7.1 implique une déviation induite de la trajectoire de l'électron, qui ne dépend que des composantes d'induction magnétique perpendiculaires à l'axe optique, *i.e*, B_x et B_y, comme illustré dans Figure 7.1a.

Le processus peut également être décrit d'un point de vue de la mécanique quantique en considérant le faisceau d'électrons comme une onde. Dans cette approche, la force de Lorentz

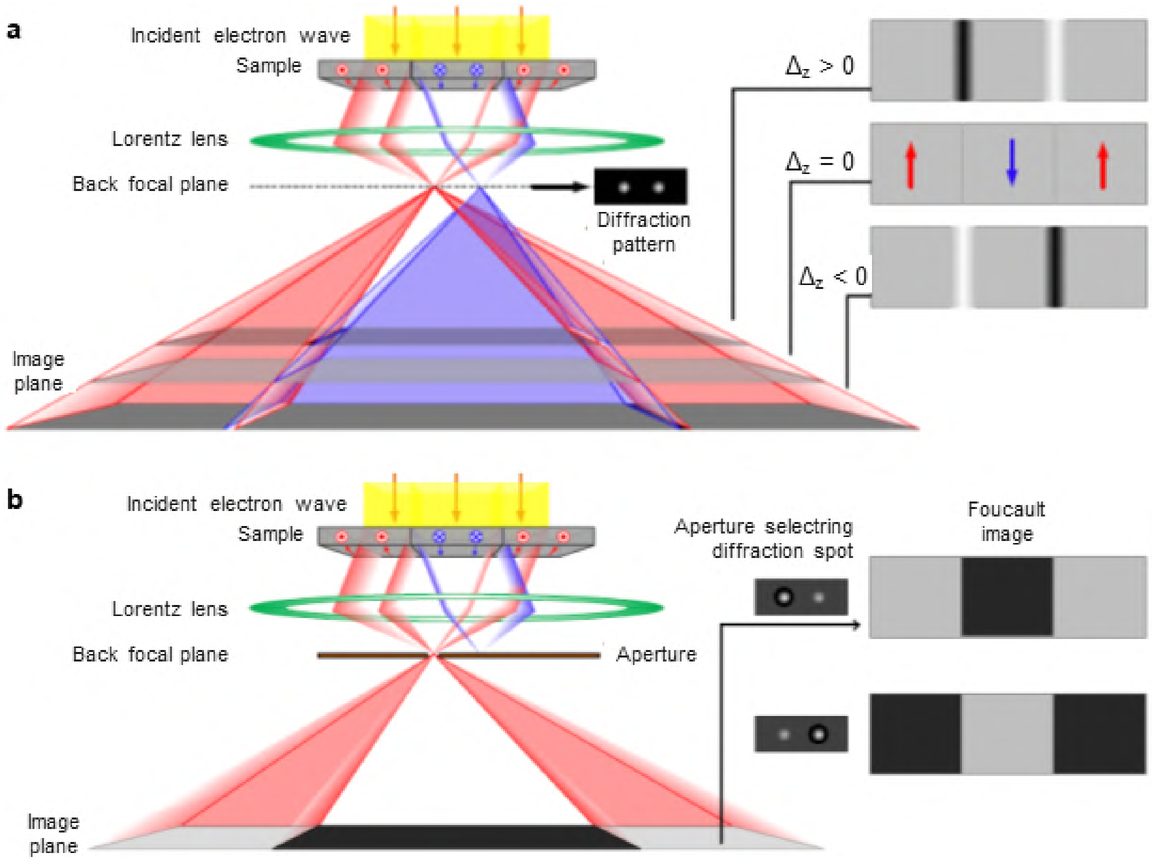

Figure 7.2: Illustration des deux modes d'imagerie de la microscopie de Lorentz : (**a**) le mode Fresnel et (**b**) le mode Foucault. Les flèches rouges et bleues de l'échantillon représentent la direction de l'aimantation.[2]

peut être décrite comme un déphasage de l'onde électronique. Ceci est illustré sur la Figure 7.1b. L'induction magnétique est alors représentée par le potentiel vectoriel magnétique à l'intérieur de l'échantillon, **A**, qui induit un déphasage sur les électrons diffusés, exprimé comme[3] :

$$\phi_M(x,y) = -\frac{\pi\gamma}{\lambda U^*}\frac{e}{\hbar}\int A_z(\mathbf{r})dz. \tag{7.2}$$

Au foyer, le processus de formation de l'image en ML est similaire à celui du MET conventionnel. Cependant, tout comme pour le processus de diffusion des électrons dû aux diffractions de Bragg sur le réseau cristallin, la diffusion due aux différentes déviations du faisceau induites par la nature magnétique de l'échantillon, créera un motif de diffraction dans le plan focal arrière de la lentille de Lorentz. En dehors des aberrations, principalement sphériques, de la lentille de Lorentz, l'intensité de l'image dans le plan image ne portera que des informations sur l'amplitude, et non sur les changements dus aux déphasages. L'information magnétique de l'échantillon ne peut donc être obtenue par ML qu'en modifiant la fonction de transfert du microscope. Il y a deux manières principales de le faire : en défocalisant l'image (*mode Fresnel*), ou en utilisant une ouverture pour sélectionner un des faisceaux déviés dans le plan focal arrière de la lentille de Lorentz (*mode Foucault*). Figure 7.2[3,4] montre des schémas illustrant les deux modes d'imagerie de Lorentz.

Le mode Fresnel (mode défocus) est le plus utilisé, et c'est également la technique utilisée dans ce travail. Ce mode offre une observation directe du contraste magnétique dû aux parois des domaines magnétiques dans l'échantillon, juste en sous-focalisant la lentille de Lorentz, pour imager un plan au-dessus du plan de l'échantillon, ou en sur-focalisant, pour imager un plan en dessous du plan de l'échantillon (Figure 7.2a).

Holographie électronique Lorsqu'une onde électronique interagit avec un matériau, son amplitude et sa phase changent. Dans le MET classique, l'information de phase est perdue et seule la distribution spatiale de l'intensité (le carré de l'amplitude) de l'onde électronique est enregistrée. Par conséquence, les informations sur le déphasage du faisceau d'électrons par rapport aux champs électromagnétiques dus à l'effet Aharonov-Bohm sont perdues. *L'Holographie électronique* (HE) est une technique d'imagerie puissante qui permet d'accéder au déphasage de l'onde électronique résultant de l'interaction avec un échantillon.[5,6] Nous pouvons ainsi récupérer des informations sur les variations locales de l'induction magnétique et du potentiel électrostatique à l'intérieur et autour de l'échantillon. De nos jours, il existe plusieurs types d'holographie électronique avec différentes configurations de microscopie qui ont été réalisées,

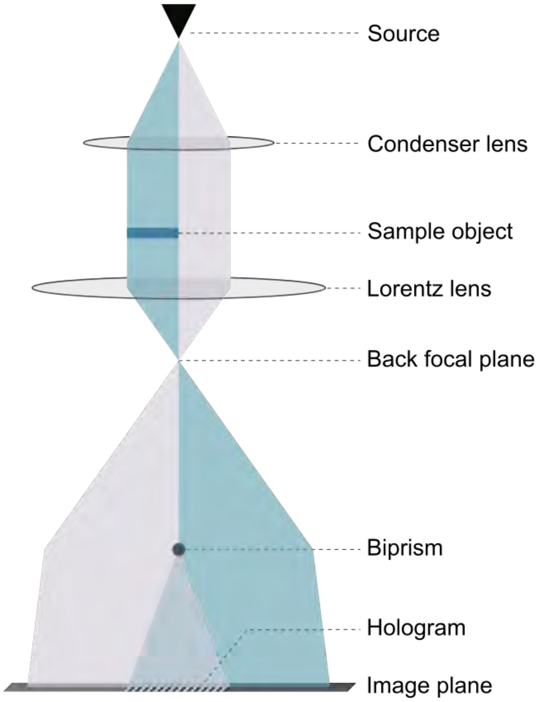

Figure 7.3: Installation principale du TEM pour l'holographie électronique hors axe

et d'autres encore sont théoriquement possibles.[5,7,8] Cependant, une configuration, appelée *holographie électronique hors axe*, a plus ou moins remplacé la configuration en ligne, car elle ne souffre pas d'une "image jumelle conjuguée" qui peut causer des perturbations dans l'image reconstruite lorsqu'on utilise l'holographie en ligne.[9] C'est ce type d'holographie qui a été utilisé dans ce travail, et il sera donc détaillé dans les sections suivantes.

L'holographie électronique hors axe est une technique d'imagerie interférométrique dans laquelle une partie d'une onde électronique hautement cohérente, appelée "onde objet", traverse l'objet échantillon, interagissant avec les champs électromagnétiques de l'échantillon et de son environnement. La deuxième partie de l'onde électronique, appelée *onde de référence*, traverse une zone uniforme de l'échantillon, idéalement le vide ou un film de carbone ultrafin et uniforme, et n'interagit donc avec aucun champ électromagnétique de l'échantillon. Ces deux ondes sont ensuite déviées par un biprisme de Möllenstedt, ce qui provoque une interférence entre les deux ondes. Une illustration de la configuration de l'holographie électronique hors axe est présentée sur la Figure 7.3. Le modèle d'interférence résultant, appelé *hologramme*, consiste à la fois en une image d'intensité, qui dépend principalement de l'amplitude de l'onde de l'objet (comme dans le MET en champ clair)[6] et en franges d'interférence, avec des variations et des décalages de périodicité locale dus à la différence de phase relative de l'onde de l'objet et de l'onde de référence induite par les champs électrostatiques et magnétiques locaux de l'échantillon. En analysant ces variations de franges locales, on peut extraire les déphasages et, ainsi, cartographier les champs électriques et magnétiques locaux.

L'onde électronique subit un déphasage ($\phi(x,y)$) en raison de son interaction avec le potentiel électromagnétique de l'objet échantillon, avec des contributions du potentiel électrostatique ($\phi_E(x,y)$) et des composantes dans le plan du champ magnétique de l'échantillon ($\phi_M(x,y)$), où le déphasage total peut être exprimé comme suit :

$$\phi(x,y) = \phi_E(x,y) + \phi_M(x,y) \tag{7.3}$$

En utilisant l'équation d'Aharanov-Bohm, les composantes dans le plan intégrées le long de la direction du faisceau d'électrons (direction z) peuvent être calculées par la fonction dérivée des déphasages respectifs. Les composantes dans le plan de l'induction magnétique sont exprimées par :

$$\frac{\delta \phi_M(x,y)}{\delta x} = \frac{e}{\hbar} \int B_y(x,y,z) dz, \; \frac{\delta \phi_M(x,y)}{\delta y} = -\frac{e}{\hbar} \int B_x(x,y,z) dz \tag{7.4}$$

Des informations quantitatives sur les propriétés magnétiques de l'échantillon peuvent ainsi être obtenues en séparant les contributions électrostatique et magnétique au déphasage. Il existe plusieurs façons de procéder à titre expérimental, la technique la plus couramment utilisée consistant à enregistrer deux images holographiques, dont l'une est prise après avoir retourné l'échantillon. Cette méthode a été proposée pour la première fois par Tonomura et al. en considérant le "fonctionnement à l'envers du faisceau électronique".[10] En retournant l'échantillon (retourné à 180°), la contribution électrostatique reste constante mais la contribution magnétique change de signe. La contribution magnétique peut donc être obtenue en évaluant la différence des images de phase des deux hologrammes divisée par deux.

Tomographie électronique à champ vectoriel holographique Une des limites de l'HE est que nous n'enregistrons que la projection des composantes dans le plan de l'induction magnétique. En imaginant un NO, nous obtenons donc une projection 2D d'un objet avec une distribution 3D de l'induction magnétique interne et externe. *La tomographie électronique à champ vectoriel holographique* (THCV) combine la technique de l'holographie électronique hors axe avec la tomographie électronique pour fournir une reconstruction 3D des potentiels électrostatiques et magnétiques dans les trois directions cartésiennes[8] avec une résolution spatiale allant jusqu'à quelques nanomètres.[11] L'un des avantages de pouvoir reconstruire une carte 3D du potentiel électrostatique de l'échantillon est qu'elle donne un aperçu de la morphologie 3D réelle de la région imagée grâce au rendu iso-surface du potentiel 3D. Cela peut améliorer considérablement toute simulation micromagnétique effectuée pour compléter l'étude expérimentale, car cela resserrera l'écart entre les objets analysés expérimentalement et les objets simulés.

Le THCV holographique a été développé par le Dr. D. Wolf et le Dr. A. Lubk de l'Institut Leibniz de Dresde. Le principe de THCV, parfois appelé tomographie holographique élec-

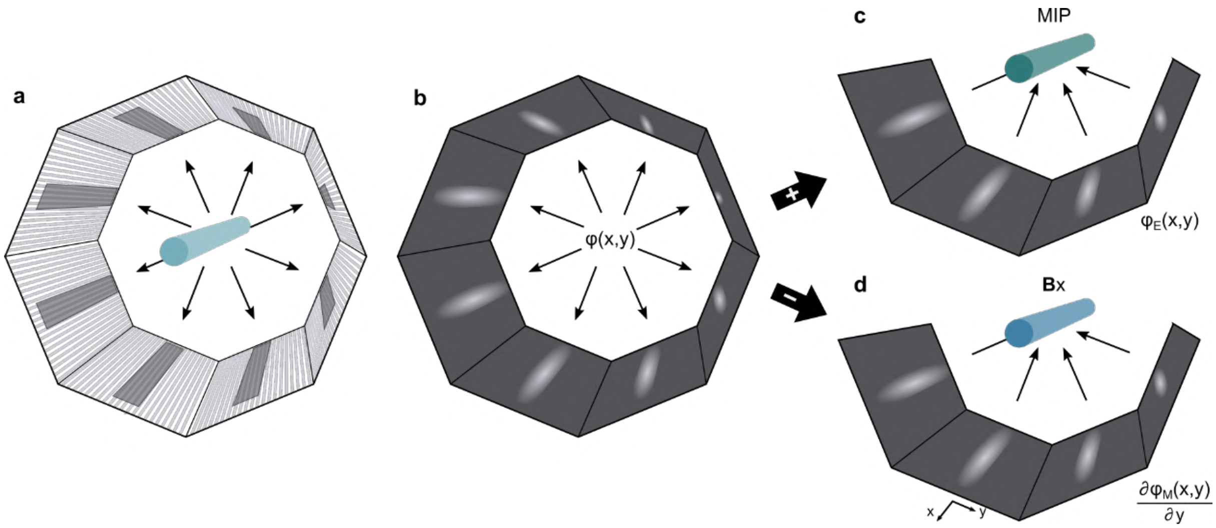

Figure 7.4: Principe de l'holographie électronique en champ vectoriel et du procédé de tomographie. (**a**) Série d'inclinaisons holographiques enregistrées de la nanostructure, couvrant idéalement une plage d'inclinaison de 360°. (**b**) Reconstruction holographique pour récupérer l'image de phase de chacune des projections holographiques de (**a**). La contribution électrostatique et magnétique au déphasage est alors séparée du calcul de la moitié de la somme ou de la différence (respectivement) entre les images de phase des projections opposées. (**c**) Les images de phase électrique peuvent ensuite être rétroprojetées pour obtenir une reconstruction tomographique 3D du potentiel électrique. (**d**) Les composantes du champ magnétique (B_x et B_y) sont récupérées séparément d'une différenciation dans la direction du plan perpendiculaire à l'axe d'inclinaison avant la reconstruction tomographique. Les séries d'inclinaison sont donc répétées pour deux axes d'inclinaison, idéalement avec une rotation de 90° l'un par rapport à l'autre, afin de récupérer les deux composantes du champ **B**.

tronique,[12,13] est illustré schématiquement sur la Figure 7.4. Elle commence par l'acquisition d'hologrammes, un avec l'objet, et un de référence, à chaque étape d'inclinaison. Idéalement, l'échantillon devrait être incliné de ±90° avec des incréments d'environ ±1°, pour enregistrer des projections à partir de 180°. Cette opération est répétée après avoir retourné l'échantillon pour enregistrer des hologrammes provenant des mêmes projections, mais opposées. Idéalement, cela donne une série complète d'hologrammes de 360° autour de l'axe de basculement, comme illustré sur la Figure 3.10a, où les flèches noires représentent les directions de projection. Ensuite, les images de phase sont reconstruites pour chacun des hologrammes électroniques dans la série d'inclinaison, comme dans le processus pour l'HE classique, comme illustré sur la Figure 3.10b. Les images de phase sont ensuite séparées en fonction de leur contribution électrostatique et magnétique au déphasage, en calculant respectivement la moitié de la somme ou la différence entre les deux images de phase de projections identiques mais opposées. On obtient ainsi une série d'inclinaisons de 180° pour chacune des contributions électrostatique et magnétique. En effectuant une reconstruction tomographique, on peut ensuite récupérer la distribution 3D du potentiel électrique (Figure 7.4c) ainsi que les composantes B_x et B_y du champ magnétique $\mathbf{B}$d. Pour reconstruire chacune des deux composantes de l'induction magnétique en 3D, des séries d'inclinaisons sont réalisées autour de deux axes d'inclinaison différents orthogonaux l'un par rapport à l'autre. À partir de chaque axe d'inclinaison, la composante axiale du champ magnétique en 3D est obtenue en différenciant l'image de phase magnétique par sa direction perpendiculaire avant le processus de reconstruction tomographique, comme indiqué sur la Figure 7.4d. Ensuite, la composante manquante de l'induction magnétique, B_z, peut être calculée en supposant que $\nabla\cdot\,\mathbf{B} = 0$ et en calculant les composantes projetées perpendiculaires à l'axe d'inclinaison dans une série (axe I), et l'utiliser pour remplacer dans la reconstruction de l'autre série d'inclinaison (axe II).[14] Les représentations vectorielles 3D résultantes sont appelées *tomogrammes.*Pour une explication plus détaillée de la reconstruction et du traitement des données, voir la publication de D. Wolf et al. (Communications Physics 2019)[15] et les informations complémentaires correspondantes.

Chap. 4 : Effets des changements structurels locaux sur la configuration magnétique des nanofils de CoNi

Pour contrôler les états d'aimantation et les mécanismes d'inversion, une analyse précise de la structure locale et de la configuration magnétique d'un seul nanofil est nécessaire. Les effets des variations locales des propriétés magnétiques, structurelles et chimiques d'un échantillon, et la façon dont les variations de l'un affectent les deux autres, doivent donc être étudiés avec une haute résolution spatiale pour être observés. Une étude aussi approfondie de la corrélation entre les différentes propriétés des échantillons exige des techniques polyvalentes et avancées avec une résolution spatiale et une sensibilité suffisantes, ce qui est unique à l'environnement MET. Dans l'étude présentée dans ce chapitre, nous exploitons cette polyvalence, en effectuant des mesures MET locales et quantitatives des caractéristiques magnétiques, structurelles et de composition des mêmes nanofils cylindriques de CoNi

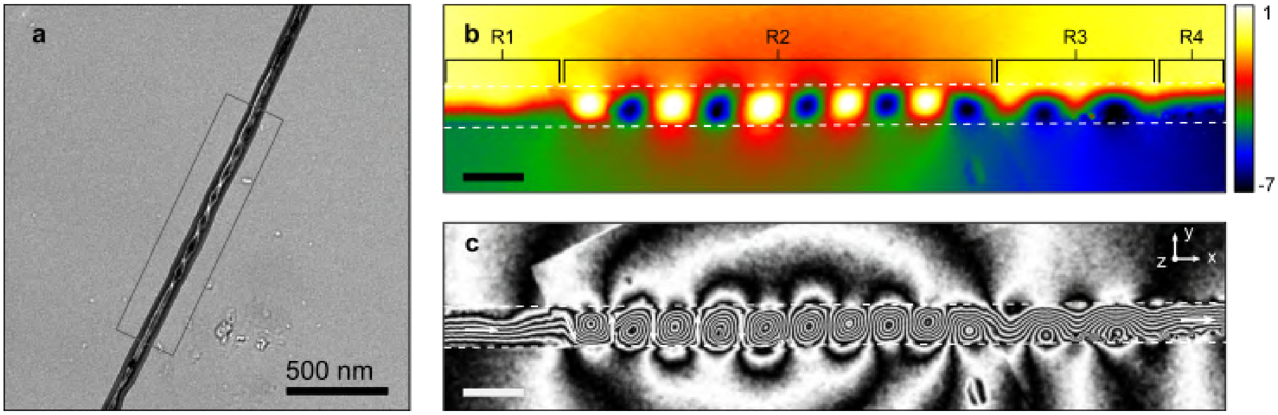

Figure 7.5: (**a**) Image de Fresnel montrant la région nanofils avec des changements locaux de la configuration magnétique. (**b**) Image de phase magnétique reconstruite à partir de l'HE, avec (**c**) montrant l'image de flux magnétique correspondante, les deux de la région nanofils dans la zone encadrée de (**a**). Les barres d'échelle en (**b**) et (**c**) indiquent 100 nm, et la région entre les lignes pointillées blanches marque la position NW.

à l'échelle du nanomètre. Les nanofils étudiés ici ont un diamètre moyen de 70 nm et une composition nominale de $Co_{85}Ni_{15}$, *i.e.*, une faible teneur en Ni.

La première étude de l'échantillon de nanofils de CoNi a porté sur la compréhension de la configuration magnétique locale et de son origine. L'état résiduel des nanofils de l'échantillon a donc été étudié à l'aide de l'HE, révélant une configuration magnétique complexe avec de grandes variations locales. Une cartographie structurale et spectroscopique complémentaire a été réalisée sur la même région que celle de l'imagerie magnétique, révélant une structure granulaire texturée composée de phases *cfc* et *hcp*. En corrélant les résultats des différentes techniques, nous avons trouvé de petites modulations dans la composition, ainsi que les changements dans les configurations magnétiques étaient liés à des variations locales dans la structure cristalline. Trois configurations magnétiques différentes ont été identifiées dans l'échantillon : une chaîne d'états tourbillonnaires transversaux, un état d'enroulement et une configuration de transition entre les deux états susmentionnés. Il ressort de l'étude corrélative que la chaîne d'états tourbillonnaires transversaux est située dans une région avec une phase cristalline *hcp* dont l'axe facile magnétocristallin (axe-c) est orienté à peu près perpendiculairement à l'axe des nanofils, tandis que les états d'enroulement ou de transition ont été trouvés dans des régions avec des phases *hcp* et *cfc* coexistant dans la même région de section transversale. Les simulations micromagnétiques ont confirmé la stabilisation de la

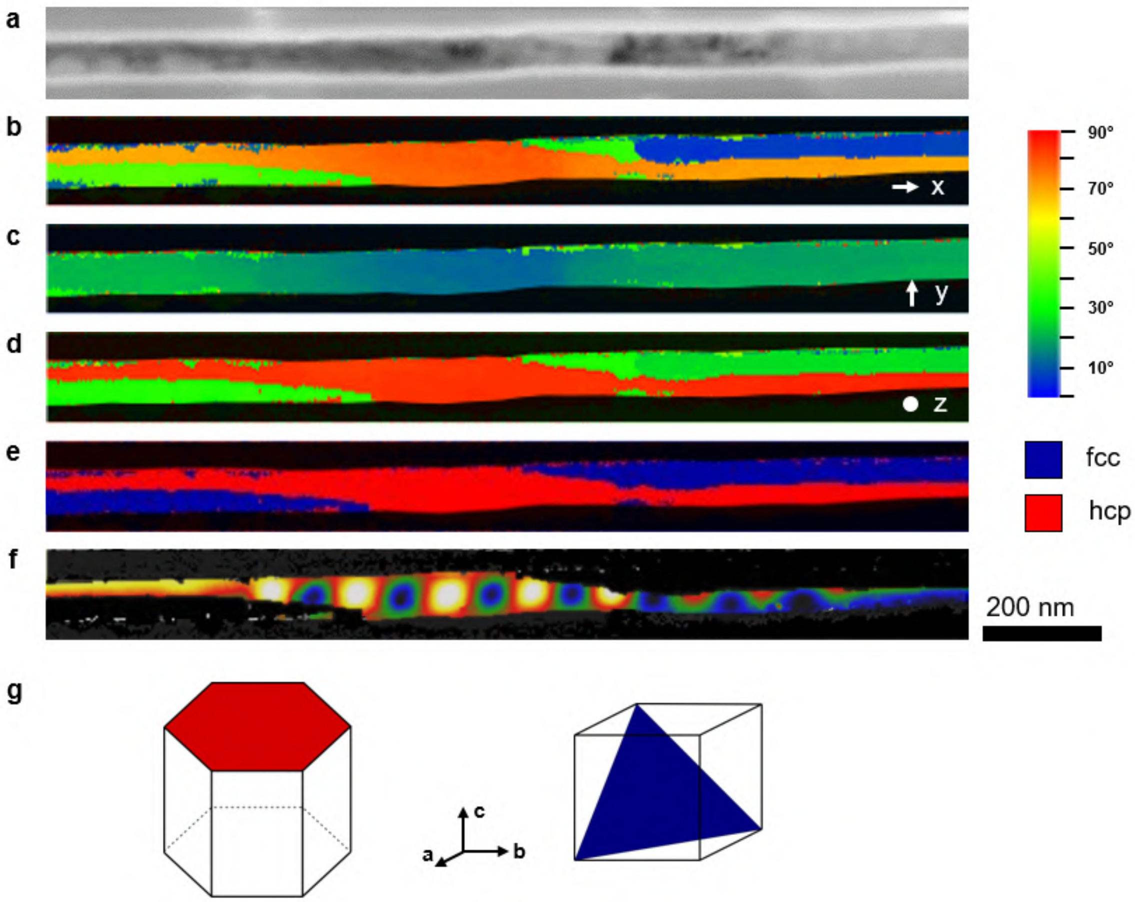

Figure 7.6: Résultats des mesures structurelles ASTAR de la région des nanofils. (**a**) Image spirituelle en champ clair de la région des nanofils cartographiée. (**b-d**) Cartes d'orientation du cristal de la région des nanofils dans (**a**) montrant les directions [111]*cfc* et [0001]*hcp* codées par couleur en fonction de l'écart angulaire par rapport aux directions (**b**) x-, (**c**) y- et (**z**). (**e**) Carte de la phase cristalline de la région des nanofils en (**a**), où la couleur bleue marque la phase *cfc* et la phase rouge *hcp*. (**f**) image de la phase magnétique montrant uniquement la région *hcp* de (**e**). (**g**) *hcp* et *fcc* plans serrés.

chaîne de tourbillons, ainsi qu'un état de tourbillon longitudinal dans un segment de nanofil de phase *hcp* monocristallin parfait, et qu'une phase *cfc* pure n'entraîne qu'une orientation parallèle des spins magnétiques le long de l'axe du fil.

La chaîne de tourbillons transversaux présentait une bonne correspondance entre les résultats expérimentaux et les simulations, ce qui a permis de quantifier les paramètres magnétiques du nanofil. La distance entre les noyaux des tourbillons dans la chaîne s'est avérée, par les simulations OOMMF micromagnétiques, varier partiellement avec l'aimantation de saturation, et a donc agi comme une bonne confirmation de sa valeur. Bien que l'existence d'un état d'enroulement dans le nanofil n'ait pas été complètement comprise à partir de cette étude, l'image de phase et la réduction du déphasage mesuré à travers l'axe du fil de l'état de tourbillon longitudinal trouvé dans certaines parties du segment *hcp* dans les simulations, ressemble aux caractéristiques de ce que nous avons appelé un état d'enroulement. Cela renforce donc notre hypothèse, mais des études supplémentaires étaient nécessaires pour conclure.

Bien que beaucoup de choses aient été révélées sur les configurations magnétiques de l'échantillon et sur la façon dont elles étaient liées aux inhomogénéités de la structure cristalline, l'étude nous a laissé avec quelques questions sans réponse, en particulier concernant l'existence et la nature de ce qu'on appelle le domaine du curling. À bien des égards, le fait que l'imagerie magnétique ne nous ait donné qu'une seule projection ainsi qu'une intégration de la contribution magnétique le long de celle-ci nous a semblé être le facteur le plus limitant pour comprendre ce système, car il s'était avéré très tridimensionnel dans sa texture de spin. Ce problème a été résolu en réalisant une étude de suivi à l'aide d'un VFET holographique pour la reconstruction 3D de l'induction magnétique, comme nous le verrons dans la suite de ce document. Cependant, il y a un autre aspect de cette expérience qui pourrait également être amélioré, à savoir la cartographie spectroscopique et structurelle. Là encore, il s'agit d'obtenir uniquement une représentation 2D d'une structure 3D. L'utilisation d'une technique de cartographie tomographique combinée avec ASTAR et EELS ou EDX pourrait apporter des informations supplémentaires, car nos résultats suggèrent que plusieurs grains, même avec une structure cristalline différente (*fcc* et *hcp*) peuvent coexister avec la même section transversale des nanofils.

Chap. 5 : États magnétiques 3D accordables en champ dans les nanofils de CoNi

Dans le prolongement de l'étude précédente, nous voulions réaliser de l'imagerie magnétique 3D sur le système de nanofils CoNi afin de caractériser et de comprendre la texture du spin dans les trois dimensions. Nous voulions également comprendre quand la chaîne observée de tourbillons transversaux se produit et tester l'effet de l'histoire magnétique en imaginant l'état

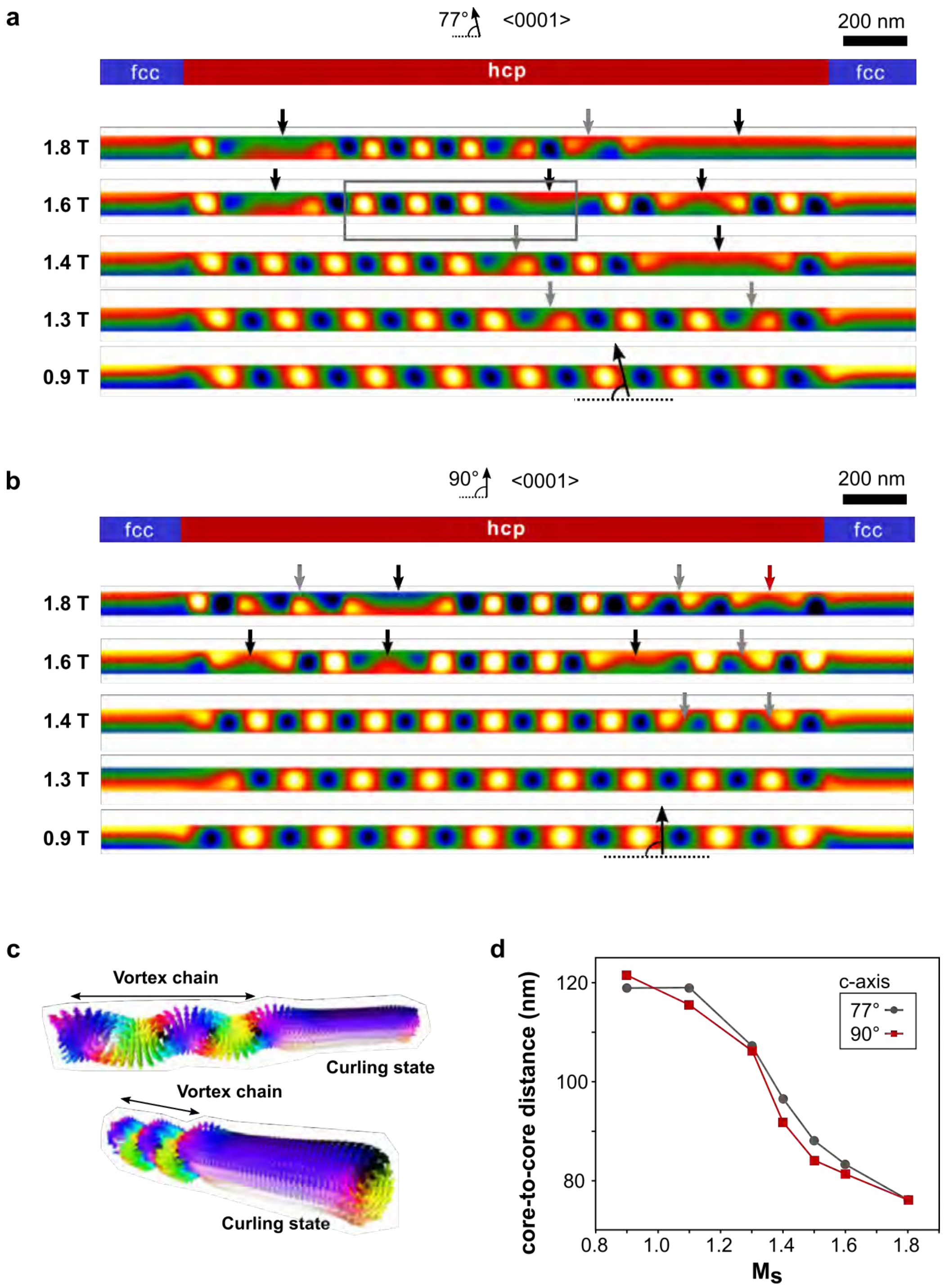

Figure 7.7: Résultats des simulations OOMMF de nanofils monocristallins *hcp* et *fcc*. (**a**) et (**b**) Haut : conteneur cylindrique simulé représentant le nanofil, avec le grain monocristallin *hcp* en rouge, entouré de deux régions *cfc*. En bas : image de phase magnétique simulée avec variation de l'aimantation de saturation, représentée pour l'orientation de l'axe facile magnétocristallin *hcp* de 77° et 90° par rapport à l'axe du nanofil, en (**a**) et (**b**), respectivement. Les flèches noires et grises marquent différentes configurations magnétiques. (**c**) Représentation vectorielle magnétique 3D de la région magnétique encadrée en (**a**). (**d**) Représentation graphique de la distance entre les tourbillons pour chaque simulation. Les tracés rouge et gris représentent respectivement l'orientation de l'axe c de 77° et 90°.

résiduel au niveau du grain *hcp* après l'application de deux champs de saturation différents : (i) perpendiculaire et (ii) parallèle à l'axe du fil. L'imagerie magnétique a été réalisée à l'aide du THCV, ce qui nous a permis de récupérer les trois composantes de l'induction magnétique dans le nanofil, révélant des configurations magnétiques complètement différentes pour les deux cas. Dans le cas d'un champ magnétique appliqué perpendiculairement à l'axe du nanofil, nous avons observé une chaîne de tourbillons transversaux, tandis que la saturation parallèle conduit à une configuration constituée de domaines de tourbillons longitudinaux séparés par des parois de domaines transversaux. On pense que ce dernier est le type de configuration magnétique que l'on appelle domaine de curling dans Chap. 4.

Les résultats des expériences d'holographie 3D, corrélés avec les simulations micromagnétiques, confirment les conclusions de l'étude précédente (Ch.4) et offrent de nouvelles perspectives et de nouveaux détails sur la configuration du spin magnétique de chacun des états. Pour la chaîne des tourbillons, nous apprenons que les noyaux des tourbillons pointent tous dans la même direction z positive qui est à la fois perpendiculaire à l'axe du fil et orthogonale à l'axe c de *hcp*, qui est la même direction que le champ de saturation appliqué. Cependant, la composante B_z mesurée est relativement faible par rapport aux composantes dans le plan (B_x et B_y). La chaîne de tourbillons transversaux peut être considérée comme une série de domaines transversaux dont l'aimantation pointe alternativement dans la direction y positive et négative, ce qui fait que les tourbillons transversaux constituent les parois des domaines. En conséquence, le système est comme un double réseau de Halbach, où l'existence des tourbillons agit pour réduire le champ parasite en dehors du nanofil. En ce qui concerne la configuration magnétique longitudinale, les domaines d'enroulement (tourbillons longitudinaux) pointent tous dans la même direction x positive, *i.e.* la direction du champ magnétique appliqué, cependant leur magnétisation tourne autour de l'axe du fil avec une hélicité opposée. Ce comportement, et l'existence d'une paroi de domaine transversale, ont été confirmés par des simulations micromagnétiques.

Bien que cette étude ait été réalisée à l'aide d'instruments THCV de pointe, nous n'avons pas réussi à résoudre tous les noyaux tourbillonnaires de la chaîne. Cependant, nous sommes actuellement à la limite de ce que nous pouvons obtenir de cette technique en raison de

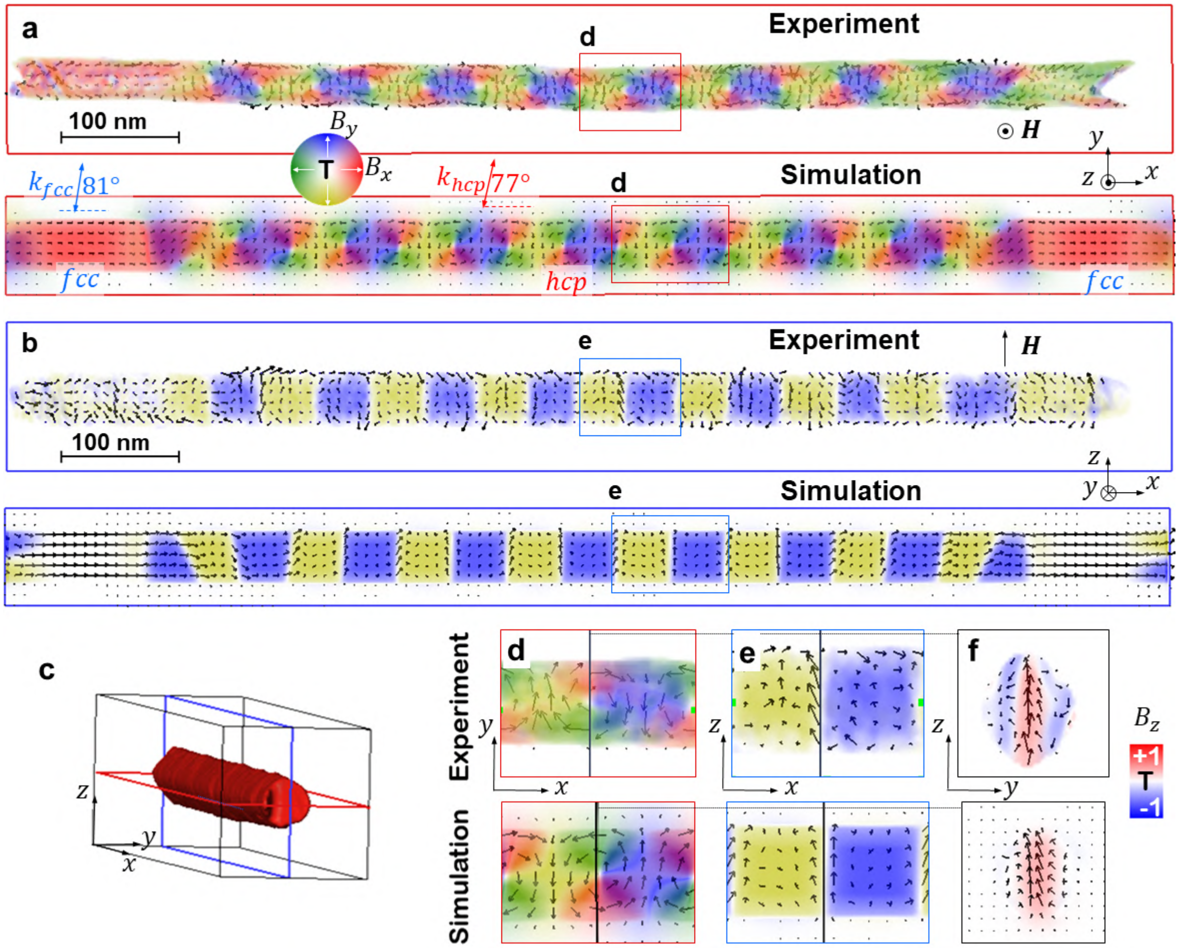

Figure 7.8: Reconstruction 3D du champ magnétique B à l'intérieur d'un nanofil de CoNi par THCV et comparaison avec la simulation micromagnétique après magnétisation du NW dans la direction z. (**a**) Tranche axiale centrale (xy) du champ B 3D dans le Nord-Ouest, représentée par un tracé fléché et un rendu volumique codé en couleur de B_x et B_y selon la roue de couleur révélant une chaîne de tourbillons dans la région *hcp*. (**b**) Axe central (xz)-coupe à travers le champ 3D B à l'intérieur du NO visualisé par un diagramme en flèches et un rendu de volume codé par couleurs de B_y. (**c**) Rendu iso-surface du potentiel électrostatique, obtenu par THCV, montre la morphologie du nanofil. La position des tranches axiales (a) et (b) est représentée par des rectangles rouges et bleus. (**d**,**e**) Zoom avant des régions indiquées en (a) et (b). (**f**) Coupe transversale (yz) à travers le noyau du vortex marqué comme une ligne verticale noire en (d,e), superposée par la composante B_z à code couleur.

sa configuration déjà complexe, ainsi que d'aspects tels que l'effet de perte de coin, qui est un problème courant parmi les techniques tomographiques. Une façon de contourner ce problème pourrait être d'effectuer des simulations détaillées d'un tourbillon transversal et de rendre des images de phase simulées à partir de différentes projections et de les comparer aux images de phase magnétique expérimentales recueillies par HE pour les mêmes orientations.

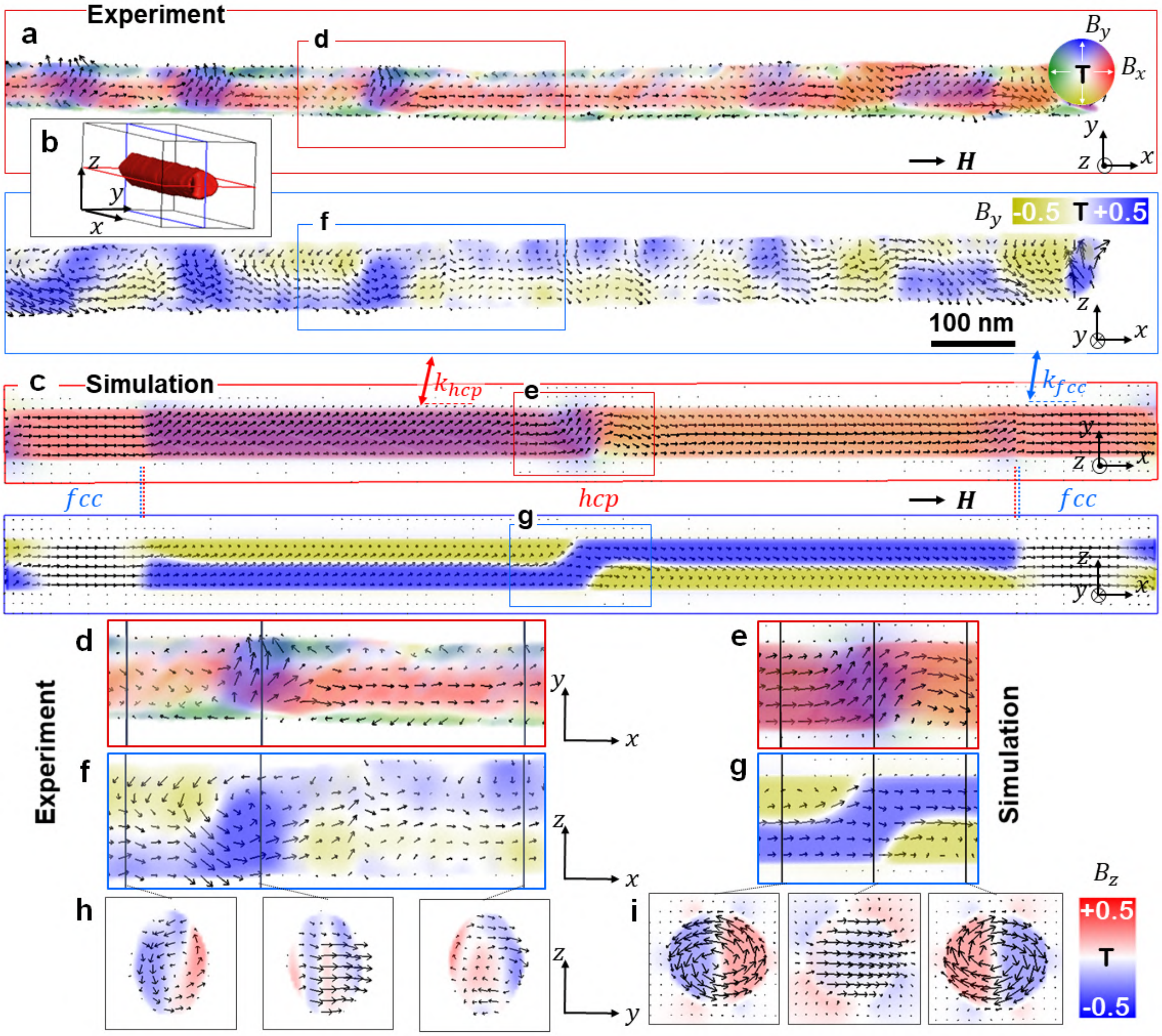

Figure 7.9: Reconstruction 3D du champ magnétique B à l'intérieur d'un nanofil de CoNi par THCV et comparaison avec la simulation micromagnétique après magnétisation du NW dans la direction axiale x. (**a**) Des coupes centrales dans la direction axiale (xy) et (xz) à travers le champ B 3D à l'intérieur du NO visualisé par des flèches et un rendu de volume codé en couleur de B_x et B_y révèlent une image complexe dans la région *hcp*. (**b**) Le rendu iso-surface du potentiel électrostatique obtenu par la THCV montre la morphologie des nanofils. Les positions des tranches axiales **a** sont représentées par des rectangles rouges et bleus. (**c**) Modèle micromagnétique du nanofil en supposant une région *hcp* entre une région *cfc* avec les axes d'anisotropie cristalline correspondants k_{hcp} et k_{cfc}. (**d-g**) Zoom avant des régions indiquées en **a** et **c**. (**h**,**i**) Les coupes transversales (yz) aux positions indiquées par des lignes verticales noires dans **d-g** superposées par la composante B_z à code couleur montrent la transition entre deux états tourbillonnaires de chiralité opposée séparés par une paroi de domaine transversale.

Bien que cette méthode soit moins idéale que l'idée de pouvoir réaliser une holographie tomographique d'un seul état de vortex transversal, elle donnerait la résolution suffisante pour résoudre un petit noyau de vortex. Il pourrait également être intéressant d'essayer de combiner la technique de pointe du THCV avec le microscope interférométrique costumé I2TEM, et un logiciel de stabilisation nouvellement ajouté, qui pourrait potentiellement améliorer la résolution spatiale finale des tomogrammes reconstruits.

Chap. 6 : Études préliminaires sur le transport magnétique *in situ* dans le MET

Enfin, une étude préliminaire concernant le changement des configurations magnétiques caractérisées dans les nanofils de CoNi lorsqu'ils sont soumis à un champ magnétique appliqué de l'extérieur ou à un courant électrique a été présentée. Ce travail avait un double objectif :

- Du point de vue de la physique, l'objectif était de tester la stabilité, la reproductibilité et le déplacement des parois de domaine observées et des configurations magnétiques formées dans les nanofils.
- Comme deuxième objectif, je voulais développer une méthode expérimentale et un protocole pour réaliser des expériences de polarisation *in situ* sur des nanofils contactés dans l'I2TEM, car cela n'était pas encore établi dans notre laboratoire.

Bien qu'il y ait encore de nombreuses améliorations à apporter sur ce dernier point, j'ai présenté un développement expérimental qui a réussi à injecter un changement détectable de la configuration magnétique dans le nanofil contacté. J'ai donc réalisé deux types d'expériences d'imagerie de Fresnel *in situ* dans l'I2TEM : en appliquant un champ magnétique externe, et en injectant une impulsion électrique.

Pour les expériences de champ magnétique *in situ*, j'ai testé la stabilité et la reproductibilité d'une chaîne de vortex en orientant le champ soit le long de l'axe NW, soit perpendiculairement à celui-ci avec des angles différents. La chaîne de tourbillons a été anéantie en appliquant une composante parallèle du champ magnétique d'environ 55 mT. En outre, la chaîne de tourbillons a été reproduite de manière cohérente lorsqu'un champ de saturation a été appliqué perpendiculairement à l'axe du fil avec une inclinaison nulle, alors que pour

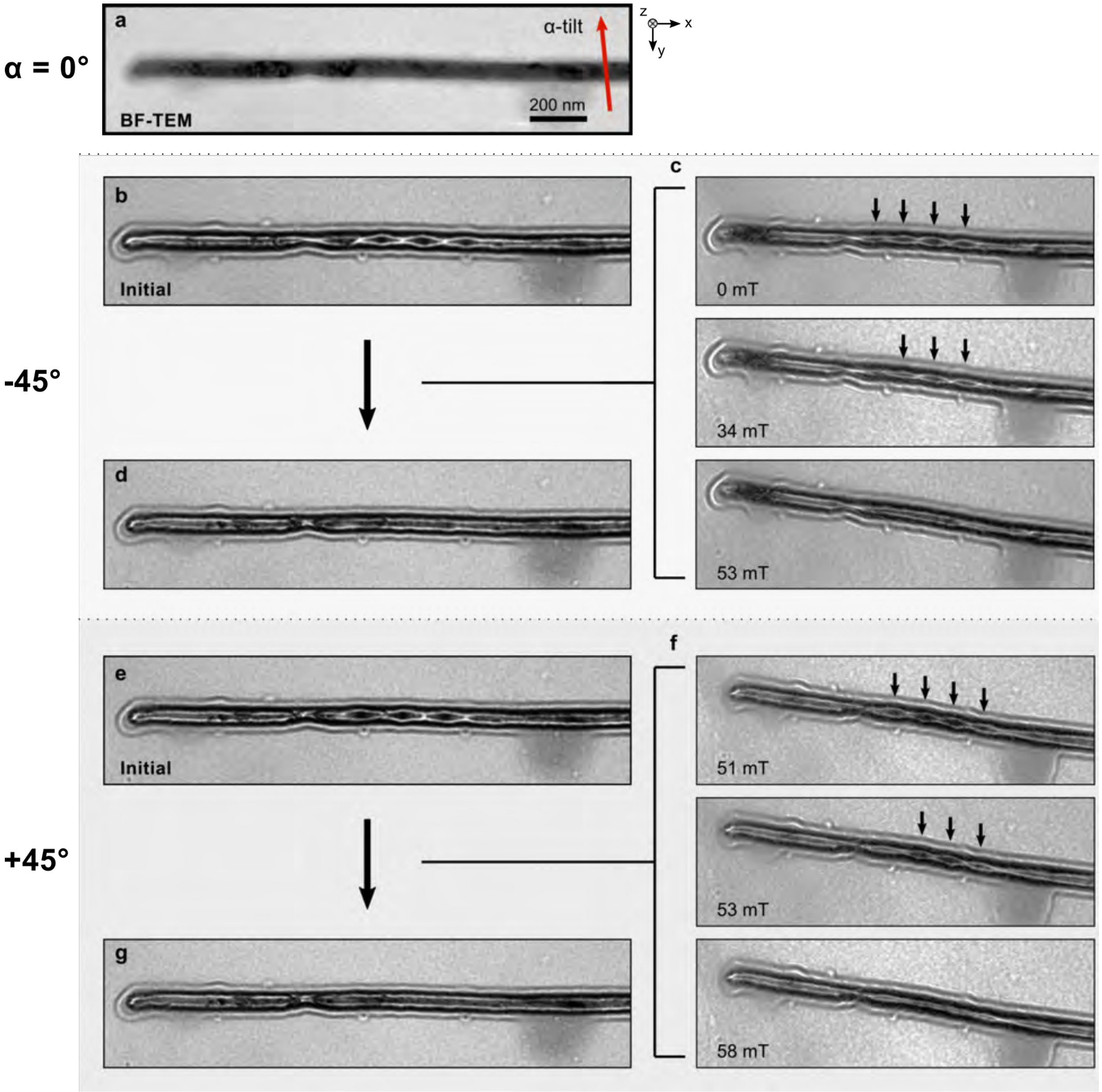

Figure 7.10: Résultats de l'application du champ magnétique *in situ* le long de l'axe des nanofils. (**a**) Image MET en champ clair du nanofil étudié, où la flèche rouge indique l'axe d'inclinaison α. (**b**)-(**g**) Images de Fresnel montrant le changement de configuration magnétique par rapport au champ appliqué le long de l'axe nanofil dans les directions x positive et négative en répétant la mesure à -45° (**b**)-(**d**) et +45° (**e**)-(**g**) α-tilt.

différentes projections (±15° inclinaison autour de l'axe du fil), elle n'a stabilisé qu'une chaîne de tourbillons réduite, ou pas de chaîne du tout (domaine du curling). Cela prouve l'existence d'une orientation idéale du champ magnétique par rapport au nanofil qui serait liée à l'orientation du grain *hcp* où se forme la chaîne de tourbillons, où le champ appliqué

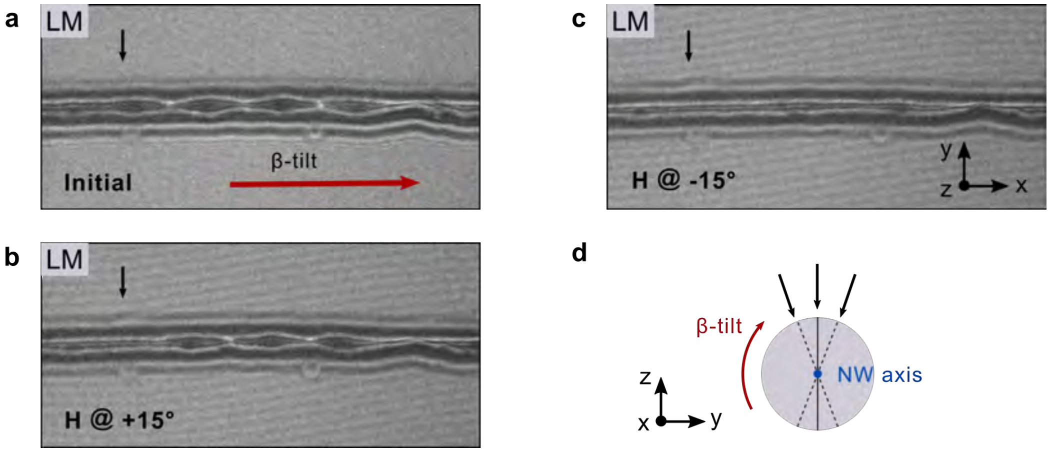

Figure 7.11: Résultats de l'application du champ magnétique *in situ* à différentes projections perpendiculaires à l'axe des nanofils. (**a**) Image de Fresnel sur-focalisée de l'état magnétique initial obtenue après application d'un champ de -1,9 T (hors du plan). Les images ont été enregistrées à l'état résiduel après application d'un champ de saturation de +1,9 T (dans le plan) à une inclinaison de β de, (**b**) +15° et (**c**) -15 °. La flèche rouge dans (**a**) indique l'axe d'inclinaison β. Toutes les images affichées sont enregistrées avec une inclinaison de 0°. (**d**) Schéma de la section des nanofils, où les flèches noires indiquent la direction du champ magnétique à différents angles d'inclinaison.

devrait être perpendiculaire à l'axe du fil, ainsi qu'orthogonal à l'axe facile magnétocristallin (axe c). De plus, une petite chaîne de vortex et une paroi de domaine tête à tête entre deux états de frisage ont été manipulées par l'injection d'une impulsion électrique à l'aide du dispositif expérimental de polarisation *in situ* présenté. La présence de parois de domaine épinglées aux interfaces des grains de cristal a également été observée.

Bien que seuls des résultats qualitatifs aient été obtenus à partir des changements observés dans la configuration magnétique déclenchés par l'injection d'impulsions, de nombreuses solutions ont été présentées pour améliorer l'échantillon et le dispositif expérimental afin d'obtenir des mesures quantitatives qui accompagneront les observations magnétiques lors d'expériences futures. Les puces électroniques devraient être améliorées et entièrement caractérisées avant les expériences, ainsi que les contacts des nanofils devraient être améliorés pour obtenir des contacts en or lithographiés à faible résistivité, pour des mesures électroniques fiables. En outre, on estime que le système actuel est limité par la largeur de bande du porte-échantillon et la lenteur de l'enregistrement des données, ce qui nous empêche, respectivement, d'envoyer des impulsions de l'ordre de la nanoseconde et d'imager les processus de commutation ou de relaxation magnétique avant et après le mouvement de la paroi du do-

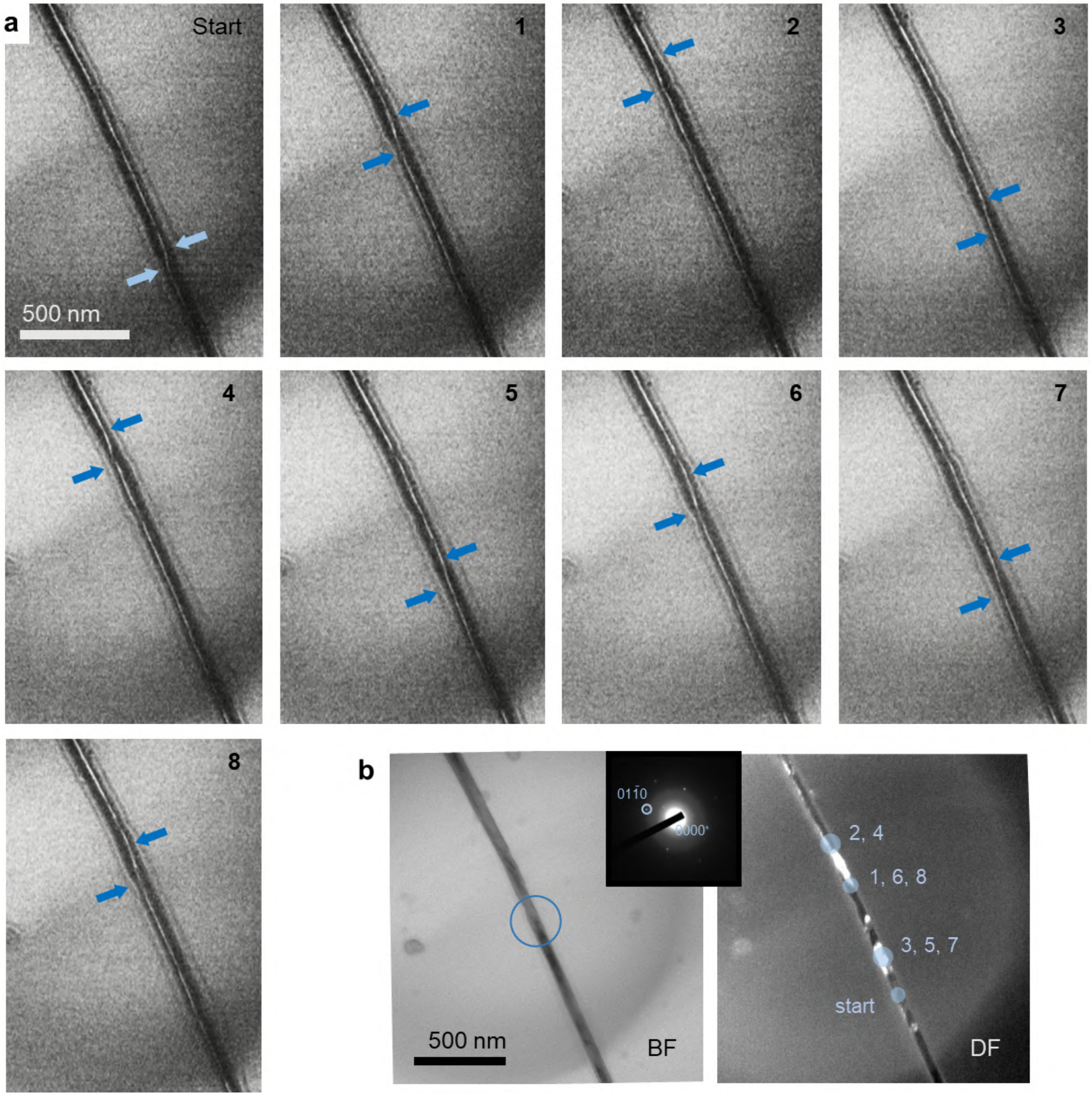

Figure 7.12: Vue d'ensemble de la propagation de la paroi du domaine par injection d'impulsions électriques *in situ* échantillon(**a**) Images de Fresnel sur-focalisées montrant l'état initial et les états détendus après huit injections d'impulsions consécutives. La paroi du domaine commence et se termine dans chaque cas est marquée par des flèches bleues. (**b**) Montre l'image MET en champ clair et l'image MET en champ sombre de la région du nanofil inspecté. L'image MET en champ sombre est formée en utilisant le point de diffraction marqué dans le modèle de diffraction (encadré) réalisé par la diffraction électronique de la zone sélectionnée sur la région encerclée dans l'image MET en champ clair. Les régions bleu clair marquées dans l'image MET en champ sombre correspondent à une position de la paroi du domaine après les impulsions indiquées.

maine. Ce sont autant de points qui devraient être améliorés pour la conduite d'expériences futures. Bien qu'il y ait de nombreuses améliorations à apporter pour parvenir à un dispositif *in situ* idéal pour effectuer des mesures de déplacement de la paroi du domaine, il existe des solutions concrètes à tous les problèmes existants, et je suis donc convaincu que nous atteindrons l'objectif, étant donné le temps et l'argent nécessaires pour réaliser les mises à niveau requises, dont beaucoup sont déjà en cours. Parmi les étapes d'amélioration qui ont déjà été lancées, il y a la production de nouvelles puces fiables avec des membranes transparentes aux électrons, l'installation d'une étape de broyage de l'argon dans la chambre avant la pulvérisation d'or pour le contact lithographique interne, le processus de commande d'une caméra à détection directe qui est plus sensible et plus rapide que la caméra existante, et les discussions en cours pour acquérir un porte-échantillon à haute fréquence de polarisation.

Chap. 7 : Conclusion générale et perspectives d'avenir

Le travail présenté dans cette thèse est un exemple de la flexibilité et de la diversité du MET et de la manière dont une variation de techniques peut être utilisée pour obtenir des informations locales et détaillées sur les propriétés d'une nanostructure et leurs configurations magnétiques par des études corrélées, à la fois en 2D et 3D.

Les configurations magnétiques intéressantes et accordables qui se stabilisent dans les régions de phase *hcp* sont une motivation pour développer des nanofils *hcp* parfaitement monocristallins dont l'axe c est perpendiculaire à l'axe du fil. Une telle structure permettrait aux longues chaînes de tourbillons de s'étendre sur la plus grande partie du fil, et de se propager sans être annihilées par le changement de phase du cristal. Le nanofil optimal aurait idéalement une section cylindrique uniforme, et une longueur de fil d'au moins 10 μm pour faciliter le contact. Pour produire ces nanofils idéaux, il serait nécessaire de mener une étude pour optimiser la croissance des nanofils.

En outre, il serait intéressant que la longueur de la chaîne de tourbillons dans un nanofil aussi uniforme *hcp* puisse être variée et contrôlée en utilisant un champ magnétique local avec une zone définie. En sachant que les états tourbillonnaires ne se stabilisent que lorsqu'on applique un champ magnétique orthogonal à l'axe des nanofils et à l'axe c, on pourrait éventuellement utiliser des têtes d'écriture magnétiques à angle différent pour former des tourbillons ou les annihiler (former un état d'enroulement) en fonction de l'orientation du champ. En outre, si l'on peut trouver un moyen de contrôler la direction ou la rotation du tourbillon, peut-être en appliquant des champs positifs ou négatifs, ils pourraient potentiellement être utilisés comme bits de mémoire pour les dispositifs à semi-conducteurs, avec trois états de lecture/écriture (haut, bas, curling). Si l'on peut également obtenir une propagation stable et contrôlée des états par injection de courant, cette structure aurait un grand impact pour les nouveaux dispositifs Spintronic basés sur la mémoire de piste de course.[16] D'un point de vue pratique, une expérience aussi complexe nécessiterait non seulement des mesures quantitatives fiables, mais aussi l'intégration de têtes d'écriture électromagnétiques contactées. Cela nécessiterait des procédures supplémentaires de préparation d'échantillons de procédés lithographiques, et les connaissances nécessaires pour produire des têtes d'écriture à petite échelle et de haute qualité.

En outre, il y a aussi l'analogie de la chaîne de tourbillons qui est considérée comme un double tableau de Halbach. On peut en déduire qu'un courant électrique pourrait induire une oscillation lors de son passage à travers la configuration de la chaîne de tourbillons, comme pour les onduleurs à aimants permanents.[17] Cela pourrait potentiellement produire un rayonnement dont la longueur d'onde dépendrait de la périodicité de la chaîne de tourbillons,[18] comme pour les lasers à électrons libres, ce qui serait très intéressant pour une application dans les dispositifs de communication. Une telle expérience peut être réalisée en utilisant des mesures de détection de rayonnement sur un nanofil contacté.

Les expériences proposées, très avancées, nécessiteraient la combinaison des connaissances et de l'expertise de plusieurs domaines disciplinaires au sein des nanotechnologies, notamment la micro et la nanofabrication avancées (croissance de nanofils, contact électrique, fabrication de têtes d'écriture magnétiques), le nanomagnétisme statique et dynamique, les techniques d'imagerie et de mesure magnétiques sensibles et les connaissances techniques sur les dispositifs électromagnétiques et les têtes de lecture. Comme peu de laboratoires sont spécialisés dans tous ces domaines, ce projet pourrait être réalisé grâce à une étroite collaboration entre les différentes installations de recherche. Ces perspectives montrent le potentiel restant de cette structure de nanofils pour de nouvelles recherches passionnantes qui pourraient avoir un grand impact sur le développement de futurs dispositifs à l'état solide.

References

[1] D. B. Williams and C. B. Carter. *Transmission Electron Microscopy.* Springer, 2007. ISBN: 978-0-387-76501-3.

[2] L. A. Rodríguez. "In Situ Lorentz Microscopy and Electron Holography in Magnetic Nanostructures". PhD thesis. Université Toulouse III Paul Sabatier, 2014.

[3] Y. Zhu, ed. *Modern Techniques for Characterizing Magnetic Materials.* Springer, 2005. DOI: 10.1007/b101202.

[4] M. de Graef and Y. Zhu. *Magnetic Imaging and Its Applications to Materials.* Academic Press, 2000. ISBN: 9780080531373.

[5] A. Tonomura. "Applications of Electron Holography". In: *Reviews of Modern Physics* **59** (1987), pp. 639–669. DOI: 10.1103/RevModPhys.59.639.

[6] A Tonomura. *Electron Holography.* 2nd ed. Springer, 1999. ISBN: 978-3-642-08421-8.

[7] J. M. Cowley. "Twenty Forms of Electron Holography". In: *Ultramicroscopy* **41** (1992), pp. 335–348. DOI: 10.1016/0304-3991(92)90213-4.

[8] P. A. Midgley and R. E. Dunin-Borkowski. "Electron Tomography and Holography in Materials Science". In: *Nature Materials* **8** (2009), pp. 271–280. DOI: 10.1038/nmat2406.

[9] P. A. Midgley. "An Introduction to Off-Axis Electron Holography". In: *Micron* **32** (2001), pp. 167–184. DOI: 10.1016/S0968-4328(99)00105-5.

[10] A. Tonomura et al. "Holographic Interference Electron Microscopy for Determining Specimen Magnetic Structure and Thickness Distribution". In: *Physical Review B* **34** (1986), pp. 3397–3402. DOI: 10.1103/PhysRevB.34.3397.

[11] D. Wolf et al. "Electron Holographic Tomography". In: *Current Opinion in Solid State and Materials Science* **17** (2013), pp. 126–134. DOI: 10.1016/j.cossms.2013.05.002.

[12] D. Wolf et al. “3D Magnetic Induction Maps of Nanoscale Materials Revealed by Electron Holographic Tomography”. In: *Chemistry of Materials* **27** (2015), pp. 6771–6778. DOI: 10.1021/acs.chemmater.5b02723.

[13] P. Simon et al. “Synthesis and Three-Dimensional Magnetic Field Mapping of Co2FeGa Heusler Nanowires at 5 Nm Resolution”. In: *Nano Letters* **16** (2016), pp. 114–120. DOI: 10.1021/acs.nanolett.5b03102.

[14] C. Phatak, M. Beleggia, and M. De Graef. “Vector Field Electron Tomography of Magnetic Materials: Theoretical Development”. In: *Ultramicroscopy* **108** (2008), pp. 503–513. DOI: 10.1016/j.ultramic.2007.08.002.

[15] D. Wolf et al. “Holographic Vector Field Electron Tomography of Three-Dimensional Nanomagnets”. In: *Communications Physics* **2** (2019), pp. 1–9. DOI: 10.1038/s42005-019-0187-8.

[16] S. S. P. Parkin, M. Hayashi, and L. Thomas. “Magnetic Domain-Wall Racetrack Memory”. In: *Science* **320** (2008), pp. 190–194. DOI: 10.1126/science.1145799.

[17] J. B. Majernik N.; Rosenzweig. “Halbach Undulators Using Right Triangular Magnets”. In: *Physical Review Accelerators and Beams* **22** (2019), p. 092401. DOI: 10.1103/PhysRevAccelBeams.22.092401.

[18] J. Bahrdt. “Shaping Photon Beams with Undulators and Wigglers”. In: *Synchrotron Light Sources and Free-Electron Lasers: Accelerator Physics, Instrumentation and Science Applications*. Ed. by E. J. Jaeschke et al. 1st ed. Springer, 2020. Chap. 16, pp. 851–933. ISBN: 978-3-030-23201-6.

Summary In this thesis, we have performed quantitative mappings on cylindrical CoNi nanowires (NW) by electron holography (EH) and holographic vector field electron tomography (VFET). The magnetic information has been correlated with quantitative structural and compositional measurements to study their effect on the magnetic configurations, and give a detailed description of the system. Holographic VFET was done on two different remnant states after being saturated (i) perpendicular and (ii) parallel to the wire axis. The results show two distinctly different magnetic configurations, revealing the ability to tune the relaxed states by the applications of external fields in different directions. Finally, a protocol for realizing in situ electric pulse injections in NWs to observe domain wall movements by Lorentz microscopy is presented together with a call to action for developments of the technique in order to get quantitative results using in situ EH observations.

Résumé Dans ce travail de thèse, nous avons réalisé des cartographies quantitatives de nanofils cylindriques de CoNi par holographie électronique (HE) et tomographie holographique de champ vectoriel (THCV). L'information magnétique a été corrélée avec les propriétés structurales et chimiques afin d'étudier leurs effets sur les configurations magnétiques et obtenir une description complète des nanofils. La technique THCV a été appliquée sur des états rémanents différents obtenus après une saturation magnétique appliquée parallèlement ou perpendiculairement à l'axe des nanofils. L'apparition de deux configurations magnétiques distinctes démontre qu'il est possible de contrôler l'état magnétique rémanent par l'application d'un champ magnétique externe selon différentes directions. Nous avons également défini un protocole précis pour réaliser in situ des injections d'impulsions de courant dans les nanofils et ainsi observer directement le mouvement de parois de domaines magnétiques par microscopie de Lorentz. Pour conclure, des pistes de développements de ces expériences in situ sont présentées pour réaliser des observations quantitatives en HE.